

INFORMATION TO USERS

This was produced from a copy of a document sent to us for microfilming. While the most advanced technological means to photograph and reproduce this document have been used, the quality is heavily dependent upon the quality of the material submitted.

The following explanation of techniques is provided to help you understand markings or notations which may appear on this reproduction.

1. The sign or "target" for pages apparently lacking from the document photographed is "Missing Page(s)". If it was possible to obtain the missing page(s) or section, they are spliced into the film along with adjacent pages. This may have necessitated cutting through an image and duplicating adjacent pages to assure you of complete continuity.
2. When an image on the film is obliterated with a round black mark it is an indication that the film inspector noticed either blurred copy because of movement during exposure, or duplicate copy. Unless we meant to delete copyrighted materials that should not have been filmed, you will find a good image of the page in the adjacent frame.
3. When a map, drawing or chart, etc., is part of the material being photographed the photographer has followed a definite method in "sectioning" the material. It is customary to begin filming at the upper left hand corner of a large sheet and to continue from left to right in equal sections with small overlaps. If necessary, sectioning is continued again—beginning below the first row and continuing on until complete.
4. For any illustrations that cannot be reproduced satisfactorily by xerography, photographic prints can be purchased at additional cost and tipped into your xerographic copy. Requests can be made to our Dissertations Customer Services Department.
5. Some pages in any document may have indistinct print. In all cases we have filmed the best available copy.

University
Microfilms
International

300 N. ZEEB ROAD, ANN ARBOR, MI 48106
18 BEDFORD ROW, LONDON WC1R 4EJ, ENGLAND

8018924

HEMBREE, LOUIS ARTHUR, JR.

AN INVESTIGATION OF SATELLITE-RADAR CORRELATION FUNCTIONS

The University of Oklahoma

PH.D.

1980

University
Microfilms
International

300 N. Zeeb Road, Ann Arbor, MI 48106

18 Bedford Row, London WC1R 4EJ, England

THE UNIVERSITY OF OKLAHOMA
GRADUATE COLLEGE

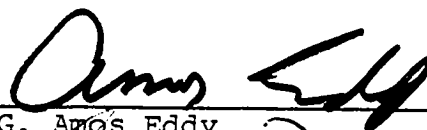
AN INVESTIGATION OF SATELLITE-RADAR CORRELATION FUNCTIONS

A DISSERTATION
SUBMITTED TO THE GRADUATE FACULTY
in partial fulfillment of the requirements for the
degree of
DOCTOR OF PHILOSOPHY

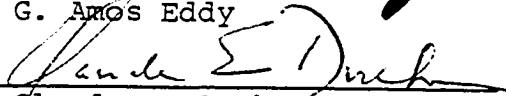
By
LOUIS A. HEMBREE
Norman, Oklahoma

1980

AN INVESTIGATION OF SATELLITE-RADAR CORRELATION FUNCTIONS



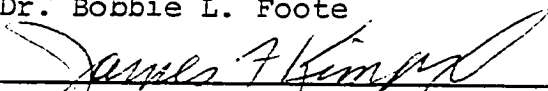
Dr. G. Amos Eddy



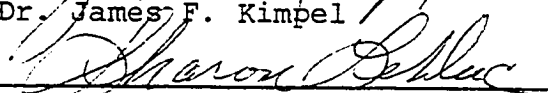
Dr. Claude E. Duchon



Dr. Bobbie L. Foote



Dr. James F. Kimpel



Dr. Sharon LaDuc

ACKNOWLEDGEMENTS

I would like to thank Dr. Amos Eddy for his creative supervision, encouragement, and helpful suggestions in this research effort. The author's appreciation is also extended to Dave Matthews of the U.S. Bureau of Reclamation (now the Department of Interior's Water and Power Resources Service) for his assistance in the execution of computer programs and for his continued interest in this project. I am also grateful to the following members of my dissertation committee: Dr. Claude Duchon, Dr. Bobbie Foote, Dr. Jeff Kimpel, and Dr. Sharon LeDuc.

Mrs. Lynda Hooper's expert help in the preparation of this manuscript was invaluable.

I would also like to express my gratitude to my family for their patience during this period. Their undying support was invaluable in the completion of this research.

Lastly, acknowledgement is made to the U.S. Bureau of Reclamation for support of this project under Contract Number 9-07-85-V0024.

ABSTRACT

The estimation of surface rainfall using satellite imagery has been the topic of much discussion in recent years. Several approaches to this problem have been developed by other researchers, and several of these are briefly reviewed. A multivariate optimal interpolation objective analysis which combines satellite, radar, and gage data will give improved results. This report addresses the problems of combining the radar and satellite data sets through the use of space time correlation fields.

These correlation fields represent the storm structure as implied by the observed data. The correlation fields are modeled using a four-dimensional Gaussian damped cosine function whose parameters reflect the storm characteristics. The function fitting also gives an estimate of the noise present in the data. The parameters of the model correlation function can also be used to classify storms with respect to their structural characteristics.

Several Montana convective storm complexes have been studied to determine the correlation fields (auto and cross) which are required for the application of optimum interpolation objective analysis and for the classification of the

storms. It is shown that suitable correlation fields can be obtained with respect to the auto-correlation fields; however, it is also shown that a more general correlation model may be required for the cross-correlation fields because these tend to be multimodal. The correlations between the satellite data and radar derived rain rates at the modes were found to range from an order of 0.2 to 0.53 at the space-time lags appropriate to maximizing the correspondence between patterns; consequently, the potential value of using the multivariate objective analysis methodology is established.

TABLE OF CONTENTS

	Page
ACKNOWLEDGEMENTS	iii
ABSTRACT	iv
LIST OF ILLUSTRATIONS	viii
LIST OF TABLES	xv
 Chapter	
I. INTRODUCTION	1
II. PREVIOUS RESEARCH	4
III. APPROACH	10
1. Objective Analysis	11
2. Covariance Model	19
3. Sensor Placement	25
IV. DATA	30
1. Radar Data	32
2. Satellite Data	33
3. Temperature Gradient	35
4. Satellite Navigation	36
5. Effects of Misnavigation	37
6. Effects of Instrument Resolution	42
V. DATA ANALYSIS	44
1. Convective Complex Number Two	46
a. Radar Rain Rates	49
b. Visible Reflectance	58
c. Infrared Temperature	65
d. Infrared Temperature Gradient Component .	70
e. Infrared Temperature Cross Visible Reflec-	
tance	74
f. Infrared Temperature Gradient Component	
Cross Visible Reflectance	81

	Page
g. Radar Rain Rates Cross Visible Reflec- tance	82
h. Radar Rain Rates Cross Infrared Temperature	84
i. Radar Rain Rates Cross Infrared Temperature Gradient Component	86
2. Convective Complex Three	88
a. Radar Rain Rates	90
b. Visible	92
c. Infrared Temperature	104
d. Infrared Temperature Gradient Component ..	106
e. Infrared Temperature Cross Visible Reflec- tance	110
f. Infrared Temperature Gradient Component Cross Visible Reflectance	111
g. Radar Rain Rates Cross Visible Reflectance	113
h. Radar Rain Rates Cross Infrared Temperature	115
i. Radar Rain Rates Cross Infrared Temperature	118
3. Convective Complex Number Five.....	118
a. Radar Rain Rates	119
b. Visible Reflectance	124
c. Infrared Temperature	126
d. Infrared Temperature Gradient Component ..	132
e. Infrared Temperature Cross Visible Reflec- tance	134
f. Infrared Temperature Gradient Component Cross Visible Reflectance	137
g. Radar Rain Rates Cross Visible Reflectance	141
h. Radar Rain Rates Cross Infrared Temperature	146
i. Radar Rain Rates Cross Infrared Temperature Gradient Component	147
4. Convective Complex Number Six	147
a. Radar Rain Rates	150
b. Visible Reflectance	154
c. IR Temperature	164
d. Infrared Temperature Gradient Component ..	169
e. Infrared Temperature Cross Visible Reflec- tance	172
f. Infrared Temperature Gradient Component Cross Visible Reflectance	172
g. Radar Rain Rates Cross Visible Reflectance	174
h. Radar Rain Rates Cross Infrared Temperature	175
i. Radar Rain Rates Cross Infrared Temperature Gradient Component	176
VI. SUMMARY AND CONCLUSIONS	177
BIBLIOGRAPHY	190

LIST OF ILLUSTRATIONS

Figure	Page
1. Scofield and Oliver's decision tree	6
1. Scofield and Oliver's decision tree (Continued)	7
2. Example of correlation matrix for radar derived rain rates	13
3. Results of univariate gage objective analysis ...	16
4. Results of univariate radar objective analysis ..	17
5. Results of bivariate gage-radar objective analysis	18
6. Change in the PAM sensor positions due to optimi- zation using the experimental design approach ...	28
7. HIPLEX experimental site	31
8. Relationship between longitude and latitude lines, horizontal and vertical scan lines, and the pixel	36
9. Objective analysis of satellite reflectance and IR temperature and radar rain rates for 1930 GMT ...	48
10. Objective analysis of radar data on finer grid ..	49
11. Plot of raw visible reflectance and IR temperature data fields	50
12. Plot of total storm volumetric rain rates and rep- resentative correlation areas for complex number 2	51
13. Plot of complex number 2 raw radar correlation fields for case M	52
14. Plot of complex number 2 raw radar correlation fields for case N	53

15.	Plots of model lag zero correlation (A_7), direction of motion (θ), and speed (V) for complex number 2 radar model fits.....	55
16.	Plots of ellipticity, (α), orientation angle (ϕ), and semi-axes of ellipse (a and b) for complex number 2 radar model fit	56
17.	Plots of XY and XYT decorrelation distances (σ 's) for complex number 2 radar model fits	57
18.	Plot of positions of complex number 2 satellite visible data	59
19.	Plots of model lag zero correlations (A_7), direction of motion (θ), and speed (V) for complex number 2 visible model fit	61
20.	Plots of ellipticity (α) and orientation angle (ϕ) for complex number 2 visible model fit	62
21.	Plots of ellipse semi-axes (a and b) and ratio of semi-axes for complex number 2 visible model fits	63
22.	Plot of speeds and directions of motion for visible and radar function fits	65
23.	Plots of raw correlation fields for complex number 2 visible cases SM (A), SN (B), and SO (C) and function fit for case SO (D)	66
24.	Plots of model lag zero correlation, (A_7), ellipticity (α) and orientation of ellipse (ϕ) for complex number 2 IR model fits	68
25.	Plots of ellipse semi-axes (a and b) and the ratio of the semi-axes (a/b) for complex number 2 IR model fits	69
26.	Plot of fitted raw correlation function for complex number 2 IR temperature case SO	71
27.	Plot of IR temperature field for complex number 2 case SN (1900 GMT)	72
28.	Plot of IR temperature gradient component field for complex number 2 case SN (1900 GMT)	73
29.	Raw correlation field and product pair count for complex number 2 temperature gradient component fields for case SN	74

30.	Plots of model lag zero correlation (A_7), offset direction (γ), and offset distance (d) for complex number 2 IR cross visible	77
31.	Plots of ellipticity (α), ellipse orientation (ϕ), and semi-axes (a and b) for complex number 2 IR cross visible	78
32.	Plots of raw correlation function and fitted model correlation function for complex number 2 IR cross visible	79
33.	Single time XY correlation fields for complex number 2 radar cross visible for cases SN, SO, and SQ	83
34.	Radar rain rates cross IR temperature correlation field for case SO (2000 GMT)	86
35.	Radar cross IR temperature gradient component correlations for threshold of 0 and case SN (1900 GMT)	87
36.	Plot of volumetric rain rate and correlation areas for complex number 3	89
37.	Complex number 3 radar returns for 2007 GMT	91
38.	Plots of raw time lag zero correlation fields for complex number 3 radar cases M and N	93
39.	Plots of model lag zero correlation (A_7), direction of motion (θ), and speed (V) for complex number 3 radar model fits	95
40.	Plots of ellipticity, (α), orientation angle (ϕ), and semi-axes of ellipse (a and b) for complex number 3 radar model fits	96
41.	Plots of decorrelation distances (σ) for complex number 3 radar model fit.....	97
42.	Plots of the objective analysis for complex number 3 cases SM (1830), SN (1900), SO (1930), and SP (2000)	98
43.	Plots of model lag zero correlation (A_7), direction of motion (θ), and speed (V) for complex number 3 visible model fits	99

Figure	Page
44. Plots of ellipticity (α), orientation angle (ϕ), and semi-axes (a and b) for complex number 3 visible model fits	100
45. Plots of decorrelation distances (σ) for complex number 3 visible model fit	101
46. Plots of raw correlation fields for complex number 3 visible cases SM and SN	103
47. Raw correlation fields for complex number 3 visible case O	105
48. Plots of model correlation function parameters for complex number 3 IR temperature XYT time lag zero	108
49. Plots of model correlation parameters for complex number 3 IR temperature gradient component XYT time lag zero	109
50. Raw correlation field for complex number 3 IR temperature gradient component cross visible for case N	112
51. Raw correlation field for complex number 3 radar cross visible case N time lag zero	114
52. Time lag -2 correlation field for radar cross visible and plots of corresponding data fields	116
53. Plot of rain rates and correlation areas for convective complex 5	120
54. Plots of model lag zero correlation (A_7), ellipticity (σ), orientation angle (ϕ), and semi-axes of ellipse (a and b) for complex number 5 radar XYT time lag zero model fit	122
55. Radar echo returns for complex number 5 at 1920, 1927, and 1957 GMT	123
56. Radar return for complex number 5 at 2012 GMT	125
57. Plots of model lag zero correlation (A_7) direction of motion (θ), and speed (\dot{V}) for complex number 5 visible model Fit	127
58. Plots of ellipticity, (α), orientation angle (ϕ), and semi-axes of ellipse (a and b) for complex number 3 visible model fit	129

Figure	Page
59. Plots of complex number 5 visible raw data fields for 1830, 1900, and 1930 GMT	129
60. Plots of model lag zero correlation (A_7), ellipticity (α), orientation of ellipse (ϕ), and semi-axes for complex number 5 IR XYT time lag zero fits	130
61. Plots of parameters for IR temperature gradient component XYT time lag zero function fits with a threshold of -1000	133
62. Plot of major axes of correlation ellipse for IR temperature and IR temperature gradient component.	134
63. Plots of parameters for IR temperature cross visible XYT time lag zero for complex number 5	136
64. Plot of maximum correlation offset for IR temperature cross visible reflectance	138
65. Plot of IR temperatures and visible reflectance for 1930, 2000, and 2030 GMT	139
66. Cross-correlation fields and product pair matrices for radar rain rates cross visible for cases SN and SO	142
67. Cross-correlation fields and product pair matrices for radar rain rates cross visible for cases SP and SQ	143
68. Plot of radar rain areas and satellite visible reflectance data with count greater than 164 for case SO	144
69. Plot of radar rain areas and satellite visible reflectance data with count greater than 164 for case SP	145
70. Radar rain rates cross IR temperature for case SP typical of cases SO and SQ.....	148
71. Single time XY correlation fields for radar cross IR temperature gradient for cases SP and SQ	149
72. Plot of volumetric rain rates and representative areas from NLP fits for convective complex number 6	151

Figure	Page
73. Plot of radar rain areas for complex number 6	152
74. Plots of model lag zero correlations (A_7), direction of motion (θ), and speed (V) for complex number 6 radar model fits	156
75. Plots of ellipticity, (α), orientation angle (ϕ), and semi-axes of ellipse (a and b) for complex number 6 radar model fits	157
76. Plot of complex number 6 raw visible reflectance data field for 2000 and 2030 GMT	158
77. Plot of complex number 6 raw visible reflectance data field for 2100 and 2130 GMT	159
78. Plot of complex number 6 raw visible reflectance data field for 2206 GMT	160
79. Plot of objective analysis of the visible data field at 2030 GMT for complex number 6.....	160
80. Plots of model lag zero correlation (A_7), direction of motion (θ), and speed (V) for complex number 6 visible model fits	162
81. Plots of ellipticity, (α), orientation angle (ϕ), and semi-axes of ellipse (a and b) for complex number 6 visible model fit	163
82. Raw correlation field for complex number 6 visible case SO	164
83. Plots of model lag zero correlation (A_7), direction of motion (θ), and speed (V) for complex number 6 IR model fit	166
84. Plots of ellipticity, (α), orientation angle (ϕ), and semi-axes of ellipse (a and b) for complex number 6 IR model fit	167
85. Plots of XY decorrelation distances (σ 's) for complex number 6 IR model fits	168
86. Plots of model lag zero correlation (A_7), ellipse orientation (ϕ), and ellipse semi-axes for complex number 6 IR temperature gradient component ..	171

87. E-W cross section of two data fields that would yield a correlation field skewed toward the east .173
88. Scatter diagram of radar rain correlation area versus volumetric rain rate178
89. Scatter diagram of visible reflectance correlation area versus volumetric rain rate179
90. Scatter diagram of visible reflectance correlation area (shifted -30 minutes in time) versus volumetric rain rate181
91. Example of IR temperature field that would result in the major axis of correlation ellipse not parallel to axis of anvil185

LIST OF TABLES

Table	Page
1. Radar storm characteristics for the four convective complexes chosen for study	31
2. Summary of satellite data sets	34
3. Case designations for convective complex number two radar data	46
4. Case designations for convective complex number two satellite data	47
5. Parameters of fitted model correlation function for complex number 2 radar rain rates	54
6. Parameters of fitted correlation function for complex number 2 visible correlation fields	60
7. Parameters of fitted correlation function for complex number 2 IR temperature correlation fields ...	67
8. Lag zero correlations for single time XY auto-correlations for complex number 2 gradient component..	75
9. Parameters of fitted model correlation function for complex number 2 IR cross visible correlation matrices	76
10. Maximum cross-correlations for complex number 2, all time lags and cases for IR temperature cross visible reflectance	76
11. Portions of raw XY correlation fields about lag zero for IR cross visible	80
12. Maximum correlations at time lags -2 and +2 and associated times	81

13.	Maximum IR temperature gradient component cross visible reflectance and corresponding lags for temperature gradient component thresholds of 0 and -1000	82
14.	Maximum correlations for complex number 2 radar cross visible reflectance for single time XY correlation fields	85
15.	Maximum cross-correlation and corresponding lags for radar rain rates cross IR temperature for each case.	86
16.	Maximum correlations for radar cross IR temperature gradient component for single time correlation fields and both thresholds	88
17.	Case designations for complex number 3 radar data ..	90
18.	Case designations for complex number 3 satellite data	90
19.	Parameters of fitted model correlation function for complex number 3 radar.....	94
20.	Parameters of fitted model correlation function for complex number 3 visible	102
21.	Parameters of fitted model correlation function for complex number 3 IR temperature	106
22.	Parameters of fitted model correlation function for complex number 3 IR temperature gradient compnent ..	107
23.	Maximum raw correlation in central modes for complex number 3 IR temperature cross visible XYT correlation fields	110
24.	Maximum correlation for each raw XY correlation field for complex number 3 IR temperature cross visible ..	111
25.	Maximum radar cross visible single time cross-correlations for complex number 3	114
26.	Maximum correlations for radar cross IR temperature for each case and corresponding lags	117
27.	Case designations for convective complex number 5 radar data	119

Table	Page
28. Case designations for convective complex number 5 satellite data	119
29. Function fits to time lag zero radar XYT auto-correlation fields for complex number 5	121
30. NLP function fits for complex number 5 visible correlation fields.....	126
31. Function fits for IR temperature correlation fields for convective complex 5	131
32. Function fits for IR temperature gradient component correlation fields with threshold of -1000 for complex number 5.....	132
33. Function fits for IR temperature cross visible reflectance XYT time lag zero correlation fields ..	135
34. Maximum correlations for each case for time lags -1,0, and +1	137
35. Maximum cross-correlations and corresponding lags for IR temperature gradient component cross visible reflectance.....	140
36. Two largest correlations and their corresponding lags for XYT cases for temperature gradient component cross visible reflectance	140
37. Maximum single time XY cross-correlation for radar rain rates cross IR temperature	146
38. Maximum single time XY cross-correlations for radar rain rates cross IR temperature gradient component and corresponding lags for complex number 5	150
39. Case designations for convective complex number 6 radar data	153
40. Case designations for convective complex number 6 satellite data	154
41. Parameters of model correlation function for complex number 6 radar	155
42. Parameters of model correlation function for convective complex number 6 visible reflectance as determined using NLP	161

43.	Model correlation parameters for complex number 6 IR temperature	165
44.	XY correlation function parameters for complex number 6 IR temperature gradient component	170
45.	Cross-correlation at maxima and corresponding lags for single time IR cross visible XY fields (bin size 6 km by 8 km)	173
46.	Cross-correlations at local maxima and corresponding lags for single time radar cross temperature XY fields (bin size 8 km by 10 km)	175
47.	Maximum radar cross satellite correlations for each convective complex	183

AN INVESTIGATION OF SATELLITE-RADAR CORRELATION FUNCTIONS

CHAPTER I

INTRODUCTION

For the past several years much attention has been given to the problem of estimating surface rainfall from convective storms by using satellite imagery. This interest is due to the potential applications in several areas.

In weather modification experiments such as the U.S. Bureau of Reclamation's High Plains Experiment (HIPLEX), the objective is to establish whether or not the modification attempts are producing changes in the convective complex. The bottom line is, however, is there an increase in precipitation? The use of conventional rain gages to measure rainfall limits one to a rather small area as the number of rain gages required to monitor a large area would be prohibitive. The use of a combination of radar and gages (Brady, 1976; Crawford, 1977; Wilson, 1970; Woodley, et al, 1975) to estimate surface rain is a partial solution. Radar covers a limited area, and the entire life cycle of a convective complex may not be contained within its coverage. The use of satellite imagery either alone or in combination with gages

and/or radar to estimate rainfall would result in a sensing system with effectively unlimited areal coverage.

The larger the area covered by the rainfall measurement system the less the time required to obtain statistically significant results. This is because as the covered area increases the number of storms that pass over the area increases. Therefore, a scheme for estimating rainfall using satellite imagery could conceivably reduce the number of storm days required to collect an adequate data sample. It would also allow any extended area effects to be more easily studied.

Another significant contribution that could be made by using satellite estimates of surface rainfall is to the field of agriculture. As the world population has grown, the demand for food has also grown. In order to manage the available food better, accurate crop yield estimates are required. These estimates could be obtained from crop yield models. One of the more critical inputs to the models is surface rainfall; however, estimates of surface rainfall for large parts of the world are not available to modelers in this country. This lack of data could be resolved if the rainfall could be estimated by using satellite imagery.

Also in recent years flash floods have resulted in an increasing number of deaths and damage in the United States. In order to reduce these losses, both timely identification of flash flood potential and warning and the securing of desired public response are required. Flash floods often occur in mountainous or hilly terrain where rain gages are

frequently inadequate. In addition, the data are usually not available in real time and radar measurement of precipitation is difficult in such terrain. Hence, the timely identification and warning of a potential flash flood may not be possible given only the availability of such data sets. However, the use of satellite imagery to estimate rainfall in real time would allow quick identification and warning.

The objective of this research is to investigate the correlation structure of satellite visible and infrared data and radar rain rates. This investigation is required in order to determine to what extent the current satellite technology will permit an optimum interpolation objective analysis technique to estimate surface rainfall from satellite data with acceptable accuracy.

In the chapters that follow, first a brief review of current efforts to estimate surface rainfall from satellite imagery will be given. Then a proposed analysis model will be outlined. The available data will then be discussed and finally the results will be analyzed.

CHAPTER II

PREVIOUS RESEARCH

There have been several researchers working on the problem of estimating surface rainfall from satellite imagery. The paper by Woodley and Sancho (1971) is one of the earliest found on the subject. Since this early work, Woodley and Griffith have continued to develop an estimation technique in conjunction with the Florida Area Cumulus Experiment (FACE) and HIPLEX projects (Woodley, et al, 1972, 1978, 1979; Griffith and Woodley, 1973, 1976). Their technique examines the time histories of the satellite imagery. The area of the cloud within some threshold reflectance or infrared (IR) temperature value is determined for each time from the satellite imagery. After the maximum such area is found the ratio of the "threshold" area to this maximum area is found for each time. This ratio is then used to find an equivalent radar echo area from an empirically determined relationship. This echo area is then used in another equation that relates echo area growth tendency and IR temperature to rain volume. The approach lends itself to automation and is, in fact, already fairly automated.

Oliver and Scofield have also been developing an estimation technique (Follansbee and Oliver, 1975; Oliver and

Scofield, 1976; Scofield, 1978). They have outlined a procedure using satellite visible and enhanced IR imagery. As indicators of rainfall location and intensity they use the following:

1. Cloud top IR temperature
2. Cloud top IR temperature gradient
3. Rate of growth of cloud top
4. Brightness and/or texture of cloud top
5. Overshooting tops
6. Cloud mergers

The decision tree used is reproduced in Fig. 1. The technique does not appear to lend itself easily to automation.

Reynolds and VonderHaar (1977) have tried Oliver and Scofield's method on a HIPLEX storm and reported that it worked well. Cadavid, Mejia, and Crutcher (1979) have also attempted to use Oliver and Scofield's approach in the tropics over Colombia with limited success. They attribute their problems to two areas: 1) missing or low quality data, and 2) the differences between storms in the tropics and those in the U.S. plains where the technique was developed. It is felt by them that, after additional cases have been investigated, they may be able to modify the technique to give improved estimates.

Stout, Martin, and Sikdar (1979) discuss a technique for estimating rainfall from tropical convective storms. Their assumptions are as follows:

1. Almost all tropical precipitation comes from deep

Half-hourly convective rainfall estimation scheme (in inches) at a station; enhanced IR and high resolution visible imagery used as input after Scofield and Oliver, 1977

STEP 1.

Examine shape of cloud to determine if convective (round, oval, carrot-shaped, triangular) USE VIS AND IR.

STEP 2

Determine if convection is deep USE ENHANCED IR.

STEP 3

Identify the active portion of the convective cloud system. Use enhanced IR and VIS. Vis (underlined) means that visible imagery is the best data for making that decision.

A. Upwind portion of anvil locates the active area of the convective system.

IR gradient is tightest around upwind end of anvil.

Clouds are brightest and sometimes textured at upwind end.

Comparison of two successive pictures shows motion of anvil edge, greatest in downwind direction.

Winds aloft (usually best at 300 mb) used for determining up wind direction.

- B. Overshooting tops show active area of anvil.

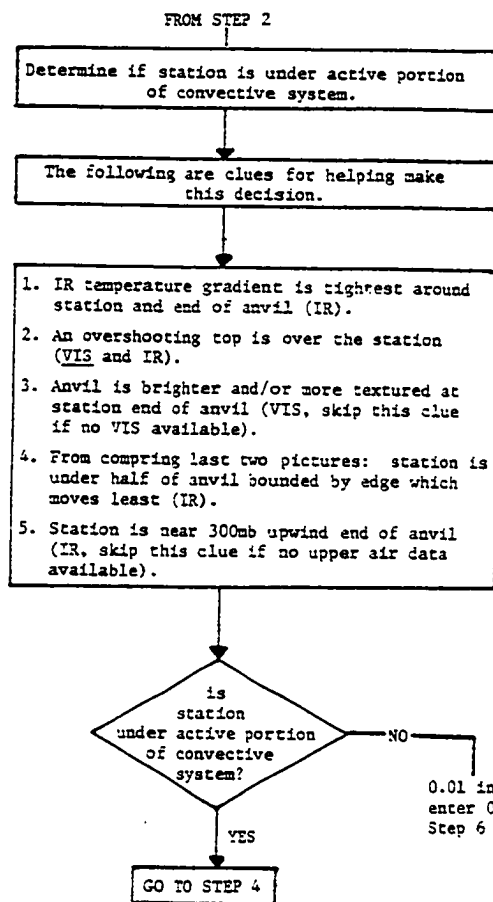
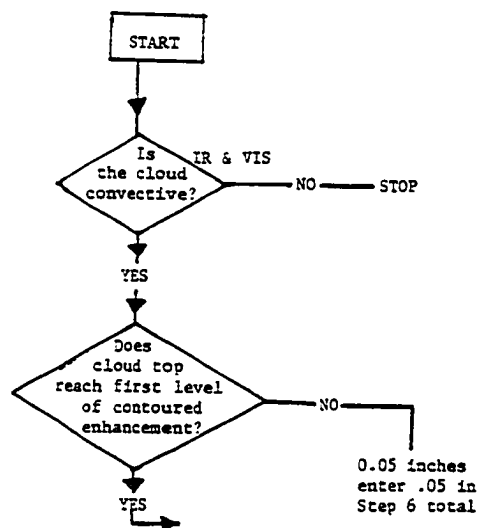
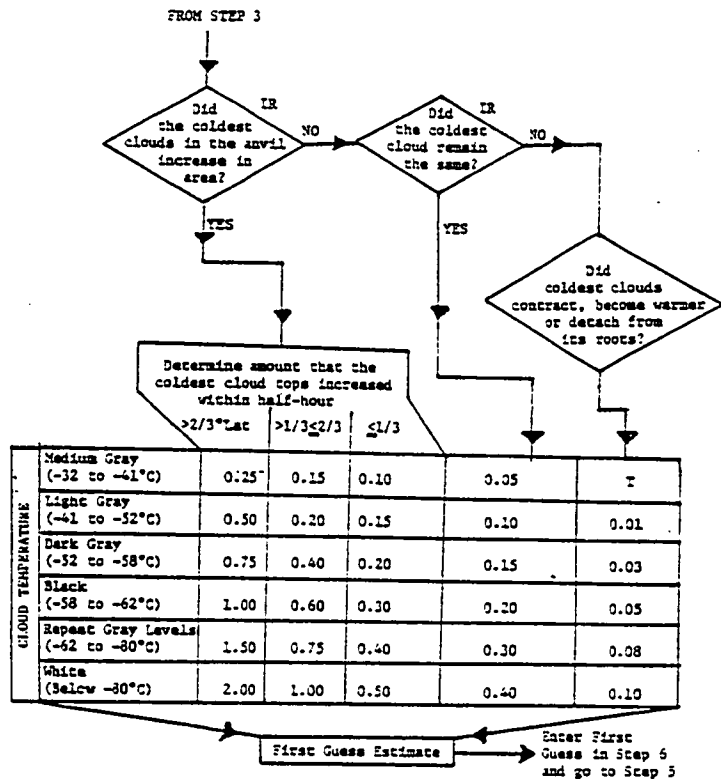


Fig. 1. Scofield and Oliver's decision tree.

STEP 4
Estimate half-hourly
precip rates as a
function of cloud top
temperature and temper-
ature change.
USE ENHANCED IR.

Rainfall is heaviest
when and where clouds
are still getting
colder and coldest
area is grivng.

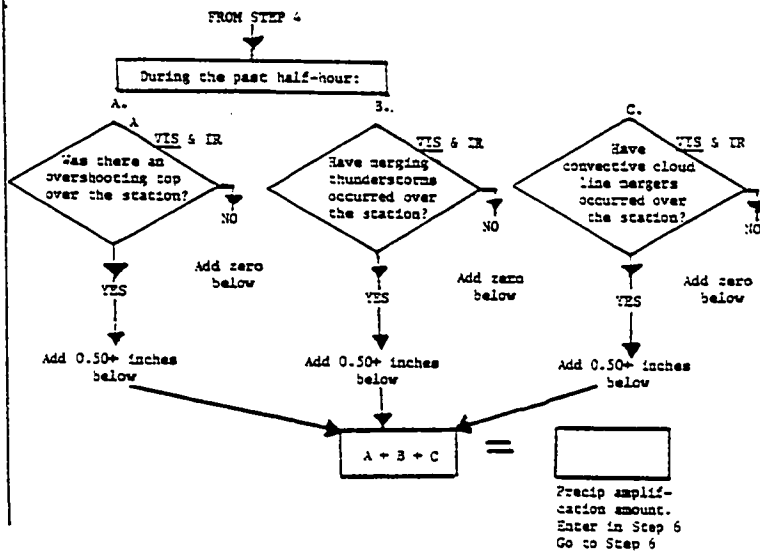


STEP 5
Analyze imagery for
presence of precip
amplifiers.
USE TIS AND ENHANCED IR.
TIS (underlined) means
that visible imagery is
the best data for
making that decision.

Overshooting tops.

Cell mergers.

Line mergers.



STEP 6
Total estimate.

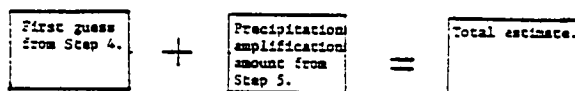


Fig. 1. Scofield and Oliver's decision tree. (continued)

convection.

2. Cumulonimbi can be readily identified in synchronous satellite images.
3. Cumulonimbus cloud area and area change are related to rainfall.

Implied in 3 is the assumption that cloud brightness and cloud top temperature are related to rainfall. They combine cumulonimbus cloud area and its change in the following simple equation to estimate rainfall:

$$R = a_0 A + a_1 dA/dt$$

where R is the volumetric rainfall of the cloud ($m^3 s^{-1}$), A the cloud area (m^2), dA/dt the time rate of change of cloud area ($m^2 s^{-1}$), and a_0 and a_1 are empirically determined constants. They concluded that the procedure yielded fairly good results in the tropics but that the values of the empirical constants would have to be redetermined if the procedure was to be applied at higher latitudes.

The above methods are primarily for estimating rainfall from convective clouds. Follansbee (1976) has worked on a method for estimating rainfall from stratoform clouds.

Follansbee divides his approach into three steps as follows:

1. delineate the area(s) covered by precipitating clouds in each of two consecutive infrared images taken at approximately 12-hour intervals;

2. using cloud motion models developed for the purpose, delineate the envelope of precipitation and isopleths of duration of precipitation in hours;
3. using an empirically derived relationship between duration of precipitation and the percentage of monthly normal precipitation, estimate amounts of precipitation for the 12-hour period at each grid point in the area of interest.

The approach seems to work well except where there are convective storms embedded in the stratoform clouds.

Barrett (1970) proposed a model to estimate monthly rainfall from satellite imagery. His procedure relates the percentage of various cloud types observed in the imagery to a rainfall coefficient that he has defined. The calculated rainfall coefficients were then compared to observed monthly rainfalls and a polynomial curve fitted. This curve was then used to estimate monthly rainfall for another case. He felt that the results obtained justified further investigation.

In a slightly different vein, Lovejoy and Austin (1979) used pattern recognition techniques to try to improve on attempts to delineate rain areas from satellite imagery using thresholds. They describe a method in which both the visible and IR data are used simultaneously to specify rain/no-rain areas. The method appears to be insensitive to diurnal and day to day variations and is different for the tropical Atlantic and Montreal areas. Their results also suggest that when the visible and the IR data are compared for thresholding the visible does a better job.

CHAPTER III

APPROACH

Objective analysis consists of the weighting together of sets of observations for the estimating of a variable field at specified points (usually a grid system) in space and time. The weights are determined in some objective manner, hence the terminology objective analysis. The uses of objective analysis are many, several of which are the following:

1. The resulting variable field can be used as the initial data field in a dynamic weather forecast model.
2. In multivariate objective analysis, the resulting variable field may be a better estimate than that obtained from any single observation set, as for example using both rain gage and radar data to estimate surface rainfall.
3. A statistical objective analysis procedure can be an aid in the objective specification of an instrument configuration in terms of type and number.

1. Objective Analysis

The objective analysis model proposed is an extension of multivariate linear regression and is described by

$$Y = X\beta + \epsilon \quad (1)$$

where X is an $n \times m$ observation matrix, Y is an $n \times 1$ predictand matrix, β is an $m \times 1$ matrix of regression weights, ϵ is an $n \times 1$ population error matrix, and ..

$$e = Y - \hat{Y} \quad (2)$$

is the residual error matrix associated with sample regression. The technique is also known as optimum interpolation objective analysis (Eddy, 1963; Gandin, 1963). The univariate objective analysis is given by

$$\hat{Y} = X\hat{\beta} \quad (3)$$

where β is a vector of estimated population weights, and \hat{Y} is an estimate of the population values of Y .

In classical regression analysis, $\hat{\beta}$ is found by

$$\hat{\beta} = (X^t X)^{-1} X^t Y \quad (4)$$

The matrix $(X^t X)^{-1}$ is a matrix of covariance between the predictors, and $X^t Y$ is a vector ($n \times 1$ matrix) of correlations between the predictand and the predictors. In the proposed approach, these will be determined from a modeled covariance function. More will be said about this later.

For the proposed model, it is beneficial to partition the X and β matrices in equation (1) such that each of the submatrices contains the observations for a given type of predictor (i.e., gage, visible satellite, etc.).

$$X = (X_G, X_R, X_S, X_O)$$

$$\beta^t = (\beta_G, \beta_R, \beta_S, \beta_O)$$

X_G = observation matrix for gages

X_R = observation matrix for radar

X_S = observation matrix for satellite

X_O = observation matrix for other parameters

β_G = regression weights for gages

β_R = regression weights for radar

β_S = regression weights for satellite

β_O = regression weights for other parameters

After multiplication, equation (1) becomes

$$Y = X_G \beta_G + X_R \beta_R + X_S \beta_S + X_O \beta_O + \epsilon \quad (5)$$

In expanding the $X^t X$ term in equation (4), we obtain

$$X^t X = \begin{bmatrix} X_G^t X_G & X_G^t X_R & X_G^t X_S & X_G^t X_O \\ X_R^t X_G & X_R^t X_R & X_R^t X_S & X_R^t X_O \\ X_S^t X_G & X_S^t X_R & X_S^t X_S & X_S^t X_O \\ X_O^t X_G & X_O^t X_R & X_O^t X_S & X_O^t X_O \end{bmatrix} \quad (6a)$$

which is a symmetric matrix since $(X_R^t X_G)^t = X_G^t X_R$, etc. Each of the terms in the above matrix represents the covariance matrix

		X LAG											
		-5	0								+5		
Y LAG	+5	-.231	-.160	-.138	-.094	-.076	-.089	-.078	-.107	-.116	-.181	-.241	CORRELATIONS
		-.081	-.105	-.097	-.018	0.047	0.027	0.015	-.045	-.123	-.145	-.214	
		-.154	-.087	0.023	0.114	0.095	0.098	0.123	0.060	-.022	-.073	0.109	
		-.152	-.024	0.085	0.182	0.161	0.198	0.263	0.145	0.076	-.032	-.114	
		-.134	0.050	0.068	0.108	0.273	0.432	0.381	0.158	0.022	-.003	-.078	
	0	-.094	-.018	0.038	0.125	0.490	0.758	0.490	0.125	0.038	-.018	-.094	
		-.078	-.003	0.022	0.158	0.381	0.432	0.273	0.108	0.068	0.050	-.134	
		-.114	-.032	0.076	0.145	0.263	0.198	0.161	0.182	0.085	-.024	-.152	
		-.109	-.073	-.022	0.060	0.123	0.098	0.095	0.114	0.023	-.087	-.154	
		-.214	-.145	-.123	-.045	0.015	0.027	0.047	-.018	-.097	-.106	-.081	
	-5	-.241	-.181	-.116	-.107	-.078	-.089	-.076	-.094	-.138	-.160	-.231	
Y LAG	+5	366	947	1667	2599	3449	3685	3198	2167	984	200	40	NUMBER OF PAIRS
		428	1018	1798	2842	3737	4269	3679	2480	1143	264	33	
		434	1027	1846	3027	4124	4892	4285	2716	1352	443	34	
		411	1045	1897	3013	4646	5627	4618	3011	1515	593	83	
		371	968	1897	3117	4649	5549	5429	3074	1669	781	171	
	0	283	910	1808	3300	5036	6074	5036	3300	1808	910	283	
		171	791	1669	3074	5429	6549	4649	3117	1897	968	371	
		83	593	1515	3011	4618	5627	4646	3013	1897	1045	411	
		34	443	1352	2716	4285	4892	4124	3027	1846	1027	434	
		33	264	1143	2480	3679	4269	3737	2842	1798	1018	428	
	-5	40	200	984	2167	3198	3685	3449	2599	1667	947	366	

LAG DISTANCE IN X DIRECTION = 3 KM

LAG DISTANCE IN Y DIRECTION = 3 KM

Fig. 2. Example of correlations matrix for radar derived rain rates.

between the corresponding variables. That is, the term $X_G^t X_G$ is the "auto" covariance matrix for the gage variables, and the $X_R^t X_G$ is the "cross" covariance matrix for the radar versus gage.

Similarly, expanding the $X^t Y$ term in equation (4), we obtain

$$(X^t Y)^t = (X_G^t Y, X_R^t Y, X_S^t Y, X_O^t Y) \quad (6b)$$

where each term represents the $n \times 1$ matrix of covariances between each of the predictor variable sets and the predictand.

In the above covariance matrices, if the original variables have been normalized such that they have a mean of zero (0) and a variance of one (1), then the matrices are correlation matrices. Fig. 2 shows the auto-correlation matrix (field) for a radar derived rain rate data set. The center value (0.758) represents the auto-correlation at lag zero ($\Delta X = \Delta Y = \Delta Z = \Delta T = 0$). It does not have a value of 1.0 due to noise in the original data. Positive X-lags are to the right, and positive Y-lags are to the top. The lag interval for both directions is 3.0 km. Therefore, if one goes two (2) positions to the right and one (1) up, one can find the auto-correlation between two (2) radar bins separated by a distance of 6 km in X and 3 km in Y is 0.158. The lower matrix in the figure gives the number of product pairs used in finding the corresponding correlations in the upper matrix.

If the correlation fields between the different variables can be modeled, then the covariance matrix can be

constructed from the models. Once the covariance matrices have been constructed, the weights (β) can be determined and the objective analysis performed.

This approach was used by both Brady (1976) and Crawford (1977) in their bivariate (gage, radar) objective analyses. Figs. 3 and 4 illustrate the results of a storm total univariate gage and radar objective analysis and Fig. 5 the bivariate gage-radar objective analysis (Eddy and Hembree, 1978). In Fig. 3 it can be seen that the univariate gage objective analysis does not have much detail. The univariate radar objective analysis has more detail; however, the general pattern is shifted to the southeast from the rain gage pattern, and the maximum rainfall is nearly three (3) times larger. The results of the bivariate objective analysis, Fig. 5, show how the pattern is now more aligned with the univariate gage pattern. In addition, the radar adds detail to the analysis. The analysis also indicated that the univariate radar objective analysis maximum rainfall was 4.2 mm while the univariate radar maximum was 3.5 mm. It should be noted that the maximum rainfall as indicated by the bivariate objective analysis was located between the gages and, therefore, was undetected.

Crawford and Brady list several positive characteristics of the above objective analysis scheme. These are among the following:

1. Data set structures compare favorably with an objectively analyzed structure (Brady, 1976);

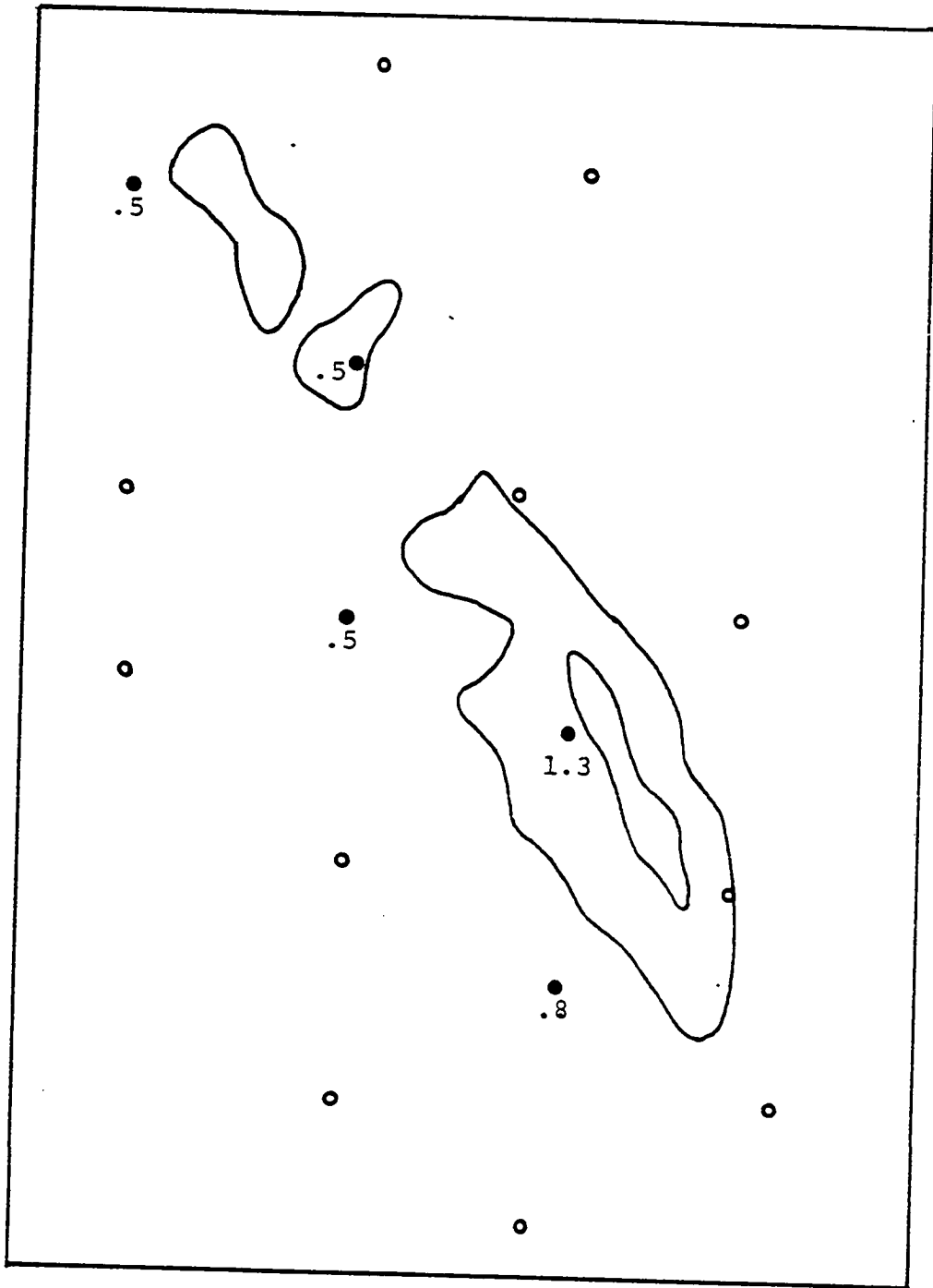


Fig. 3. Results of univariate gage objective analysis. Contour interval is 0.5 mm. Low contour is 0.5 mm. Positions of rain gages and rain amounts shown. (Eddy and Hembree, 1978)

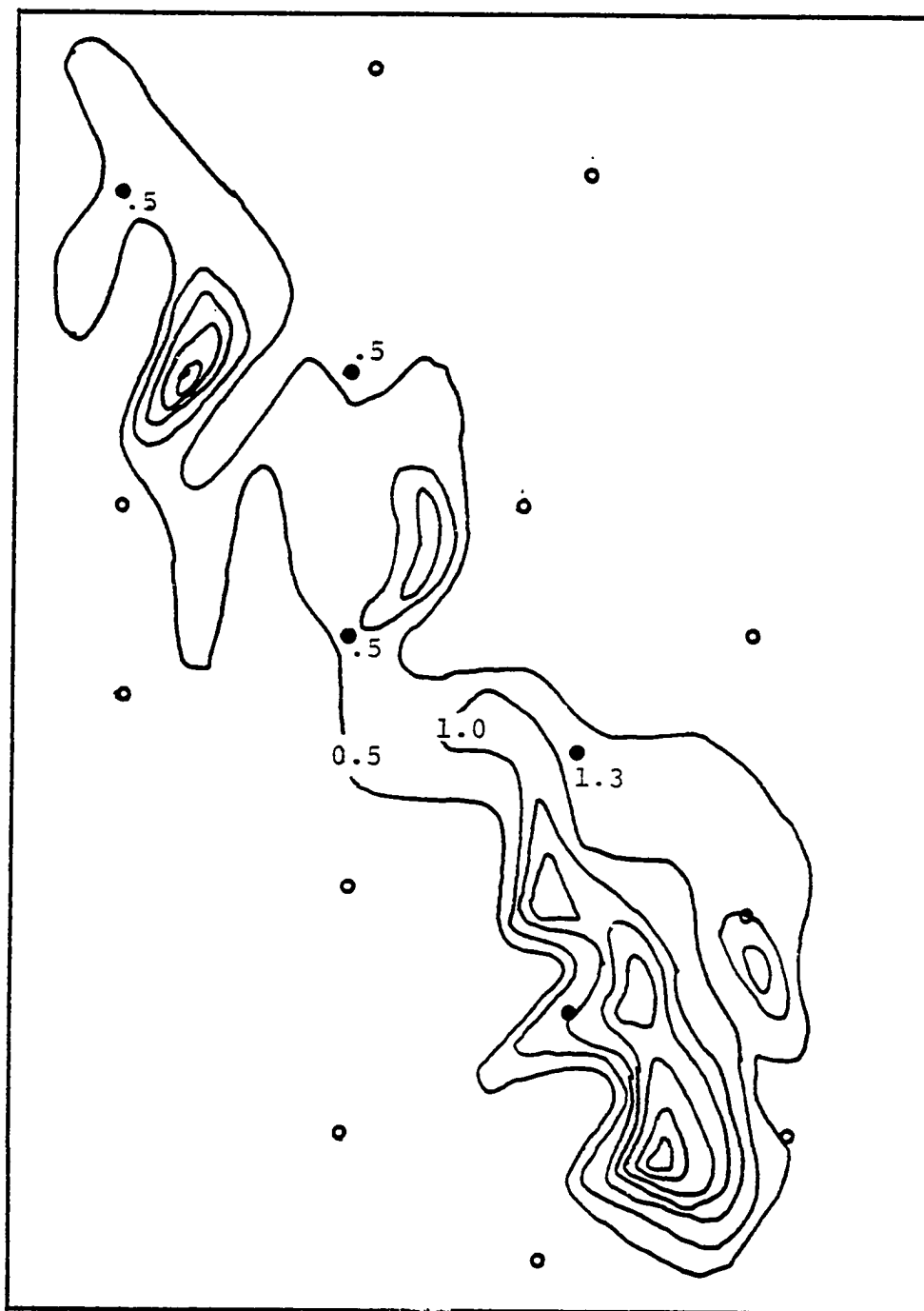


Fig. 4. Results of univariate radar objective analysis. Contour interval is 0.5 mm. Low contour is 0.5mm. Positions of rain gages and rain amounts are shown. (Eddy and Hembree, 1978)

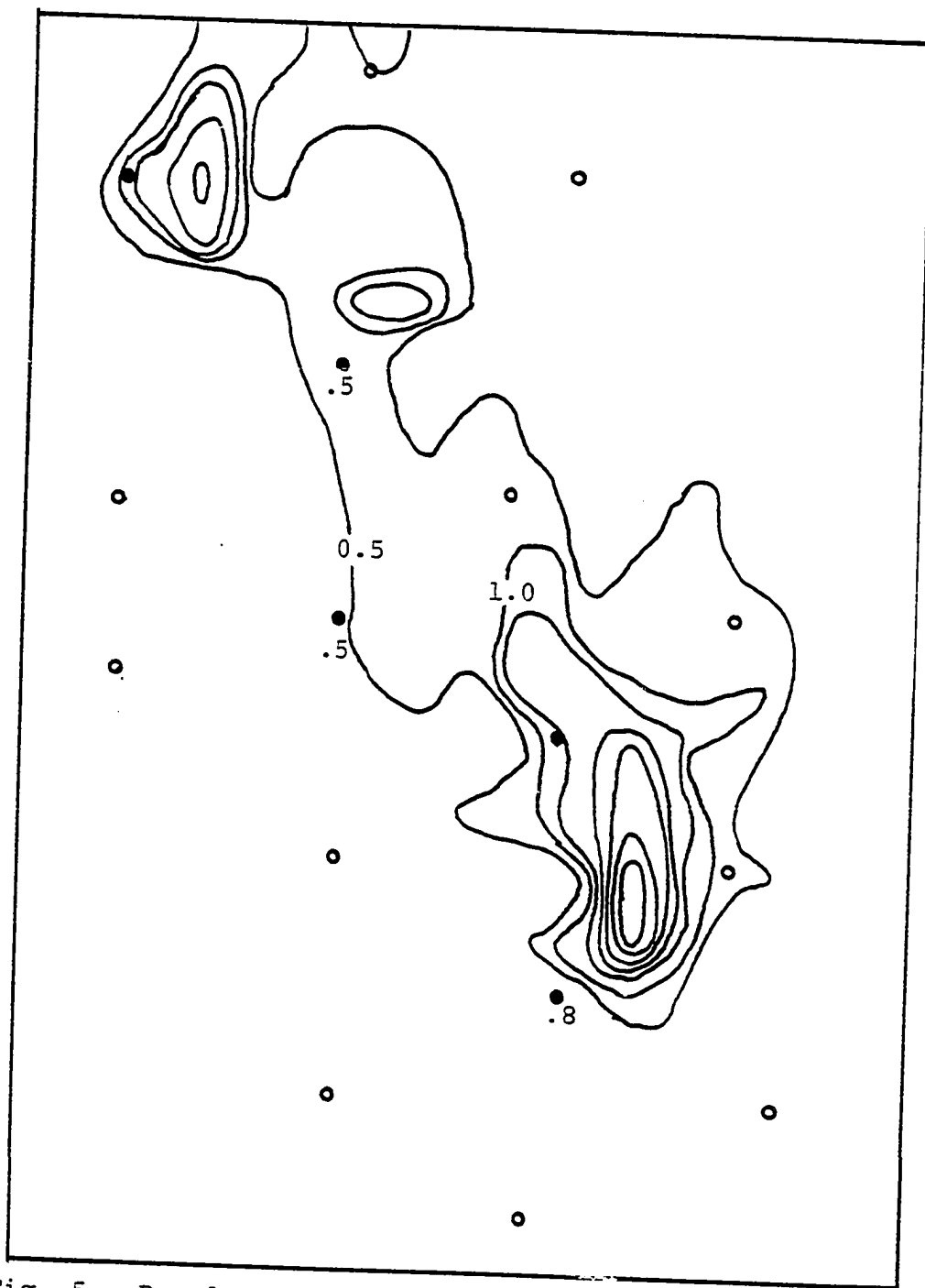


Fig. 5. Results of bivariate gage-radar objective analysis. Contour interval is 0.5mm. Low contour is 0.5 mm. Positions of rain gages and rain amounts shown. (Eddy and Hembree, 1978)

2. Signal-to-noise ratios are significantly larger in objectively analyzed data sets than in raw data sets (Brady, 1976);
3. The technique, compared to other analysis methods, performs best with minimum data persistence (Lacy, 1973). This point is supported strongly by Phillips (1976) and Thiebaut (1977);
4. The methodology apparently encounters no data boundary problems (Pasteris, 1975) compared to some analysis schemes (Brandes, 1975);
5. Residual errors essentially are Gaussian distributed (Eddy, 1976);
6. Analysis residuals exhibit no significant space auto-correlation implying that the analysis abstracted the significant data-set signal and filtered most of the data set noise (Eddy, 1967; Eddy and McDonald, 1977).

2. Covariance Model

The optimum interpolation objective analysis technique discussed above obtains the estimates of the weights from the data set structure as expressed in terms of auto- and cross-correlation fields of the data set. Using discrete time and space lags raw correlation matrices representative of the data structure can be calculated. These raw correlation matrices could be incorporated directly into the objective analysis program. However, one is then faced with the problem of interpolating between the observed correlations in

up to four (4) dimensions at once. Also, the influences of noise and of an inadequate data sample can be a problem. If the value of a "raw" coefficient does not fit the general observed pattern in the correlation field, then an error (bias) in the objective analysis will be likely. This error (bias) is the result of the assignment of incorrect weights (too high or too low) to the predictors. A reduction of these effects is required in order to obtain acceptable analyses. By fitting a functional model to the raw correlation fields, and weighting the fit at each point by the number of observation pairs used to determine the correlation at that point, the effect of the noise can be reduced.

Also, it is often difficult to conceptualize the structure of the data set by studying the raw correlation fields. However, the parameters of an appropriately chosen and fitted functional form can reflect the relevant physical and statistical information about the system.

The covariance model to be used is an extension of that used by Brady (1976) and Crawford (1977) in their investigations of the correlation fields between surface rainfall and radar estimates of rainfall. Their studies showed that the multidimensional correlation field between the surface rainfall and radar estimates could be represented by the function

$$f_{12}(\Delta x, \Delta y, \Delta z, \Delta t) = A_7 \cos \left[\frac{2\pi\sqrt{K+J}}{4} \right] \exp - \left[\frac{K}{2(1-\alpha^2)} + \frac{J}{2} \right] \quad (7)$$

where

$$K = \frac{\Delta x^2}{\sigma_x^2} - \frac{2\alpha\Delta x\Delta y}{\sigma_x\sigma_y} + \frac{\Delta y^2}{\sigma_y^2}$$

and

$$J = \frac{\Delta z^2}{\sigma_z^2} + \frac{\Delta t^2}{\sigma_t^2}$$

where

$f_{12}(\Delta x, \Delta y, \Delta z, \Delta t)$ = correlation between variables 1 and 2

$\Delta x, \Delta y, \Delta z, \Delta t$ = separation distance between the gage estimate (variable 1) and the radar estimate (variable 2) in the Cartesian coordinates and time,

α = an ellipticity parameter in the X - Y plane, and

A_7 = the lag zero ($\Delta x = \Delta y = \Delta z = \Delta t = 0$) correlation coefficient,

$\sigma_x, \sigma_y, \sigma_z, \sigma_t$ = Decorrelation distance in x, y, z, and t respectively.

The above correlation function is a function (in its space dimension) of separation distance and direction only, and, therefore, the correlation field may be anisotropic in nature. The difference $(1-A_7)$ is a measure of the noise in the signal (data). In preliminary work, equation (7) has been further refined (Hembree and Eddy, 1977, 1978) to allow the point of maximum cross-correlation to occur at other than lag zero in the X-Y plane ($\Delta x = \Delta y = 0$) and to allow movement

of the point of maximum cross-correlation with time. The modification consists of defining Δx and Δy as follows:

$$\Delta x = x_1 - x_2 + x_0 + C_x \Delta t$$

and

$$\Delta y = y_1 - y_2 + y_0 + C_y \Delta t \quad (8)$$

x_0 , y_0 = offset distances at time lag zero in the X and Y directions, respectively,

C_x , C_y = "velocity" of the point of maximum correlation along the X and Y axes respectively.

The subscripts 1 and 2 refer to variables 1 and 2, respectively.

The observed correlation field is obtained by finding the correlation between all points such that the separation distances Δx , Δy , and Δz are within some interval, such as,

$$\begin{aligned} (l-\frac{1}{2})\delta_x < \Delta x \leq (l+\frac{1}{2})\delta_x : l=0, \pm 1, \pm 2, \dots \pm L \\ (m-\frac{1}{2})\delta_y < \Delta y \leq (m+\frac{1}{2})\delta_y : m=0, \pm 1, \pm 2, \dots \pm M \\ (n-\frac{1}{2})\delta_z < \Delta z \leq (n+\frac{1}{2})\delta_z : n=0, \pm 1, \pm 2, \dots \pm N \end{aligned} \quad (9)$$

where

$\delta_x, \delta_y, \delta_z$ = the box sizes used to find the correlations,
and

L, M, N = the maximum number of lags in x, y, and z directions respectively.

Currently the procedure requires the data to be at fixed and equal time intervals.

The function as given in equation (7) or after modification by equation (8) is fitted to an observed correlation field using nonlinear programming techniques (Brady, 1976; Crawford, 1977). The function is fitted in such a manner that the correlation at $+\Delta x$ need not be equal to the correlation at $-\Delta x$. This results in the definition of two σ_x 's (σ_y 's): one for the plus x (y) direction and one for the negative x (y) direction. The σ 's can be interpreted as the distance from the maximum correlation along their respective axes at which the correlation goes to zero (0). The results of fitting the correlation function to a raw correlation matrix representing the correlation between gage and radar derived storm total rainfall in the study discussed above (Figs. 3-5) (Eddy and Hembree, 1978) are

	Positive	Negative
σ_x (km)	17.6	26.5
σ_y (km)	10.9	23.9
α	-0.97	
A_7	0.58	
x_0 (km)	-0.96	
y_0 (km)	0.58	

The x_0 and y_0 imply that the gage storm total data is most correlated with the radar storm total data approximately 1.1 km to the west-northwest. The non-equality of the positive and negative σ 's shows that the gages are correlated with the radar for a greater distance in one direction than

in the other.

The correlation function has the general shape of an ellipse. The more equal the positive and negative σ 's are the more closely elliptical is the storm. If one assumes an elliptical shape and uses the average of the positive and negative σ 's as an estimate of σ_x and σ_y , then the orientation of the ellipse with respect to the positive x-axis is given by

$$\phi = \text{ARCTAN} (2\alpha \sigma_y \sigma_x / (\sigma_x^2 - \sigma_y^2)) \quad (10)$$

The axes of the ellipse are given by

$$a = \sigma_x^2 \cos^2 \theta + \sigma_y^2 \sin^2 \theta - 2\alpha \sigma_x \sigma_y \sin \theta \cos \theta \quad (11)$$

$$b = \sigma_x^2 \sin^2 \theta + \sigma_y^2 \cos^2 \theta + 2\alpha \sigma_x \sigma_y \sin \theta \cos \theta \quad (12)$$

where the major axis is taken to be the MAX(a,b). The area of the ellipse is given by

$$A = \pi ab \quad (13)$$

For the example above

$$\sigma_x = 22.05 \text{ km}$$

$$\sigma_y = 17.4 \text{ km}$$

$$\phi = -38.1^\circ$$

$$a = 7.41 \text{ km}$$

$$b = 27.09 \text{ km}$$

$$A = 630.09 \text{ km}^2$$

The axes and areas are convenient for characterizing the covariance function as they are constant under rotation. This is important in that if two (2) storms are basically the same except for orientation, then using the ellipse axes they could be identified as being basically the same as far as correlation structure is concerned. It is still to be determined if the above estimates of the angle and the major and minor axes are the best to use.

3. Sensor Placement

The objective analysis technique described earlier also is readily adapted for sensor placement (experimental design) purposes. The approach was developed by Eddy (1973, 1974) and applied by Eddy (1976), Yerg (1973), Kays (1974), Brady (1976), Crawford (1977), and Hembree and Eddy (1978).

The objective analysis technique described above can not only determine estimates of the parameter field, but also estimates of the amount of variance in the original data sample that has been explained by the given sampling pattern with respect to some specified analysis grid. It can be shown that the amount of variance explained by the objective analysis is not dependent solely upon the observation field, but upon the covariance function, orientation, and mesh size), and the sensor mix. By moving the sensors around one can find the optimum locations for the sensors for a given covariance function. This

approach has made use of a nonlinear programming algorithm to produce an experimental design model (Brady, 1976; Crawford, 1977).

Brady (1976) demonstrated the practical validity of this approach and then extended the model to detect signal variations by accounting for the predictand mean values which scale the analysis field. Crawford (1977) extended the model to include both the parameter means and variances. The objective function that Crawford used in his experimental design is

$$F = \frac{1}{G} \sum_i^G \eta_i \left[\begin{aligned} & (1-R_i^2) + \frac{(1 - \sum_{j=1}^J \beta_{Gj})^2}{M_G} + \frac{(\sigma_R/\sigma_G \sum_{k=1}^K \beta_{Rk})^2}{M_R} \\ & - \frac{2(\sigma_R/\sigma_G)\bar{\rho}}{(M_G M_R)^{1/2}} \left(\sum_{k=1}^K \beta_{Rk} - \sum_{k=1}^K \beta_{Rk} \sum_{j=1}^J \beta_{Gj} \right) \end{aligned} \right] \quad (14)$$

where M_G and M_R are the number of gages and radar data points respectively, η_i is a weighting factor, ρ is the gage-radar correlation, J is a subset of M_G , K is a subset of M_R , G is the number of analysis points, β_i is the multiple correlation coefficient between the observation Y and the objective analysis \hat{Y} at the i th analysis point, and the β 's are the regression weights for the gage and radar predictors for the i th analysis point. In order to evaluate the R_i 's and β 's one needs to know the gage and radar auto-correlation function and the gage-radar cross-correlation function.

Crawford's objective function was used by Hembree and Eddy (1978) in the analysis of the sensor deployment in the National Severe Storm Laboratory's (NSSL) 1977 severe storm

observational program. In this study the experimental design model was used to determine optimal sensor placements for 15 sensors comprising NCAR's Portable Automated Mesonet (PAM) among the permanent NSSL sensors. Fig. 6 shows both the initial and final sensor placements. Improvements in the residual variance of up to 11.6 percent were realized depending upon the analysis grid mesh size, orientation, and position.

Crawford used the experimental design package to place rain gages with respect to radar. After proper extension of the model to handle more predictor variables, the same basic procedure could be used to place rain gages and radars so that they could be used in conjunction with satellites to extract more information (at a reasonable cost).

Hembree and Eddy (1977) used a modified version of the experimental design package to investigate the decimation of SMS satellite data. Correlation models of the storms under study were developed, and then from these models, sampling rates in space and time which would produce a dense enough observation set to define such systems without an unwarranted redundancy of the data were developed. It was determined that for these cases one could eliminate 5/6 of the data along a scan line and 2/3 of the scan lines and still explain 85 percent of the variance.

The experimental design (sensor placement) is application sensitive and is dependent upon the analysis grid and the correlation functions chosen. Above, the application was in terms of a single storm, inasmuch as an objective

Scale: Grid 30 km * 30 km

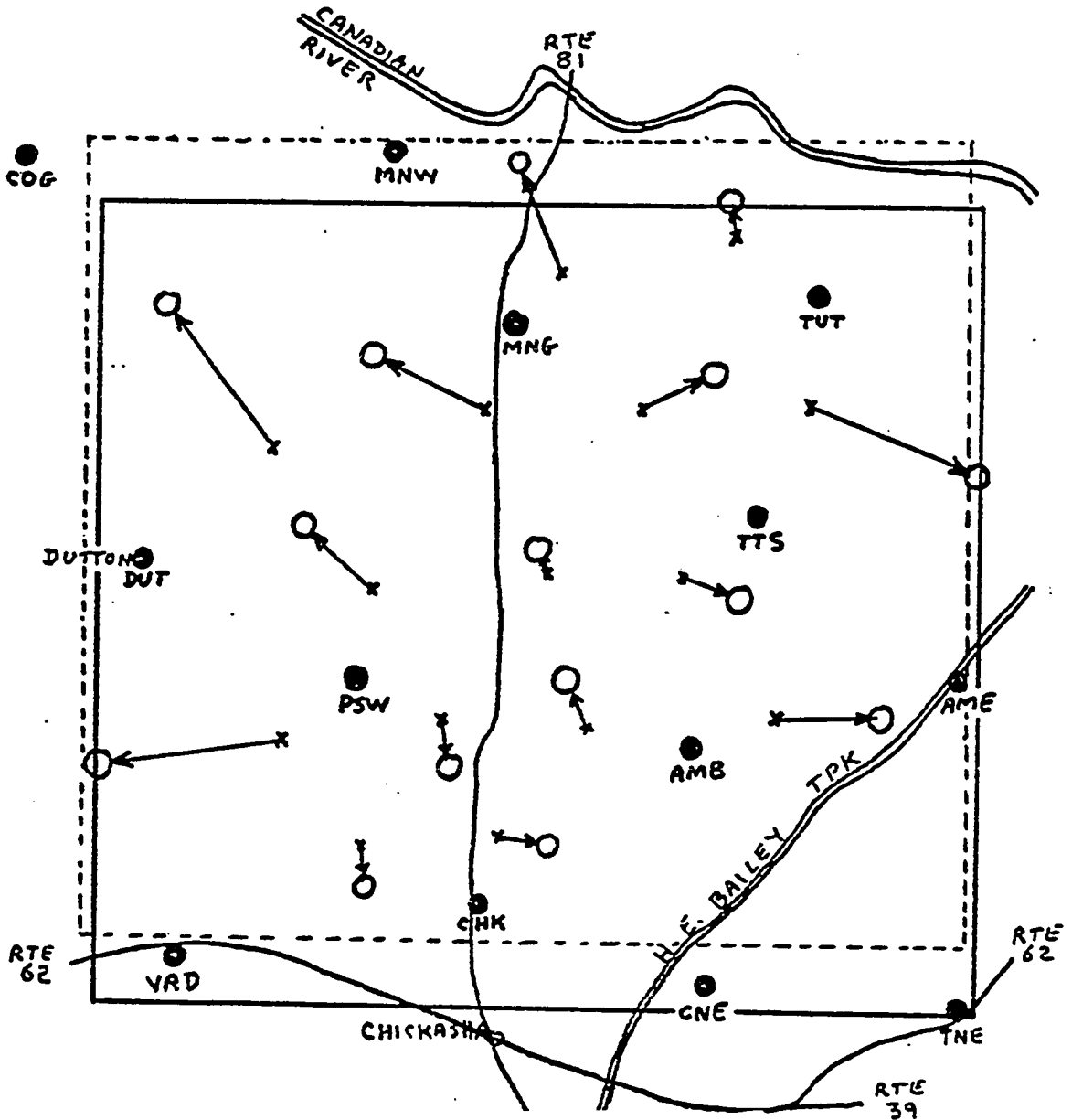


Fig. 6. Change in the PAM sensor positions due to optimization using the experimental design approach. Solid grid outline is optimal with respect to the analysis of the 13 solid (fixed) stations on a 3 km mesh. indicates positions of fixed NSSL network. "x" indicated positions of initial PAM network as placed subjectively by J. Stephens "O" indicated the final positions of PAM network after optimization. (Hembree and Eddy, 1978)

analysis was performed on a single storm. Then an optimum sensor placement was found for that storm. Instead of doing a sensor placement for each storm after the fact, a climatology of correlation functions can be developed and a representative correlation function chosen.

CHAPTER IV

DATA

The data available for this study consist of rain gage, radar, and satellite observations. They derive from the U.S. Bureau of Reclamation's HIPLEX project located at Miles City, Montana. Fig. 7 shows the location of the experimental site. John Middleton (of the U.S. Bureau of Reclamation) with the aid of an automatic radar cell tracking routine has identified many convective complexes. The term "convective complex" is defined as a collection of convective cells grouped in such a manner that they appear to belong to the group scale of organization which is somewhat larger than that of the individual cell. Of these, four have been chosen as possible cases for study because the satellite data are readily available. These are summarized in Table 1.

In the discussion of the results several terms may be used interchangeably and others need some clarification. These are as follows:

1. The area of the correlation ellipse discussed in section 2 of Chapter III will be referred to as the correlation area and/or representative area.

Table 1. Radar storm characteristics for the four convective complexes chosen for study.

Storm Number	2	3	5	6
Time of Origin (GMT)	18:12	18:22	18:16	18:52
Date	5/27/77	5/27/77	5/27/77	5/27/77
Duration Minutes	265	400	230	150
Maximum dBZ 1 DEG Scan	52	56	42	49
Time of MAX dBZ	19:37	21:32	19:37	22:17
Number of Volume Scans	51	76	47	30
First Echo At Origin	Yes	Yes	Yes	Yes
Merged with Complex	-	-	3	-

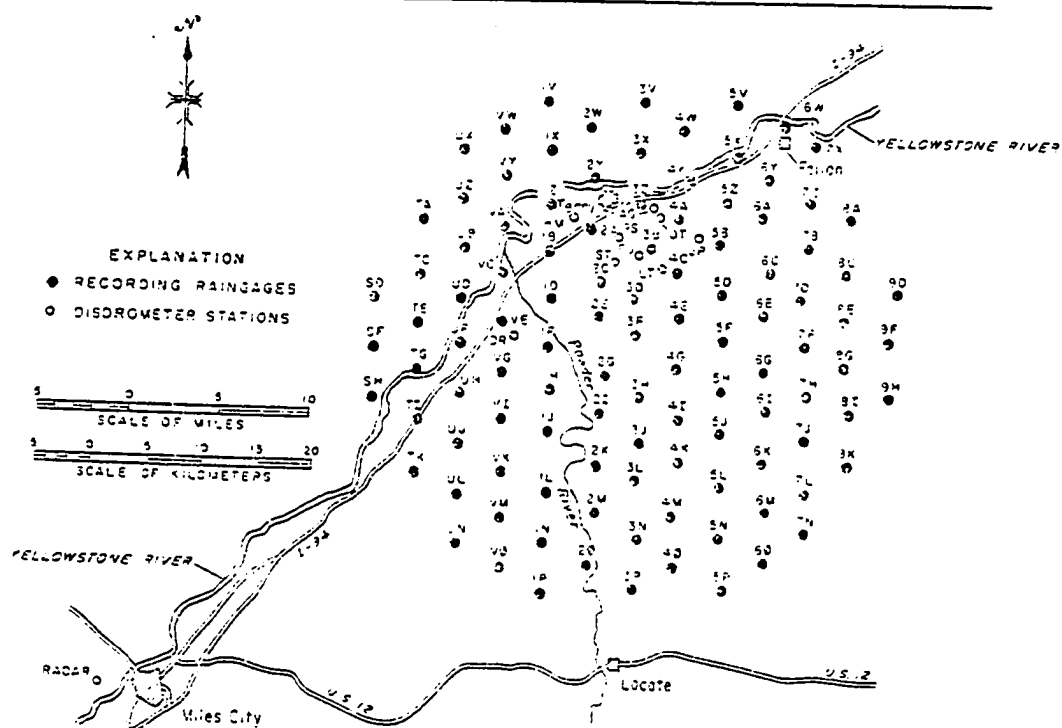


Fig. 7. HIPLEX experimental site.

2. Often "radar" will be used in place of "radar rain rate" when the usage is clear. This is often the case in table and figure captions.
3. The terms visible and visible reflectance are used interchangeably.
4. The terms IR and IR temperature are used interchangeably.
5. The IR temperatures have been subtracted from a constant value such that the expected cross-correlations will be positive.

Only storm number three passed over the gage network; however, the satellite data for that period when the storm was over the gages are not readily available. Consequently, it is not possible to perform any direct correlations between surface rainfall and the satellite imagery. However, there are radar reflectivities available at time corresponding to the satellite imagery. As the relationship between radar reflectivities and rain rates is well established, the cross-correlation between radar derived rain rates and the satellite imagery can yield some beneficial results.

1. Radar Data

The radar data consist of digitized 5 cm radar returns. The radar required five minutes to complete a volume scan of 12 elevation angles from 1° to 12° of 360° each. Only the 1° elevation angle is used in this study. The use of higher angles was investigated; however, the portions of the complex included within the returns varied too much for our purpose. (i.e. close in we would be looking at the base and not much

further away we would be looking at the top of the system.) The beam width of the radar is 0.98° and the bin size is .05 km. The closest gate is at 25 km and the farthest is at 150 km.

The reflectivities were converted to rain rates using Jones' (1956) Z-R relationship:

$$R = 0.010938 (Z)^{0.72993}$$

where R is in mm/hr. These rain rates were then processed to obtain estimates of 15 minute average rain rates at 15 minute intervals starting on the hour. The average life time of cells defined by the 10 dBz echo for the 1977 Montana HIPLEX season was 40 minutes (Brady, et al, 1979).

2. Satellite Data

The satellite data consist of visible reflectance and IR radiance and are summarized in Table 2. The visible reflectance data are measures of the brightness of the cloud top, reported on an arbitrary scale from 0 to 255, and have a resolution of 1 km at the satellite subpoint. The higher the number, the brighter the cloud top with 0 corresponding to deep space and 255 corresponding to the sun. The IR radiance is also reported as a digital count on a scale from zero (0) to 255. It is calibrated to give an estimate of the cloud top temperature. The equations that relate the IR digital count to temperature are

$$T = 330.0 - 0.5DC : 0 < DC \leq 176$$

$$T = 418.0 - DC : 176 < DC \leq 255$$

where T is the temperature in degrees Kelvin, and DC is the

Table 2. Summary of satellite data sets.

Complex	Time GMT	Area Sq KM	Maximum Brightness	Maximum IR Count	Number of Visible Data Pts.
2	1830	424	162	208	425
	1900	1235	169	220	1849
	1930	2120	171	216	3591
	2000	3366	163	200	6319
	2030	4623	149	196	6319
	2100	4704	147	192	5049
	2130	4505	136	232	5005
3	1830	266	158	196	357
	1900	643	166	200	735
	1930	1252	164	204	1287
	2000	2546	157	200	2301
	2030	2927	156	196	2301
5	1830	411	139	180	525
	1900	515	166	204	697
	1930	579	173	208	961
	2000	1687	167	204	2828
	2030	2840	159	200	2665
6	2000	858	148	188	1225
	2030	1302	148	192	273
	2100	1460	153	196	2989
	2130	1911	153	188	3621
	2206	3697	151	184	5727

digital count. The resolution of the satellite IR sensor is 4 km north-south and 8 km east-west at the satellite subpoint.

The geometry of the satellite data is given in Fig. 8. As the satellite spins, a sensor's field of view sweeps across the surface of the earth along what is known as a scan line (horizontal scan line in Fig. 8). Discrete samples are taken along this scan line, digitized, and stored for transmission to a ground based receiver. While the sensor is pointing away from the earth a mirror is stepped in the vertical to obtain the next scan line. Due to the geometry of the earth-satellite system, the scan lines are concave in the

northern hemisphere with the amount of concavity being greater the further northward the scan line is from the sub-satellite point. For the purpose of discussion, the locus of points that would be generated if the satellite stopped spinning at some point and the mirror stepped through its range will be called a vertical scan line. The vertical and horizontal scan lines are perpendicular only along the line that is the projection of the satellite's spin axis on the earth's surface. Also the field of view of the sensor is circular only at the nadir. As the field of view proceeds away from the nadir it becomes more elliptical and the resolution decreases.

3. Temperature Gradient

As discussed earlier the highest temperature gradient should be associated with the higher rain rates (Scofield and Oliver, 1978). This is basically because the higher temperature gradients are at the upwind end of the storm where the mature cloud is located. For the purposes of this study, the IR temperature gradient has been defined as the negative component of the actual gradient along the vector ϕ where the vector ϕ is the downwind direction. It is believed the orientation angle of the IR temperature correlation ellipse (see Section 2, Chapter III, page 24) will be a good indicator of the downwind direction. Therefore, it is used for the angle ϕ .

There is some question as to whether the entire gradient field should be used in the correlation calculations or just the areas of positive gradient component. In an attempt

to shed some light on this the correlation field involving the temperature gradient was calculated twice: once with the threshold level set to zero which allowed only positive gradients to enter into the calculations and once with the threshold set to -1000 which effectively allowed the entire gradient field to be used.

4. Satellite Navigation

An earlier attempt at navigation (locating the pixels on the earth's surface) by the author (Hembree and Eddy, 1977) involved the determination of surface features in the visible picture and finding the longitude and latitude of those

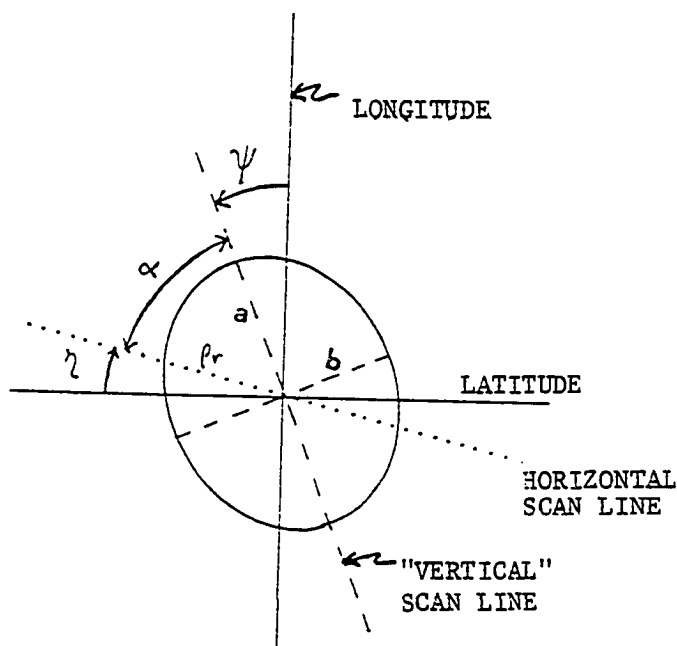


Fig. 8. Relationship between longitude and latitude lines, horizontal and vertical scan line, and the pixel. Configuration is for longitude west of satellite meridian and in northern latitudes. Angles are exaggerated for clarity. (Eddy and Hembree, 1977)

points. A procedure was then developed that allowed one to find the longitude and latitude of any pixel by stepping along the scan lines. The approach gave only approximate results due to the assumptions made. However, since the only concern was with satellite data, high accuracy was not necessary.

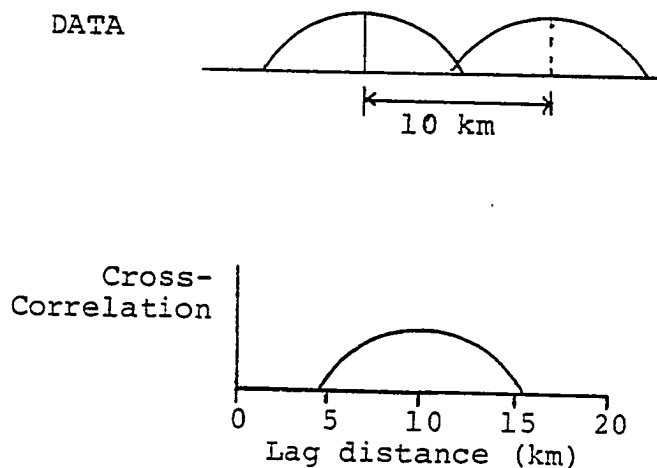
In the proposed research the satellite data are to be correlated with data fixed with respect to the earth's surface. This requires a higher degree of accuracy than did the earlier study, and the procedure developed could not be used. A computer program has been obtained from the Atmospheric Science Department at Colorado State University and has been implemented on the U.S. Bureau of Reclamation's computer system. This program gives the best navigation obtainable at this time. The accuracy of the navigation is dependent upon the degree of accuracy to which the satellite navigation parameters can be determined and at best is approximately ± 10.0 km. The program uses the satellite orbital parameters, the scan line number, pixel number, and the height of the cloud top to find the longitude and latitude of a given pixel. The satellite orbital parameters are those obtained along with the image and then improved by using surface features identifiable in the image.

5. Effects of Misnavigation

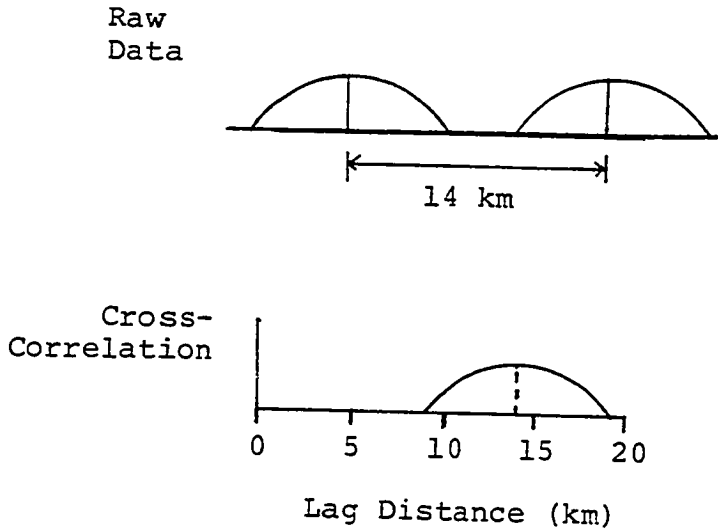
There are basically two effects of misnavigation: (1) in cross-correlation calculations the absolute lag (displacement between the variables) at which the maximum correlation

occurs may be indeterminate; and, (2) it may not be possible to determine XYT correlation matrices. Each of these will now be discussed.

First consider two one-dimensional data sets that are navigated correctly with respect to each other and that 10 km separate their respective maxima. If the cross-correlation between the two data sets is calculated, it will be found that the maximum cross-correlation occurs at a lag of 10 km.



Next assume that the variable on the right is misnavigated such that 14 km separate the maxima. If the cross-correlation is then calculated, it is found that the shape of the cross-correlation curve is the same; however, the maximum now occurs at a lag of 14 km.



Therefore, the only information that is lost is the lag at which the maximum correlation occurs. It would be helpful to have this information although still present are both the shape of the cross-correlation function and the magnitude of the cross-correlation. If the data sets are two-dimensional then the same argument applies. The only difference is that the lag is a two-dimensional vector and the cross-correlation is a two-dimensional function.

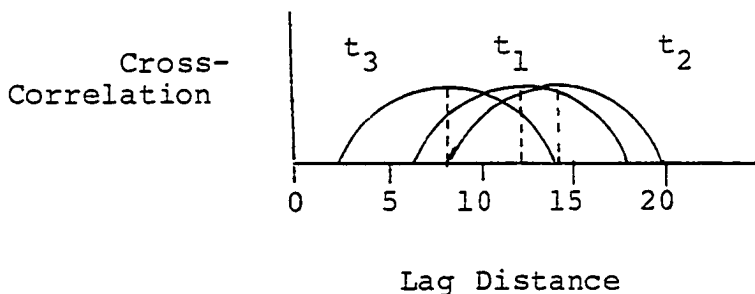
The second effect arises when the navigation error is not constant in time. This causes a problem because of the manner in which the calculations are performed. Suppose that there are three observation times (t_1 , t_2 , and t_3) and two variables (A and B). Now the time lag zero cross-correlation field is a composite of the cross-correlation fields at each time. That is, A cross B at t_1 , A cross B at t_2 ,

and A cross B at t_3 are composited. A similar compositing is performed at other time lags. If the data sets are all navigated correctly then there is no problem as the maximum cross-correlations all occur where they would naturally (even though this lag changes with time). Even if the navigation is in error but constant with time all that is lost is the actual (average) lag at which the maximum correlations occur. However, if the navigation error is not constant with time then the lag at which the maximum correlation occurs varies in the obscure manner.

Suppose the relative navigation errors for each time are

TIME	NAVIGATION ERROR
t_1	+2
t_2	+4
t_3	-2

and that the true separation should be 10. Then the cross-correlation functions would be as shown with the maxima occurring at lags 12, 14, and 8, respectively.



If the navigation was constant, the maxima of these three correlation functions would essentially occur at the

same lag and a compositing would yield a realistic cross-correlation function. However, under the navigation assumption used, any compositing would yield an unrealistic cross-correlation function. In the example the function would be too broad.

A more formal argument illustrating this is as follows. The covariance matrix of \hat{Y} in classical regression can be shown to be

$$\begin{aligned} \text{COV } \hat{Y} &= X (\text{Var } \hat{\beta}) X^t \\ &= \begin{bmatrix} \text{Var } (\hat{Y}_1) & \dots & \text{COV } (\hat{Y}_i, \hat{Y}_j) \\ \text{COV } (\hat{Y}_j, \hat{Y}_i) & \dots & \text{Var } (\hat{Y}_n) \end{bmatrix} \end{aligned}$$

and

$$\text{COV } \hat{\beta} = (X^t X)^{-1} \sigma_{\epsilon}^2$$

where

X = The observation matrix, and

σ_{ϵ}^2 = the population error variance

Hence,

$$\text{COV } \hat{Y} = X (X^t X)^{-1} X^t \sigma_{\epsilon}^2$$

and the variance of the objective analysis, \hat{Y} , is a function of the covariance of the observations and the observations themselves and not of the "position" of the covariance function. Therefore, even though an actual objective analysis under the

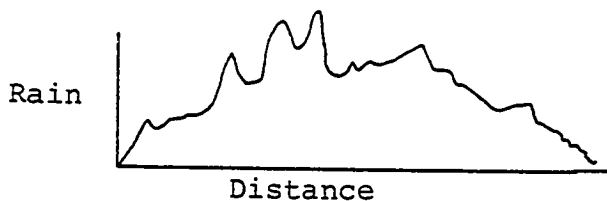
current navigation constraints cannot be performed, the potential value of using one of the fields to analyze another can be shown.

6. Effects of Instrument Resolution

One effect of instrument resolution concerns the number of non-redundant samples that can be taken. An earlier study (Eddy and Hembree, 1978) determined that a minimum of 20 observations is required to obtain a stable correlation function. If the covariance function is not known via other means, this criterion in itself will set a limit on the minimum size storm that can be analyzed depending upon the resolution of the sensor. If the relevant convective complex covariance functions are known from, say climatology, then only ten observations for a univariate analysis or five for a bivariate analysis are required to produce acceptable results. In any case, the data resolution ultimately determines the smallest size storm which can be analyzed.

If the scale of the features being investigated is the same as the resolution of the sensor, then any correlations that are found are probably due to noise or some large scale features. It should be pointed out that what is considered noise is relative. In this study the interest is in the entire rain producing area of the cloud and not necessarily individual cells. In this context the variations of individual cells about the overall pattern could be looked

upon as noise. (see figure below)



The difference in resolution between two sensor types is not as big a problem as it first appears due to the manner in which the cross-correlations are calculated. The net effect of the method is that (using lag zero as an example) all of the higher resolution data points below the area covered by each of the lower resolution data points are used in performing the correlation calculations. There is, therefore, an "averaging" of the higher resolution data points. The maximum correlation found though will be smaller than it would be if the resolution of the lower resolution sensor was better.

If all of the features present in the higher resolution data set are covered by only a few of the low resolution data points, then any cross-correlation field will at most have only a small area of significant correlations. If the significant features are all included in only one low resolution data point, the cross-correlation field will essentially represent noise with respect to the correlation field (not necessarily with respect to the data field). Care must also be taken in assigning effective degrees of freedom to the correlation values.

CHAPTER V

DATA ANALYSIS

Before the results are discussed the symbols used for the various correlation function and correlation ellipse parameters will be reviewed or defined. These are

σ = decorrelation distances in space, km
(page 21),

α = ellipticity (page 21),

A_7 = model lag zero correlation (page 21),

x_0, y_0 = offset distance, km (page 22),

C_x, C_y = components of "velocity" of the function
maximum along axes, km/hr (page 22),

ϕ = orientation of major axis of the correlation ellipse, degrees from north (page 24)

a, b = semi-axes of the correlation ellipse,
km (page 24),

A = representative area of correlation ellipse, km² (page 24),

ρ_0 = raw lag zero correlation, from north

θ = direction of motion of the function
maximum, degrees from north

$$\theta = \arctan (C_y/C_x)$$

$$V = (C_y^2 + C_x^2)^{1/2}, \text{ resultant speed of maximum km/hr.}$$

$$\gamma = \arctan (y_o/x_o), \text{ direction of offset in cross-correlation fields, degrees from north}$$

$$d = (x_o^2 + y_o^2)^{1/2}, \text{ magnitude of offset, km}$$

Also in the following discussion the following terminology is used. The phrase "single time XY correlation" will be used to refer to the correlation fields found using data at a single time. It is a two dimensional function of space only and represents the correlation field at a fixed time. The phrase "XYT lag zero" will be used to refer to the time lag zero correlation field of the XYT correlation set (see below). It is also a two dimensional function of space and represents a composite of the single time XY correlation fields for the times used in the XYT calculations. The phrase "XYT correlation" will be used to refer to the three dimensional (x and y is space and time) correlation fields. It consists of a series of XY correlation fields, one for each time lag. The single time XY correlation and XYT time lag zero correlation fields are always symmetrical and therefore σ_x^+ equals σ_x^- and σ_y^+ equals σ_y^- . Because of this equality the values of these parameters are listed under σ_x^+ and σ_y^+ only. In the discussion of the correlation fields the magnitudes of the correlations at the modes are referred to as the maximum correlations. Therefore, in multimodal fields there may be more than one maximum.

1. Convective Complex Number Two

The first radar echo for complex number two (2) was at 1812 GMT on 27 May. The complex dissipated while within radar range at 2230 GMT. During this period the apparent motion was toward the east. The radar data were acquired for the period 1830 to 2145 GMT and converted to rainfall rates at 15 minute intervals. The data for later times were not obtained because the last satellite image available was at 2130 GMT. Table 3 gives the times used in the radar auto-correlations.

Table 3. Case designations for convective complex number two radar data.

Time	Radar Auto-Correlation		Radar Cross-Correlation	
	<u>XYT</u>	<u>XY</u>	<u>XYT</u>	<u>XY</u>
1830	M	SM	M	SM
1900	M			
1900	MN	SN	MN	SN
1915	MN			
1930	NO	SO	MNO	SO
1945	NO			
2000	OP	SP	NOP	SP
2015	OP			
2030	PQ	SQ	OPQ	SQ
2045	Q			
2100	QR	SR	PQ	SR
2115	QR	SS		
2130	R	ST	Q	SS
2145	R			

The times at which satellite data are available for convective complex number two (2) and the case designations are given in Table 4. The navigation of the satellite data appears to be consistent from one time to the next.

This complex consists of a single well defined cell in

Table 4. Case designations for convective complex number two satellite data.

Time	Correlation Cases	
	<u>XYT</u>	<u>XY</u>
1830	M	SM
1900	MN	SN
1930	MNO	SO
2000	NOP	SP
2030	OPQ	SQ
2100	PQ	SR
2130	Q	SS

the radar echoes and shows the classic anvil growth in the satellite imagery. Fig. 9 shows the objective analysis of the visible reflectance, IR temperature, and radar data at 1930 GMT. Note that in the plots of the IR data the vertical axis is inverted, and the temperature decreases upward. The flat area in the southwest corner is where no data were available. The axis of the cloud is seen to be approximately north-south, and as expected, the visible and IR axes are nearly colinear. The IR analysis does not have as sharp a drop off as the visible; this is probably due to the coarser resolution of the IR. The radar rain, appearing as a spike because of the analysis grid spacing, is located under the southern end of the cloud. Fig. 10 is a plot of an additional objective analysis (blowup of Fig. 9c) performed on the radar using a finer grid. The east-west width of the brighter visible area at line A-B is approximately 37 km. Fig. 11 is a plot of the raw visible reflectance and IR temperature fields. The axes are not orthogonal as the data have been plotted with unrectified coordinates. The arrow indicates approximate north.

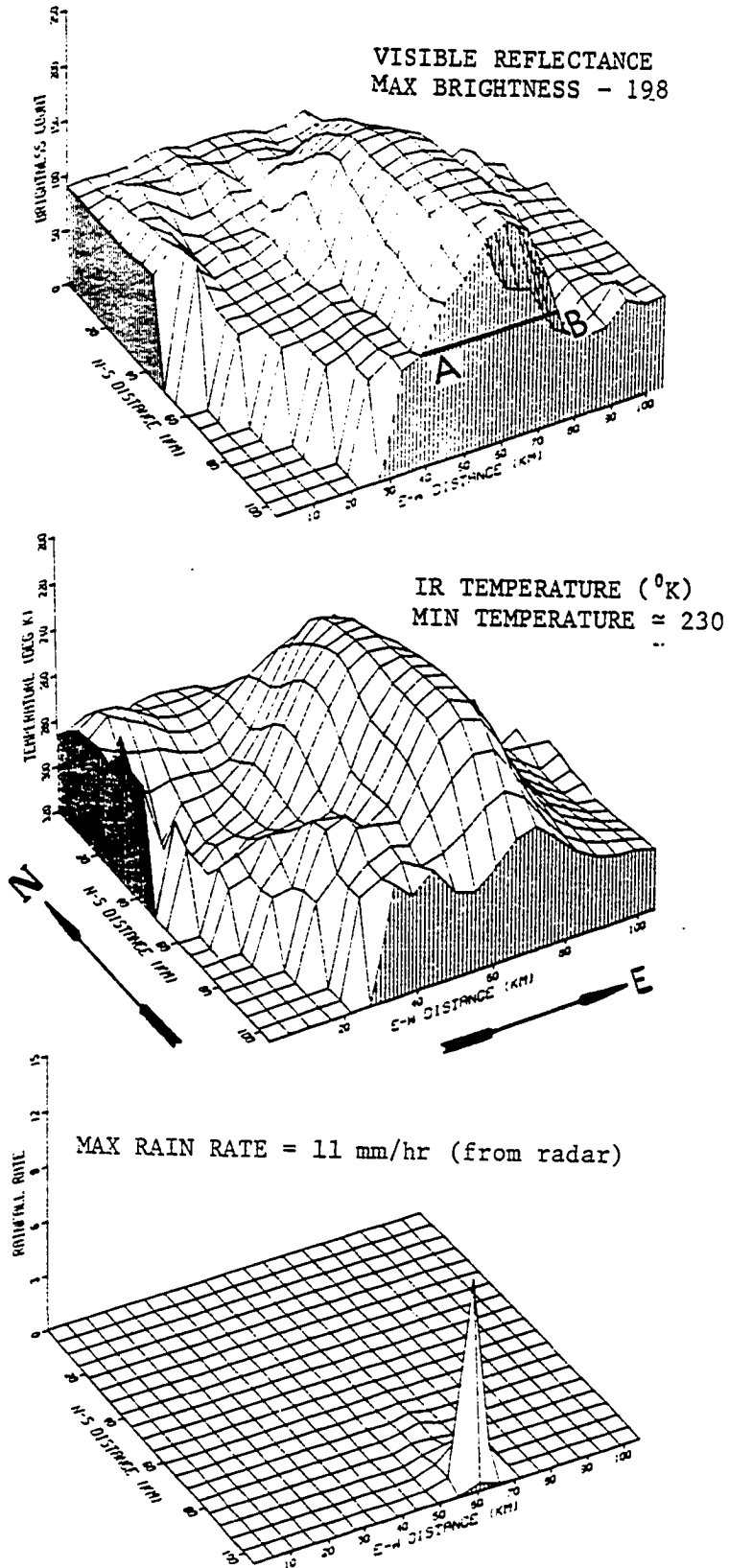


Fig. 9. Objective analysis of satellite reflectance and IR temperature and radar rain rates for 1930 GMT. (grids are orthogonal)

Fig. 12 is a plot of the total storm volumetric rain rates for the period 1830 to 2145 GMT and representative correlation areas. The period of data can be seen to cover only the developing stage of the complex. Further reference will be made to this figure later.

a. Radar Rain Rates

Figs. 13 and 14 are plots of the raw XYT correlation fields for radar cases M and N. It is seen that the radar becomes more coherent as time increases. Also comparing the plots for time lag zero and time lag one (30 minutes), one sees that the point of maximum correlation has moved toward the east-northeast.

From Fig. 14 it can be estimated that at time lag one the maximum correlation is displaced 6 km eastward and 1.5 km northward. This is interpreted as indicating that the

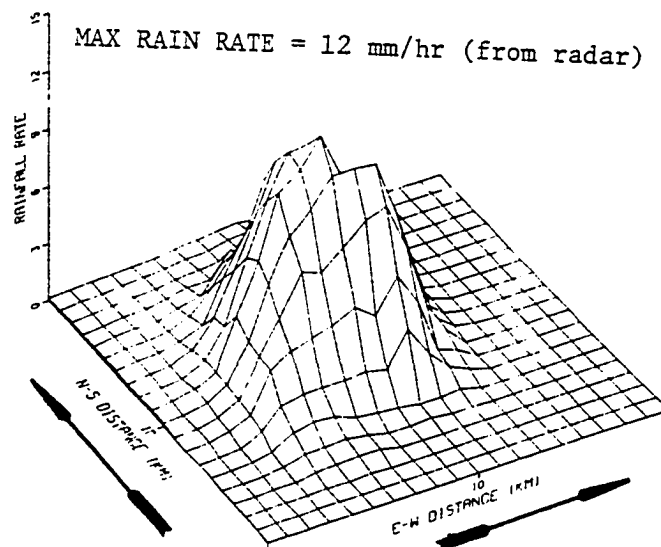


Fig. 10. Objective analysis of radar data on finer grid.

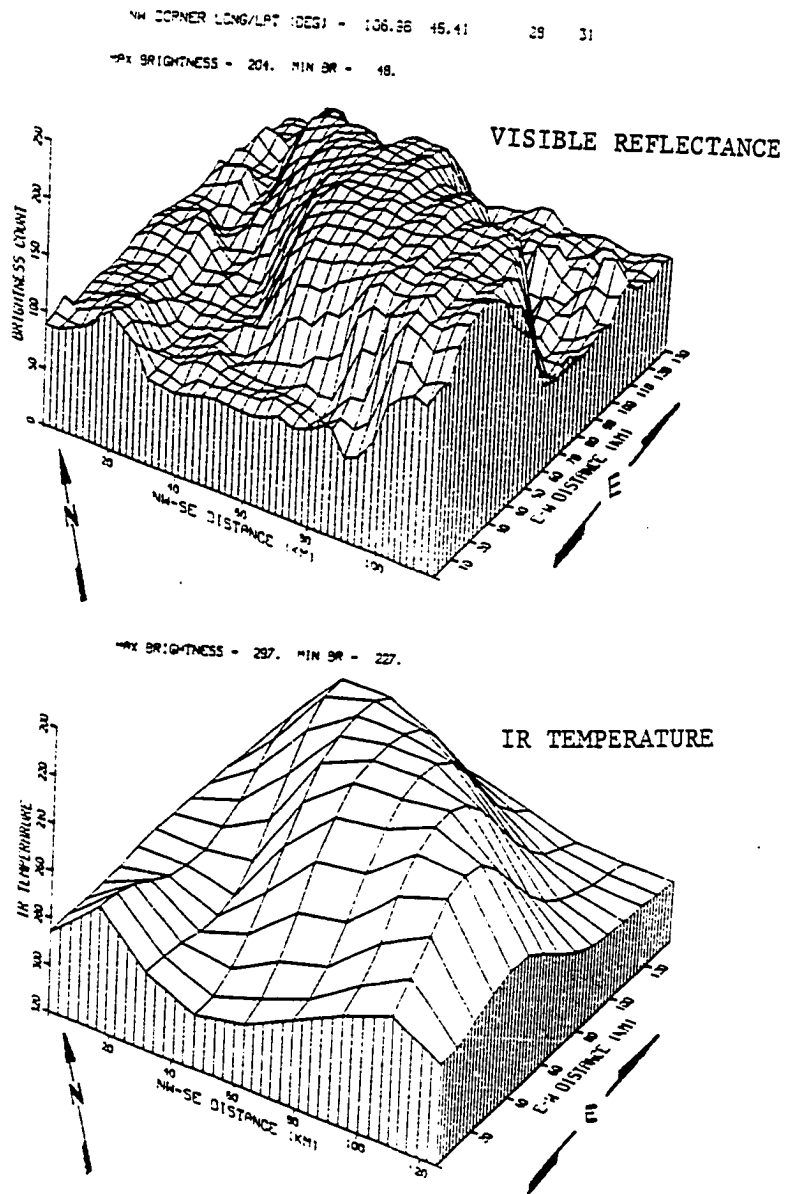


Fig. 11. Plot of raw visible reflectance and IR temperature data fields. (axes are not orthogonal)

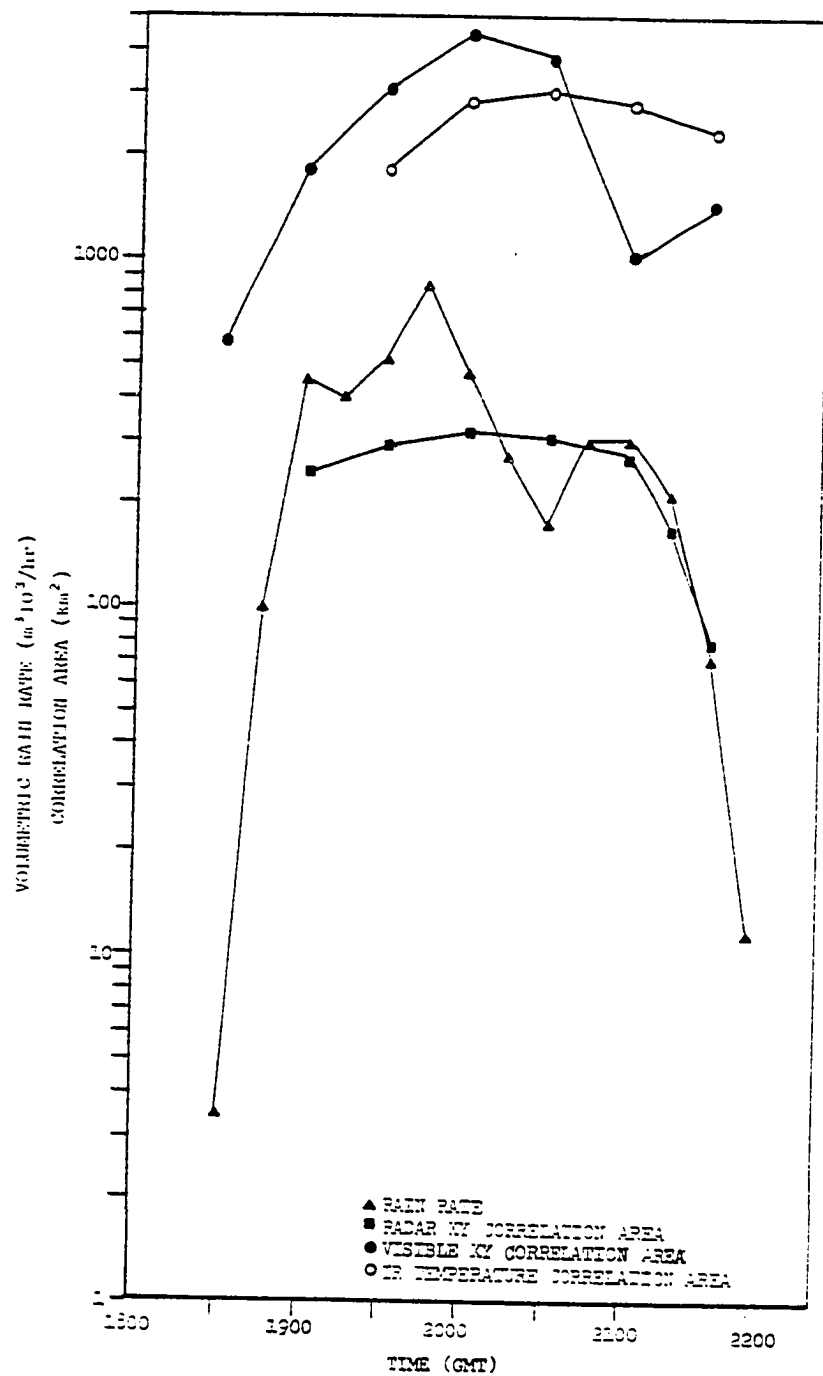


Fig. 12. Plot of total storm volumetric rain rates and representative correlation areas for complex number 2.

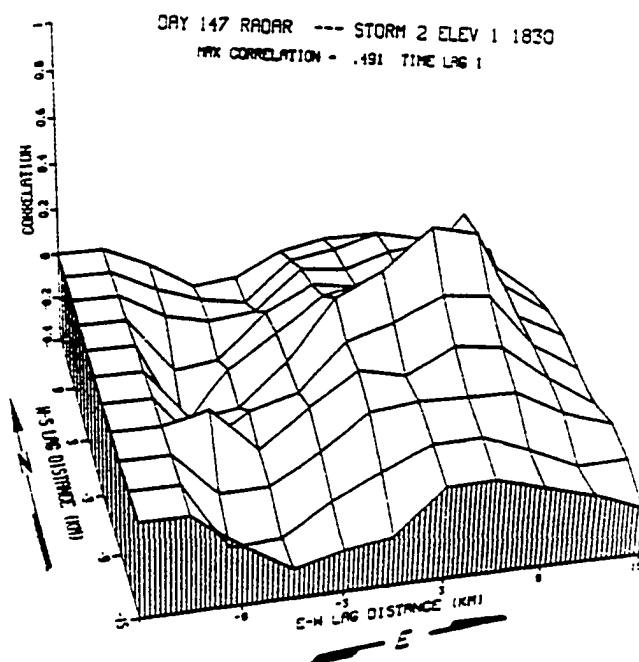
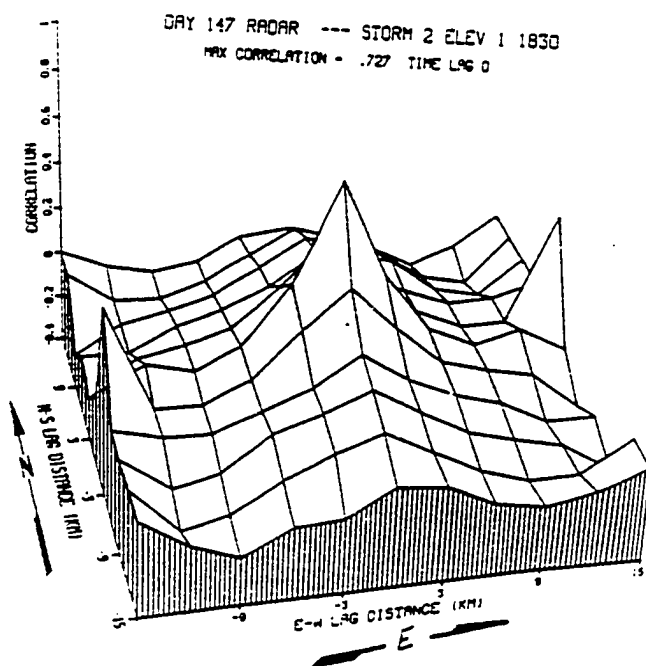


Fig. 13. Plot of complex number 2 raw radar correlation fields for case M. (grids are orthogonal)

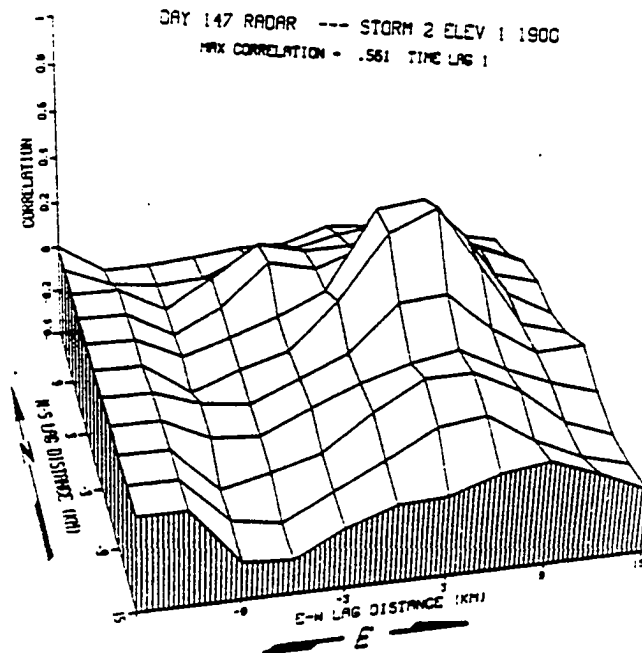
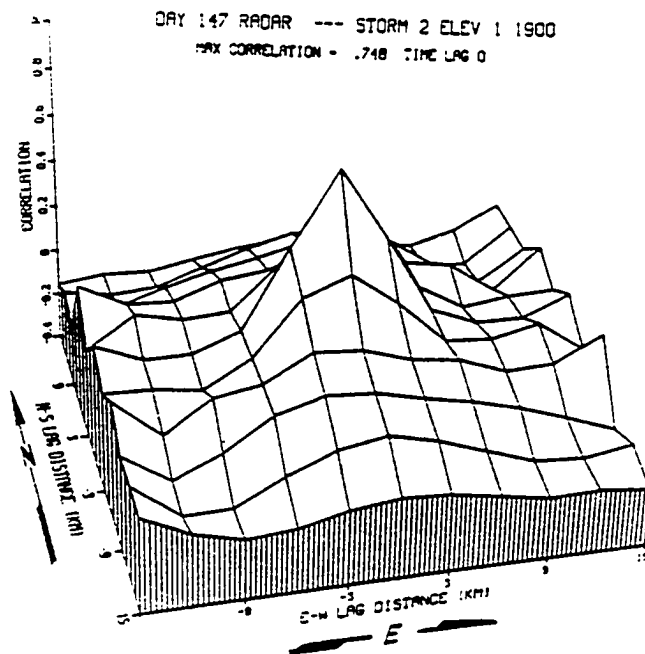


Fig. 14. Plot of complex number 2 raw radar correlation fields for case N.

correlation between a radar bin at one time and another radar bin 30 minutes later is a maximum if the later bin is 6 km east and 1.5 km north of the earlier bin. This implies that during the 30 minutes the storm has moved that distance on the average. Converting the displacement to a velocity, one obtains 12.09 km/hr at a heading of 76° . Table 5 shows the results of the function fits which are also plotted in Figs. 15 to 17. Looking at the velocity obtained for case N, one sees that the fit came up with 13.36 km/hr at 78° which is close to the rough estimate obtained above. Initially the motion is toward the east and then after a short time becomes east-northeasterly. This agrees with the statement at the beginning of this section.

Table 5. Parameters of fitted model correlation function for complex number 2 radar rain rates. (see pages 44 and 45)

	CASE	TIME (GMT)	σ_{x+} km	σ_{x-} km	σ_{y+} km	σ_{y-} km	σ_z min	ρ_r	ρ_θ	α	β ($^\circ$)	γ km	δ km	A km ²	V km/hr	θ ($^\circ$)
SINGLE TIME XY	SM	1830	----	----	----	----	----	----	----	----	----	----	----	----	----	----
	SN	1900	6.5	----	12.4	----	----	0.51	0.31	0.21	9	12.5	6.3	246	----	----
	SO	1930	7.6	----	12.4	----	----	0.54	0.83	-0.01	-1	12.4	7.6	295	----	----
	SP	2000	10.7	----	11.3	----	----	0.59	0.80	0.57	40	14.2	7.3	326	----	----
	SQ	2030	12.6	----	9.6	----	----	0.52	0.64	0.59	56	14.3	6.9	308	----	----
	SR	2100	11.5	----	8.0	----	----	0.61	0.75	0.27	72	11.8	7.5	278	----	----
	SS	2115	5.9	----	9.3	----	----	0.65	0.77	-0.09	-5	9.4	5.8	170	----	----
	ST	2130	4.3	----	6.9	----	----	0.74	0.66	-0.52	-23	7.4	5.4	79	----	----
XYT ($\Delta t=0$)	M		6.7	----	14.2	----	----	0.41	0.73	0.06	2	14.2	6.7	297	----	----
	N		9.4	----	12.7	----	----	0.44	0.75	0.06	7	12.8	9.3	373	----	----
	O		10.7	----	12.4	----	----	0.46	0.77	0.01	3	12.4	10.7	417	----	----
	P		8.8	----	9.1	----	----	0.59	0.74	0.38	43	10.5	7.1	233	----	----
	Q		8.1	----	8.3	----	----	0.56	0.75	0.13	40	8.8	7.7	212	----	----
	R		6.5	----	9.9	----	----	0.64	0.79	-0.09	-6	10.0	6.5	203	----	----
XYT	M		7.9	7.4	12.7	12.9	250	0.40	0.73	0.04	2	12.8	7.6	308	9.1	94
	N		8.5	9.2	13.0	13.8	320	0.46	0.75	0.02	1	13.4	8.8	371	10.6	80
	O		9.7	10.3	11.7	12.0	159	0.47	0.77	0.10	15	12.0	9.9	373	12.1	73
	P		8.8	8.9	9.3	10.7	184	0.53	0.74	0.33	35	11.0	7.6	262	15.5	69
	Q		7.2	7.9	8.1	8.2	121	0.58	0.75	0.11	26	8.4	7.3	192	12.0	73
	R		6.7	6.3	9.4	11.0	90	0.65	0.79	-0.15	-9	10.3	6.4	207	12.3	64

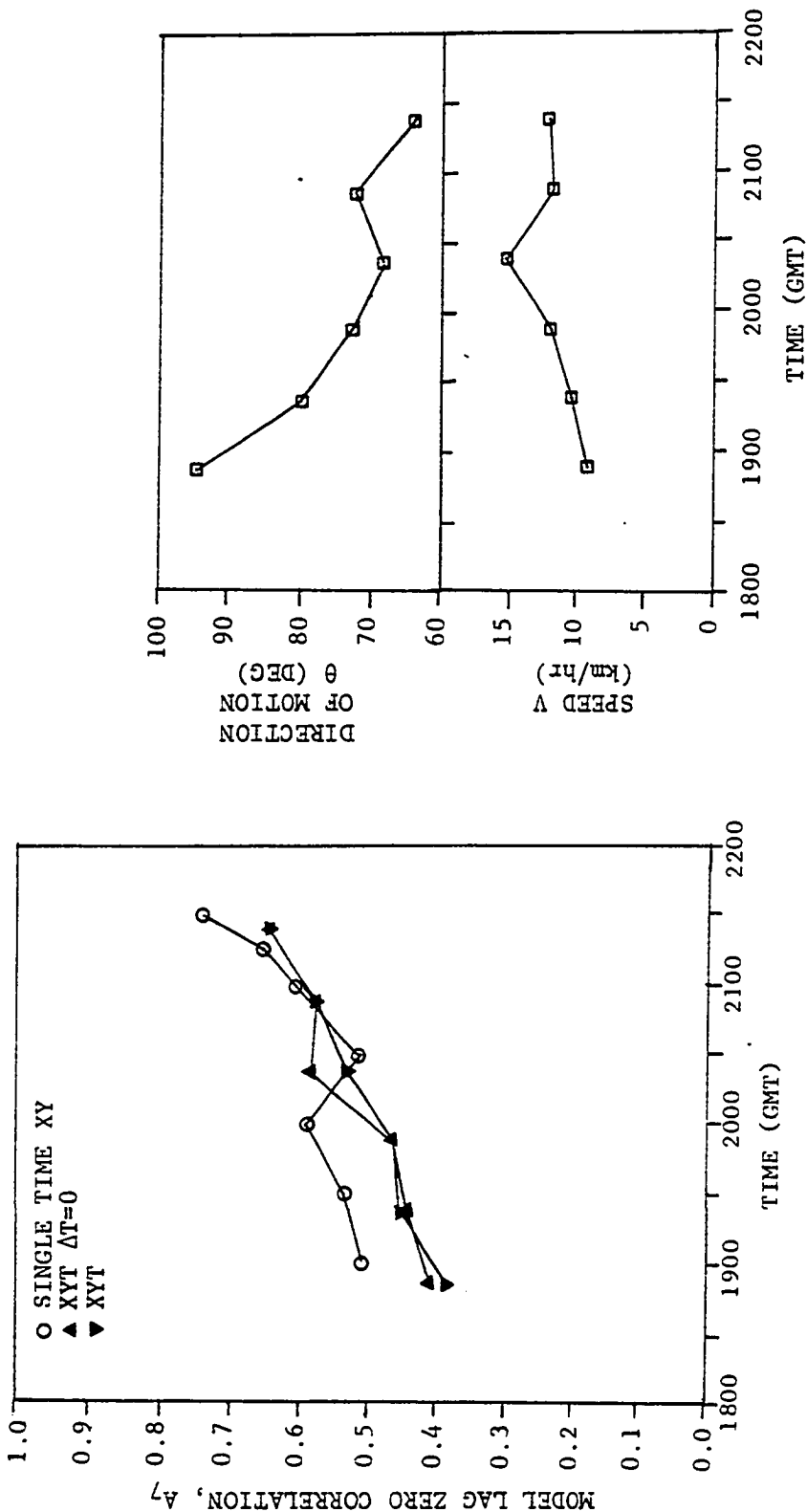


Fig. 15. Plots of model lag zero correlation (A_7), direction of motion (θ), and speed (V) for complex number 2 radar model fits.

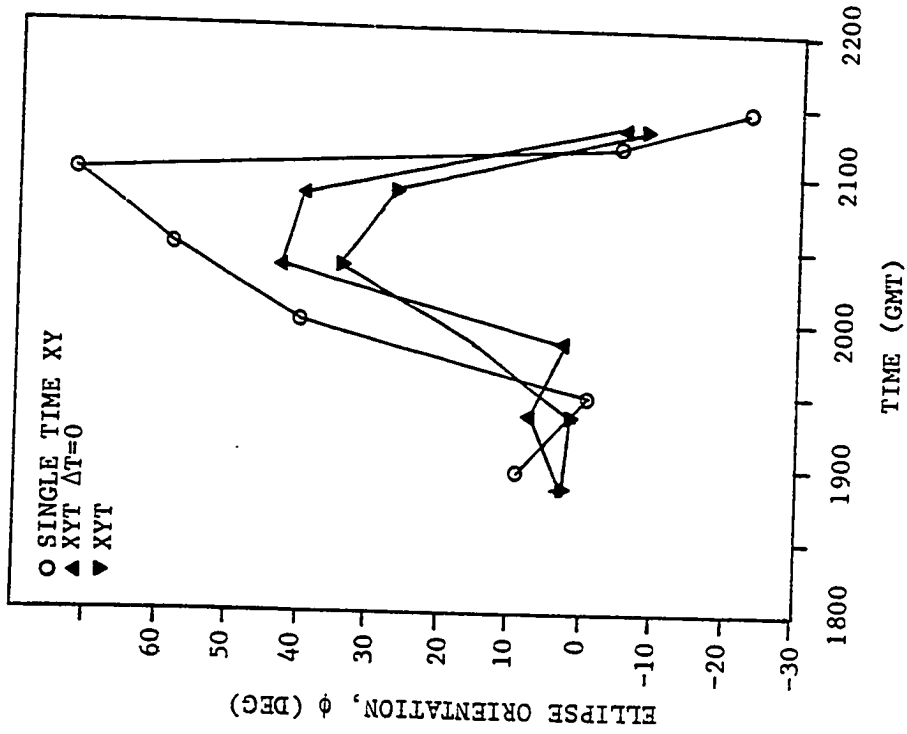
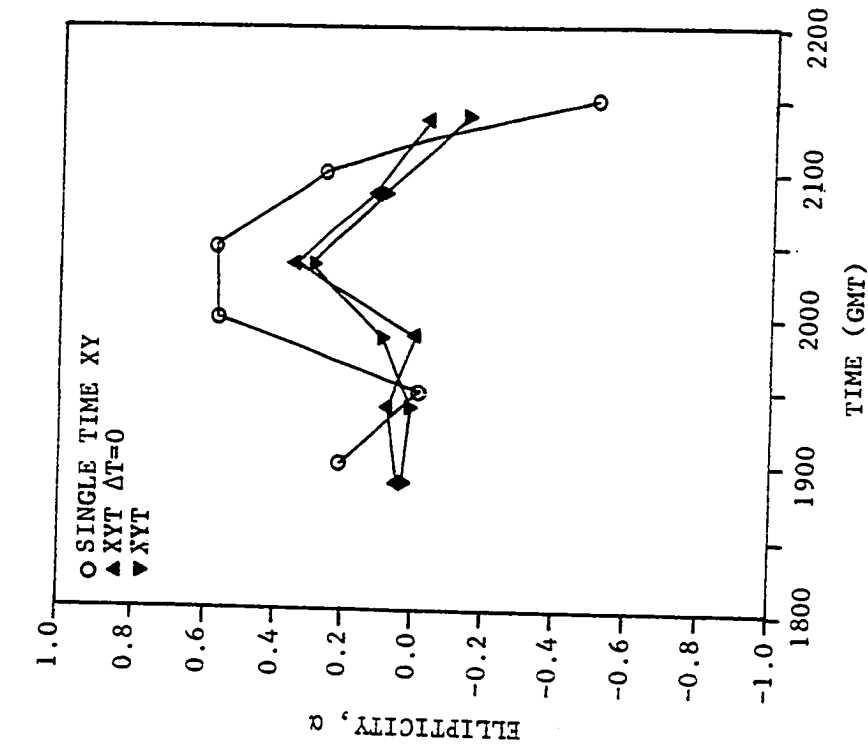


Fig. 16. Plots of ellipticity, (α), orientation angle (ϕ), and semi-axes of ellipse (a and b) for complex number 2 radar model fit.

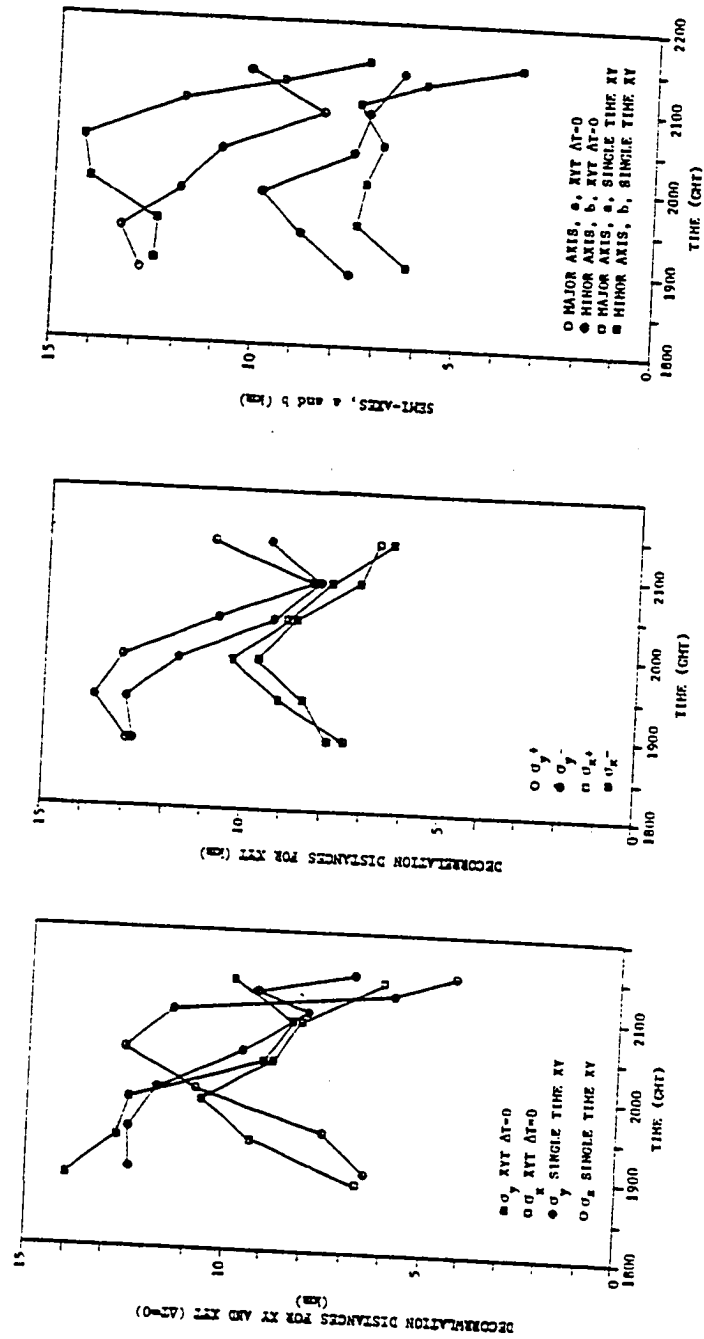


Fig. 17 Plots of XY and XYT decorrelation distances (σ 's) for complex number 2 radar model fits.

It is difficult to determine much from the σ 's. This is because individually they are not a conservative property upon rotation of the correlation ellipse. However, the major and minor semi-axes of the correlation ellipse are conservative upon rotation (Sec.2, Chapter III). The plots of the semi-axes show how the axes start out small, grow as the storm matures, and then decrease as the storm dissipates. The semi-axes for case SM (1830 GMT) were not available because a function fit was not possible; the correlation field was too small. The σ 's change because the orientation of the correlation ellipse changes with time. Referring to Fig. 12, it can be seen that the radar representative correlation areas tend to follow the trend in the rain rate curve. The peak area for the single time XY correlation fields appears to lag the peak rain rate. It is believed, however, that this may be due to the time resolution of the data because the peak rain rate occurs between the time at which the areas of the correlation ellipses were determined.

b. Visible Reflectance

An inspection of the plots of the position of the visible reflectance data, Fig. 18, suggests that the center of the bright area is moving toward the east-northeast or northeast initially and easterly near the end. The maximum area is at 2000 GMT. There is some question as to the navigation; however, the navigation parameters have been checked and no errors were found. Table 6 gives the results of the function fits to the raw correlation matrices. The parameters

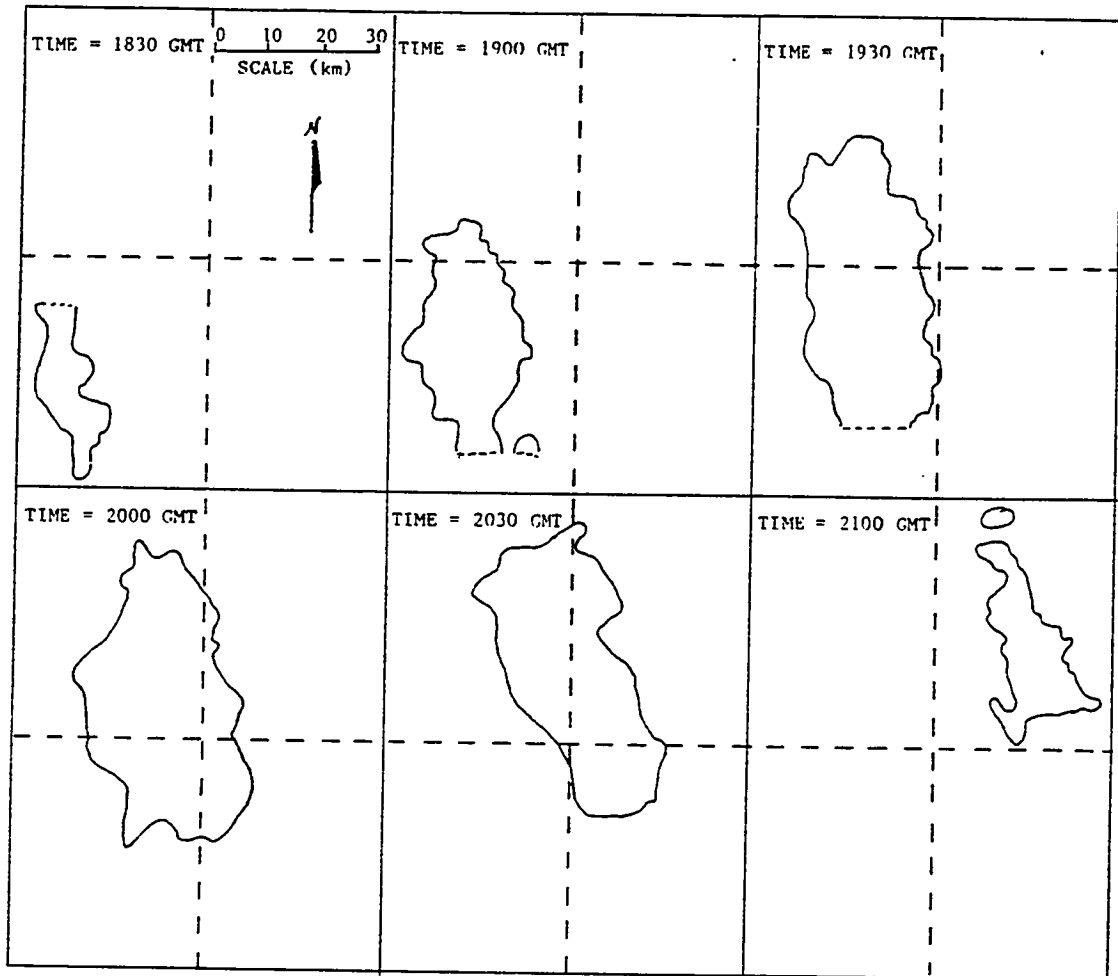


Fig. 13. Plot of positions of complex number 2 satellite visible data. (contoured at a reflectance digital count of 164 and grid is fixed in space)

Table 6. Parameters of fitted correlation function for complex number 2 visible correlation fields. (see pages 44 and 45)

	CASE	TIME (GMT)	σ_{x+}	σ_{x-}	σ_{y+}	σ_{y-}	σ_t	Λ_1	Λ_2	α	ϕ	a	b	A	V	θ
			km	km	km	km	min				(°)	km	km	km ²	km/hr	(°)
SINGLE TIME XY	SN	1830	9.5	----	47.9	----	---	0.55	0.60	-0.91	-10	48.7	3.8	588	----	---
	SN	1900	15.9	----	37.4	----	---	0.83	0.87	0.00	0	37.4	15.9	1868	----	---
	SO	1930	18.7	----	57.0	----	---	0.71	0.88	-0.37	-8	57.4	17.3	3112	----	---
	SP	2000	26.9	----	52.7	----	---	0.64	0.85	-0.13	-7	52.9	26.3	4380	----	---
	SQ	2030	26.3	----	52.6	----	---	0.68	0.83	-0.50	-17	54.6	21.9	3759	----	---
	SR	2100	15.0	----	24.9	----	---	0.75	0.78	-0.50	-22	26.4	12.3	1020	----	---
	SS	2130	19.2	----	35.9	----	---	0.77	0.79	-0.75	-24	39.0	11.8	1444	----	---
XYT ($\Delta t=0$)	M		15.2	----	39.3	----	---	0.55	0.76	0.23	6	39.4	14.7	1826	----	---
	N		18.0	----	46.8	----	---	0.69	0.87	-0.01	0	46.8	18.0	2649	----	---
	O		23.0	----	40.2	----	---	0.77	0.87	-0.26	-12	40.8	21.9	2803	----	---
	P		22.2	----	-3.4	----	---	0.69	0.79	-0.35	-20	34.8	20.0	2182	----	---
	Q		20.6	----	34.2	----	---	0.71	0.76	-0.59	-25	36.8	15.4	1782	----	---
XYT	M		13.8	14.0	42.2	48.6	154	0.54	0.76	0.20	4	45.5	13.6	1941	27.5	37
	N		DID NOT CONVERGE													
	O		23.1	24.2	43.6	49.4	---	0.73	0.87	-0.25	-40	26.5	20.5	3351	36.2	25
	P		22.1	22.7	34.8	38.3	119	0.66	0.79	-0.33	-16	37.6	20.5	2421	30.9	49
	Q		21.1	21.2	43.6	43.6	77	0.56	0.76	-0.56	-18	45.4	16.9	2407	22.2	91

are plotted in Figs. 19 to 21. The direction of motion obtained from the XYT fit agrees with the conclusion reached above. Fig. 22 is a plot of the speeds and directions of motions for the visible, and radar data. The satellite values are different from those of the radar. This is because of the growth of the anvil toward the north. It was initially felt that the increase in the ellipticity parameter, σ , was a reflection of the growth of the anvil. However, an examination of the ratio of the major to minor axes shows that this is not true. If the ratio reflected the growth of the anvil, the ratio would be expected to increase. This is because the width (minor axes) would not increase as fast or as much as the length (major axes). An examination of a plot of the a/b ratio, Fig. 21, does not in-

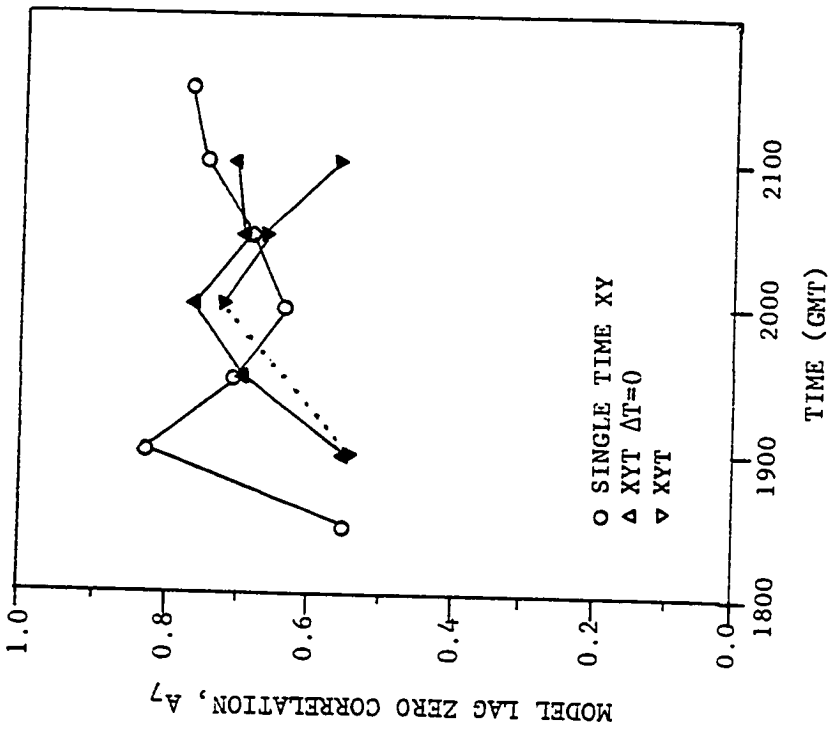
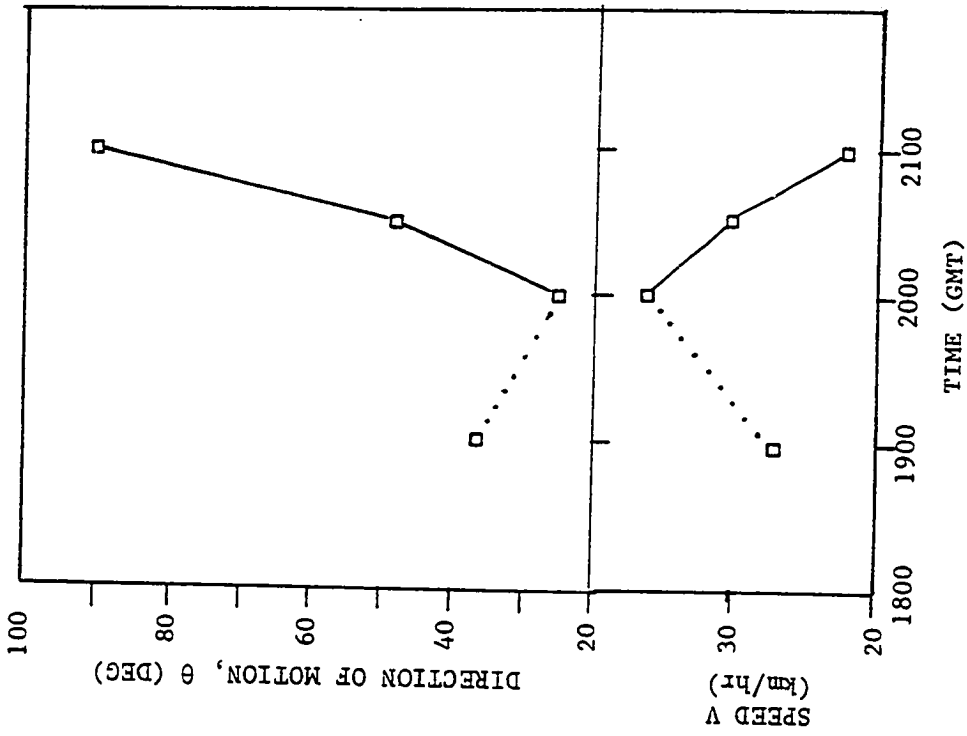


Fig. 19 Plots of model lag zero correlation (A_7), direction of motion (θ), and speed (V) for complex number 2 visible model fit.

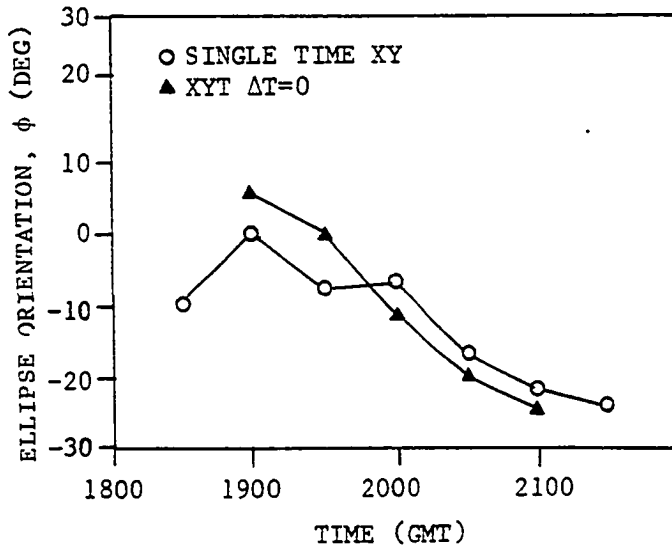
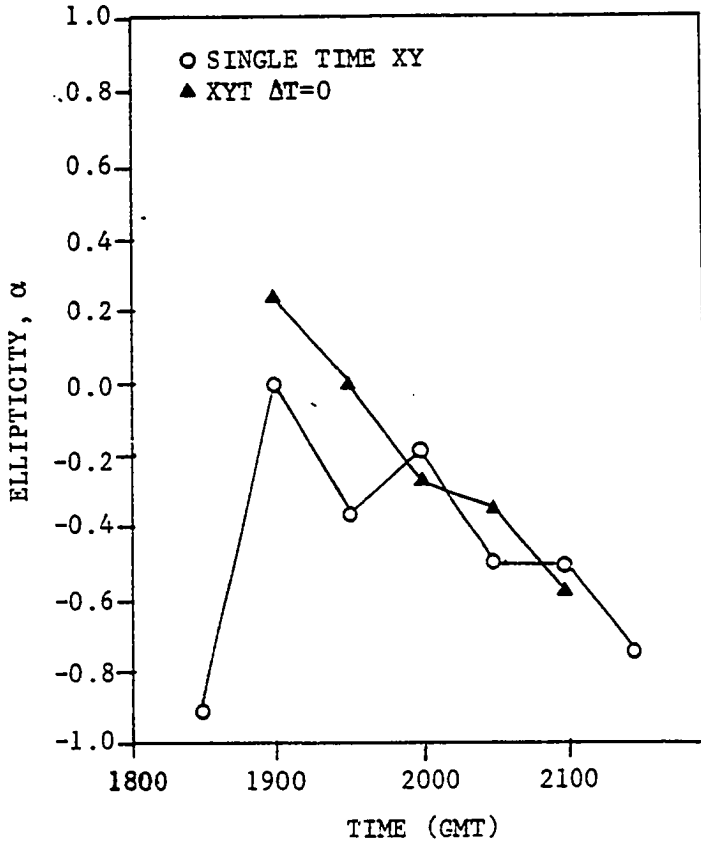


Fig. 20. Plots of ellipticity (α) and orientation angle (ϕ) for complex number 2 visible model fit.

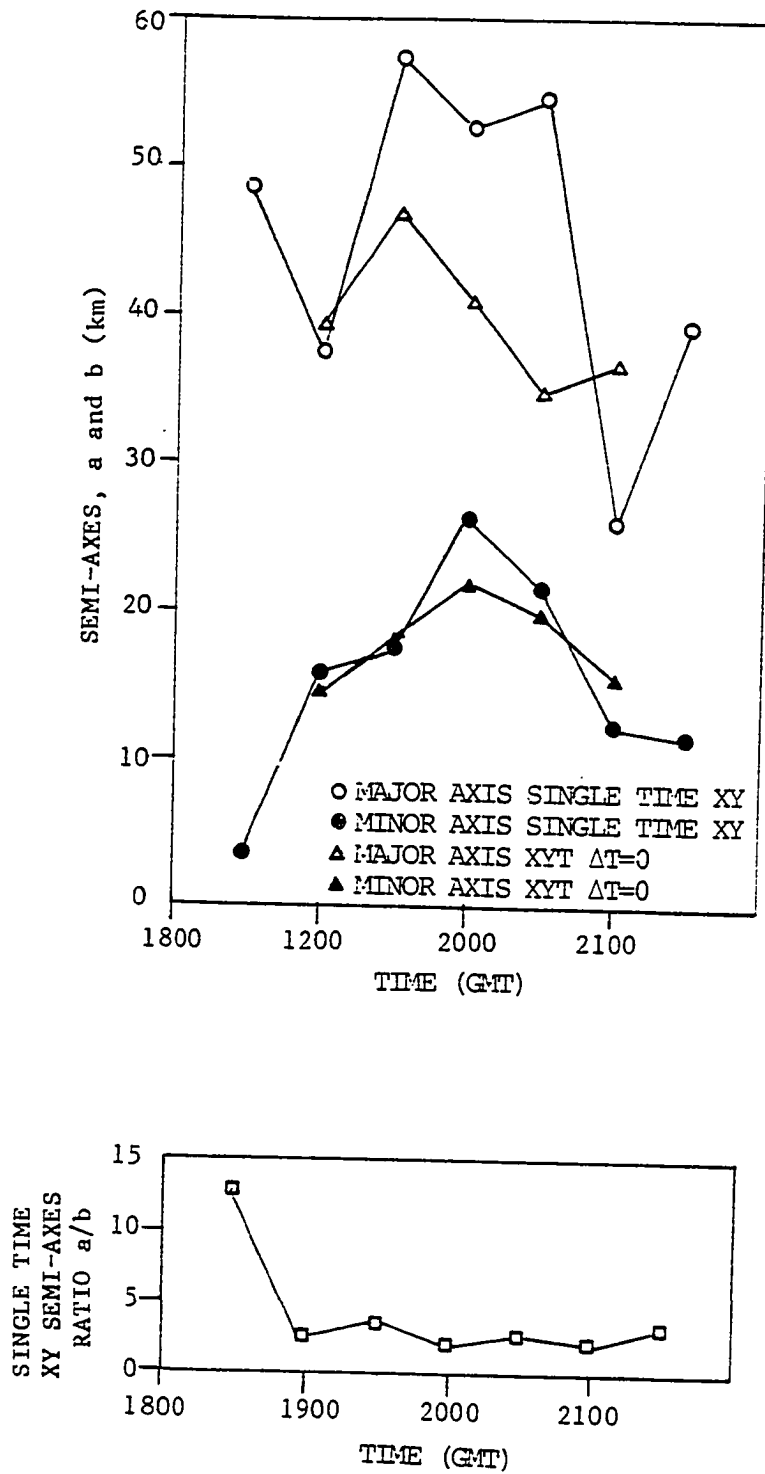


Fig. 21. Plots of ellipse semi-axes (a and b) and ratio of semi-axes for complex number 2 visible model fits.

dicating any such increase. Other than for case SM (1830 GMT), the ratio is nearly constant, exhibiting random variations.

Referring to Fig. 12 we see that the peak correlation areas in the XY fits appear to be more responsive. This should be expected as the XY fit to the time lag zero is a composite of three times. The representative area for the visible data is an order of magnitude larger than the corresponding radar areas. Woodley (1979) found a similar ratio for the areas he used. Fig. 23 is a plot of the raw XY correlation functions for cases SM, SN, and SO. Also shown is a plot of the fitted model correlation function for case SO. The three raw correlation fields illustrate how the correlation field for the visible data evolves with time. During the early stages of development the correlation field is very noisy. As the system becomes more organized, the correlation field becomes smoother, and the area of positive correlation becomes large as the system grows and then decreases when the system is dissipating. This is associated with an increase in anvil size at the same time the active precipitation related area is growing smaller. Earlier it was pointed out that the east-west dimension of the brighter area of the cloud at 1930 GMT was approximately 37 km, see Figure 9. Notice that the value of the σ_x parameter at 1930 GMT for the simple XY fit is 18.68 km. This is approximately 1/2 of the total width of the cloud. If one interprets an east-west slice through the cloud as the positive lobe of a sine wave, then the σ_x could be considered as the quarter wavelength of the sine wave. The plot of the function fit looks narrower than the

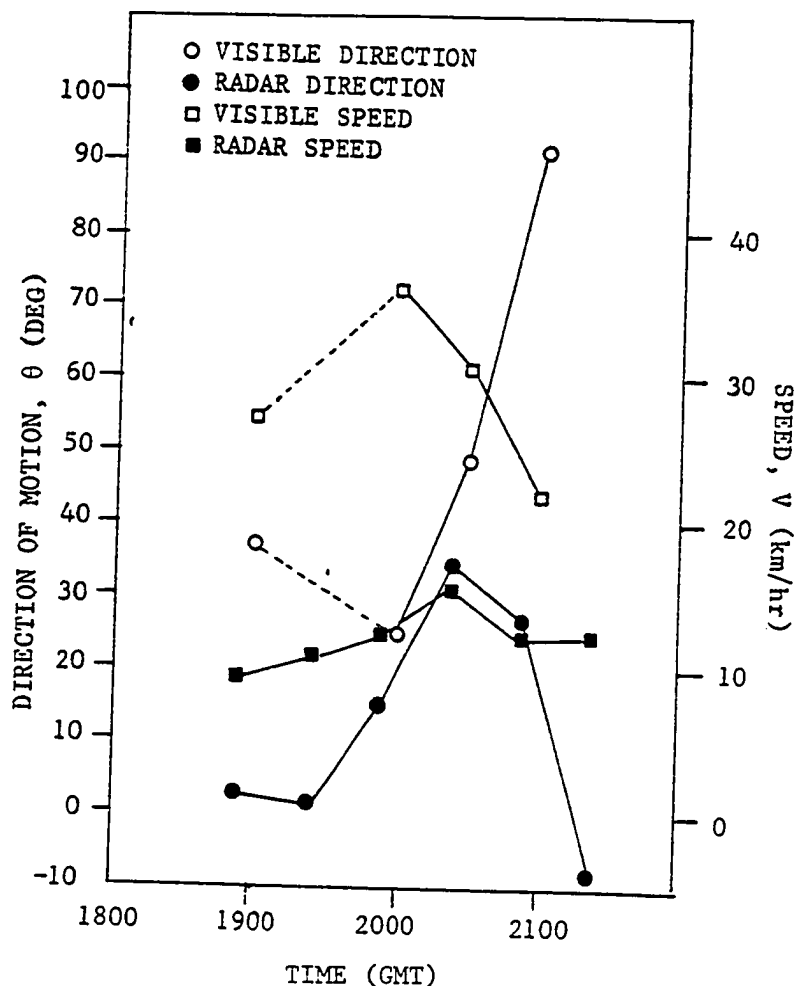


Fig. 22. Plot of speeds and directions of motion for visible and radar function fits (complex number 2)

raw field because it is plotted on a different scale. The similarity between the raw and fitted fields is apparent.

c. Infrared Temperature

Analysis of plots of the colder regions of the IR temperature fields seems to indicate that the apparent motion of the IR cloud top is basically the same as for the visible, as would be expected. Table 7 gives the correlation function parameters obtained by the NLP function fits. The parameters

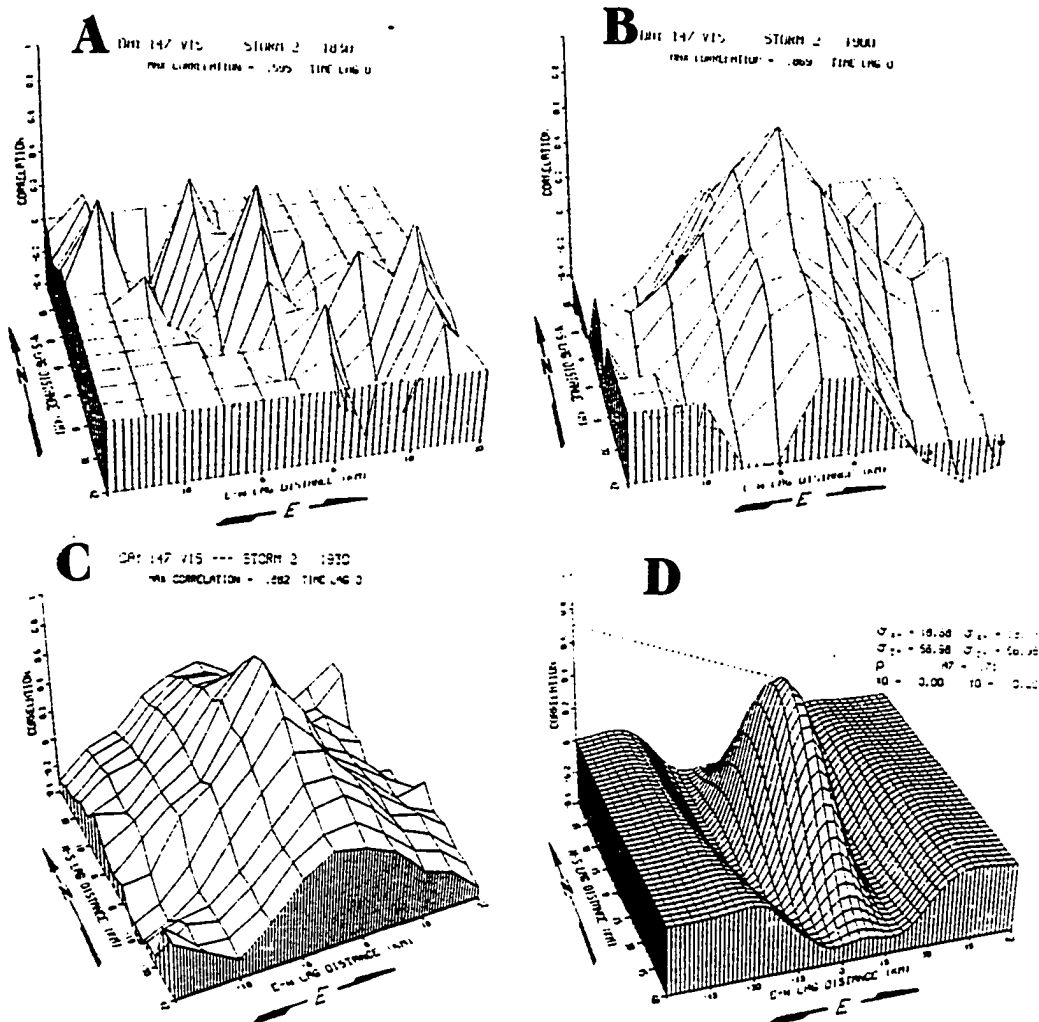


Fig. 23. Plots of raw correlation fields for complex number 2 visible cases SM (A), SN (B), and SO (C) and function fit for case SO (D). (note the different scales on the raw and function plots)

are plotted in Figs. 24 to 25 except area which is plotted in Fig. 12. The function fit for case S0 is plotted in Fig. 26. Representative velocities from function fits to the raw XYT correlation functions were not available because the NLP routine could not be made to converge. Subjective estimates of the velocities were made from the raw XYT correlation velocities. For the first three (3) cases the IR directions of motion agree with the visible directions. For the remaining two (2) cases, the IR directions maintain the same basic heading as the first three (3) and do not become easterly as did the visible. This is probably due to the fact that the bright visible areas were decreasing in size when the storm was dissipating whereas the colder IR temperatures continued to spread northward.

The orientation of the correlation function is essentially the same as for the visible data. It is nearly north-south during the early and middle stages and turns to the

Table 7. Parameters of fitted correlation function for complex number 2 IR temperature correlation fields. (see pages 44 and 45)

	CASE	TIME (GMT)	τ_{x+} km	τ_{x-} km	τ_{y+} km	τ_{y-} km	σ_t min	A_x	C_n	α	θ ($^\circ$)	η km	h km	A km ²	V km/hr	ϕ ($^\circ$)
SINGLE TIME XY	SM	1830	----	----	----	----	----	----	----	----	----	----	----	----	----	----
	SN	1900	16.5	----	36.8	----	----	1.0	0.66	-0.30	-9	37.2	15.6	1820	----	----
	SO	1930	14.7	----	39.6	----	----	1.0	0.65	-0.15	-4	39.7	14.5	1804	----	----
	SP	2000	18.2	----	55.6	----	----	0.92	0.65	-0.44	-9	56.3	16.2	2861	----	----
	SQ	2030	18.0	----	64.0	----	----	0.89	0.69	-0.53	-9	64.4	15.1	3057	----	----
	SR	2100	26.5	----	43.9	----	----	0.86	0.63	-0.65	-25	47.8	18.6	2789	----	----
XYT ($\Delta t=0$)	SS	2130	27.1	----	46.5	----	----	0.82	0.57	-0.80	-27	51.8	14.5	2361	----	----
	M		16.5	----	43.4	----	----	0.84	0.69	-0.10	-2	43.4	16.4	2233	----	----
	N		16.7	----	56.0	----	----	0.71	0.67	-0.28	-5	56.2	16.0	2824	----	----
	O		18.5	----	76.0	----	----	0.60	0.67	-0.51	-7	76.6	15.8	3805	----	----
	P		18.3	----	49.2	----	----	0.82	0.65	-0.60	-14	50.6	14.2	2257	----	----
	Q		20.0	----	45.1	----	----	0.88	0.60	-0.69	-19	47.4	13.8	2047	----	----

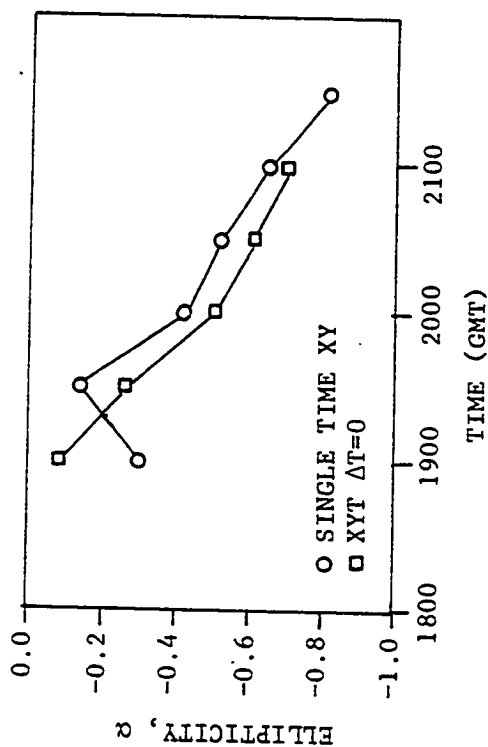
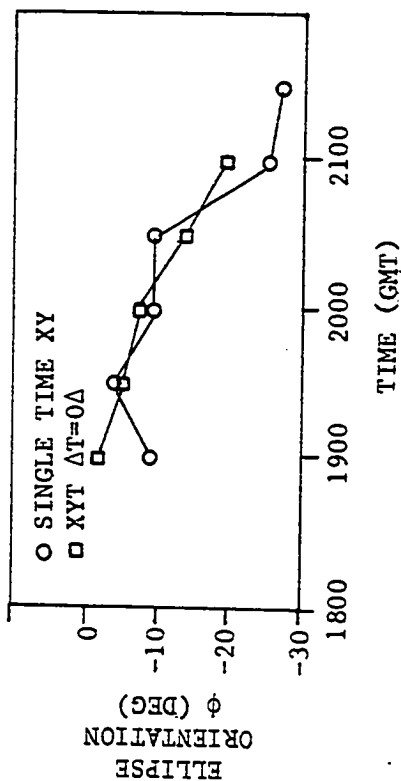
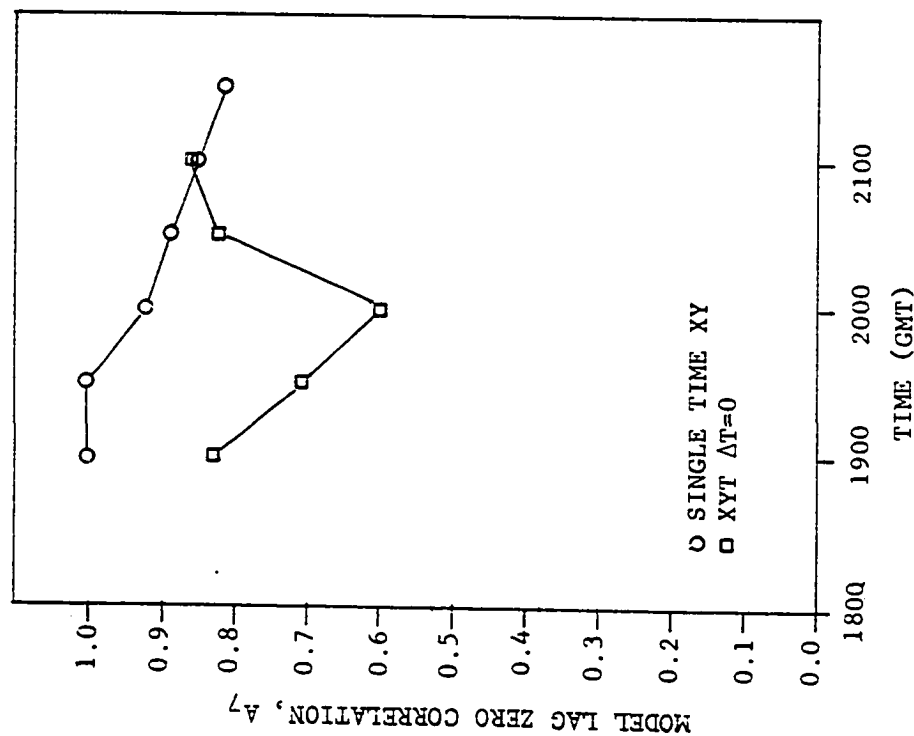


Fig. 24. Plots of model lag zero correlation, (A_7), ellipticity (α) and orientation of ellipse (ϕ) for complex number 2 IR model fits.

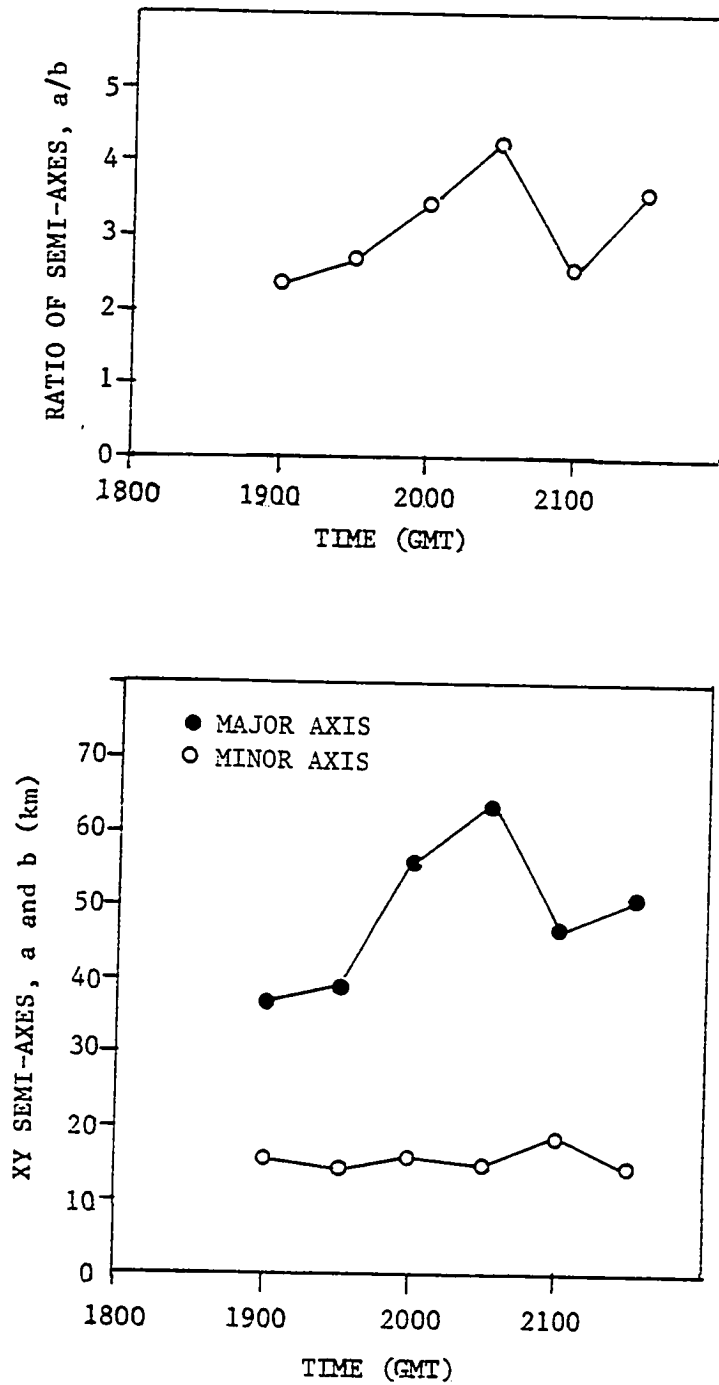


Fig. 25. Plots of ellipse semi-axes (a and b) and the ratio of the semi-axes (a/b) for complex number 2 IR model fits.

NNE-SSW during the latter stages. The agreement is best for the single time XY correlations. The increasing magnitude of the ellipticity reflects the growth of the anvil as it did for the visible data. Referring to Fig. 12 we see that the peak area for the XY fit to the time lag zero XYT raw correlation function occurs at the same time as it did for the visible. However, the peak area for the single time XY fit occurred 30 minutes later than did the corresponding visible peak, and an hour after the rain peak.

Referring to the plots of the semi-axes, a and b , in Fig. 25 it is seen that they follow the behavior suggested in the visible discussion that would reflect anvil growth. The minor axis remains essentially constant; while the major axis increases in length. The decrease in the major axis at the end reflects the dissipation of the system. This behavior indicates that the IR temperature may be a better indicator of the anvil growth.

d. Infrared Temperature Gradient Component

The IR temperature gradient components, as defined in Section 3, Chapter 4, auto-correlation fields are not as well behaved as those for the radar, visible, and the IR temperature data. Correlation fields were found for two (2) thresholds (see Section 3, Chapter 4). The thresholds were zero and -1000. The zero threshold allowed only positive gradients to be used in the determination of the correlation fields. The -1000 threshold was negative enough to allow the entire

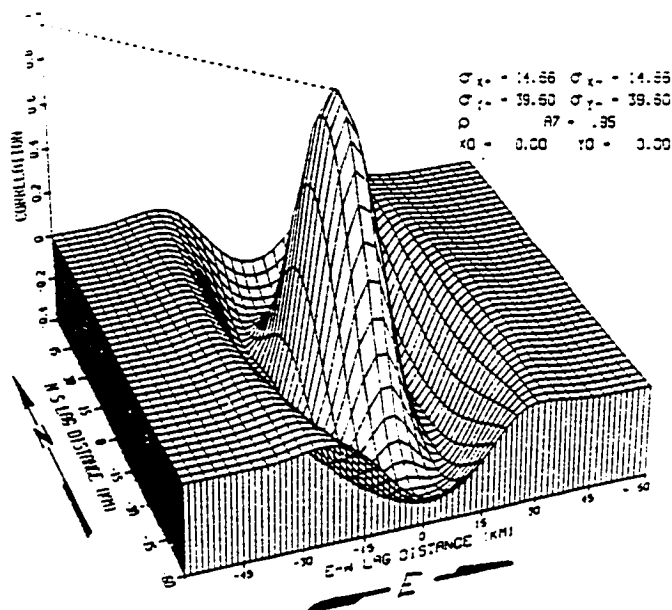


Fig. 26. Plot of fitted raw correlation function for complex number 2 IR temperature case S0.

gradient field to be used. Both sets of correlation fields were multimodal in structure. The secondary modes for the threshold zero fields are more pronounced than those for the -1000 threshold fields. The single time XY auto-correlation fields for data set thresholds at zero are very noisy as the number of data pairs available for finding the correlation was small. The secondary modes indicate that there is more than one area of positive temperature gradients. This does not, however, in turn imply two cold regions. For example, Fig. 27 is a representation of the IR temperatures at 1900 GMT (case SN). There is basically only one cold region in the cloud. On the other hand there are two regions of positive temperature gradients when taken along the indicated vectors, Fig. 28. The regions of positive gradient are

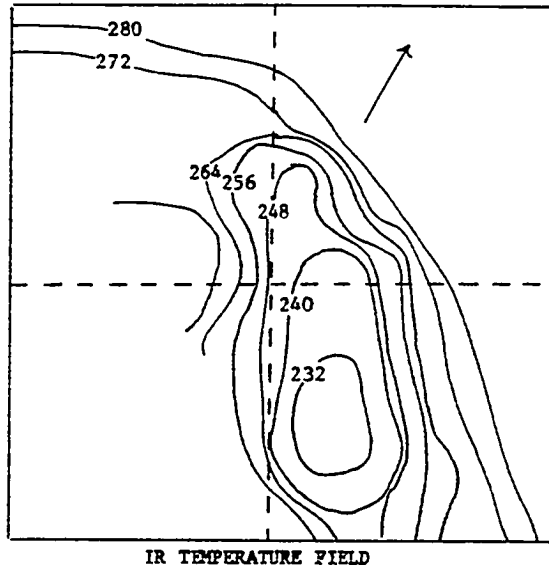


Fig. 27. Plot of IR temperature field for complex number 2 case SN.(1900 GMT)

indicated by the shaded area. Notice that the individual major axes of the positive areas are along an approximate heading of 140° while the more southern positive area is on an approximate heading of 165° from the northern one. Fig. 29 is the raw correlation matrix for 1900 GMT with the data threshold at -1000. When one estimates the orientation of the major axes for the central positive correlation area, one obtains 130° which is close to the previous estimate. Likewise an estimate of 160° was obtained for the heading between the central maximum and secondary maximum which is close to the previous estimate. An attempt was made to fit the correlation function to this field. The results are the following:

$$\sigma_x = 33.46 \text{ km}$$

$$\sigma_y = 91.81 \text{ km}$$

$$A_7 = 0.459$$

$$\alpha = -0.781$$

$$\theta = 163^\circ$$

Notice that the angle determined is closer to the orientation between the positive gradient areas than the major axis orientation. Also the value of the estimate of θ has been influenced by the presence of the larger correlations around the secondary modes (see Fig. 29). Therefore, because of the presence of these secondary maxima, it was felt that any further attempts at fitting the model would not be beneficial as the model is not the best one for the observed correlation fields.

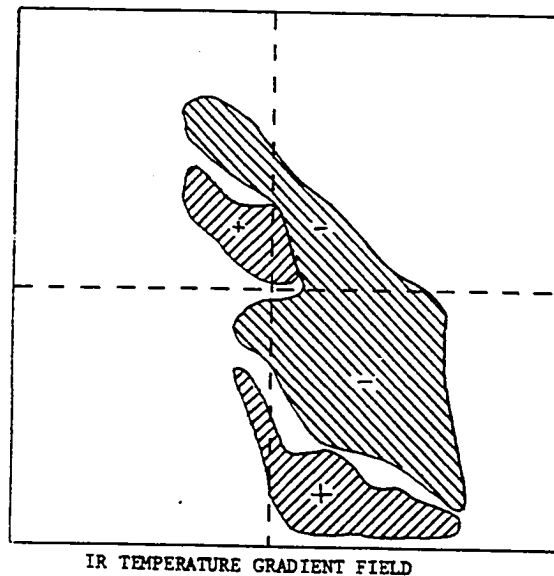


Fig. 28. Plot of IR temperature gradient field for complex number 2 case SN.(1900 GMT)

The gradient fields are fairly coherent in space as suggested by the lag zero correlations in the single time XY correlations for a data threshold of -1000. These are given in Table 8. Other than when the storm system is first becoming organized the lag zero correlations are all high.

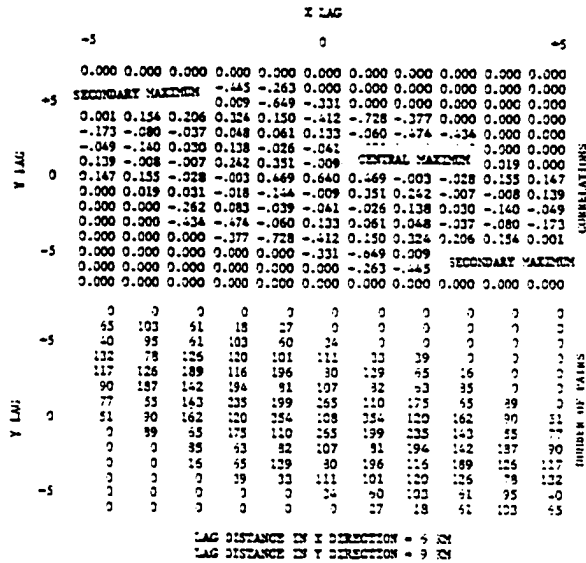


Fig. 29. Raw correlation field and product pair count for complex number 2 temperature gradient component fields for case SN.

e. Infrared Temperature Cross Visible Reflectance

It is expected that the cross-correlation between the IR temperature fields and the visible reflectance will be high. Table 9 gives the NLP function fits to the raw cross-correlation fields and the parameters are plotted in Figs. 30 and 31. Fig. 32 (1930 GMT) is a plot of the raw correlation field and the fitted model correlation function for case SO. Notice how the maximum correlation does not occur at lag zero but is displaced. Except for one time, the values for the parameter A_7 for the single time XY fits are all greater

Table 8. Lag zero correlations for single time XY auto-correlations for complex number 2 IR gradient component (threshold at -1000)

Case	Time GMT	Lag Zero Correlation
SM	1830	0.400
SN	1900	0.640
SO	1930	0.728
SP	2000	0.840
SQ	2030	0.755
SR	2100	0.796
SS	2130	0.786

than 0.7. The one time that is not is during the very early stages of storm development. Table 10 is a listing of the maximum cross-correlation for each XYT case and all time lags. The maximum correlation does not consistently occur at the same time lag. It was determined that the correlation values for time lags 0, +1, and -1 are biased toward the low side. This bias arises from the fact that the offset of the maximum correlation (x_0 and y_0) vary with time. Table 11 shows the portions of the single time raw cross-correlation matrices about lag zero for times 1900 (SN), 1930 (SO), and 2000 GMT (SP). The time lag zero XYT raw matrix is a composite of these. As mentioned before the peak correlation does not occur at lag zero every time. If one assumes that the variances of the IR temperature and visible reflectance are constant for the period in question, then one can estimate the value of the composited lag zero correlation for XYT case M by forming an average weighted by the number of pairs in each of the corresponding single time XY correlation field. The estimate obtained is 0.551, close to the actual value of 0.531 reported. A more informative estimate of A_7 would be a weighted

Table 9. Parameters of fitted model correlation function for complex number 2 IR cross visible correlation matrices. (see pages 44 and 45)

	CASE	TIME (GMT)	σ_{x+} km	σ_{x-} km	σ_{y+} km	σ_{y-} km	σ_t min	A_7	ρ_0	α	ϕ (°)	a km	b km	A km ²	V km/hr	θ (°)	d km	γ (°)
SINGLE TIME XY	SM	1830	DID NOT CONVERGE															
	SN	1900	17.5	14.0	32.6	45.3	---	0.84	0.78	-0.19	-5	39.1	15.4	1890	----	---	3.9	-14
	SO	1930	12.3	16.6	40.3	45.3	---	0.81	0.81	-0.28	-6	43.0	13.8	1863	----	---	15.4	-3
	SP	2000	16.7	20.1	49.2	41.6	---	0.80	0.80	-0.39	-10	46.1	16.7	2410	----	---	31.4	-19
	SQ	2130	18.6	23.3	52.2	57.0	---	0.72	0.67	-0.46	-11	55.6	18.3	3192	----	---	14.3	-3
XYT ($\Delta t=0$)	M		17.0	14.5	34.4	84.9	---	0.81	0.60	-0.02	0	59.6	15.8	2958	----	---	2.5	-19
	N		17.8	12.1	29.7	62.2	---	0.53	0.53	-0.29	-6	46.1	14.2	2063	----	---	2.0	-25
	O		17.8	17.2	34.4	61.2	---	0.52	0.58	-0.41	-10	48.4	15.8	2397	----	---	11.3	-4
	P		29.6	15.7	43.6	52.1	---	0.44	0.51	-0.53	-16	49.6	18.5	2888	----	---	17.6	-9
	Q		35.0	21.4	55.8	57.5	---	0.34	0.36	-0.83	-24	61.5	14.7	2836	----	---	14.6	-3
XYT	M		17.9	16.1	46.9	77.3	173	0.56	0.60	-0.21	-4	62.2	16.6	3242	60.5	19	7.2	-7
	N		DID NOT CONVERGE															
	O		20.0	18.6	40.3	61.9	1566	0.47	0.58	-0.53	-13	52.2	16.0	2623	33.3	33	13.5	-6
	P		24.6	18.7	59.9	67.1	420	0.41	0.51	-0.57	-12	64.8	17.4	3550	30.6	57	21.4	-13
	Q		DID NOT CONVERGE															

average of the peak values for each time. The estimate so obtained is 0.790. As can be seen the A_7 values are underestimated, and therefore, the time lag at which the maximum correlation occurs cannot be determined.

Table 10. Maximum cross-correlations for complex number 2 all time lags and cases for IR temperature cross visible reflectance. (see page 45)

Case	Maximum Correlations Time Lag				
	-2	-1	0	+1	+2
M	0.538	0.566	0.603	0.495	0.387
N	0.636	0.592	0.531	0.553	0.728
O	0.697	0.524	0.580	0.382	0.601
P	0.622	0.564	0.509	0.488	0.495
Q	0.488	0.509	0.361	0.279	0.437

The XYT matrices are not useless though. The time lags -2 and +2 are not composites but are the cross-correlations between the first and last times in each case. For

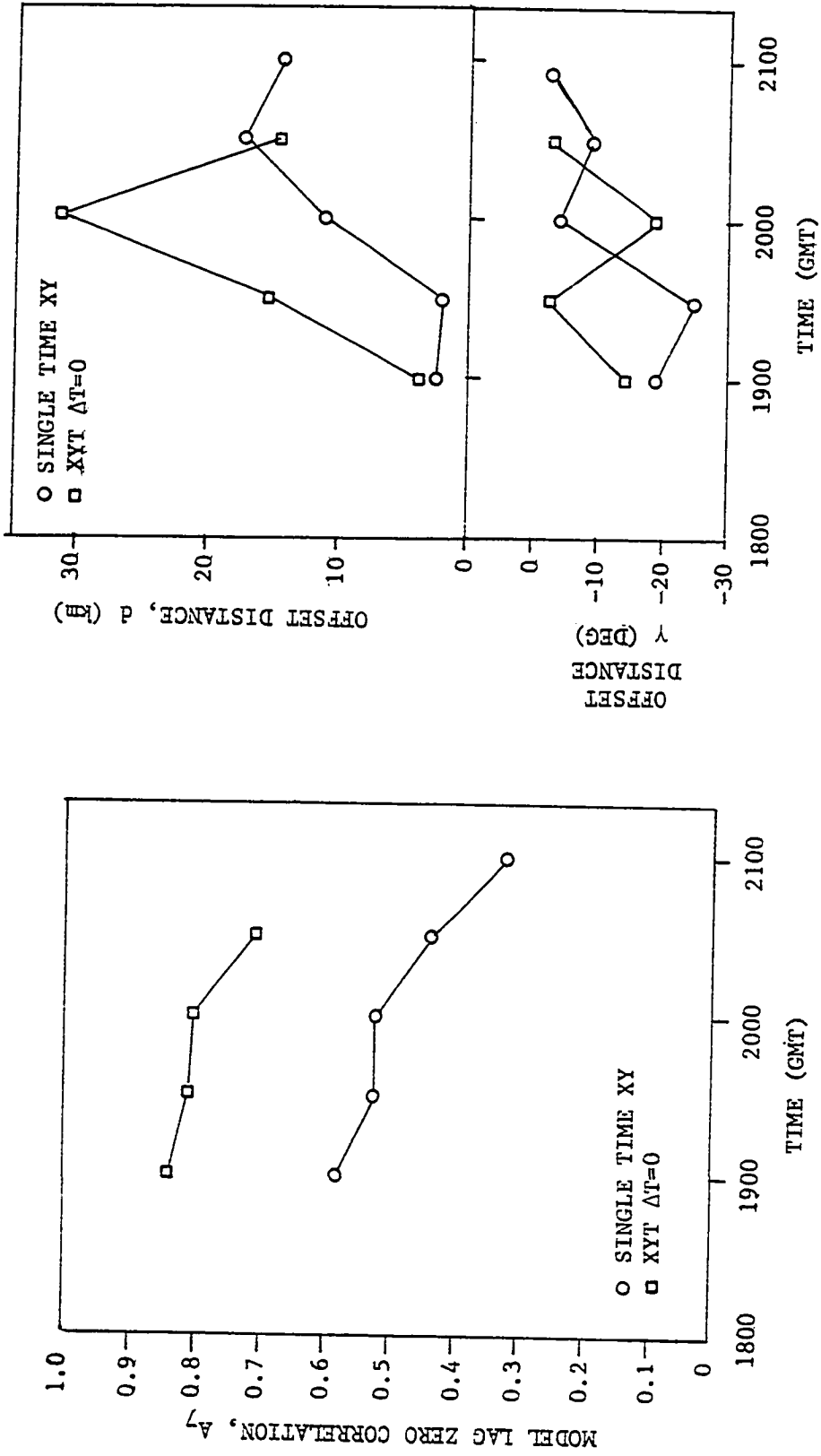


Fig. 30. Plots of model lag zero correlation (A_7), offset direction (γ), and offset distance (d) for complex number 2 IR cross visible.

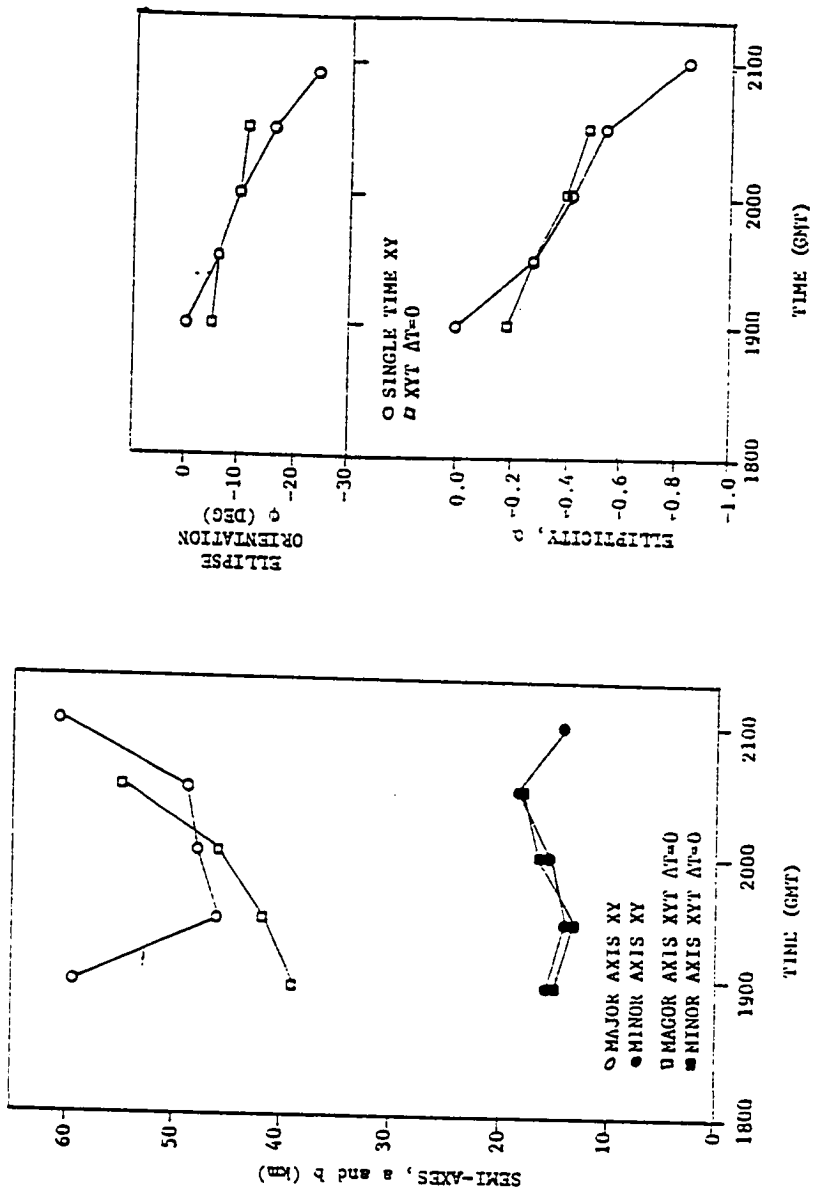


Fig. 31. Plots of ellipticity (α), ellipse orientation (ϕ), and semi-axes (a and b) for complex number 2 IR cross visible.

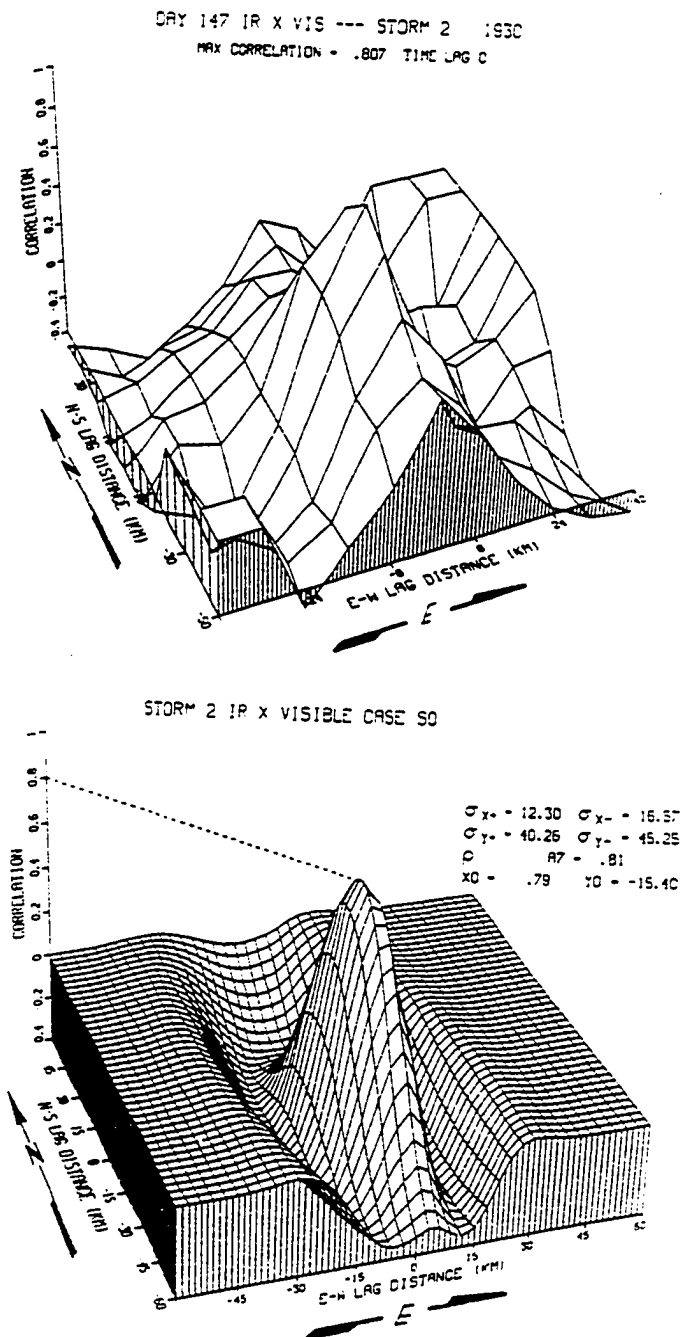


Fig. 32. Plots of raw correlation function and fitted model correlation function for complex number 2 IR cross visible.

Table 11. Portions of raw XY correlation fields about lag zero for IR cross visible (complex number 2).

		1900 GMT			
		X Lag			
		-1	0	+1	
Y Lag	2	0.055	0.197	0.128	
	1	0.561	0.598	0.401	
	0	0.378	0.424	0.363	
	-1	0.122	0.206	0.182	

		1930 GMT			
		X Lag			
		-1	0	+1	
Y Lag	2	0.268	0.364	0.321	
	1	0.509	0.595	0.512	
	0	0.309	0.343	0.266	
	-1	0.209	0.290	0.249	

		2000 GMT			
		X Lag			
		-1	0	+1	
Y Lag	2	0.223	0.274	0.256	
	1	0.455	0.503	0.434	
	0	0.424	0.440	0.357	
	-1	0.318	0.384	0.339	

example, for case N, the -2 time lag is the cross-correlation between the visible reflectance at 1900 GMT and the IR temperature at 2000 GMT, and the +2 time lag is the cross-correlation between the IR temperature at 1900 and the visible reflectance at 2000 GMT. Table 12 is a listing of the time lags -2 and +2 maximum correlations and the data sets and times they represent. As can be seen there is considerable correlation in time other than when one of the data sets involved was in the developing or dissipating stages.

A study of the function fits to the single time XY

correlation matrices shows that the growth of the anvil is not manifested in the a/b ratio. The behavior reflects the random nature of the equivalent IR ratios. The orientation of the correlation ellipses agrees with those obtained for the IR and visible auto-correlations.

Table 12. Maximum correlations at times lags -2 and +2 and associated times (note that the first variable in parenthesis is associated with the earlier time). (see page 45)

Times	Time Lags	
	-2 (VxIR)	+2 (IRxV)
1830-1930	0.538	0.387
1900-2000	0.636	0.728
1930-2030	0.697	0.601
2000-2100	0.622	0.495
2030-2130	0.488	0.437

f. Infrared Temperature Gradient Component
Cross Visible Reflectance

The calculation of the visible cross IR temperature gradient XYT correlation matrices encountered the same problem as was encountered in the visible cross IR temperature. For this reason only the single time XY cross-correlation matrices are discussed.

Table 13 lists the maximum cross-correlations and the lags at which they occur for thresholds of 0 and -1000. Maxima other than for case SM are all significant. As mentioned earlier, case SM is during the early stages of the storm's development. Even though the displacement of the position of the maximum cross-correlation from lag zero varies, it

Table 13. Maximum IR temperature gradient component cross visible reflectance and corresponding lags for temperature gradient component thresholds of 0 and -1000. (see page 45)

Case	Threshold = 0		Threshold = -1000	
	Maximum Correlation	Lag X Y	Maximum Correlation	Lag X Y
SM	0.320	1 0	0.247	0 1
SN	0.680	1 4	0.723	1 4
SO	0.571	-1 5	0.482	0 1
SP	0.584	1 4	0.539	2 2
SQ	0.542	1 2	0.466	1 2

can generally be said that the IR temperature gradient component appears to be more correlated with visible reflectance to the north or northeast.

g. Radar Rain Rates Cross Visible Reflectance

The radar cross visible correlation matrix patterns are not consistent from case to case. Examples of three single time XY cross-correlations matrices are given in Fig. 33. An examination of these shows how the point of maximum correlation changes considerably from case to case. For case SN the maximum cross-correlation is just south of lag zero. For case SO it is to the north-northwest, while for case SQ it is more to the west-northwest.

Two possible explanations are navigation errors, or the fact that the relationship between the radar rain rates and the visible reflectance changes that dramatically in 30 minutes. For the second explanation to be feasible then a mechanism must be found by which the radar rain rates can be correlated with the visible reflectance 26 km to the south-southeast. I know of no such mechanism. I feel that the

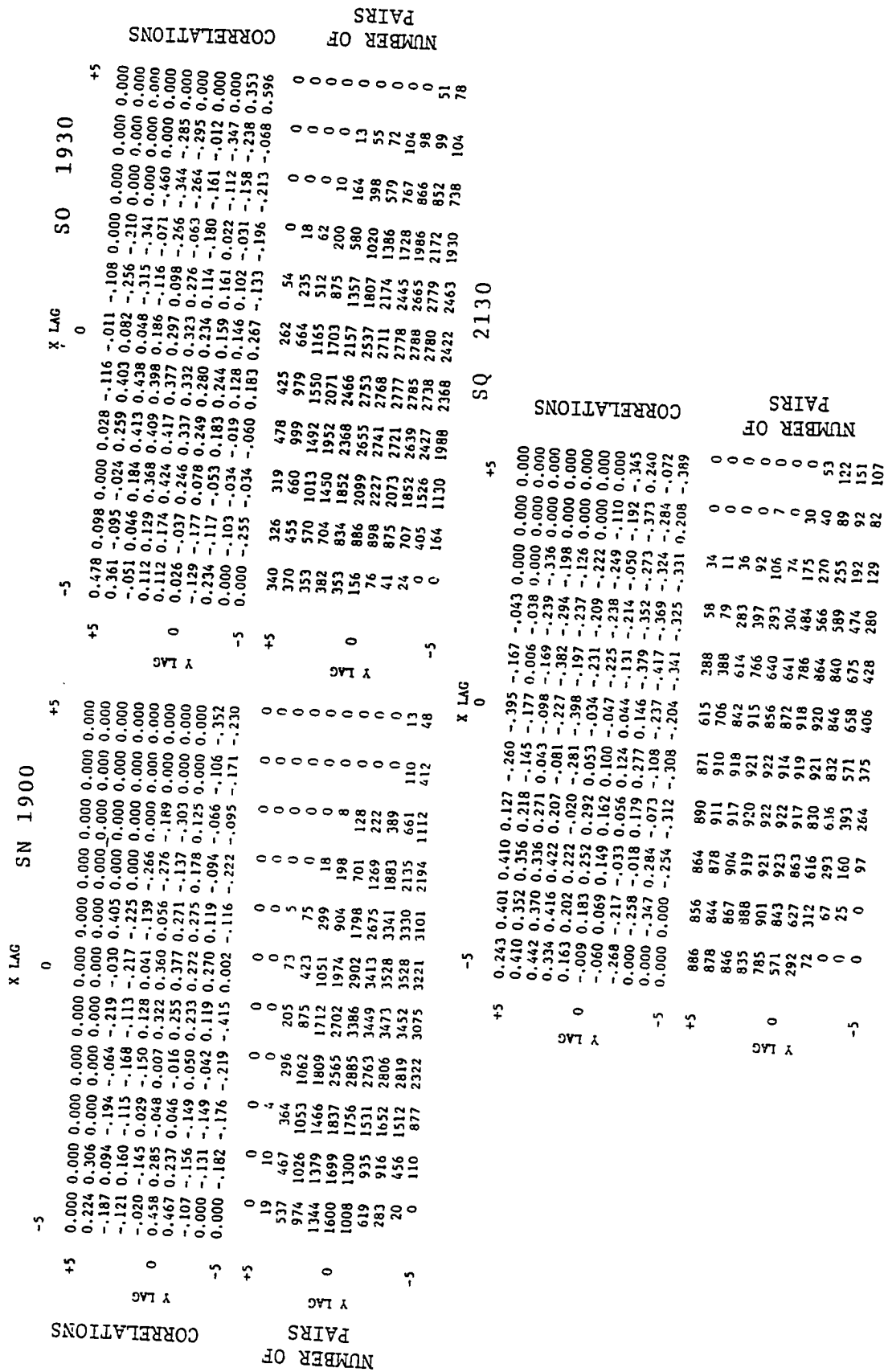


Fig. 33. Single Time XY correlation fields for complex number 2 radar cross visible for cases SN, SO, and SQ.

first explanation is the proper one. Because of this apparent navigation problem the XYT cross-correlation matrices can not be analyzed until this data acquisition problem is resolved for the same reason that the visible reflectance cross IR temperature XYT correlation matrices were not analyzed.

Using the single time XY cross correlation fields it can still be determined whether or not there is correlation between the two data fields. Table 14 gives the maximum correlations for each single time case. There does appear to be some significant correlation between the radar rain rates and visible reflectance. All of these correlations are based on at least 300 product pairs. Even if we assume that $3/4$ of the degrees of freedom are lost due to auto-correlation in the signal and due to the method of finding the correlations, the cross-correlations are significant at the 99 per cent level. That is, there is less than one chance in a thousand that these cross-correlations are in reality zero. The pattern of positive correlations about these maxima is fairly consistent with a major axis orientation between east-northeast and northeast. There are at times secondary maxima along this axis reflecting the finer structure of the cloud.

h. Radar Rain Rates Cross Infrared Temperature

Because of the apparent difficulties with the navigation of the satellite data only the single time XY cross-correlation matrices will be discussed. Fig. 34 is a reproduction of the correlation matrices for case SO (2000 GMT). This is a

Table 14. Maximum correlations for complex number 2 radar cross visible reflectance for single time XY correlation fields. (see page 45)

Case	Maximum Correlation Grid (km)	
	3 x 5	6 x 8
SM	----	----
SN	0.41	0.38
SO	0.51	0.44
SP	0.47	0.47
SQ	0.53	0.44
SR	----	----
SS	----	0.52

typical radar rain rate cross IR temperature correlation matrix for this storm. The major axis of the positive correlation region is generally north to south or NNW to SSE paralleling the major axis of the storm. This orientation is generally the same for the other XY correlation matrices.

Table 15 is a listing of the maximum cross-correlations for each case. No value is reported for case SM (1830 GMT) because there were no significant correlations. All of these correlations are conservatively estimated to be significant at the 95 per cent level. Also included in the table are the X and Y lags at which the maxima occurred. As can be seen the displacement varies considerably from case to case. One consistent feature is that the radar rain is generally to the southeast of the IR temperature with which it has maximum correlation. Also the greater the north-south separation the greater the east-west separation. This type of relationship is consistent with possible navigation errors caused by errors in the height input to the navigation programs.

		X LAG								
		0								
		-3							+3	
Y LAG	+5	0.000	0.000	0.000	0.000	0.000	0.000	0.000	0.000	CORRELATIONS
		0.000	-.271	-.068	0.278	-.346	-.243	0.000		
		0.000	-.214	0.120	0.270	-.115	0.200	0.000		
		0.000	-.103	0.144	0.414	0.215	-.154	-.522		
		-.193	-.015	0.351	0.391	0.331	-.126	-.356		
	0	0.410	0.030	0.323	0.338	0.253	0.108	-.248		
		-.527	0.026	-.097	0.028	0.227	0.135	-.150		
		0.000	-.111	-.205	0.030	0.211	0.088	-.113		
		0.000	-.148	-.221	-.011	0.088	-.009	-.118		
	-5	0.000	-.048	-.164	-.047	-.068	-.209	-.233		
Y LAG	+5	0	0	0	0	0	0	0		NUMBER OF PAIRS
		0	21	84	108	61	8	0		
		0	47	185	241	163	44	0		
		0	106	299	385	318	131	14		
	0	27	170	424	499	450	261	77		
		29	231	541	593	550	399	193		
		13	230	518	580	577	504	320		
		0	208	481	577	580	551	409		
		0	139	424	576	563	569	468		
		0	75	366	518	552	584	503		
	-5	0	30	265	391	485	576	482		

LAG DISTANCE IN X = 8.0 km
LAG DISTANCE IN Y = 10.0 km

Fig. 34. Radar rain rates cross IR temperature correlation field for case SO. (2000 GMT)

Table 15. Maximum cross-correlation and corresponding lags for radar rain rates cross IR temperature for each case.

Case	Correlation	Lag
SM	-----	-----
SN	0.349	0, -3
SO	0.414	-1, 2
SP	0.420	-3, 5
SQ	0.510	-4, 6
SR	0.526	-5, 6
SS	0.380	-3, 3

i. Radar Rain Rates Cross Infrared Temperature Gradient Component

Because of the apparent satellite navigation error only the single time XY cross-correlation fields will be discussed. The fields are rather noisy. An example of one (case SN) is

given in Fig. 35. There are two significant maxima in this cross-correlation field along a south-southeast heading. This feature is present in most of the cross-correlation fields. Table 16 gives the maximum and secondary maximum correlations. There appears to be significant cross-correlation present at most times.

		X LAG										CORRELATIONS	
		-5		0						+5			
Y LAG													
		-0.344	-0.431	0.112	-0.345	-0.125	0.000	0.000	0.000	0.000	0.000	0.000	
		-0.510	-0.166	0.141	0.079	-0.076	-0.047	0.133	0.000	0.000	0.000	0.000	
+5		-0.315	0.014	0.061	0.414	0.144	-0.474	0.032	0.000	0.000	0.000	0.000	
		0.113	0.117	-0.047	0.040	0.127	-0.072	-0.208	-0.010	0.000	0.000	0.000	
		0.000	-0.113	-0.181	-0.315	-0.057	0.081	-0.177	0.096	0.000	0.000	0.000	
0		0.000	0.000	-0.006	0.061	0.047	0.248	-0.043	-0.117	0.000	0.000	0.000	
		0.000	0.000	0.437	0.259	0.176	0.073	-0.014	-0.046	0.000	0.000	0.000	
		0.000	0.000	0.295	0.418	0.532	0.456	0.381	0.063	0.039	0.000	0.000	
-5		0.000	0.000	0.000	0.569	0.552	0.455	-0.462	0.216	0.016	0.000	0.000	
		0.000	0.000	0.000	0.062	0.311	0.262	0.332	0.262	0.059	0.000	0.000	
		0.000	0.000	0.000	0.000	0.281	0.139	0.045	-0.080	0.085	0.000	0.000	
		0.000	0.000	0.000	0.000	0.655	0.197	0.075	-0.088	-0.217	0.000	0.000	
		0.000	0.000	0.000	0.000	0.000	0.000	0.000	0.000	0.000	0.000	0.000	
		0.000	0.000	0.000	0.000	0.000	0.000	0.000	0.000	0.000	0.000	0.000	
Y LAG												NUMBER OF PAIRS	
		205	377	400	386	361	0	0	0	0	0		0
		154	400	509	500	472	312	31	0	0	0		0
-5		61	300	472	500	505	435	186	0	0	0	0	
		8	180	435	529	529	501	303	63	0	0	0	
		0	35	324	471	493	493	405	152	0	0	0	
0		0	0	218	461	532	530	502	285	0	0	0	
		0	0	109	358	489	495	490	367	0	0	0	
		0	0	29	254	469	529	540	489	258	0	0	
+5		0	0	0	131	356	416	425	424	291	0	0	
		0	0	0	53	232	312	331	349	305	0	0	
		0	0	0	9	109	195	212	222	215	0	0	
-5		0	0	0	0	8	53	68	81	96	0	0	
		0	0	0	0	0	0	0	0	0	0	0	
		0	0	0	0	0	0	0	0	0	0	0	
		0	0	0	0	0	0	0	0	0	0	0	
LAG DISTANCE IN X DIRECTION = 8.0 KM													
LAG DISTANCE IN Y DIRECTION = 7.0 KM													

LAG DISTANCE IN X DIRECTION = 8.0 KM

LAG DISTANCE IN Y DIRECTION = 7.0 KM

Fig. 35. Radar cross IR temperature gradient component correlations for threshold of 0 and case SN. (1900 GMT)

Table 16. Maximum correlations for radar cross IR temperature gradient component for single time correlation fields and both thresholds. (see page 45)

Case	Time	Threshold = -1000 Maximum		Threshold = 0 Maximum	
		Southern	Northern	Southern	Northern
SM	1830	no significant correlation			
SN	1900	0.57	--	0.57	0.54
SO	1930	0.54	0.52	0.56	0.53
SP	2000	0.64	0.55	0.31	0.52
SQ	2030	(missing)			
SR	2100	no significant correlation			
SS	2130	0.40	0.34	0.40	0.29

2. Convective Complex Three

The first radar echo for complex number three (3) was at 1822 GMT (GMT) on 27 May. The complex was dissipating when it moved out of radar range at 0042 GMT 28 May. The radar data were acquired for the period 1830 through 2100 GMT and converted to rainfall rates at 15 minute intervals. The data for later times were not used because the available satellite data stopped at 2030 GMT. Table 17 gives the times used in the radar auto-correlation cases and those used in the cross-correlation calculations. The times at which satellite data are available for convective complex number three and the case designations are given in Table 18. The navigation of the satellite data for this convective complex seems to be relatively good. The radar echoes tend to align with the southern ends of the visible satellite data and the highest reflectivities. The alignment is not as good with the colder cloud top regions as defined by the satellite IR measurements. The volumetric rain rates and representative correlation areas

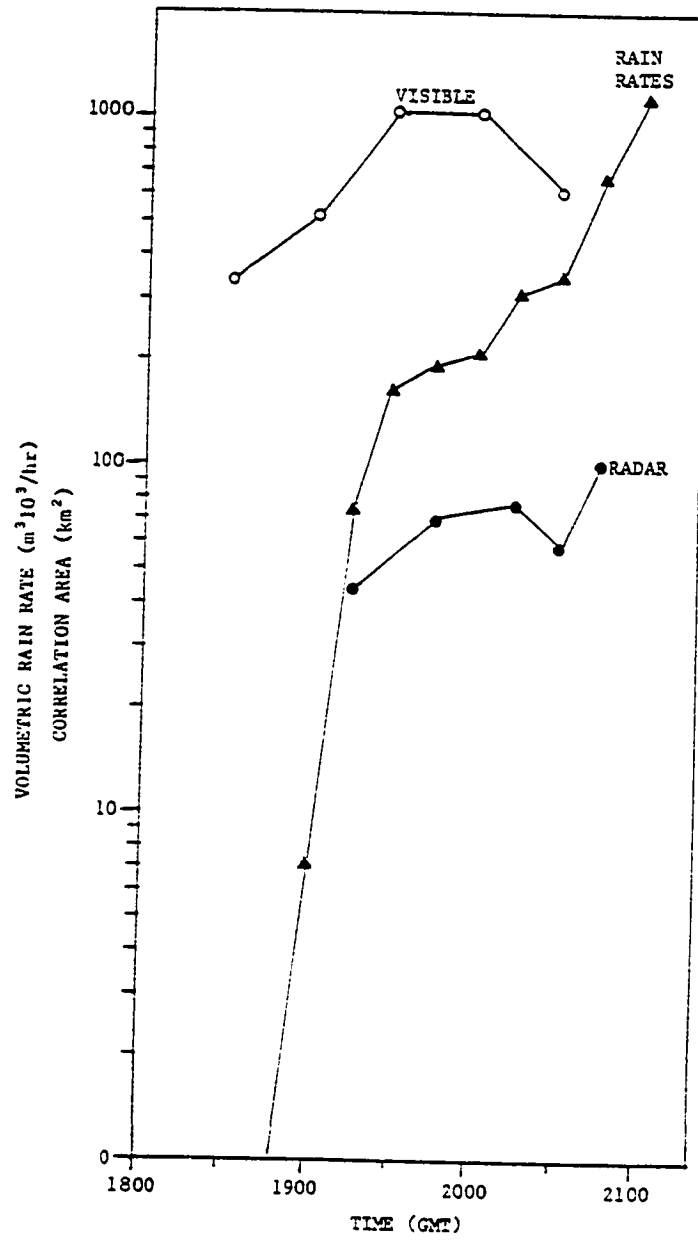


Fig. 36. Plot of volumetric rain rate and correlation areas for complex number 3.

Table 17. Case designations for complex number 3 radar data.

Time (GMT)	Auto-correlation		Cross-correlation	
	XYT	XY	XYT	-XY
1830	M	SM	M	SM
1845	M			
1900	MN	SN	MN	SN
1915	MN			
1930	NO	SO	MNO	SO
1945	NO			
2000	OP	SP	NO	SP
2015	OP			
2030	P	SQ	O	SQ
2045	P	SR		

are plotted in Fig. 36. Reference will be made to this Fig. later.

Table 18. Case designations for complex number 3 satellite data.

Time (GMT)	Correlation Case	
	XYT	XY
1830	M	SM
1900	MN	SN
1930	MNO	SO
2000	NO	SP
2030	O	SQ

a. Radar Rain Rates

The early echoes indicated only one cell, but by 1902 GMT there are three well-defined cells-two with returns above 20 dBz and one with returns of nearly 40 dBz. As the storm develops, the structure becomes even more complex. Fig. 37 shows the radar echo returns for this complex at 2007 GMT. During the early stages the direction of movement was somewhat difficult to determine; however, it seemed to be generally

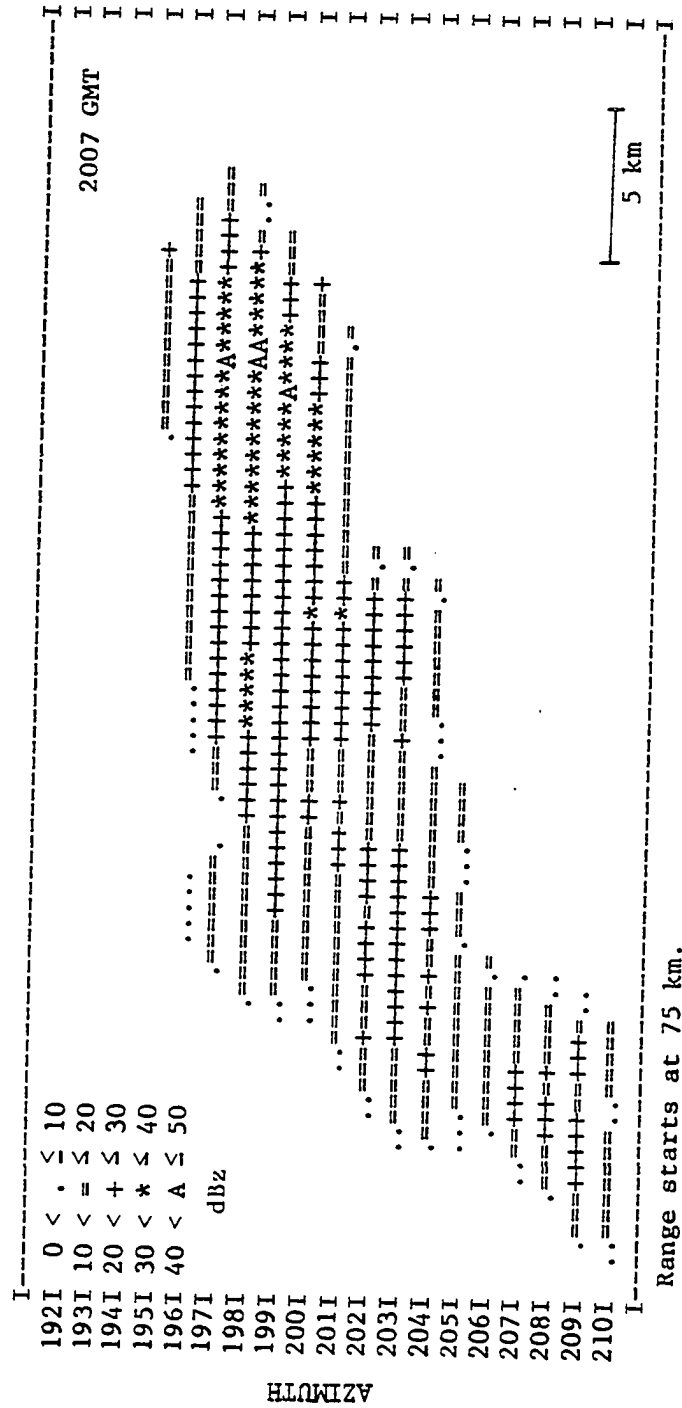


Fig. 37. Complex number 2 radar returns of 2007 GMT.

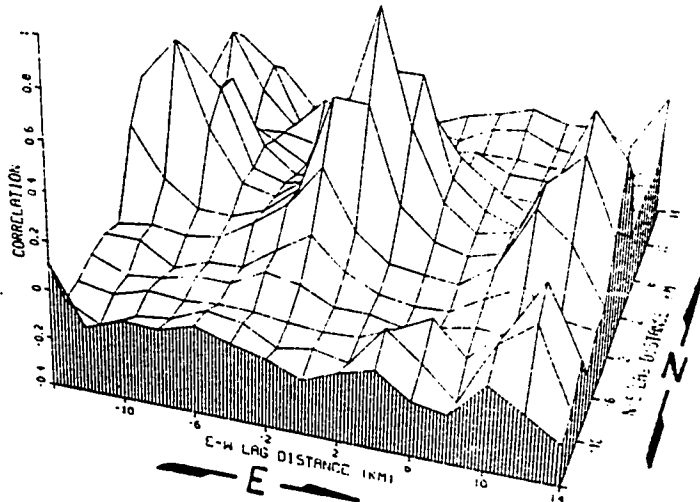
toward the east-northeast.

Raw auto-correlation functions were calculated for each of the cases and NLP fits of the correlation function determined. There is some indication of the multicellular structure of the convective complex in the raw correlation functions. Fig. 38 shows plots of the time lag zero raw correlation matrices for cases M and N. From these it can be seen that the individual cells are organized in a general north-northeast direction while the cells lie along a northwest to southeast line. Table 19 lists the parameters of the model correlation function as determined from the NLP fit. The parameters are also plotted in Figs. 39 and 41. The complex structure of this convective complex is manifested in the variation of the parameters with time. This variation is due to the development and dissipation of cells within the convective complex. From the XYT NLP it can be seen that the direction of storm movement is indicated to be initially toward the northeast then with time it turns toward the east-northeast. During this period the velocity varies from a minimum of 4.7 km/hr to a maximum of 7.1 km/hr.

b. Visible

The centroid of the visible imagery appears to be moving toward the northeast or north-northeast. From the data available, it was not possible to determine the direction of anvil growth. The shape of the visible cloud changes markedly over time. Initially, at 1830 GMT, it is long and

CASE SM
 MAXIMUM CORRELATION = 0.815



CASE SN
 MAXIMUM CORRELATION = 0.794

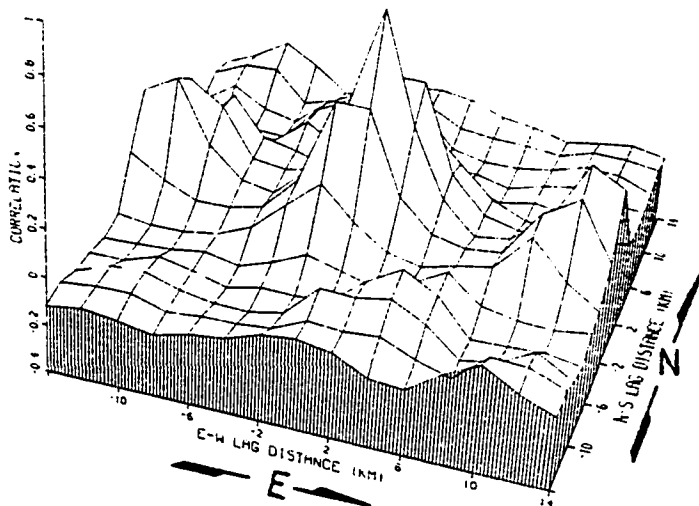


Fig. 38. Plots of raw time lag zero correlation fields for complex number 3 radar cases M and N.

Table 19. Parameters of fitted model correlation function for complex number 3 radar. (see pages 44 and 45)

	CASE	TIME (GMT)	σ_{x+} km	σ_{x-} km	σ_{y+} km	σ_{y-} km	σ_t min	A_7	ρ_0	α	ϕ (°)	a km	b km	A km ²	V km/hr	θ (°)
SINGLE TIME XY	SM	1845	---	---	---	---	---	---	---	---	---	---	---	---	---	---
	SN	1915	4.6	---	5.4	---	---	0.53	0.71	0.83	39	6.8	2.1	44	---	---
	SO	1945	5.6	---	5.3	---	---	0.66	0.81	0.68	47	7.1	3.1	69	---	---
	SP	2015	4.1	---	6.0	---	---	0.58	0.72	0.28	18	6.2	3.8	75	---	---
	SQ	2030	4.2	---	5.6	---	---	0.46	0.67	0.64	33	6.5	2.8	57	---	---
	SR	2045	4.6	---	7.0	---	---	0.58	0.79	-0.01	-6	7.0	4.6	101	---	---
XYT ($\Delta t=0$)	M		5.2	---	6.5	---	---	0.62	0.82	0.63	35	7.6	3.5	82	---	---
	N		5.2	---	5.7	---	---	0.61	0.79	0.62	41	7.0	3.4	38	---	---
	O		5.2	---	5.5	---	---	0.55	0.75	0.59	42	6.7	3.4	71	---	---
	P		5.0	---	7.2	---	---	0.49	0.66	-0.11	-8	7.2	5.0	112	---	---
XYT	M		5.4	5.0	6.9	7.0	69	0.60	0.82	0.69	33	8.0	3.3	83	4.7	43
	N		5.3	5.9	6.2	6.2	88	0.54	0.79	0.69	41	7.7	3.2	78	5.0	48
	O		5.3	5.1	6.0	5.9	57	0.47	0.75	0.67	39	7.2	3.2	72	7.1	45
	P		6.2	4.4	6.1	7.3	75	0.45	0.66	0.23	23	6.9	5.0	108	6.2	60

narrow with the major axis oriented approximately 160°. At 1900 GMT it is nearly circular, and by 1930 GMT it is elliptical. At 2000 GMT the beginnings of two parallel bright areas are noticeable and by 2030 GMT the two bands are fully developed and are oriented approximately north-south. Fig. 42 shows the objective analysis for cases SM to SP. The objective analysis was performed on a grid that was coarser than the resolution of the raw data. The flat area was beyond the limits of the data. Notice how this storm is much more complex than storm number 2. There are large changes in the cloud top structure from case to case.

The raw correlation matrices were found for the visible data and the model correlation parameters determined. These are listed in Table 20 and are plotted in Figs. 43 to 45. The values of the major and minor axes and the ellipse orientation found for the XY correlations agree with the above

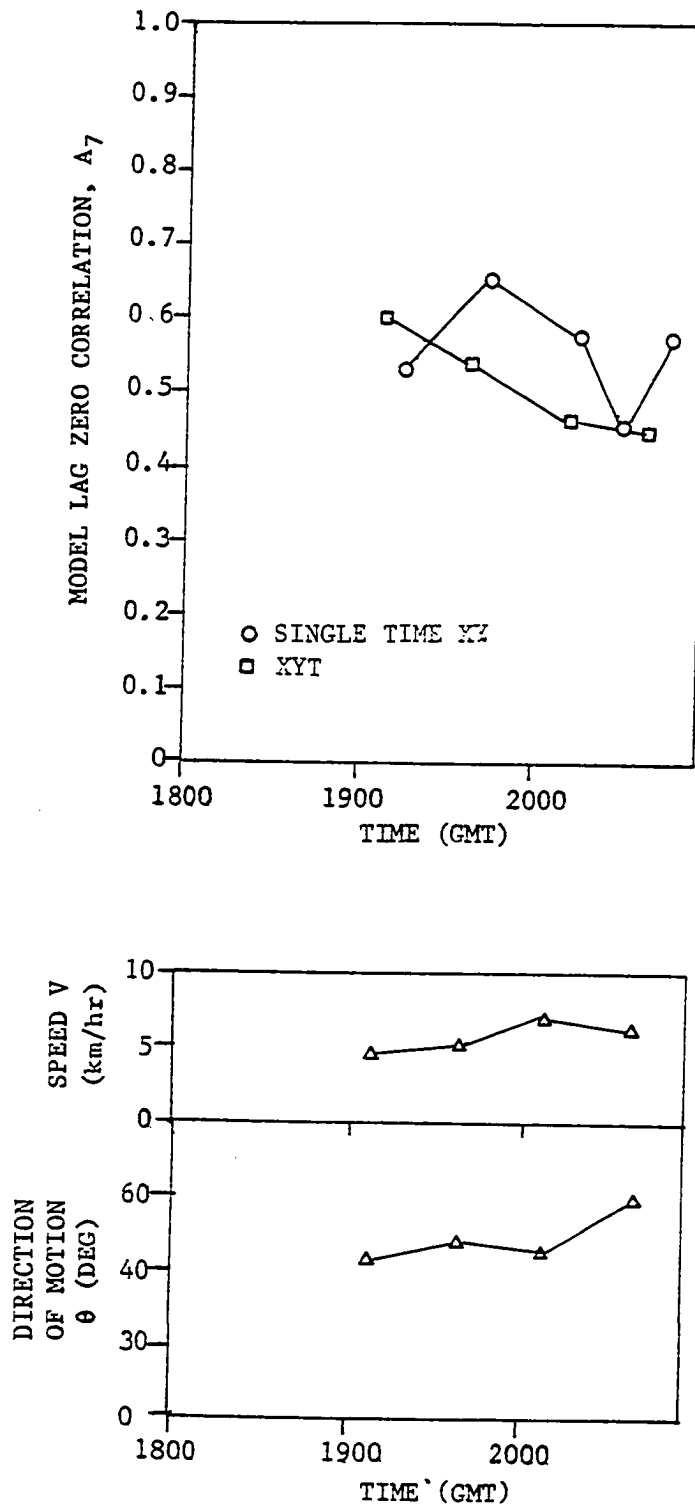


Fig. 39. Plots of model lag zero correlation (A_7), direction of motion (θ), and speed (V) for complex number 3 radar model fits.

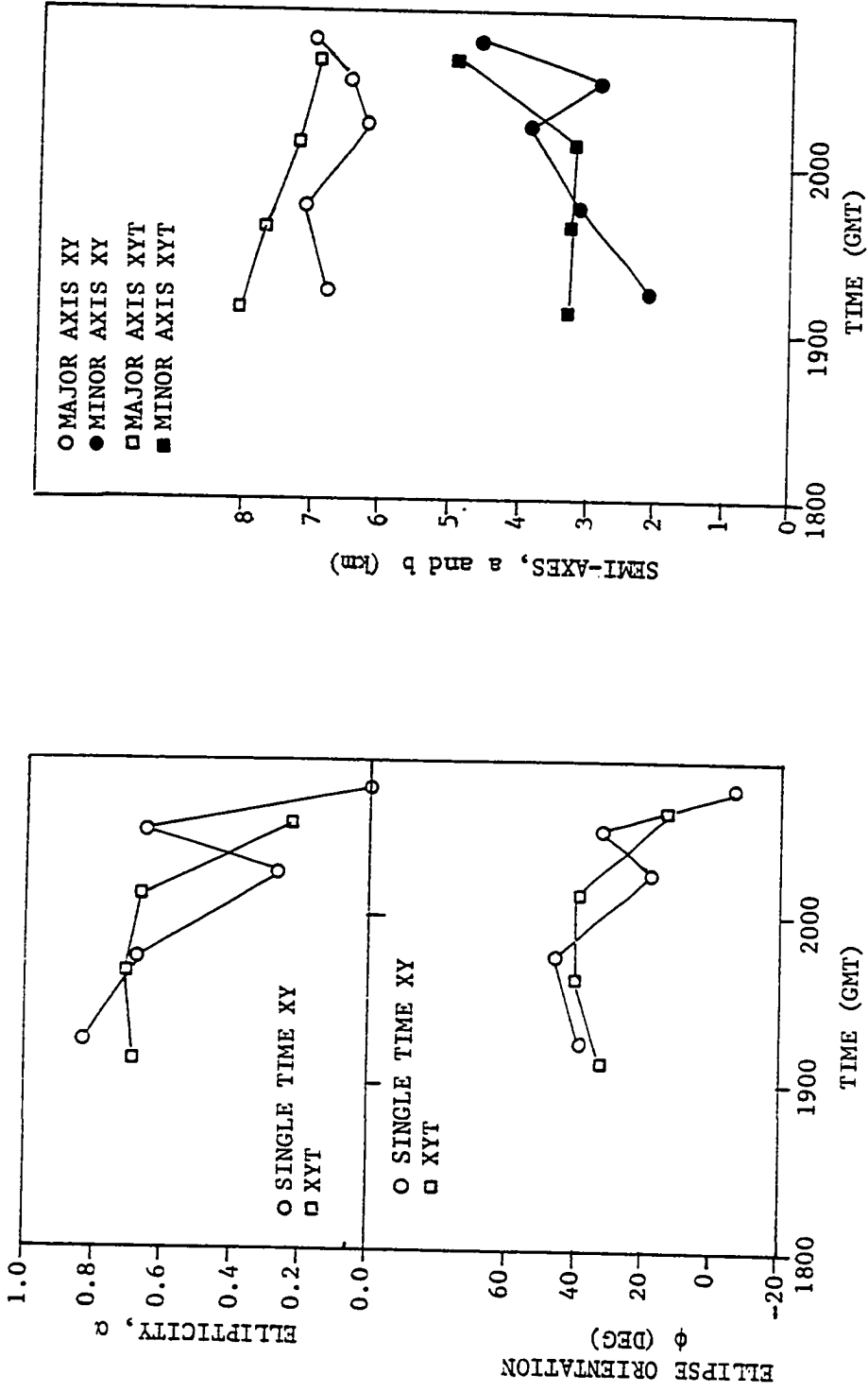


Fig. 40. Plots of ellipticity, (α), orientation angle (ϕ), and semi-axes of ellipse (a and b) for complex number 3 radar model fits.

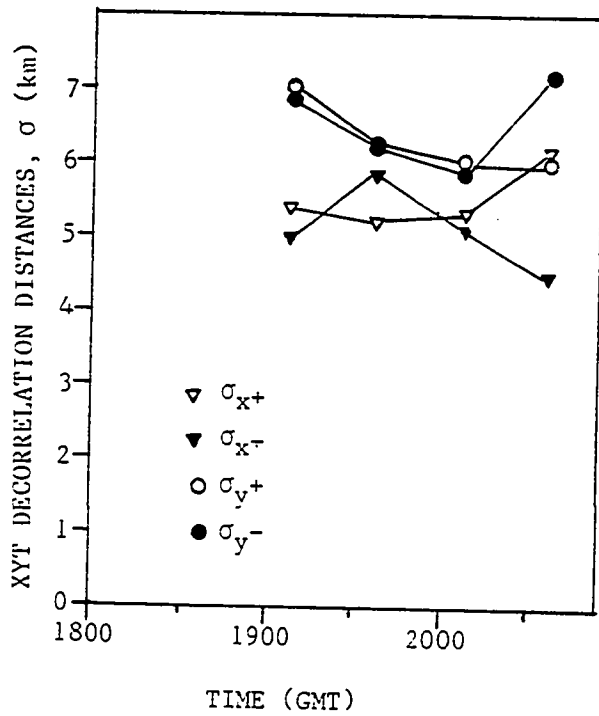
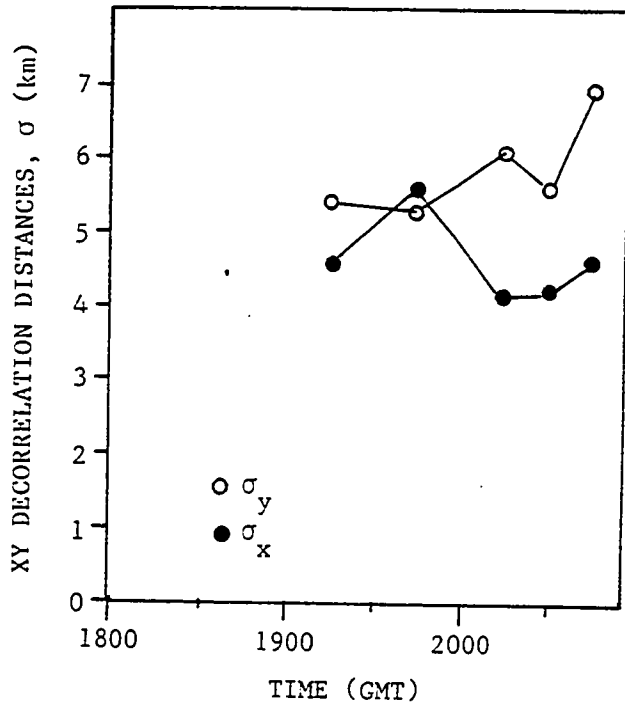


Fig. 41. Plots of decorrelation distances (σ) for complex number 3 radar model fit.

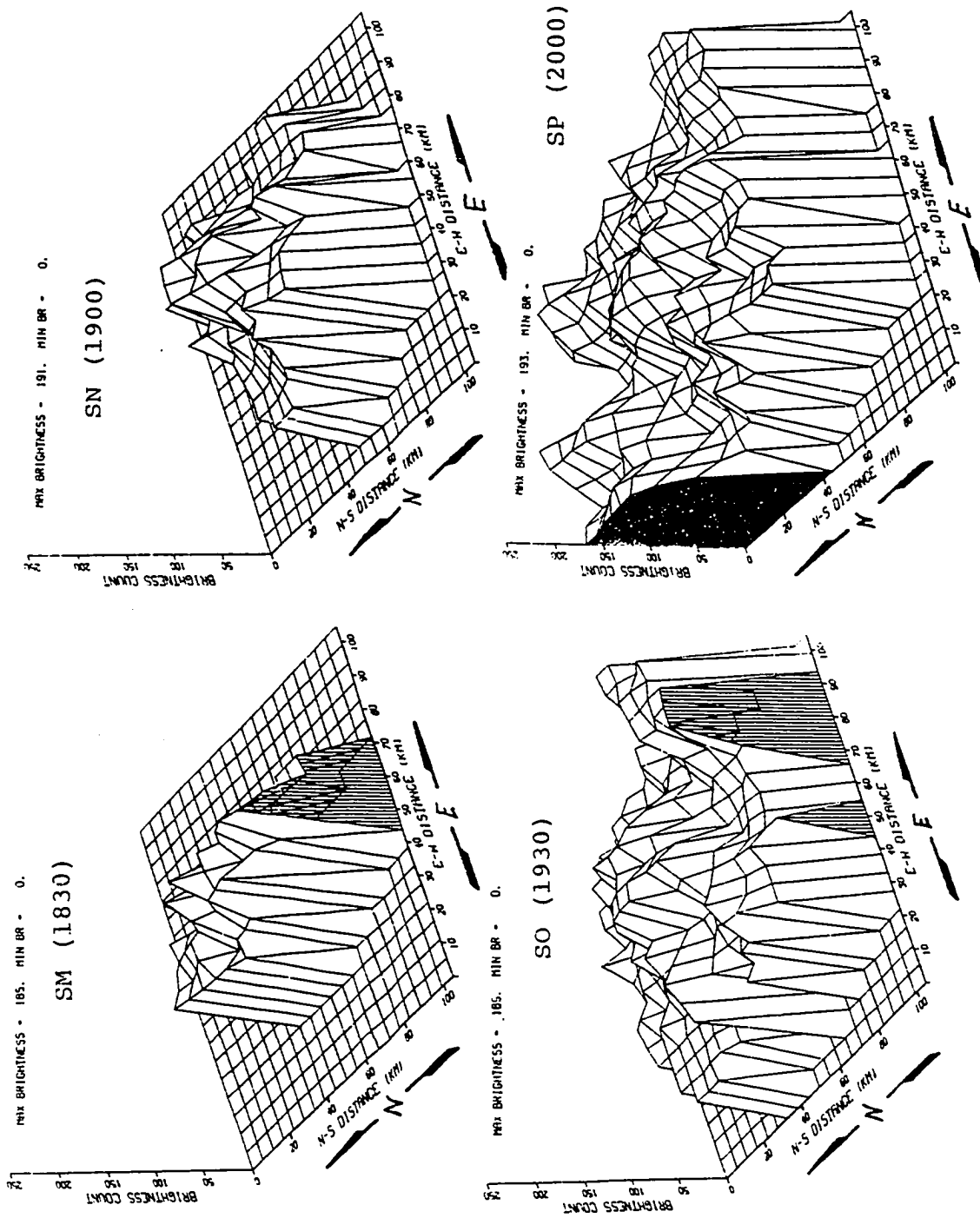


Fig. 42. Plots of the objective analysis of visible reflectance for complex number 3 cases SM (1830), SN (1900), SO (1930), and SP (2000).

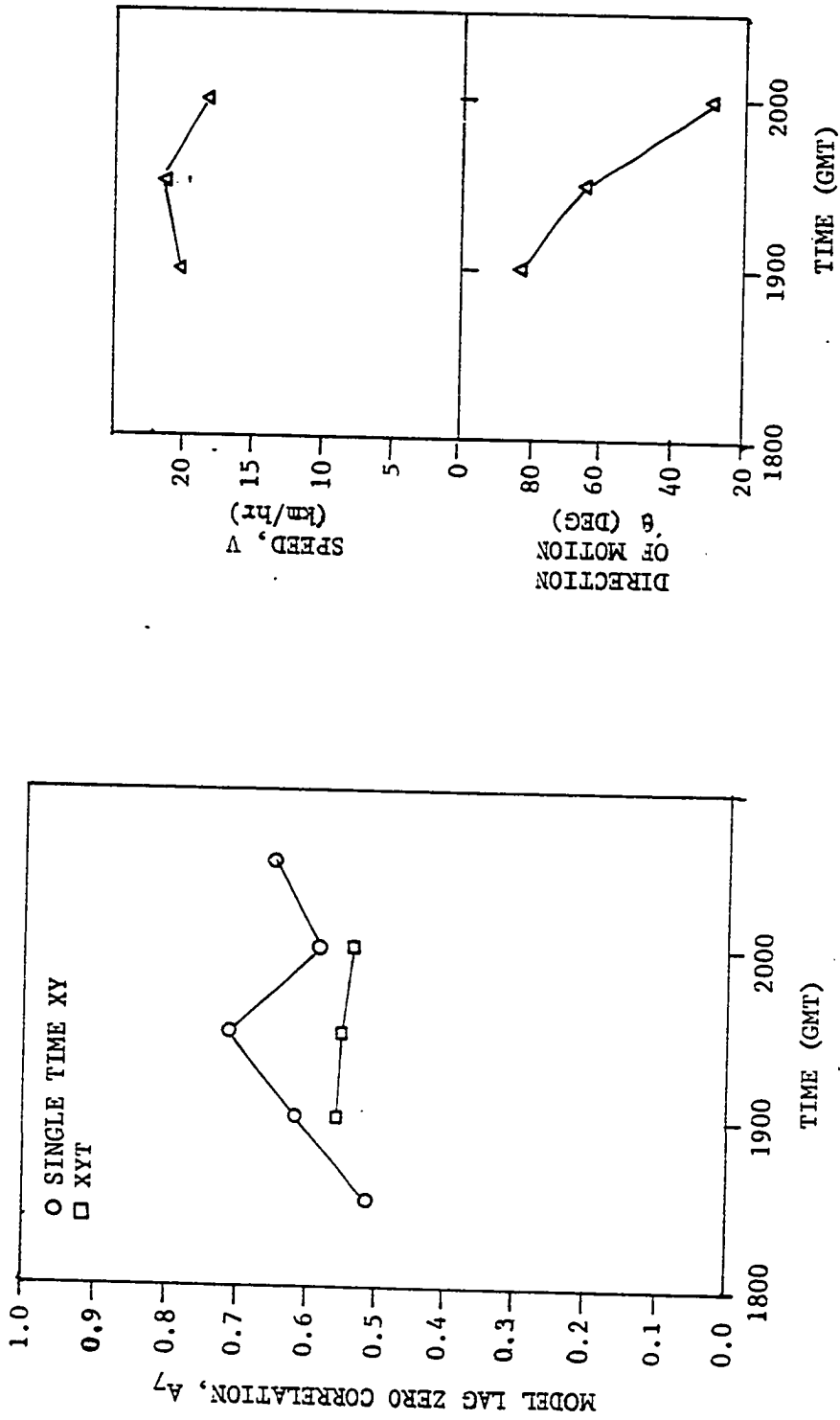


Fig. 43. Plots of model lag zero correlation (A_7), direction of motion (θ), and speed, (V), for complex number 3 visible model fits.

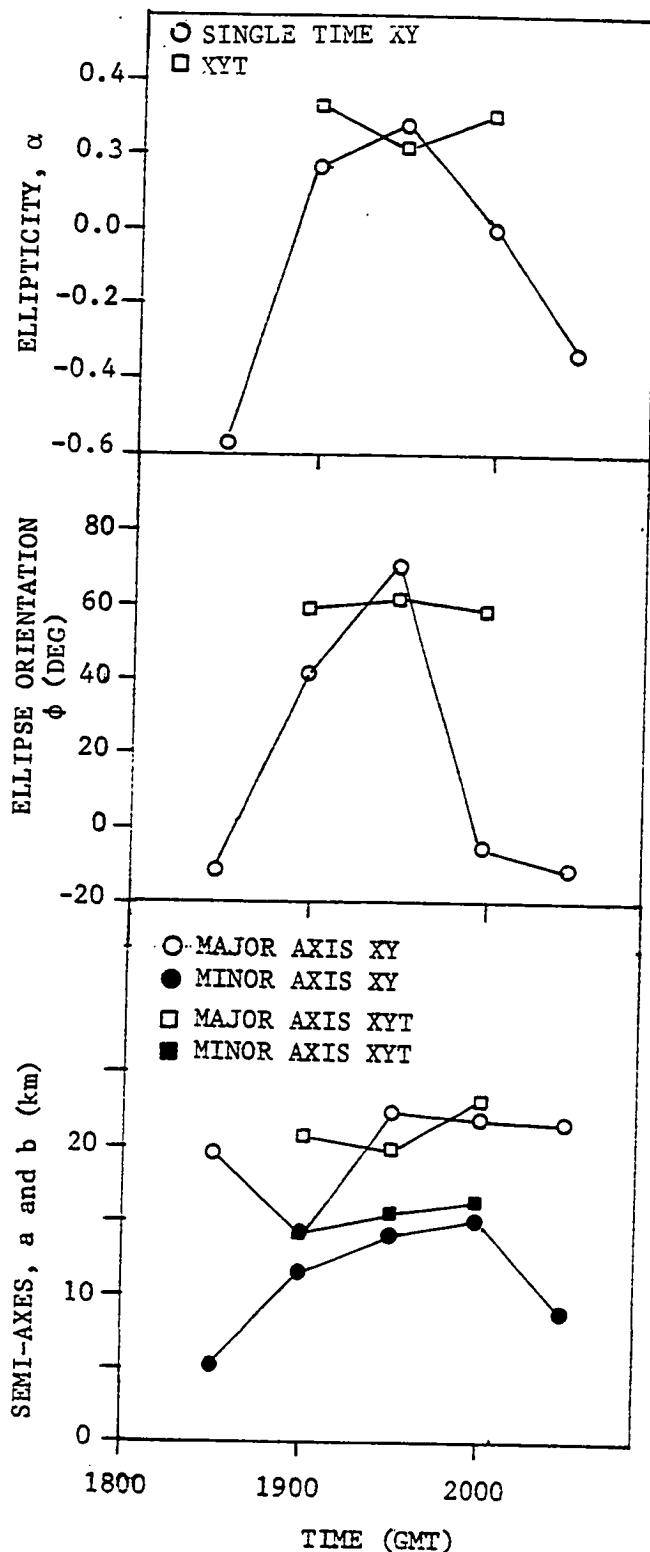


Fig. 44. Plots of ellipticity (α), orientation angle (ϕ), and semi-axes (a and b) for complex number 3 visible model fits.

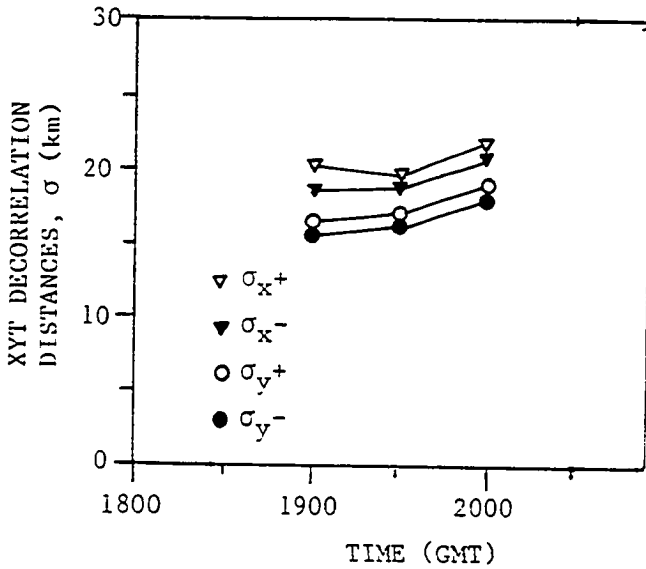
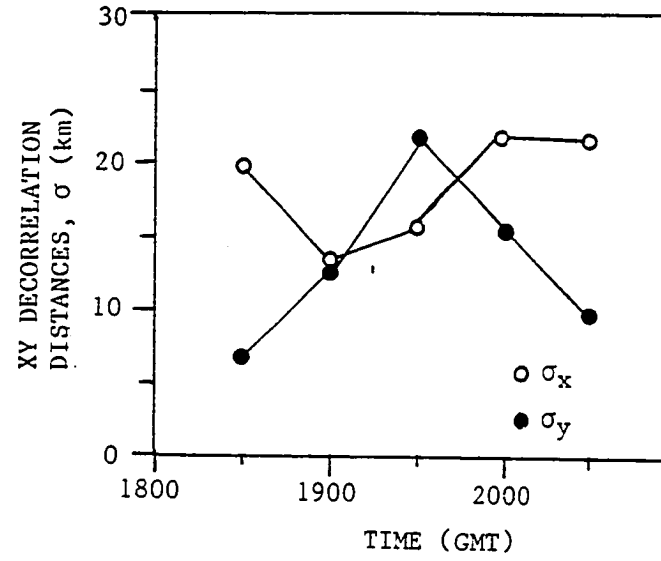


Fig. 45. Plots of decorrelation distances (σ) for complex number 3 visible model fit.

Table 20. Parameters of fitted model correlation function for complex number 3 visible. (see pages 44 and 45)

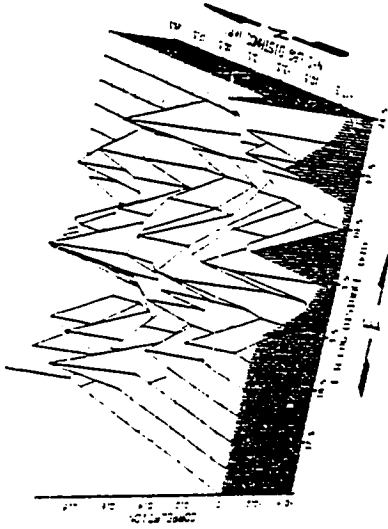
	CASE	TIME (GMT)	σ_{x+} km	σ_{x-} km	σ_{y+} km	σ_{y-} km	σ_t min	A_7	ρ_0	α	ϕ (°)	a km	b km	A km ²	V km/hr	θ (°)
SINGLE TIME XY	SM	1830	6.7	----	19.5	----	---	0.52	0.65	-0.57	-12	19.9	5.4	337	----	---
	SN	1900	12.9	----	13.1	----	---	0.62	0.80	0.17	42	14.1	11.8	522	----	---
	SO	1930	21.8	----	15.6	----	---	0.72	0.85	0.28	70	22.5	14.5	1024	----	---
	SP	2000	15.1	----	21.9	----	---	0.59	0.80	-0.09	-8	21.9	15.0	1031	----	---
	SQ	2030	9.6	----	21.5	----	---	0.65	0.81	-0.34	-12	21.8	8.9	611	----	---
XYT ($\Delta t=0$)	M		19.3	----	15.7	----	---	0.60	0.81	0.33	61	20.6	13.8	895	----	---
	N		18.1	----	16.0	----	---	0.63	0.83	0.27	57	19.4	14.3	871	----	---
	O		18.9	----	16.9	----	---	0.62	0.83	0.28	56	20.4	14.9	961	----	---
XYT	M		20.1	18.5	15.9	16.5	118	0.56	0.81	0.33	59	20.8	14.2	925	20.6	43
	N		19.7	18.7	16.0	17.1	115	0.55	0.83	0.21	61	19.8	15.5	960	21.4	26
	O		21.9	20.6	18.1	18.7	199	0.54	0.83	0.31	58	23.0	16.2	1169	18.4	-12

subjective discussion. Fig. 46 shows plots of the XY raw correlations field and function fits for cases SM and SN. This clearly illustrates the changing nature of the correlation structure. The structure is much more elliptical for case SM (1830) than for case SN (1900). A comparison of the XYT and XY function fits to the raw data fields seems to indicate that a series of XY correlations may better describe the correlation structure of the data field. The velocities obtained by fitting the model correlation function do not correspond to those obtained from the radar. The magnitudes are larger by factors of three (3) to five (5), and the direction is close only early in the life of the convective complex. These differences are due to the influence of the anvil on the correlation matrix as discussed previously for convective complex two (2).

The velocity determined by the NLP fit for case O is

SM

MAXIMUM CORRELATION = 0.646



SN

MAXIMUM CORRELATION = 0.799

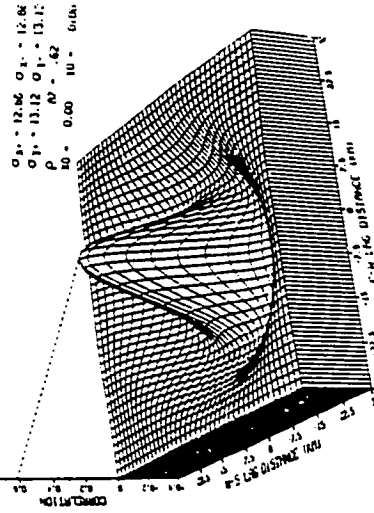
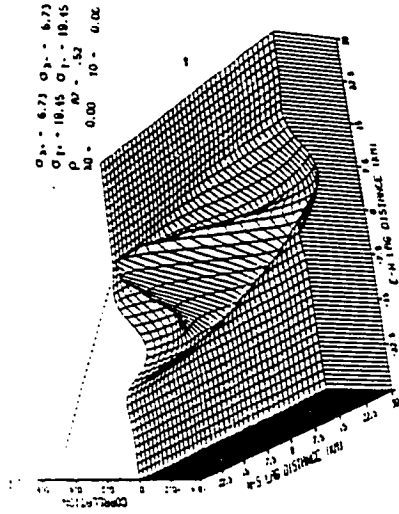
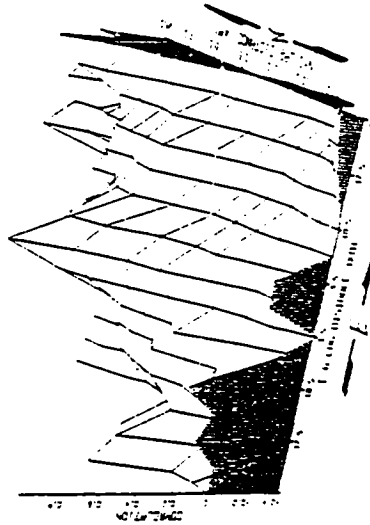


Fig. 46. Plots of raw correlation fields for complex number 3 visible cases SM and SN.

questionable. An examination of the raw correlation fields, Fig. 47, yields an estimate of the velocity of 22 km/hr along a heading of 17 degrees which more closely agrees with that obtained for cases M and N. Further examination of correlation matrices and the weighting matrices offers a possible explanation. The time lag zero correlation matrix is symmetric while the time lag one (1) correlation matrix is highly asymmetric, being skewed toward the negative X direction. The time lag zero matrix weights are much larger than the weights for time lag one; therefore, the NLP tries to fit a symmetrical function to the asymmetrical field. This results in the centroid of maximum correlation for time lag one (1) being shifted in the negative X direction. A possible solution to this problem will be discussed in the conclusions and suggestions.

c. Infrared Temperature

The amount of IR data available is borderline for the calculation of the correlation matrices for 1830, 1900, and 1930 GMT. The time lag zero XYT correlation field for case M (1830, 1900, 1930 GMT) is essentially the XY correlation for case SO (1930 GMT) and the time lag one matrix is so sparse that an XYT function fit is not possible. Table 21 gives the results of the NLP fits obtained, and the parameters are plotted in Fig. 48. The XY correlation matrices for single times were unstable because the data were so sparse and fits could not be obtained. Even the fits to the XYT time lag zero fields show considerable variation. All of the correlation matrices are noisy, especially those at

		X LAG										TIME LAG 0											
		-5					0					+5											
Y LAG	+5	-0.386	-0.362	-0.224	-0.166	-0.190	-0.193	-0.214	-0.130	-0.058	-0.095	-0.016	-0.386	-0.362	-0.261	-0.135	-0.109	-0.174	-0.184	-0.148	-0.060	-0.076	-0.114
		-0.353	-0.350	-0.224	-0.102	-0.028	-0.028	-0.091	-0.096	-0.037	-0.053	-0.129	-0.301	-0.301	-0.171	-0.013	-0.133	-0.105	-0.092	-0.012	-0.060	-0.069	-0.020
		-0.180	-0.177	-0.071	-0.099	-0.292	-0.322	-0.246	-0.143	-0.187	-0.185	-0.109	-0.098	-0.027	-0.014	-0.198	-0.390	-0.479	-0.370	-0.266	-0.245	-0.263	-0.110
		-0.076	-0.103	-0.159	-0.260	-0.524	-0.648	-0.484	-0.331	-0.298	-0.264	-0.141	-0.117	-0.237	-0.229	-0.333	-0.602	-0.832	-0.602	-0.333	-0.229	-0.237	-0.117
		-0.141	-0.264	-0.299	-0.331	-0.484	-0.648	-0.524	-0.280	-0.159	-0.100	-0.076	-0.110	-0.263	-0.245	-0.286	-0.370	-0.479	-0.390	-0.163	-0.014	-0.027	-0.098
		-0.109	-0.185	-0.187	-0.143	-0.246	-0.322	-0.292	-0.099	-0.071	-0.177	-0.180	-0.020	-0.089	-0.060	-0.012	-0.092	-0.105	-0.133	-0.016	-0.171	-0.301	-0.301
		-0.129	-0.033	-0.037	-0.096	-0.091	-0.028	-0.028	-0.102	-0.224	-0.350	-0.353	-0.114	-0.076	-0.060	-0.143	-0.184	-0.174	-0.109	-0.136	-0.261	-0.362	-0.389
		-0.016	-0.035	-0.056	-0.130	-0.214	-0.193	-0.190	-0.166	-0.224	-0.362	-0.386											
Y LAG	0	8726	8457	7670	7594	7703	7508	5822	3976	4698	4683	2864	7730	9516	0863	8594	8101	7181	8604	6005	4194	4562	4413
		6913	9259	9755	13497	9320	8447	6873	8940	6756	4447	4431	11367	8192	10333	9341	14656	9949	8497	7150	8261	7444	4725
		92521	2950	0495	2390	97131	4997	12592	3025	7859	7282	7970	90221	0146	13479	12942	13501	110301	128031	3772	7858	8215	6274
		100471	0254	1295	4169	17616	13387	112861	19251	3723	8677	8176	93231	2027	12101	1993	13004	15794	130041	19981	12101	2027	9323
		8176	8577	13723	11925	112861	3387	17616	41691	12951	0254	10047	6274	8215	7858	13721	2803	10301	13501	12942	13479	10495	9022
		7970	7292	7859	8025	12592	4997	97131	2390	10495	12900	9252	4725	7444	8261	7150	8497	9949	14656	9341	10333	8192	11367
		4431	4447	6756	8940	5873	8447	93201	3497	9755	9359	6913	4413	4562	4194	6005	8604	7181	8101	8594	10863	9516	7730
		-5	2864	4683	4698	3976	5822	7508	7703	7594	7670	8457	8726										
		X LAG										TIME LAG 1											
		-5					0					+5											
Y LAG	+5	-0.125	-0.032	-0.049	-0.114	-0.252	-0.213	-0.157	-0.157	-0.082	-0.010	-0.067	-0.019	-0.043	-0.110	-0.220	-0.251	-0.275	-0.240	-0.239	-0.211	-0.103	-0.032
		-0.027	-0.119	-0.160	-0.235	-0.337	-0.342	-0.335	-0.304	-0.271	-0.173	-0.031	-0.031	-0.180	-0.244	-0.272	-0.337	-0.434	-0.413	-0.361	-0.252	-0.177	-0.067
		-0.109	-0.193	-0.293	-0.313	-0.336	-0.422	-0.453	-0.404	-0.271	-0.141	-0.061	-0.154	-0.209	-0.274	-0.316	-0.305	-0.362	-0.401	-0.411	-0.281	-0.100	-0.003
		-0.096	-0.169	-0.252	-0.291	-0.267	-0.304	-0.290	-0.275	-0.211	-0.040	-0.086	-0.069	-0.133	-0.238	-0.267	-0.234	-0.149	-0.193	-0.171	-0.092	-0.071	-0.163
		-0.069	-0.051	-0.172	-0.173	-0.165	-0.122	-0.088	-0.093	-0.034	-0.083	-0.227	-0.047	-0.036	-0.098	-0.139	-0.104	-0.043	-0.002	-0.006	-0.017	-0.095	-0.199
		-0.073	-0.106	-0.019	-0.038	-0.019	-0.053	-0.086	-0.106	-0.092	-0.139	-0.241	-0.084	-0.124	-0.115	-0.026	-0.018	-0.091	-0.148	-0.147	-0.151	-0.151	-0.252
		-0.123	-0.104	-0.093	-0.067	-0.076	-0.094	-0.195	-0.204	-0.129	-0.147	-0.218	-0.135	-0.214	-0.155	-0.143	-0.078	-0.116	-0.212	-0.277	-0.165	-0.155	-0.211
		-5	-0.187	-0.170	-0.226	-0.217	-0.208	-0.148	-0.225	-0.307	-0.245	-0.194	-0.237										
Y LAG	0	6031	6304	6282	5967	5756	6706	4437	5107	3636	4289	3080	6075	6209	7245	6190	6410	5652	6901	4523	5136	3673	4008
		6106	6503	6439	7795	6532	6706	5955	6451	5099	4919	3795	6463	6715	6805	6971	7638	6693	6714	6161	5730	5425	4509
		5903	6669	7500	7022	7599	7494	7400	6608	6276	5077	5519	5748	6805	6810	7659	7049	7861	6710	7538	6316	5971	4766
		5890	5486	7557	6583	7854	7209	8085	6256	7091	6332	5347	4547	6393	5405	7870	6507	7562	6689	7762	6345	6203	6288
		4680	4650	6257	5597	7367	6775	6687	7034	6732	6342	5365	3701	4787	4694	5703	5554	6548	6508	5750	6698	5751	5835
		3152	3706	4505	5002	5288	5576	5967	6113	5147	6094	5157	3416	2901	3700	4102	4934	4579	5058	5233	5424	4807	5133
		1958	3391	2792	3567	3848	4664	4577	4501	4772	4631	4462	2073	1822	3090	2729	3174	3578	3847	4505	3741	4198	3960
		-5	1365	1922	1819	2692	2723	2712	3398	3159	4290	3177	3549										

CORRELATIONS

NUMBER OF PAIRS

CORRELATIONS

NUMBER OF PAIRS

CORRELATIONS

NUMBER OF PAIRS

CORRELATIONS

NUMBER OF PAIRS

Fig. 47. Raw correlation fields for complex number 3 visible case 0.

Table 21. Parameters of fitted model correlation function for complex number 3 IR temperature. (see pages 44 and 45)

	CASE	TIME (GMT)	σ_{x+}	σ_{x-}	σ_{y+}	σ_{y-}	σ_t	A_1	ρ_0	α	ϕ	a	b	A	V	θ
			km	km	km	km	min				(°)	km	km	km ²	km/hr	(°)
SINGLE TIME XY	SM	---	---	---	---	---	---	---	---	---	---	---	---	---	---	---
	SN	---	---	---	---	---	---	---	---	---	---	---	---	---	---	---
	SO	---	---	---	---	---	---	---	---	---	---	---	---	---	---	---
XYT ($\Delta t=0$)	M		16.2	---	17.3	---	---	1.0	0.80	-0.28	-39	19.0	14.1	846	---	---
	N		45.4	---	21.4	---	---	0.68	0.91	0.27	81	45.8	20.3	2929	---	---
	O		151.1	---	41.2	---	---	0.53	0.95	-0.24	94	151.4	39.8	18957	---	---
XYT	M		DID NOT CONVERGE				---	---	---	---	---	---	---	---	---	---
	N		38.7	37.8	21.1	20.7	---	0.76	0.90	0.21	81	38.6	20.2	2453	18.2	7
	O		104.0	175.8	36.9	30.5	---	0.60	0.95	-0.21	93	140.1	32.9	14497	53.3	-76

time lags one and two. There is some indication that for this storm the IR pattern initially lies perpendicular to the visible pattern, and as the storm develops, the IR pattern begins to align itself with the visible pattern. Also as in complex number 2, the a/b ratio for the IR temperature tend to reflect the growth of the anvil more so than the ratios for the visible.

d. Infrared Temperature Gradient Component

Since the IR temperature gradient is derived from the IR temperature data, the previous comments concerning the sparse IR data also apply to the temperature gradient. Table 22 gives the parameters determined in the NLP fits to the XYT and XY raw correlations. The parameters are also plotted in Fig. 49. The XYT fit for case O did not converge, and there was insufficient data to fit cases SM and SN. From the function fit to the time lag zero matrices, it is seen that as the storm grows older the major axis of the correlation

Table 22. Parameters of fitted model correlation function for complex number 3 IR temperature gradient. (see pages 44 and 45)

	CASE	TIME (GMT)	σ_{x+} km	σ_{x-} km	σ_{y+} km	σ_{y-} km	σ_t min	A_7	ρ_0	α	ϕ (°)	a km	b km	A km ²	V km/hr	e (°)
SINGLE TIME XY	SM	1830	----	----	----	----	----	----	----	----	----	----	----	----	----	----
	SN	1900	----	----	----	----	----	----	----	----	----	----	----	----	----	----
	SO	1930	25.3	----	69.5	----	----	0.70	0.71	0.82	17	72.7	13.9	3172	----	----
	SP	2000	46.9	----	84.1	----	----	0.69	0.48	-0.97	-29	95.8	9.4	2834	----	----
	SQ	2030	54.7	----	124.3	----	----	0.60	0.55	-0.83	-21	132.4	28.3	11832	----	----
XYT ($\Delta t=0$)	M		41.5	----	28.2	----	----	0.64	0.67	-0.84	-58	48.4	13.3	2025	----	----
	N		21.0	----	40.2	----	----	0.58	0.58	-0.82	-25	44.0	11.0	1514	----	----
	O		35.7	----	77.2	----	----	0.43	0.60	-0.80	-22	82.7	20.2	5244	----	----
XYT	M		47.7	41.8	25.9	30.2	46	0.62	0.67	-0.85	-60	51.2	12.8	2060	21.8	-54
	N		20.9	20.1	36.8	36.5	123	0.48	0.58	0.34	15	37.5	18.8	2218	21.9	-23
	O		DID NOT CONVERGE													

ellipse becomes oriented along a north-northwest to south-southeast direction. Comparing this to the NLP fits for cases SN to SO for the visible, it appears that the major axes are tending to align themselves. This may indicate that the IR gradient found may be that across the storm instead of along it. This in turn suggests that the major axis determined for the IR temperature is not the proper one. This may be due to either the lack of IR data or the wrong threshold being used in finding the correlation matrices.

The lag zero ($\Delta T = \Delta X = \Delta Y = 0$) correlation, A_7 , indicates that the IR temperature gradient field is fairly coherent. However, the amount of noise seems to increase with time as evidenced by the decrease in the A_7 values.

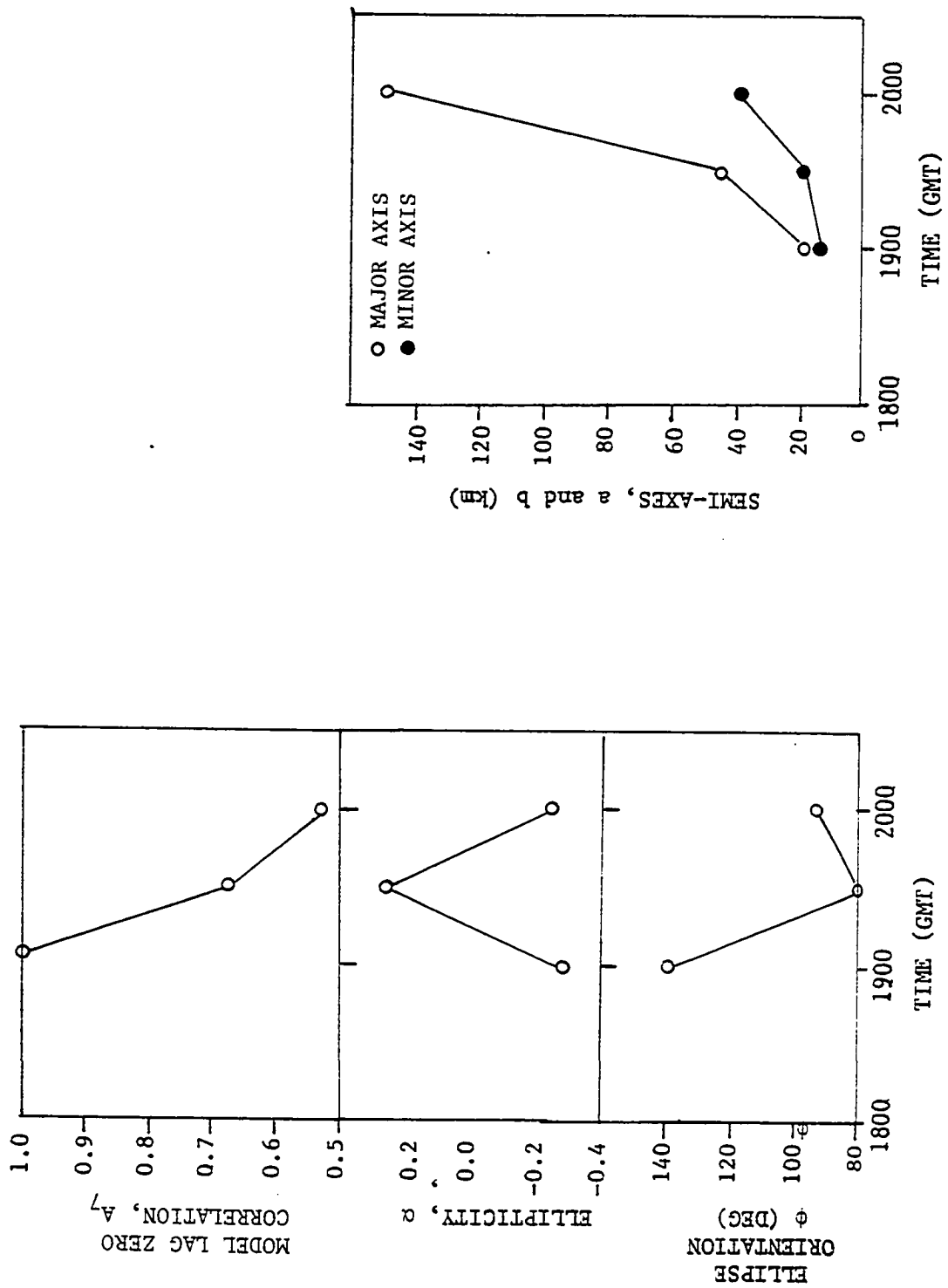


Fig. 48. Plots of model correlation function parameters for complex number 3 IR temperature XYT time lag zero.

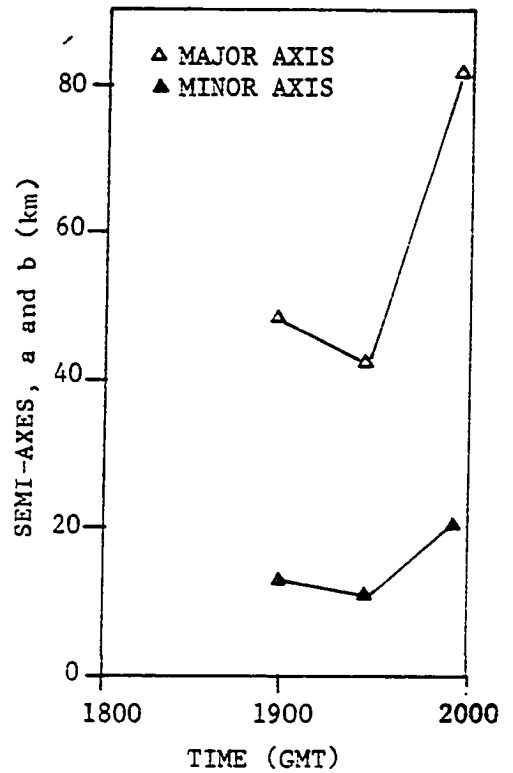
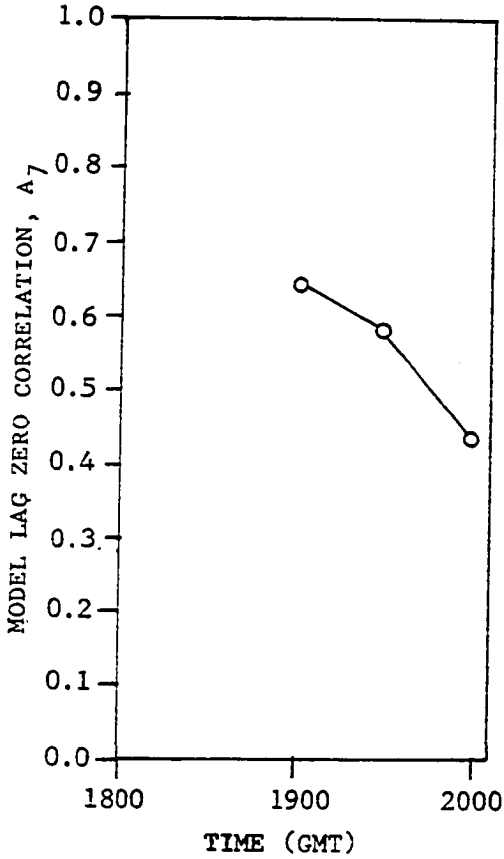
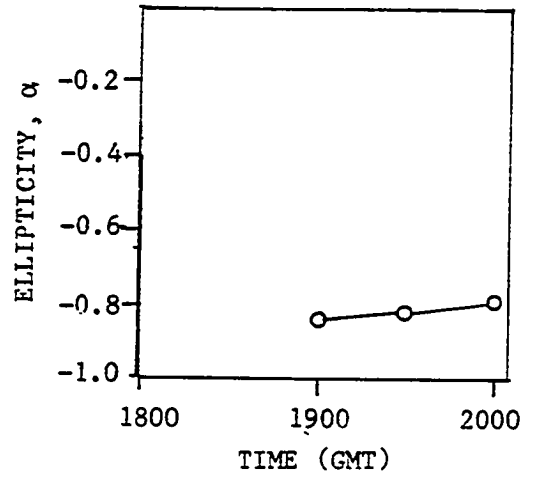
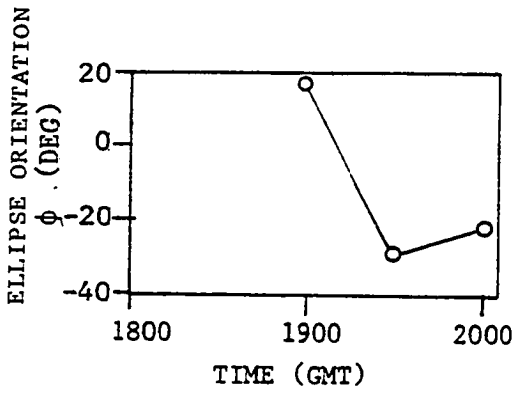


Fig. 49. Plots of model correlation parameters for complex number 3 IR temperature gradient XYT time lag zero.

e. Infrared Temperature Cross Visible Reflectance

The raw correlation matrices found for the IR temperature cross visible were multimodal, again suggesting the presence of several cells lying approximately along a northwest to southeast line. It was not possible to obtain XYT function fits to the XYT raw correlation matrices due to their behavior. Table 23 lists the maximum raw correlations for the central modes for each time lag and case. As can be seen the maximum correlation does not occur at time lag zero but at time lag -1. This indicates that the IR temperature is slightly more correlated with the visible reflectance that occurred approximately 30 minutes earlier. This apparent lag in the IR temperature may be due to the difference in spatial resolution of the two sensing systems. Since the resolution of the visible sensor is much better than that of the IR sensor, it can detect changes in the cloud earlier.

Table 23. Maximum raw correlation in central modes for complex number 3 IR temperature cross visible XYT correlation fields.

Case	Time Lag				
	-2	-1	0	1	2
M	0.422	0.467	0.417	0.311	-----
N	0.292	0.451	0.349	0.374	0.368
O	0.501	0.569	0.371	0.306	0.386

Table 24 lists the maximum correlation in each of the raw XY cross-correlation matrices. There is no value given for case SM because there were so few IR temperatures below the threshold that it was not possible to determine a correla-

tion matrix. There is indication that the correlation between the IR temperature and visible imagery increases with time. This would be expected because as the storm grows older it becomes more organized, and cloud top features become large enough to affect the IR sensors.

Table 24. Maximum correlation for each raw XY correlation field for complex number 3 IR temperature cross visible.

Case	Correlation
SM	----
SN	0.309
SO	0.546
SP	0.548
SQ	0.475

f. Infrared Temperature Gradient Component
Cross Visible Reflectance

The IR temperature gradient cross visible correlation matrices are rather chaotic. Sometimes the maximum correlation is positive; at other times, it is negative. Sometimes the maximum correlation is at time lag one, and at others it is at time lag -1. It is believed that this is due in part to the uncertainty in determination of the major axis of the IR correlation field along which the temperature gradient component was taken. Also because the IR temperature gradient is derived from the sparse IR data, it is itself sparse.

The correlation patterns for the two thresholds are somewhat similar; however, the magnitudes may be different. Fig. 50 shows the raw correlation matrices for time lags zero and one for case N for both thresholds. As can be seen, for

THRESHOLD = -1000

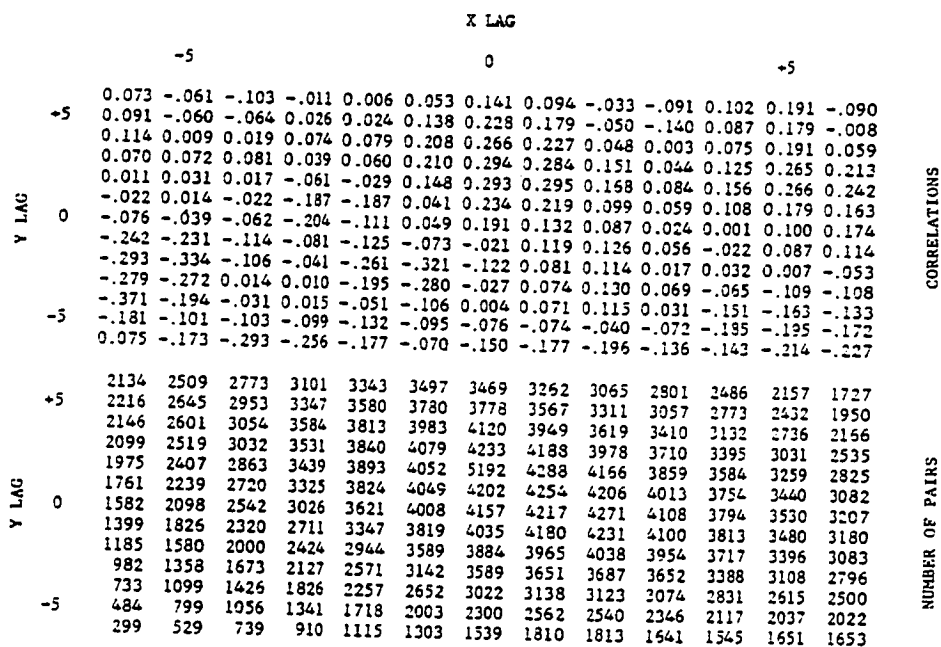
TIME	LAG	0	LAG 2	0
-1537	223	0.000	0.000	0.000
-1536	412	0.000	0.000	0.000
-1535	601	0.000	0.000	0.000
-1534	790	0.000	0.000	0.000
-1533	979	0.000	0.000	0.000
-1532	1168	0.000	0.000	0.000
-1531	1357	0.000	0.000	0.000
-1530	1546	0.000	0.000	0.000
-1529	1735	0.000	0.000	0.000
-1528	1924	0.000	0.000	0.000
-1527	2113	0.000	0.000	0.000
-1526	2302	0.000	0.000	0.000
-1525	2491	0.000	0.000	0.000
-1524	2680	0.000	0.000	0.000
-1523	2869	0.000	0.000	0.000
-1522	3058	0.000	0.000	0.000
-1521	3247	0.000	0.000	0.000
-1520	3436	0.000	0.000	0.000
-1519	3625	0.000	0.000	0.000
-1518	3814	0.000	0.000	0.000
-1517	4003	0.000	0.000	0.000
-1516	4192	0.000	0.000	0.000
-1515	4381	0.000	0.000	0.000
-1514	4570	0.000	0.000	0.000
-1513	4759	0.000	0.000	0.000
-1512	4948	0.000	0.000	0.000
-1511	5137	0.000	0.000	0.000
-1510	5326	0.000	0.000	0.000
-1509	5515	0.000	0.000	0.000
-1508	5704	0.000	0.000	0.000
-1507	5893	0.000	0.000	0.000
-1506	6082	0.000	0.000	0.000
-1505	6271	0.000	0.000	0.000
-1504	6460	0.000	0.000	0.000
-1503	6649	0.000	0.000	0.000
-1502	6838	0.000	0.000	0.000
-1501	7027	0.000	0.000	0.000
-1500	7216	0.000	0.000	0.000
-1499	7405	0.000	0.000	0.000
-1498	7594	0.000	0.000	0.000
-1497	7783	0.000	0.000	0.000
-1496	7972	0.000	0.000	0.000
-1495	8161	0.000	0.000	0.000
-1494	8350	0.000	0.000	0.000
-1493	8539	0.000	0.000	0.000
-1492	8728	0.000	0.000	0.000
-1491	8917	0.000	0.000	0.000
-1490	9106	0.000	0.000	0.000
-1489	9295	0.000	0.000	0.000
-1488	9484	0.000	0.000	0.000
-1487	9673	0.000	0.000	0.000
-1486	9862	0.000	0.000	0.000
-1485	10051	0.000	0.000	0.000
-1484	10240	0.000	0.000	0.000
-1483	10429	0.000	0.000	0.000
-1482	10618	0.000	0.000	0.000
-1481	10807	0.000	0.000	0.000
-1480	10996	0.000	0.000	0.000
-1479	11185	0.000	0.000	0.000
-1478	11374	0.000	0.000	0.000
-1477	11563	0.000	0.000	0.000
-1476	11752	0.000	0.000	0.000
-1475	11941	0.000	0.000	0.000
-1474	12130	0.000	0.000	0.000
-1473	12319	0.000	0.000	0.000
-1472	12508	0.000	0.000	0.000
-1471	12697	0.000	0.000	0.000
-1470	12886	0.000	0.000	0.000
-1469	13075	0.000	0.000	0.000
-1468	13264	0.000	0.000	0.000
-1467	13453	0.000	0.000	0.000
-1466	13642	0.000	0.000	0.000
-1465	13831	0.000	0.000	0.000
-1464	14020	0.000	0.000	0.000
-1463	14209	0.000	0.000	0.000
-1462	14398	0.000	0.000	0.000
-1461	14587	0.000	0.000	0.000
-1460	14776	0.000	0.000	0.000
-1459	14965	0.000	0.000	0.000
-1458	15154	0.000	0.000	0.000
-1457	15343	0.000	0.000	0.000
-1456	15532	0.000	0.000	0.000
-1455	15721	0.000	0.000	0.000
-1454	15910	0.000	0.000	0.000
-1453	16099	0.000	0.000	0.000
-1452	16288	0.000	0.000	0.000
-1451	16477	0.000	0.000	0.000
-1450	16666	0.000	0.000	0.000
-1449	16855	0.000	0.000	0.000
-1448	17044	0.000	0.000	0.000
-1447	17233	0.000	0.000	0.000
-1446	17422	0.000	0.000	0.000
-1445	17611	0.000	0.000	0.000
-1444	17800	0.000	0.000	0.000
-1443	17989	0.000	0.000	0.000
-1442	18178	0.000	0.000	0.000
-1441	18367	0.000	0.000	0.000
-1440	18556	0.000	0.000	0.000
-1439	18745	0.000	0.000	0.000
-1438	18934	0.000	0.000	0.000
-1437	19123	0.000	0.000	0.000
-1436	19312	0.000	0.000	0.000
-1435	19501	0.000	0.000	0.000
-1434	19690	0.000	0.000	0.000
-1433	19879	0.000	0.000	0.000
-1432	20068	0.000	0.000	0.000
-1431	20257	0.000	0.000	0.000
-1430	20446	0.000	0.000	0.000
-1429	20635	0.000	0.000	0.000
-1428	20824	0.000	0.000	0.000
-1427	21013	0.000	0.000	0.000
-1426	21202	0.000	0.000	0.000
-1425	21391	0.000	0.000	0.000
-1424	21580	0.000	0.000	0.000
-1423	21769	0.000	0.000	0.000
-1422	21958	0.000	0.000	0.000
-1421	22147	0.000	0.000	0.000
-1420	22336	0.000	0.000	0.000
-1419	22525	0.000	0.000	0.000
-1418	22714	0.000	0.000	0.000
-1417	22903	0.000	0.000	0.000
-1416	23092	0.000	0.000	0.000
-1415	23281	0.000	0.000	0.000
-1414	23470	0.000	0.000	0.000
-1413	23659	0.000	0.000	0.000
-1412	23848	0.000	0.000	0.000
-1411	24037	0.000	0.000	0.000
-1410	24226	0.000	0.000	0.000
-1409	24415	0.000	0.000	0.000
-1408	24604	0.000	0.000	0.000
-1407	24793	0.000	0.000	0.000
-1406	24982	0.000	0.000	0.000
-1405	25171	0.000	0.000	0.000
-1404	25360	0.000	0.000	0.000
-1403	25549	0.000	0.000	0.000
-1402	25738	0.000	0.000	0.000
-1401	25927	0.000	0.000	0.000
-1400	26116	0.000	0.000	0.000
-1399	26305	0.000	0.000	0.000
-1398	26494	0.000	0.000	0.000
-1397	26683	0.000	0.000	0.000
-1396	26872	0.000	0.000	0.000
-1395	27061	0.000	0.000	0.000
-1394	27250	0.000	0.000	0.000
-1393	27439	0.000	0.000	0.000
-1392	27628	0.000	0.000	0.000
-1391	27817	0.000	0.000	0.000
-1390	28006	0.000	0.000	0.000
-1389	28195	0.000	0.000	0.000
-1388	28384	0.000	0.000	0.000
-1387	28573	0.000	0.000	0.000
-1386	28762	0.000	0.000	0.000
-1385	28951	0.000	0.000	0.000
-1384	29140	0.000	0.000	0.000
-1383	29329	0.000	0.000	0.000
-1382	29518	0.000	0.000	0.000
-1381	29707	0.000	0.000	0.000
-1380	29896	0.000	0.000	0.000
-1379	30085	0.000	0.000	0.000
-1378	30274	0.000	0.000	0.000
-1377	30463	0.000	0.000	0.000
-1376	30652	0.000	0.000	0.000
-1375	30841	0.000	0.000	0.000
-1374	31030	0.000	0.000	0.000
-1373	31219	0.000	0.000	0.000
-1372	31408	0.000	0.000	0.000
-1371	31597	0.000	0.000	0.000
-1370	31786	0.000	0.000	0.000
-1369	31975	0.000	0.000	0.000
-1368	32164	0.000	0.000	0.000
-1367	32353	0.000	0.000	0.000
-1366	32542	0.000	0.000	0.000
-1365	32731	0.000	0.000	0.000
-1364	32920	0.000	0.000	0.000
-1363	33109	0.000	0.000	0.000
-1362	33298	0.000	0.000	0.000
-1361	33487	0.000	0.000	0.000
-1360	33676	0.000	0.000	0.000
-1359	33865	0.000	0.000	0.000
-1358	34054	0.000	0.000	0.000
-1357	34243	0.000	0.000	0.000
-1356	34432	0.000	0.000	0.000
-1355	34621	0.000	0.000	0.000
-1354	34810	0.000	0.000	0.000
-1353	35000	0.000	0.000	0.000
-1352	35189	0.000	0.000	0.000
-1351	35378	0.000	0.000	0.000
-1350	35567	0.000	0.000	0.000
-1349	35756	0.000	0.000	0.000
-1348	35945	0.000	0.000	0.000
-1347	36134	0.000	0.000	0.000
-1346	36323	0.000	0.000	0.000
-1345	36512	0.000	0.000	0.000
-1344	36701	0.000	0.000	0.000
-1343	36890	0.000	0.000	0.000
-1342	37079	0.000	0.000	0.000
-1341	37268	0.000	0.000	0.000
-1340	37457	0.000	0.000	0.000
-1339	37646	0.000	0.000	0.000
-1338	37835	0.000	0.000	0.000
-1337	38024	0.000	0.000	0.000
-1336	38213	0.000	0.000	0.000
-1335	38402	0.000	0.000	0.000
-1334	38591	0.000	0.000	0.000
-1333	38780	0.000	0.000	0.000
-1332	38969	0.000	0.000	0.000
-1331	39158	0.000	0.000	0.000
-1330	39347	0.000	0.000	0.000
-1329	39536	0.000	0.000	0.000
-1328	39725	0.000	0.000	0.000
-1327	39914	0.000	0.000	0.000
-1326	40103	0.000	0.000	0.000
-1325	40292	0.000	0.000	0.000
-1324	40481	0.000	0.000	0.000
-1323	40670	0.000	0.000	0.000
-1322	40859	0.000	0.000	0.000
-1321	41048	0.000	0.000	0.000
-1320	41237	0.000	0.000	0.000
-1319	41426	0.000	0.000	0.000
-1318	41615	0.000	0.000	0.000
-1317	41804	0.000	0.000	0.000
-1316	41993	0.000	0.000	0.000
-1315	42182	0.000	0.000	0.000
-1314	42371	0.000	0.000	

time lag one, the pattern of the positive region, the left halves of the matrices are very similar but the magnitudes of the correlations within this region are different.

g. Radar Rain Rates Cross Visible Reflectance

There is some indication of linear correlation between the radar rain rates and the visible reflectance. However, the maximum correlation is only approximately 0.3 in both the XYT and XY matrices. It is not possible to fit the correlation model to the correlation fields as it is not an appropriate model for the correlation patterns present. Fig. 51 shows the XYT time lag zero correlation matrix for case N. The XY correlation matrices are similar in structure except for case SN (1900 GMT) which is still in the early stages of the storm development.

The location of the point of maximum correlation stays relatively constant for the cases. Table 25 is a listing of the maximum single time cross-correlations. The decrease in the magnitude of the cross-correlation with time reflects the increasing complexity of the storm system. For the last three cases (times) the displacement seems to be fairly constant. The location indicates that the radar bins are most correlated with the visible pixels located 1.5 km east and 7 km north. It should be noted that some of this displacement may be due to navigational errors associated with the visible data; however, any error present appears to be constant over time and, therefore, will not have any appreciable effect on the velocity



LAG DISTANCE IN X AND Y DIRECTIONS IS 3 KM EACH.

Fig. 51. Raw correlation fields for complex number 3 radar cross visible case N time lag zero.

calculations. The apparent velocity of the maximum correlation was calculated by simply measuring the change in the displacement between time lag zero and time lag one and converting it to a velocity. The velocities found are

Case	Velocity	Direction
N	27.1 km/hr	354
O	21.0 km/hr	45

The previous discussion under convective complex two on the interpretation of these velocities also applies here.

Table 25. Maximum radar cross visible single time cross-correlations for complex number 3. (see page 45)

Case	Maximum Correlation	Lags	
		X	Y
SN	0.319	-5,	2
SO	0.356	1,	2
SP	0.256	0,	1
SQ	0.247	1,	2

The time lag -2 cross-correlation field for case 0 is a good illustration of the care that must be taken in interpreting the correlation fields. This correlation field represents the correlation between the radar 2030 GMT and the visible at 1930 GMT. Fig. 52 shows the correlation field and plots of the corresponding data fields. The large area of positive correlation in the lower right portion of the correlation field represents the correlation between the radar rain area marked B and the visible reflectance. However, the rain area marked A is the dissipating remnant of the cell which produced the cloud at 1930 GMT. The cell at B is a newly developed cell and therefore has no physical connection to the cloud at 1930 GMT. The positive correlation comes about merely because there is a similar structure in the two data fields.

h. Radar Rain Rates Cross Infrared Temperature

There appears to be about as much linear correlation between these two data fields as for the radar cross visible. In the discussion of the radar cross visible correlation matrices, it was mentioned that the maximum correlation appeared to lie 1.5 km to the east and 7 km to the north of lag zero in X and Y. If one converts this displacement into the bin size used for the radar cross IR calculations, it is seen that in general the corresponding bin in the XYT time lag zero correlation fields is the highest or next to the highest correlation in the central region. The locations of the single

		X LAG																CORRELATIONS
		-5				0				+5								
+5		.085-	.111-	.005	.079	.292-	.008-	.330-	.323-	.172-	.262-	.323-	.367-	.341-	.244	.210		
		.193	.057	.017	.163	.255	.041	.294	.365	.199	.193	.193	.262	.157	.014	.012		
		.152	.024	.089	.199	.232	.115	.214	.316	.141	.069	.113	.019	.051	.050	.092		
		.195	.036	.081	.185	.196	.160	.118	.233	.152	.037	.246	.219	.145	.065	.249		
		.156	.071	.053	.196	.218	.157	.012	.137	.124	.093	.174	.231	.131	.141	.238		
0		.159	.031	.015	.185	.191	.129	.042	.074	.207	.174	.124	.227	.139	.019	.091		
		.139	.116	.015	.093	.116	.025	.006	.067	.225	.171	.152	.255	.258	.211	.101		
		.203	.125	.011	.021	.096	.022	.016	.059	.176	.134	.094	.241	.264	.147	.328		
		.073	.055	.059	.024	.010	.052	.024	.018	.147	.155	.071	.304	.347	.199	.232		
		-.071	-.039	.132	.101	.107	.127	.009	.045	.167	.165	.002	.208	.413	.351	.062		
-5		-.224	-.035	.071	.148	.197	.154	.117	.136	.213	.177	.176	.023	.375	.372	.174		
		-.169	.004	.011	.109	.171	.143	.191	.201	.140	.218	.302	.044	.346	.329	.166		
		-.036	.003	.057	.039	.232	.097	.113	.165	.111	.150	.205	.024	.246	.247	.039		
		-.023	.162	.119	.163	.256	.155	.164	.082	.042	.061	.065	.045	.152	.137	.110		
		-.264	.419	.280	.334	.379	.331	.323	.132	.038	.107	.139	.011	.065	.040	.038		
+5		1687	1902	2044	1937	1684	1702	1416	1203	985	784	729	662	578	417	294		
		1797	1991	2146	2140	2013	1898	1636	1422	1209	1021	916	826	716	522	342		
		1849	1998	2146	2139	2109	2053	1926	1672	1462	1229	1049	939	826	652	426		
		1918	1975	2159	2262	2237	2241	2100	1995	1656	1412	1200	1029	892	712	503		
		1772	1931	2103	2236	2338	2391	2263	2095	1824	1551	1301	1059	924	740	536		
0		1729	1955	2046	2204	2334	2401	2363	2225	1978	1679	1382	1072	853	710	562		
		1714	1854	1995	2151	2320	2424	2362	2243	2016	1777	1403	1104	856	713	550		
		1664	1828	1939	2034	2235	2340	2335	2214	2002	1743	1417	1097	863	671	552		
		1520	1719	1651	1898	2011	2139	2193	2102	1928	1657	1317	1070	820	617	560		
		1335	1555	1649	1697	1767	1908	1979	2007	1831	1546	1289	1056	784	611	583		
-5		1119	1291	1430	1475	1523	1638	1766	1523	1681	1426	1227	1020	769	638	591		
		909	1064	1173	1244	1265	1421	1527	1523	1510	1314	1134	951	779	645	598		
		724	856	939	1019	1070	1158	1301	1374	1352	1176	1029	867	761	649	575		
		584	682	770	823	847	934	1021	1163	1134	956	889	787	676	622	555		
		447	500	561	619	628	662	765	861	864	768	673	608	552	514	463		

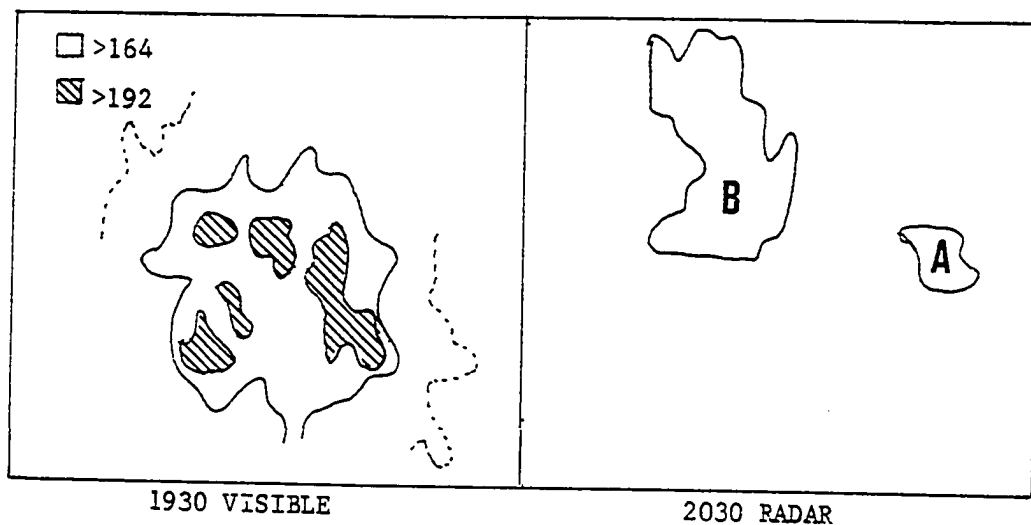


Fig. 52. Time lag -2 correlation fields for radar cross visible and plots of corresponding data fields (complex number 3).

time XY maxima are not as well behaved as the corresponding locations for the radar cross visible maxima. Table 26 is a listing of the maxima and their corresponding lags. While the magnitudes of the cross-correlations do not decrease as they do for the radar cross visible the location of the maxima is more variable.

Table 26. Maximum correlations for radar cross IR temperature for each case and corresponding lags (complex 3). (see page 45)

Case	Maximum Correlation	Lags	
		X	Y
SN	(0.293)	1,	-1
SO	0.322	1,	1
SP	0.345	-1,	2
SQ	0.330	3,	-1

 Parenthesis = question on significance

Recalling that in the discussion of the cross-correlation fields between the IR and visible data, it was suggested that the IR probably lags behind the visible data in detecting changes in the cloud structure. For this reason, and considering that the maximum cross-correlation between the radar and visible data was at time lag zero, one might expect that the maximum correlation between the radar and IR data to occur at time lag one. Examination of the correlation fields supports this.

The overall correlation pattern, however, is not as consistent as for radar cross visible. This is again probably due in part to the sparsity of the IR data. Another contributing factor is the interaction of the IR resolution

data and the area of rainfall. The rainfall area is such that two or three IR pixels would cover the entire area.

i. Radar Rain Rates Cross Infrared
Temperature Gradient Component

The correlation field between the radar rain rates and the IR temperature gradient components appears to be about as good as the IR temperature gradient component cross visible fields. The correlations about lag zero are for the most part negative. This lends credence to the earlier statement that the component of the IR temperature gradient was taken along the wrong vector.

The IR temperature gradient component as it is defined appears to have little linear correlation with the rain rates. The cross-correlation fields are noisy, and the magnitudes of the correlations small. At times the maximum correlation is negative while at others positive. The only similarity between the various cross-correlation fields is that for the time lag zero fields and the XY fields there is a tendency for a region of negative cross-correlations about spatial lag zero. However, the shape of this region and the location of the maximum cross-correlation varies considerably between the various times. Also the maximum cross-correlation magnitude is not always negative.

3. Convective Complex Number 5

Only the first two hours (1830 to 2030 GMT) of satellite data were available for this convective complex. Because

of this only the radar data between 1830 and 2100 GMT are used. Tables 27 and 28 give the times and case identifiers for the radar and satellite data, respectively. Fig. 53 is a plot of the total storm volumetric rain rates for the period 1830 to 2130 GMT and representative correlation areas for complex number five. There is little rain until 1930 GMT.

Table 27. Case designations for convective complex number 5 radar data.

Time (GMT)	Auto-correlation Case		Cross-correlation Case	
	XYT	XY	XYT	-XY
1830	M	SM	M	SM
1845	M			
1900	MN	SN	MN	SN
1915	MN			
1930	NO	SO	MNO	SO
1945	NO			
2000	OP	SP	NO	SP
2015	OP			
2030	P	SQ	O	SQ
2045	P	SR		

Table 28. Case designations for convective complex number 5 satellite data.

Time (GMT)	Correlation Case	
	XYT	XY
1830	M	SM
1900	MN	SN
1930	MNO	SO
2000	NO	SP
2030	O	SQ

a. Radar Rain Rates

Table 29 gives the NLP function fits for the radar XYT time lag zero cases which are also plotted in Fig. 54. NLP

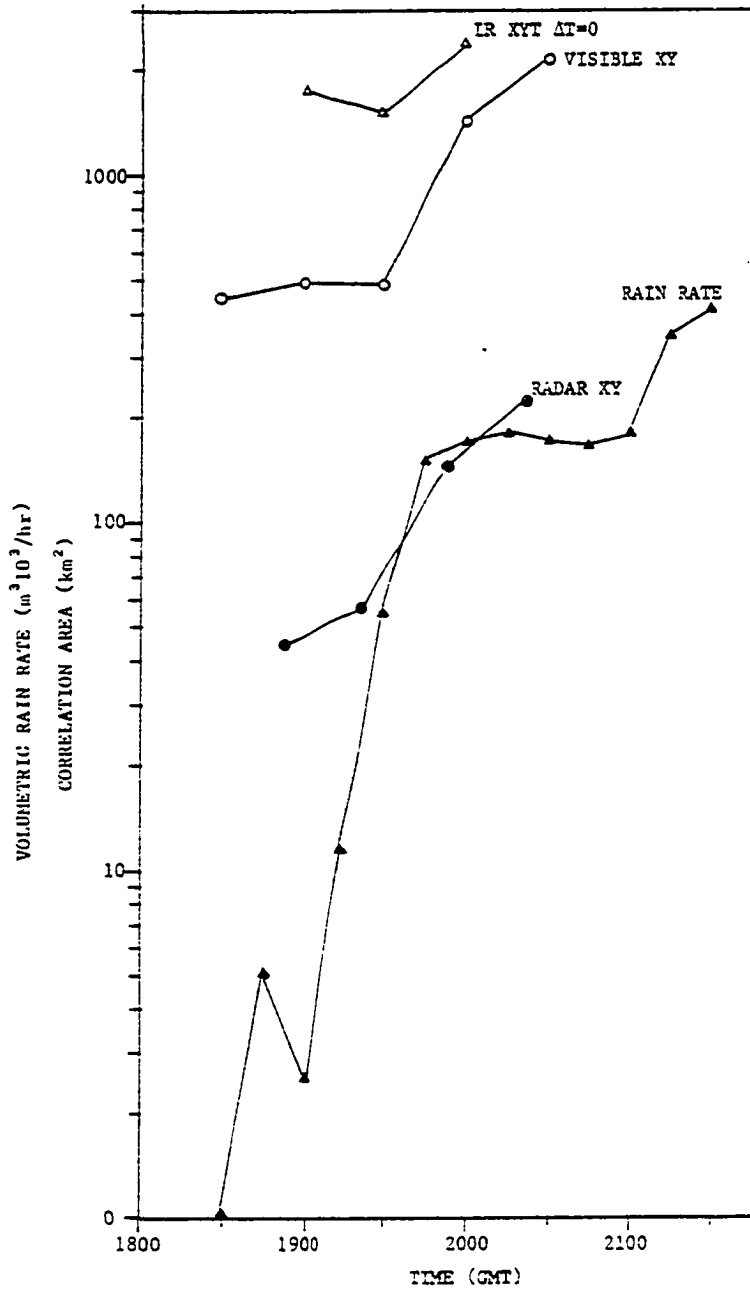


Fig. 53. Plot of rain rates and correlation areas for convective complex 5.

Table 29. Function fits to time lag zero radar XYT auto-correlation fields for complex number 5. (see pages 44 and 45)

CASE XYT ($\Delta t=0$)	TIME	σ_{x+}	σ_{x-}	σ_{y+}	σ_{y-}	σ_t	Λ_7	ρ_0	α	ϕ	a	b	A	V	θ
	(GMT)	km	km	km	km	min				($^\circ$)	km	km	km ²	km/hr	($^\circ$)
M		3.8	----	4.4	----	---	0.54	0.50	0.55	38	5.2	2.7	44	----	---
N		4.1	----	6.1	----	---	0.63	0.68	0.68	29	6.8	2.7	57	----	---
O		8.4	----	6.2	----	---	0.41	0.66	0.47	62	9.2	5.6	145	----	---
F		8.6	----	8.4	----	---	0.35	0.66	0.62	3	8.6	8.4	227	----	---

fits for the single time auto-correlation fields were not possible for two reasons: (1) the field was too sparse, and (2) the field was multimodal.

The σ 's indicate that the storm is continuously growing. This is also reflected in the area which is a function of the σ 's. The increase in area appears to lag slightly the increase in rain rate, Fig. 53. As noted earlier this may be due to the time resolution and the "averaging" done in the XYT correlation calculations. This is supported by radar returns for 1902, 1927, and 1957 GMT shown in Fig. 55. As can be seen there is a significant increase in echo area between these times.

The lag zero auto-correlation initially starts increasing with time and then decreases. This decrease occurs while the complex is still growing. The decrease in the lag zero

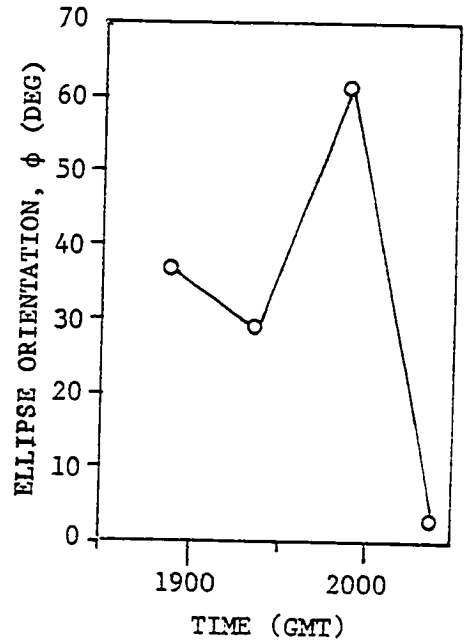
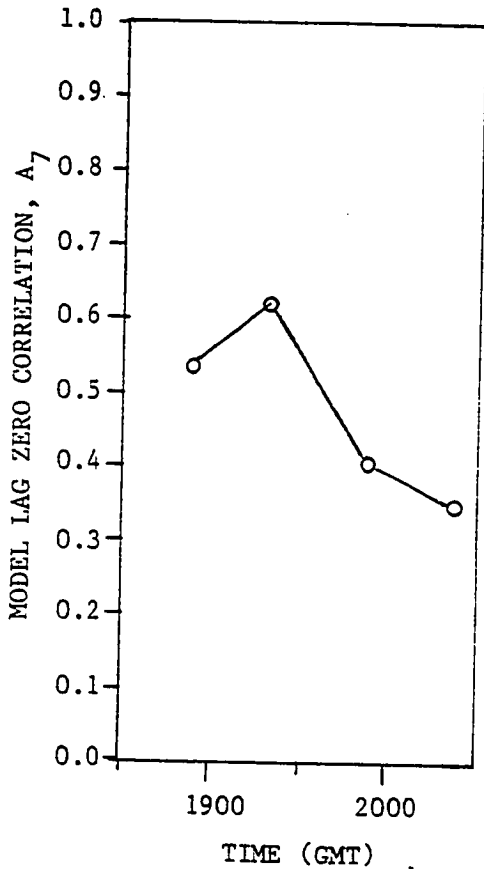
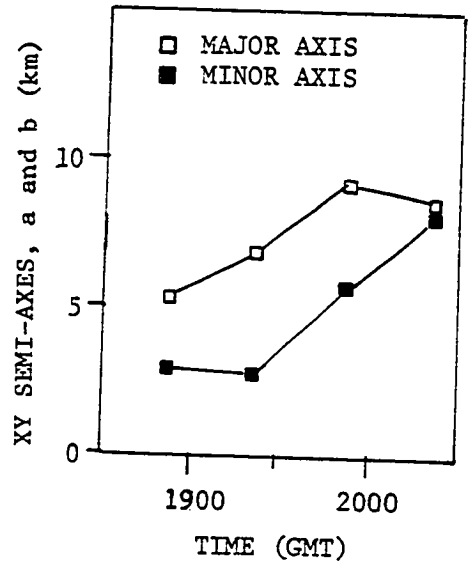
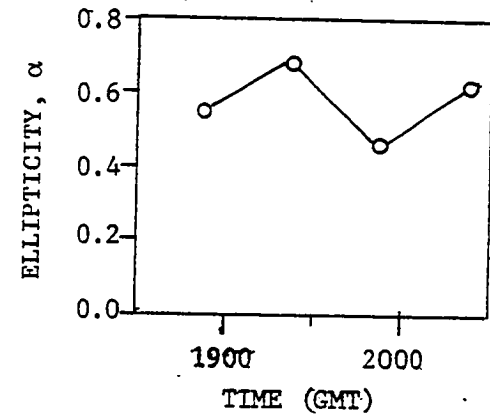


Fig. 54. Plots of model lag zero correlation (A_7), ellipticity, (α), orientation angle (ϕ), and semi-axes of ellipse (a and b) for complex number 5 radar XYT time lag zero model fit.

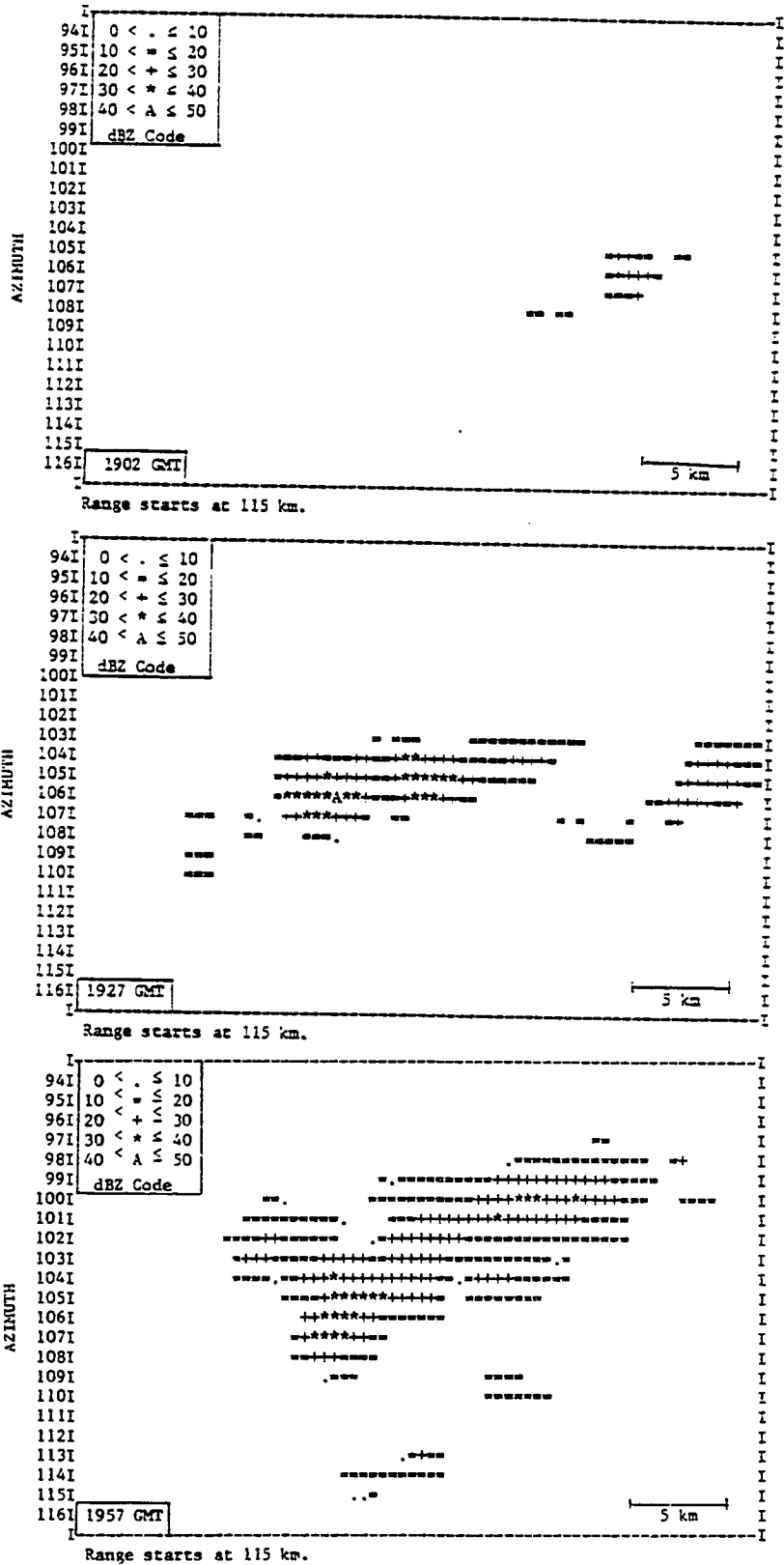


Fig. 55. Radar echo returns for complex number 5 at 1902, 1927, and 1957 GMT.

correlation can be explained by the observation that even though the complex is still growing, it is growing in a fragmented manner as illustrated in Fig. 56.

The changing nature of the radar return is evident in the ellipticity parameter, and the orientation angle of the major axis ϕ . These parameters reflect the development of new rain areas at varying locations around the existing rain areas.

b. Visible Reflectance

The results of the NLP function fits are given in Table 30 and plotted in Figs. 57 to 58. The direction of motion, θ , as determined by the XYT function fits agrees with estimated directions obtained from subjective analysis of plots of the brighter areas. The visible cloud top initially appears to move north-northwest and then begins turning toward the north-northeast. The σ 's for the single time XY correlation functions indicate the increasing size of the visible cloud top. The growth though is better illustrated in the growth of the semi-axes of the correlation ellipse. Other than for the kink at 1900 GMT there is a general increase in the size of the semi-axes. This kink is also evident in the σ 's and reflects an actual change in the storm characteristics. Fig. 59 is a plot of the visible fields for 1830, 1900, and 1930 GMT. From the figure the relationship between the raw data and the function parameters is evident. The rapid increase in area lags the rapid increase in rain rates; however, this apparent lag again appears to be due to the time

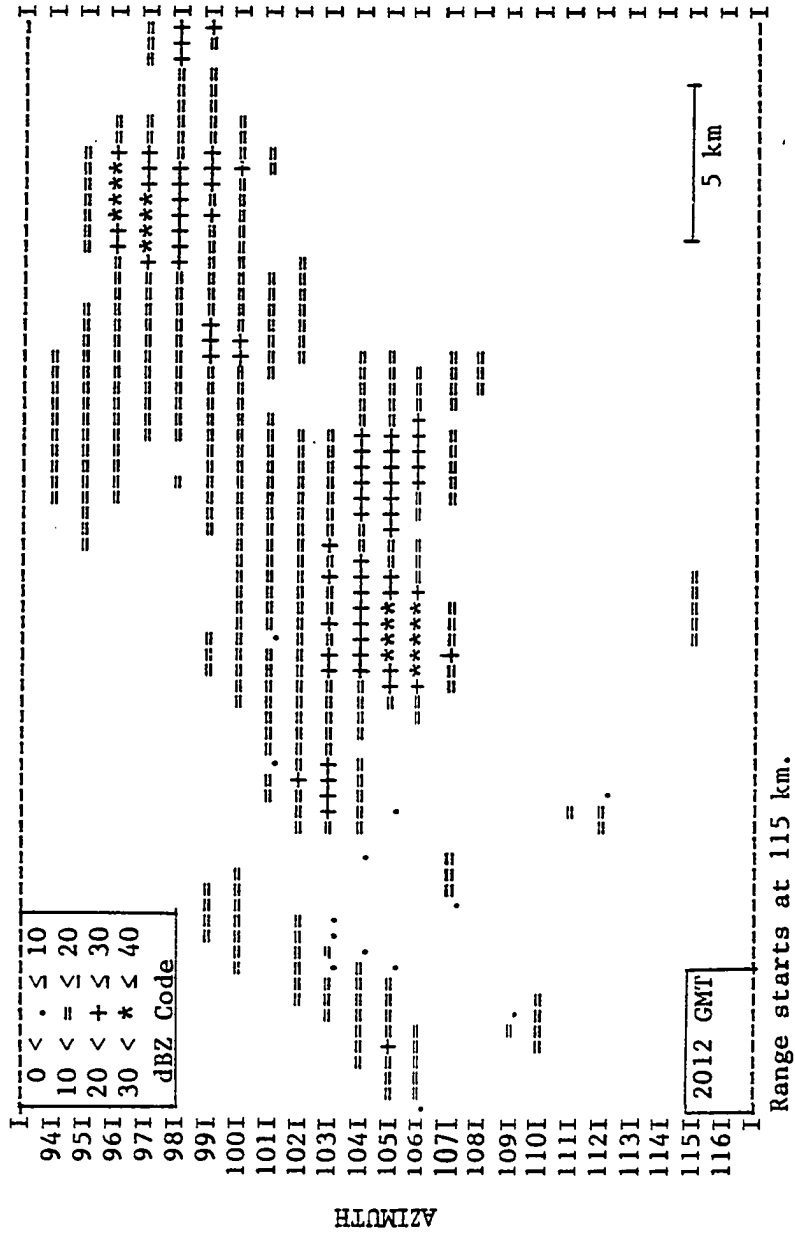


Fig. 56. Radar return for 2012 GMT.

resolution of the satellite imagery.

The lag zero correlation, A_7 , displays the same behavior as the corresponding parameter for the radar. It initially increases and then decreases. The reason is the same. There are numerous small bright areas surrounding the main bright area which will have the effect of reducing the magnitude of A_7 .

The ellipticity parameter reflects the growth of the anvil with time as it has in the previous storms.

Table 30: NLP function fits for complex number 5 visible correlation fields. (see pages 44 and 45)

	CASE	TIME	σ_{x+}	σ_{x-}	σ_{y+}	σ_{y-}	σ_t	A_7	ρ_0	α	ϕ	a	b	A	V	θ
		(GMT)	km	km	km	km	min				(°)	km	km	km ²	km/hr	(°)
SINGLE TIME XY	SM	1830	10.8	---	13.1	---	---	0.27	0.55	-0.09	-12	13.2	10.7	442	---	---
	SN	1900	23.6	---	6.8	---	---	0.56	0.70	-0.22	94	23.6	6.7	494	---	---
	SO	1930	11.1	---	13.9	---	---	0.76	0.82	-0.14	-16	14.2	10.8	482	---	---
	SP	2000	19.6	---	26.6	---	---	0.66	0.82	0.49	29	29.1	15.6	1429	---	---
	SQ	2030	32.6	---	31.2	---	---	0.44	0.79	0.75	47	42.2	16.1	2128	---	---
XYT ($\Delta t=0$)	M		18.5	---	17.1	---	---	0.49	0.76	0.33	52	20.6	14.6	942	---	---
	N		17.3	---	19.2	---	---	0.53	0.79	0.41	38	21.8	14.0	954	---	---
	O		19.9	---	22.5	---	---	0.55	0.81	0.54	39	26.5	14.2	1181	---	---
XYT	M		20.6	18.6	16.1	15.3	63	0.51	0.76	0.27	64	20.3	14.3	915	23.5	-22
	N		18.1	17.7	18.5	20.2	289	0.47	0.79	0.40	40	22.1	14.4	999	14.3	8
	O		22.6	22.0	22.9	24.2	248	0.53	0.81	0.59	42	28.9	14.6	1328	14.8	23

c. Infrared Temperature

Table 31 gives the results of the NLP function fits to the IR XYT correlation field. Fig. 60 are plots of the function parameters for the time lag zero fit. Function fits were not possible for the single time XY fits because the fields

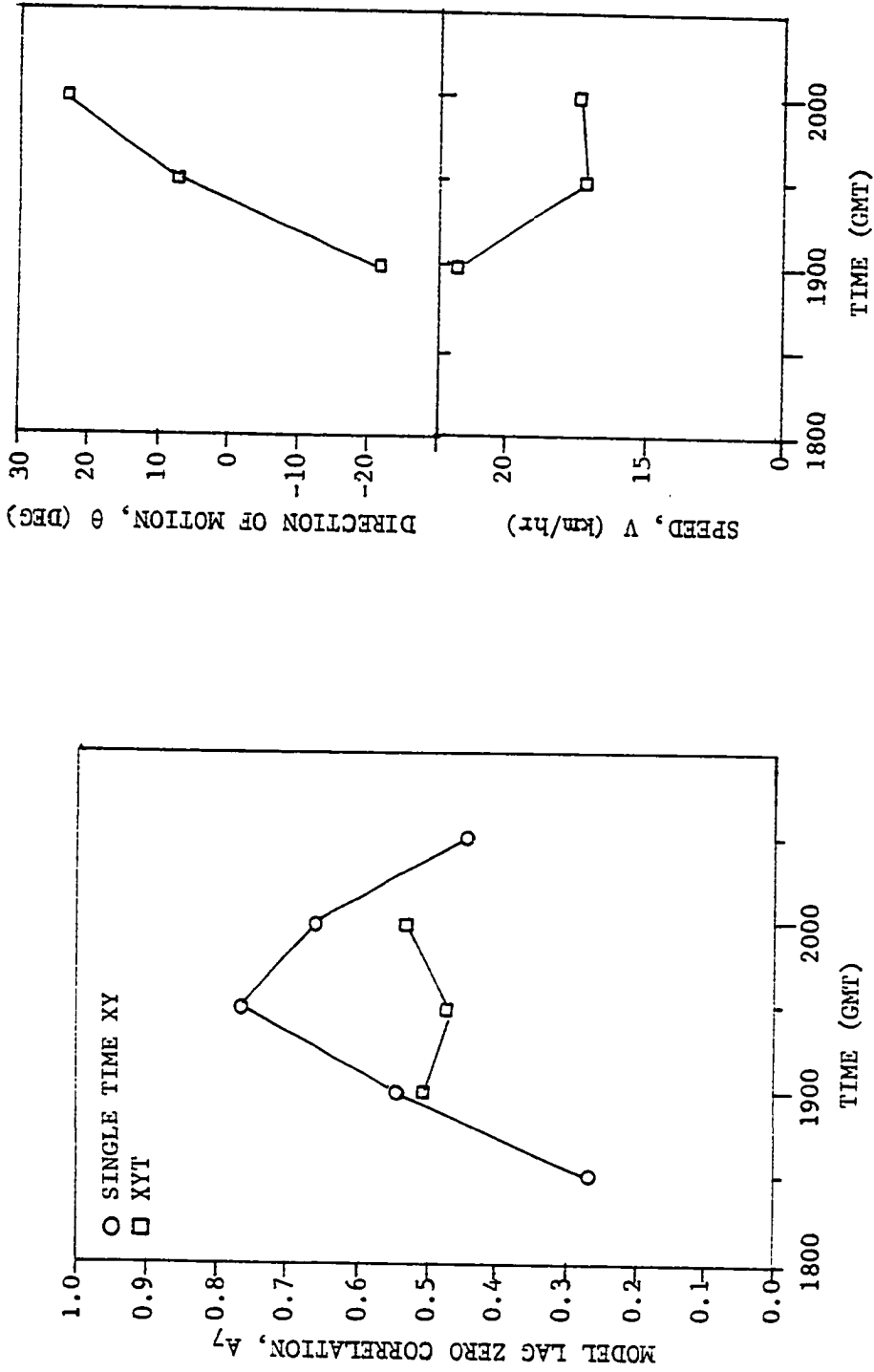


Fig. 57. Plots of model lag zero correlation (A_7), direction of motion (θ), and speed, (V) for complex number 5 visible model fit.

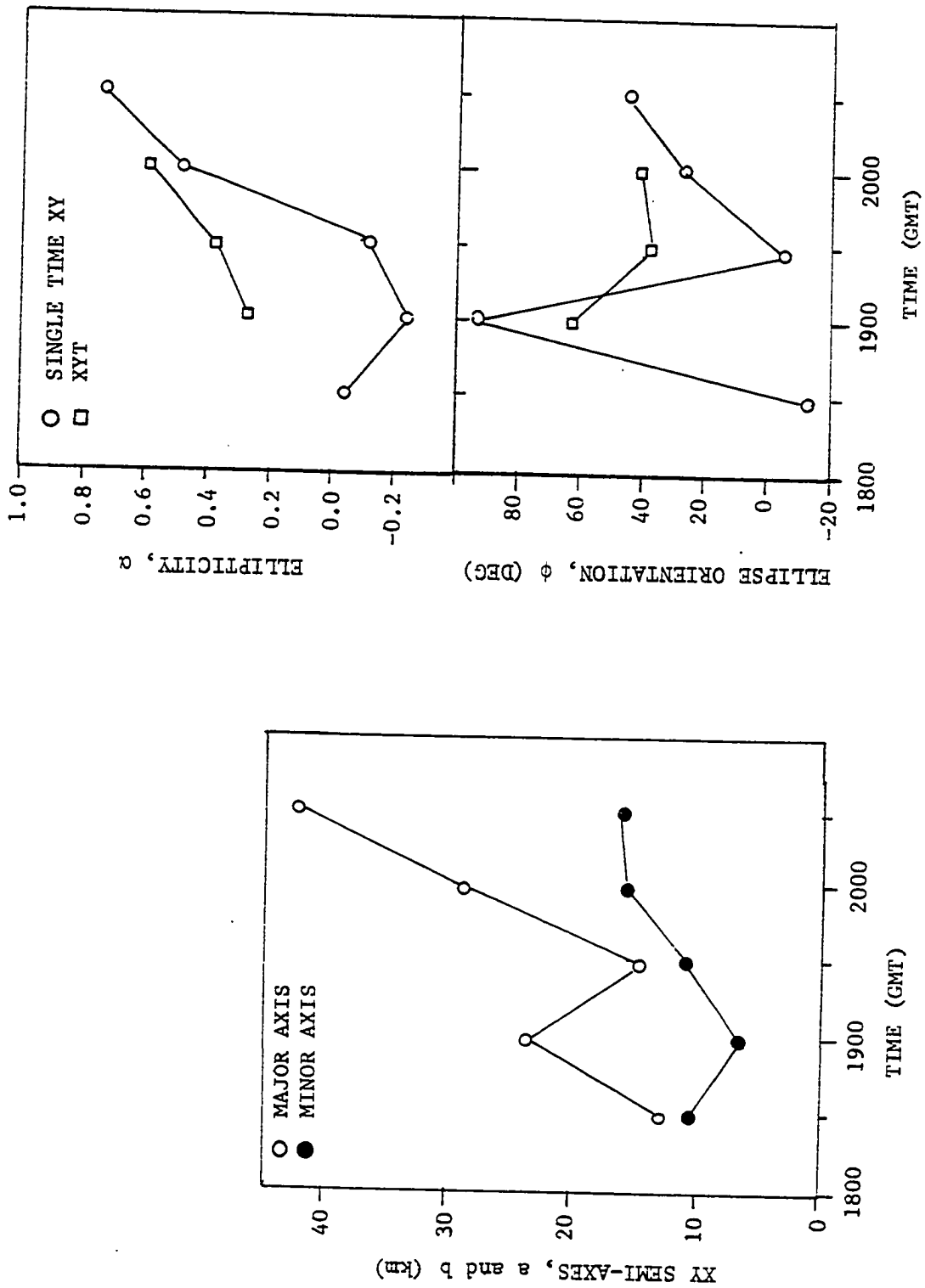


Fig. 58. Plots of ellipticity, (α), orientation angle (ϕ), and semi-axes of ellipse (a and b) for complex number 3 visible model fit.

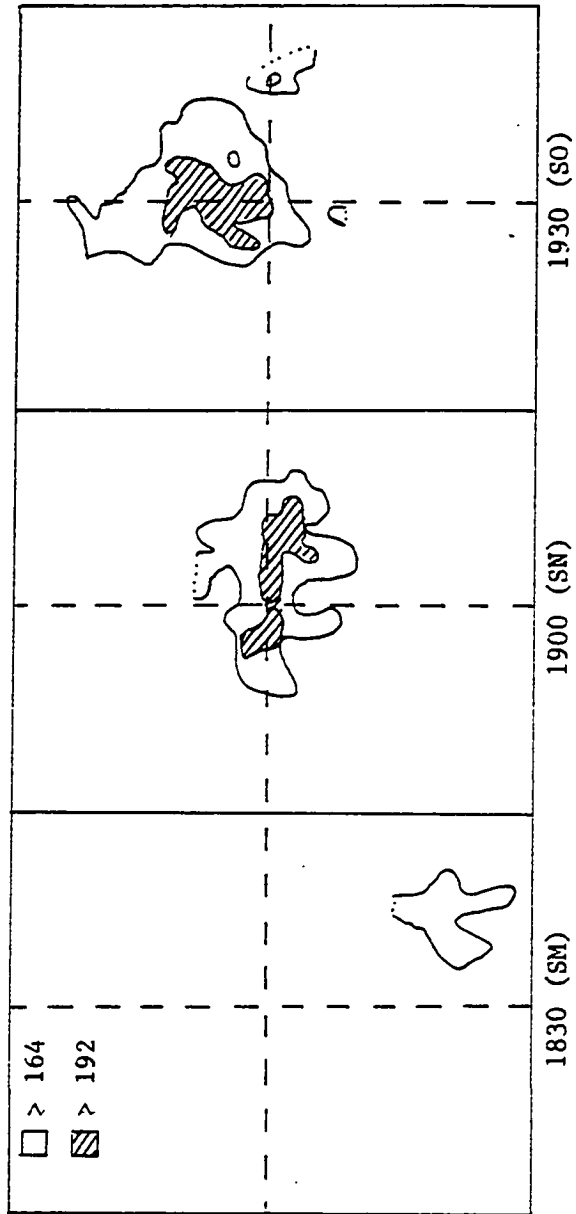


Fig. 59. Plots of complex number 5 visible raw data fields for 1830, 1900, and 1930 GMT (note the grid is fixed in space with time).

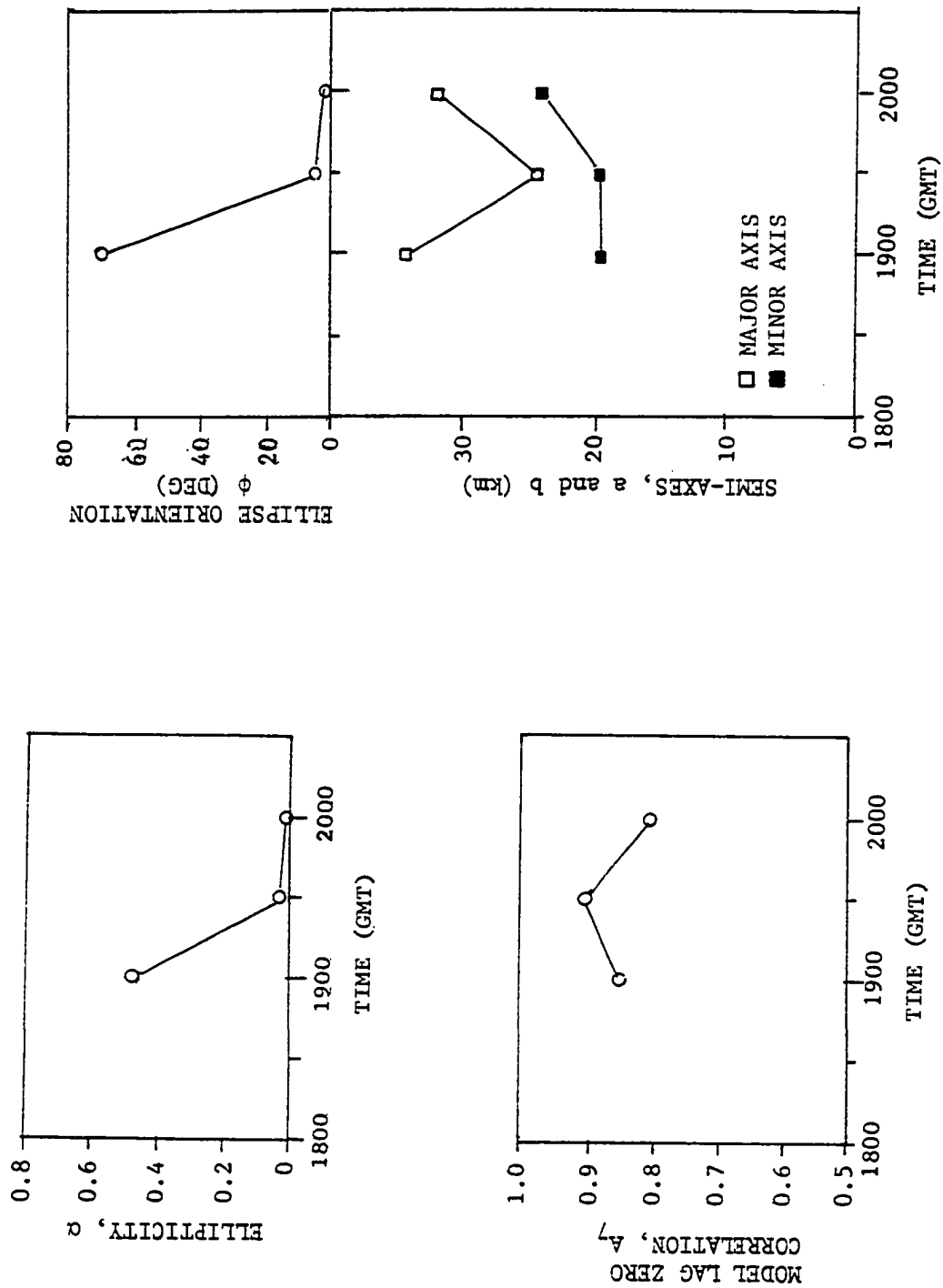


Fig. 60. Plots of model lag zero correlation (A_7), ellipticity (α), orientation of ellipse (ϕ), and semi-axes for complex number 5 IR XYT time lag zero fits.

Table 31. Function fits for IR temperature correlation fields for convective complex 5. (see pages 44 and 45)

CASE	TIME (GMT)	σ_{x+} km	σ_{x-} km	σ_{y+} km	σ_{y-} km	σ_t min	A_1	ρ_0	α	ϕ (°)	a km	b km	A km ²	V km/hr	θ (°)
XYT ($\Delta t=0$)	M	32.8	---	19.1	---	---	0.85	0.88	0.48	70	34.4	20.0	1726	---	---
	N	19.9	---	24.6	---	---	0.90	0.91	0.03	5	24.6	19.9	1538	---	---
	O	23.9	---	32.5	---	---	0.80	0.94	0.02	2	32.5	23.9	2439	---	---
XYT	M	---	---	---	---	---	---	---	---	---	---	---	---	---	---
	N	20.7	20.3	23.2	24.6	87	0.90	0.91	0.06	---	---	---	---	---	-12 [†]
	O	24.1	25.7	32.4	32.4	95	0.76	0.94	0.10	11	24.0	20.4	1537	14.0	62
										10	32.9	24.6	2541	44.0	29

† Estimated

were too sparse. For cases SM, SN, and SO there are so few IR temperatures colder than the threshold of 273°K that no correlation fields could be calculated.

The representative areas found for the fits to the time lag zero XYT correlation fields are plotted in Fig. 53. The time variation of these areas is more marked than the corresponding areas for the visible. The tendency appears to be the same with the areas increasing as the rain rates increase. As has been noted before the representative areas for the satellite data are an order of magnitude greater than the corresponding radar areas.

The direction of motion for the IR is similar to that for the visible except for case N. This discrepancy is probably due to the fact that the colder IR temperatures rapidly expanded eastward from 1300 to 2000 GMT and thereby overwhelmed

any other motion. Note that the direction of motion given for case M is a subjective estimate obtained from the raw XYT auto-correlation fields.

The IR temperature field appears to be much more coherent than the visible and radar data fields. However, the lag zero correlation, A_7 , does exhibit the same behavior as it did in the visible and radar function fits, that of increasing and decreasing.

d. Infrared Temperature Gradient Component

The results of the function fits are given in Table 32. The time lag zero parameters are plotted in Fig. 61. Fits

Table 32. Function fits for IR temperature gradient component correlation fields with threshold of -1000 for complex number 5. (see pages 44 and 45)

	CASE	TIME	σ_{x+}	σ_{x-}	σ_{y+}	σ_{y-}	σ_z	A_7	C_0	α	ϕ	a	b	A	V	θ
		(GMT)	km	km	km	km	min				(°)	km	km	km ²	km/hr	(°)
XYT ($\Delta t=0$)	M		10.4	----	35.5	----	---	0.81	0.62	0.48	9	35.9	9.1	1020	----	---
	N		55.5	----	29.8	----	---	0.68	0.92	-0.72	114	60.0	19.3	3632	----	---
	O		51.8	----	33.4	----	---	0.66	0.90	-0.81	120	59.2	17.3	3216	----	---
XYT	M		DID NOT CONVERGE													
	N		60.4	65.4	31.2	29.8	142	0.65	0.92	-0.74	111	67.3	19.1	4045	7.2	141
	O		57.8	60.8	35.9	35.4	104	0.63	0.90	-0.83	119	67.0	17.4	3667	21.8	79

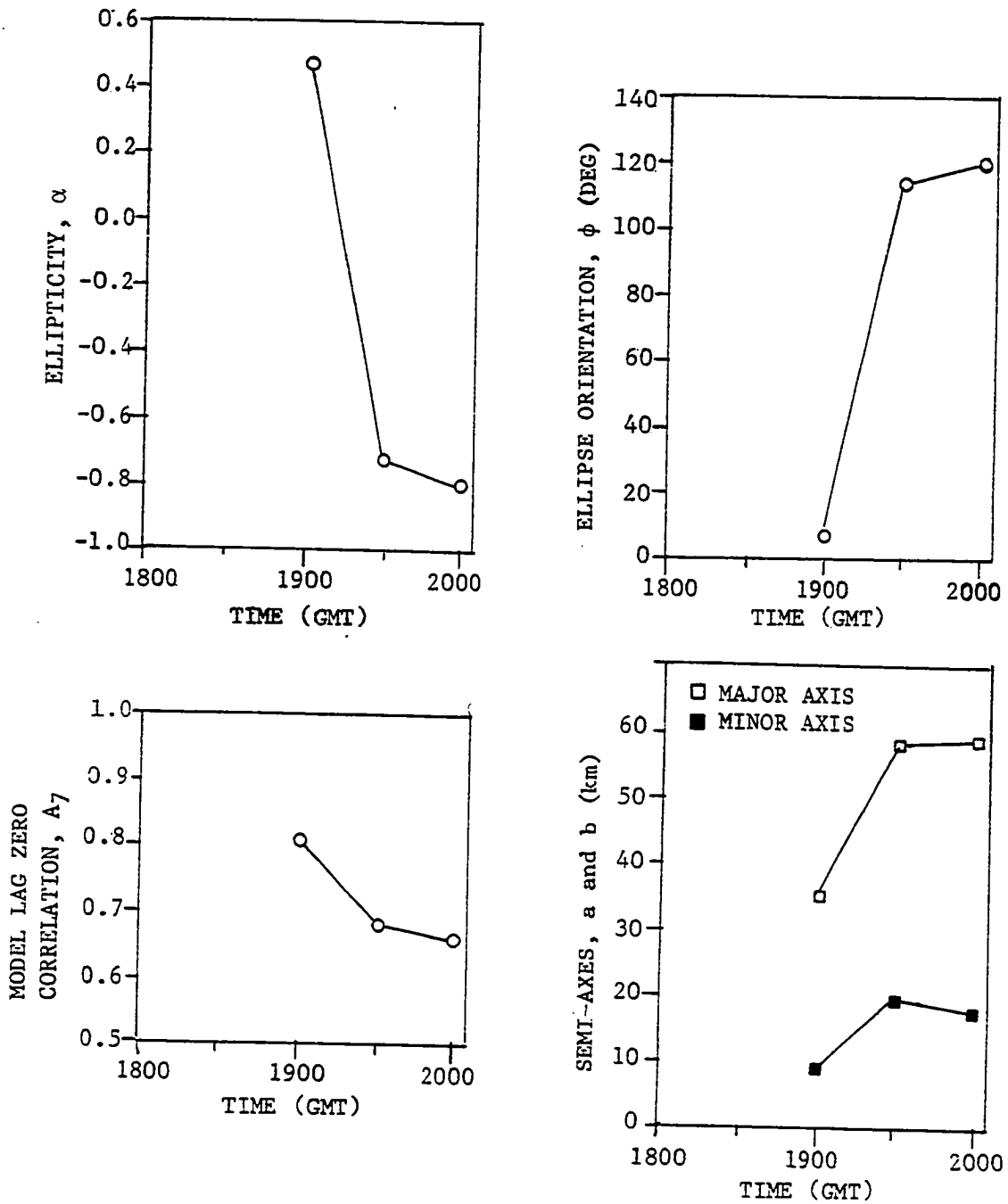


Fig. 61. Plots of parameters for IR temperature gradient component XYT time lag zero function fits with a threshold of -1000.

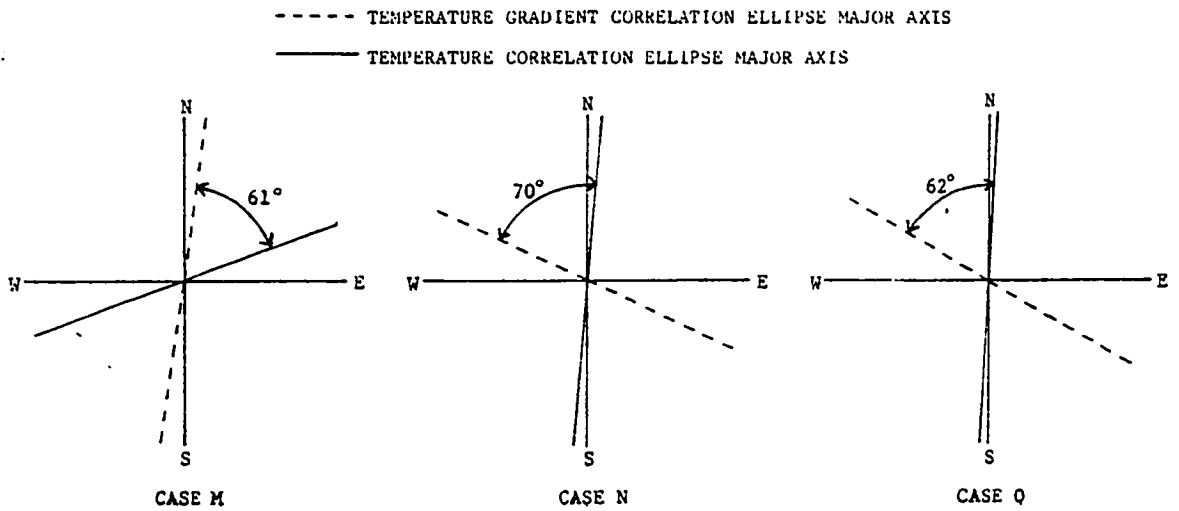


Fig. 62. Plot of major axes of correlation ellipse for IR temperature and IR temperature gradient component.

were only obtainable for cases with a threshold of -1000 because those with a threshold of 0 were too sparse. The temperature gradient component fields are also fairly coherent. However, the lag zero correlation, A_7 , varies in a different manner in that it steadily decreases from a maximum. The orientation of the gradient field with respect to the IR temperature field appears to vary about -65° . This is illustrated in Fig. 62 where the major axes of the two fields are plotted.

e. Infrared Temperature Cross Visible Reflectance

The NLP fits for the XYT time lag zero cross-correlations are listed in Table 33. The parameters determined in the fits

are plotted in Fig. 63. Function fits were not obtained for the single time cross-correlations because, other than for cases SO and SQ, the fields were either nonexistent or too sparse.

Table 33. Function fit for IR temperature cross visible reflectance XYT time lag zero correlation fields. (see pages 44 and 45)

	CASE	TIME (GMT)	σ_{x+}	σ_{x-}	σ_{y+}	σ_{y-}	σ_t	A_7	ρ_0	α	ϕ	a	b	A	V	θ	d	γ
			km	km	km	km	min				(°)	km	km	km ²	km/hr	(°)	km	(°)
XYT (dt=0)	M		13.1	31.2	11.6	14.5	---	0.58	0.60	0.21	80	22.4	12.6	889	---	---	4.2	15
	N		17.4	23.0	18.6	20.4	---	0.55	0.60	0.36	48	23.2	15.9	1157	---	---	8.8	24
	O		19.9	21.8	27.1	13.5	---	0.50	0.50	0.23	48	22.9	18.0	1292	---	---	2.2	168

There appears to be significant cross-correlation present between IR temperature and visible reflectance. The magnitude of the correlation is approximately the same as for complex number two and larger than those for complex number three. I feel that this is remarkable considering the difference in the shape of the IR and visible data fields.

The maximum cross-correlation does not always occur at time lag zero. Table 34 lists the maximum correlations for time lags -1, 0, and +1 for all cases. Notice that the maximum correlation is initially at time lag +1, then at time lag 0, and finally at time lag -1. I feel that this reflects

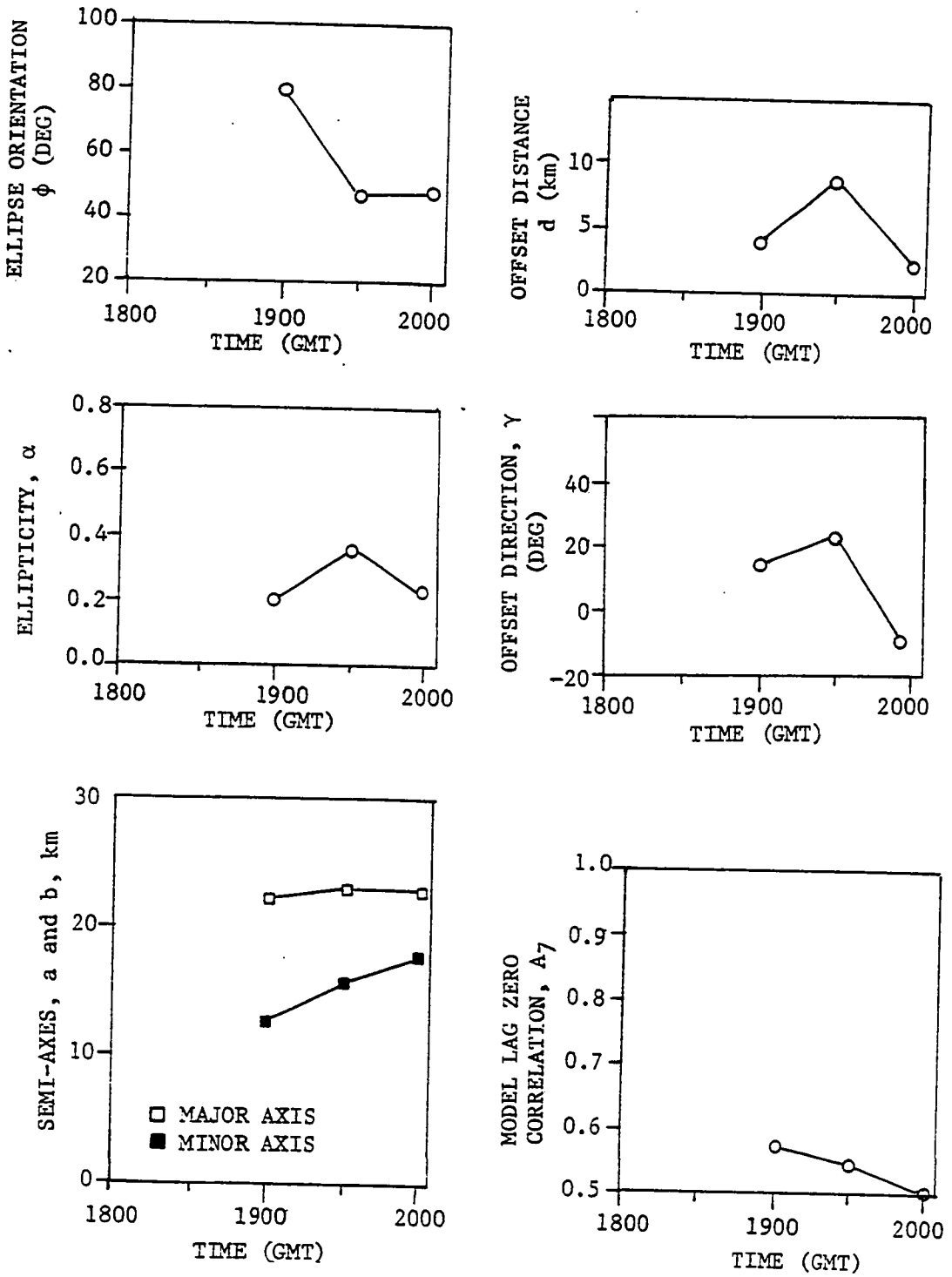


Fig. 63. Plots of model parameters for IR temperature cross visible for complex number 5.

Table 34. Maximum correlations for each case for time lags -1, 0, and +1. (see page 45)

Case	Time Lag		
	-1	0	+1
M	0.569	0.598	0.741
N	0.408	0.595	0.536
O	0.514	0.503	0.445

the developing nature of the storm. Recall that for storm 3 the maximum cross-correlation between the IR and visible occurred at time lag -1 also.

There is an offset present in the cross-correlation and it varies with time. Fig. 64 is another plot of these offset distances and directions. According to the function fits, initially (cases M and N) the IR temperature is most correlated with the visible data to the north, then for case O it is correlated with the visible data slightly to the south. A study of the raw data fields indicates that this variation is due to the changing nature of the IR temperature field. Fig. 65 is a plot of portions of the IR temperature and visible reflectance fields for the last three times. Notice that the visible reflectance does not move as rapidly as does the IR temperature field.

f. Infrared Temperature Gradient Component Cross Visible Reflectance

There is significant cross-correlation between the IR temperature gradient component and visible reflectance. There are multiple maxima. Table 35 is a listing of the single time cross-

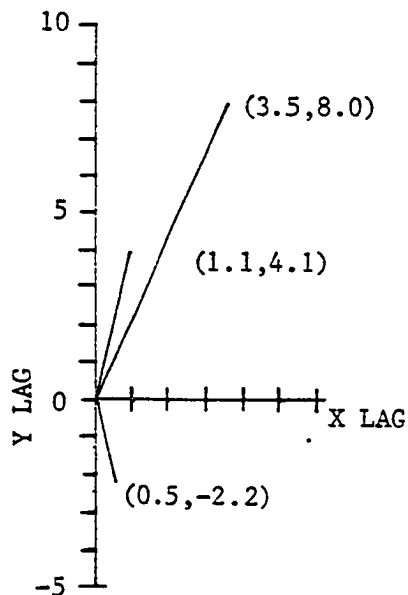


Fig. 64. Plot of maximum correlation offset for IR temperature cross visible reflectancs.

correlation maxima for both thresholds and the lags at which they occur. As can be seen the positions of the maxima move around considerably, and the number of maxima increases with time. This variability is probably a manifestation of the rapid development of the storm.

An examination of the time lag zero XYT raw correlation matrices indicates that the variation of the position of the absolute maximum cross-correlation is beginning to decrease by the end of the period. Table 36 is a listing of the time lag zero XYT maximum cross-correlations and their corresponding

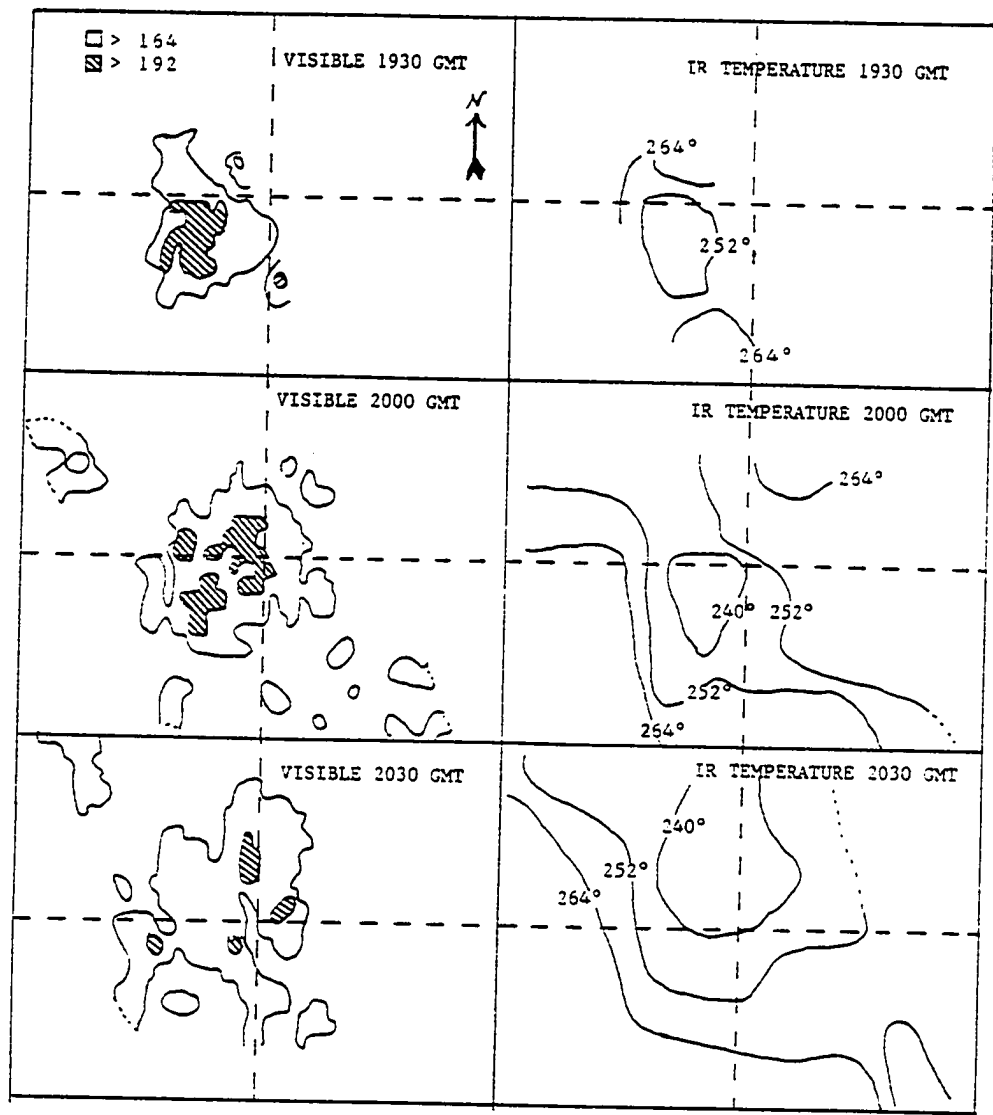


Fig. 65. Plot of IR temperatures and visible reflectance for 1930, 2000, and 2030 GMT.

Table 35. Maximum cross-correlation and corresponding lags for IR temperature gradient component cross visible reflectance.

Case	- 1000		Threshold	
	Maximum Correlation	Lag X Y	Maximum Correlation	Lag X Y
SM	---	---	---	---
SN	0.416	-4,1	0.444	3,0
SO	0.449	0,1	0.558	0,2
SP	0.554	3,2	0.573	3,2
	0.460	-5,3	0.660	0,-5
	0.376	-2,-4	0.630	5,-4
			0.386	-5,4
SQ	0.515	4,1	0.466	4,1
	0.636	-2,7	0.654	2,-6
	0.532	2,-6	0.551	-2,-6
	0.350	-3,3	0.344	-3,-3
			0.482	2,2

lags. Recall that these represent a composite of three single time cross-correlation fields. Note that the maximum cross-correlation composite position is at an X lag of 4 and a Y lag of 1, corresponding to a displacement of 27 km at a heading of 69°. This indicates that at this stage of the storm development the temperature gradient component is most correlated with the visible reflectance 27 km to the east-northeast.

Table 36. Two largest correlations and their corresponding lags for XYT cases for temperature gradient component cross visible reflectance. (see page 45)

Case	-1000		Threshold	
	Maximum Correlation	Lag X Y	Maximum Correlation	Lag X Y
M	0.315	-1,3	0.656	4,3
	0.238	-3,3		
N	0.401	4,1	0.641	4,1
	0.291	-6,-3	0.644	5,1
O	0.362	4,1	0.389	3,1
	0.227	-2,-3	0.397	-2,-3

g. Radar Rain Rates Cross Visible Reflectance

The radar rain rate cross visible reflectance correlation field is also multimodal. This applies to both the XYT and single time XY cross-correlation fields. There appears to be little consistency in the correlation pattern from one case to the next for the single time cross-correlations. Figs. 66 and 67 present the raw cross-correlation matrices and the corresponding product pair count for cases SN to SQ. There is no matrix for case SM because there was insufficient data for this time. Notice that not only do the patterns change shape but they both move around. As previously discussed, any misnavigation present will not change the correlation pattern but will only change its position. It is felt the changing patterns merely reflect the changing nature of the storm.

This changing nature is reflected in Figs. 68 and 69 where the corresponding radar rain areas and bright areas are shown individually and then overlayed for cases SO and SP, respectively. Notice that the rain area as depicted by the radar changes markedly in the 30 minutes separating the cases. The rain areas closely match up with the higher reflectance (brighter) areas. A study of the figures suggests the source of the correlation patterns. For example, in the correlation field for case SP the central maximum is 1 lag east (3 km) of lag zero. In Fig. 69 one can see that the center of the southernmost highest reflectance lies just east of the center of the southwest end of the radar rain area. It is then noted

CASE SN											
X LAG											
-5 0 +5											
Y LAG	+5	0.000	0.000	0.000	0.000	0.000	0.000	0.000	0.000	0.000	0.000
		0.000	0.000	0.000	0.000	0.000	0.000	0.000	0.000	0.000	0.000
		0.048	0.445	0.461	0.004	-0.181	-0.571	0.000	0.000	0.000	0.000
		-0.069	-0.147	-0.324	-0.288	-0.259	-0.635	-0.578	0.000	0.000	0.000
		0.291	-0.097	-0.329	-0.216	0.129	-0.382	-0.556	0.000	0.000	0.000
	0	0.278	0.397	0.309	0.338	0.335	0.139	-0.266	-0.123	0.000	0.000
		0.501	0.349	0.449	0.416	0.439	0.429	0.100	0.004	0.000	0.000
		0.125	0.193	0.375	0.252	0.251	0.348	0.461	-0.075	-0.168	0.000
		-0.466	-0.343	0.225	0.400	-0.342	0.012	0.008	-0.186	-0.090	0.000
		0.139	-0.023	0.041	0.063	-0.305	-0.402	-0.235	-0.253	0.019	0.000
	-5	0.341	0.247	0.076	-0.311	-0.453	-0.517	-0.371	0.170	0.468	0.532
CORRELATIONS											
Y LAG	+5	17	14	19	15	18	18	15	9	6	6
		35	35	37	39	36	36	35	34	30	19
		57	54	48	47	47	44	44	40	34	28
		77	75	78	73	74	66	41	44	39	30
	0	81	84	82	85	85	80	50	41	41	31
		78	80	85	83	86	94	61	42	42	36
		77	83	83	91	73	78	79	44	42	42
		80	74	82	77	86	84	82	60	39	40
		53	63	75	80	78	77	75	64	23	15
		43	41	52	50	48	44	51	32	11	7
	-5	37	40	35	38	25	19	26	10	14	5
NUMBER OF PAIRS											

CASE SO											
X LAG											
-5 0 +5											
Y LAG	+5	-0.320	-0.195	0.007	0.206	0.217	0.045	-0.146	-0.390	-0.180	0.061
		-0.545	-0.354	-0.193	0.213	0.357	0.203	0.015	-0.250	-0.399	-0.395
		-0.366	-0.466	-0.266	-0.056	0.293	0.307	0.173	0.005	-0.140	-0.267
		-0.432	-0.400	-0.160	0.026	0.247	0.310	0.259	0.132	0.004	-0.226
	0	-0.441	-0.426	-0.096	0.014	0.288	0.333	0.232	0.100	-0.055	-0.291
		-0.451	-0.239	-0.282	0.135	0.215	0.268	0.229	-0.002	0.067	-0.048
		-0.260	0.020	-0.081	0.220	0.198	0.310	0.300	0.142	0.115	-0.173
		-0.218	-0.053	-0.013	0.063	0.174	0.179	0.101	0.039	-0.202	-0.315
		-0.350	-0.057	0.161	0.095	0.111	-0.090	-0.165	-0.255	-0.141	-0.096
		-0.340	0.072	0.258	0.100	0.073	-0.290	-0.303	-0.289	-0.058	-0.054
	-5	-0.467	0.056	0.286	0.106	0.208	-0.042	-0.060	-0.138	-0.030	-0.316
CORRELATIONS											
Y LAG	+5	718	822	862	811	781	689	616	481	361	225
		645	737	827	905	838	779	712	572	440	297
		581	737	827	847	882	812	768	651	508	366
		559	683	830	890	916	887	797	721	568	435
	0	556	710	922	926	935	914	843	754	657	491
		527	684	808	930	980	950	869	795	699	565
		525	559	759	868	933	962	926	830	742	605
		427	553	657	811	950	975	927	844	729	643
		302	442	505	767	876	929	868	794	691	647
		224	348	504	536	707	755	745	701	639	606
	-5	154	253	328	388	500	564	628	601	634	647
NUMBER OF PAIRS											

66. Cross-correlation fields and product pair matrices for radar rain rates cross visible for cases SN and So.

		CASE SP												
		X LAG												
		-5 0 +5												
Y LAG	+5	-0.199	-0.207	-0.216	-0.112	0.205	0.261	0.171	0.134	0.184	0.290	0.353	CORRELATIONS	
		-0.198	-0.142	-0.135	-0.078	0.129	0.223	0.205	0.207	0.216	0.264	0.294		
		-0.128	-0.110	-0.058	0.002	0.085	0.197	0.215	0.257	0.233	0.235	0.214		
		-0.115	-0.167	-0.056	0.066	0.007	0.185	0.190	0.260	0.271	0.228	0.151		
		-0.160	-0.177	-0.083	0.050	0.006	0.187	0.210	0.257	0.237	0.156	0.137		
	0	-0.231	-0.123	-0.043	0.004	-0.026	0.186	0.275	0.251	0.144	0.031	0.041		
		-0.234	-0.156	-0.046	-0.049	0.029	0.119	0.216	0.147	0.060	-0.106	-0.052		
		-0.135	-0.116	-0.219	-0.153	-0.126	-0.023	0.089	0.068	0.021	-0.006	-0.028		
		-0.075	-0.213	-0.369	-0.193	-0.159	-0.097	0.012	0.032	0.017	0.084	-0.049		
		-0.088	-0.249	-0.297	-0.175	-0.145	-0.228	-0.077	0.022	-0.094	-0.041	0.017		
Y LAG	-5	-0.235	-0.180	-0.124	-0.136	-0.059	-0.187	-0.100	-0.091	-0.224	-0.048	0.056	CORRELATIONS	
		807	848	970	989	1038	1042	1047	1038	1051	1042	1019		
		783	865	964	1032	1059	1068	1069	1059	1076	1079	1043		
		786	892	984	1059	1049	1079	1068	1077	1083	1062	1062		
		808	917	978	1064	1056	1053	1085	1072	1071	1074	1033		
		826	882	965	1011	1056	1079	1065	1077	1049	1067	1042		
	0	807	871	942	1006	1054	1082	1072	1066	1075	1059	1053		
		768	866	943	991	1045	1065	1089	1075	1084	1064	1068		
		732	872	926	991	999	1030	1049	1040	1059	1036	995		
		714	836	922	960	971	1012	1001	1006	991	946	908		
Y LAG	+5	667	788	884	941	964	994	977	969	911	893	873	NUMBER OF PAIRS	
		607	730	826	913	941	943	933	909	887	842	855		

		CASE SQ												
		X LAG												
		-5 0 +5												
Y LAG	+5	0.245	0.382	0.383	0.339	0.236	0.125	0.017	-0.012	0.092	0.246	0.155	CORRELATIONS	
		0.148	0.261	0.326	0.312	0.212	0.077	-0.115	-0.127	0.005	0.133	0.168		
		0.052	0.100	0.175	0.205	0.211	0.076	-0.144	-0.287	-0.222	-0.020	0.009		
		0.164	0.053	0.066	0.084	0.164	0.142	-0.122	-0.339	-0.266	-0.198	-0.095		
		0.164	0.029	-0.029	-0.021	0.071	0.164	0.016	-0.237	-0.276	-0.316	-0.289		
	0	0.022	-0.166	-0.251	-0.185	-0.122	0.022	0.057	-0.134	-0.198	-0.259	-0.290		
		-0.113	-0.204	-0.310	-0.374	-0.324	-0.170	-0.094	-0.124	-0.031	-0.069	-0.123		
		-0.125	-0.046	-0.229	-0.439	-0.333	-0.293	-0.241	-0.108	0.054	0.120	0.017		
		0.018	-0.067	-0.141	-0.243	-0.353	-0.344	-0.328	-0.101	-0.012	0.075	0.020		
		-0.078	-0.075	-0.086	-0.163	-0.279	-0.278	-0.222	-0.113	-0.074	-0.082	0.053		
Y LAG	-5	-0.215	-0.124	-0.046	-0.108	-0.111	-0.123	-0.154	-0.062	-0.143	-0.171	-0.112	CORRELATIONS	
		1636	1656	1684	1675	1677	1658	1632	1564	1426	1292	1135		
		1620	1676	1684	1702	1707	1679	1674	1608	1484	1361	1199		
		1589	1670	1679	1686	1711	1710	1681	1640	1537	1431	1286		
		1555	1648	1669	1712	1706	1704	1700	1644	1614	1479	1342		
		1509	1585	1650	1688	1722	1713	1701	1683	1625	1539	1369		
	0	1455	1570	1639	1694	1696	1719	1707	1683	1610	1537	1377		
		1448	1519	1595	1647	1649	1686	1707	1653	1584	1484	1398		
		1383	1487	1531	1552	1616	1630	1630	1597	1560	1443	1351		
		1318	1420	1457	1465	1542	1570	1556	1549	1486	1424	1365		
Y LAG	+5	1247	1309	1349	1411	1434	1488	1508	1459	1418	1395	1318	NUMBER OF PAIRS	
		1092	1163	1216	1277	1328	1400	1400	1409	1376	1288	1236		

Fig. 67. Cross-correlation fields and product pair matrices for radar rain rates cross visible for cases SP and SQ.

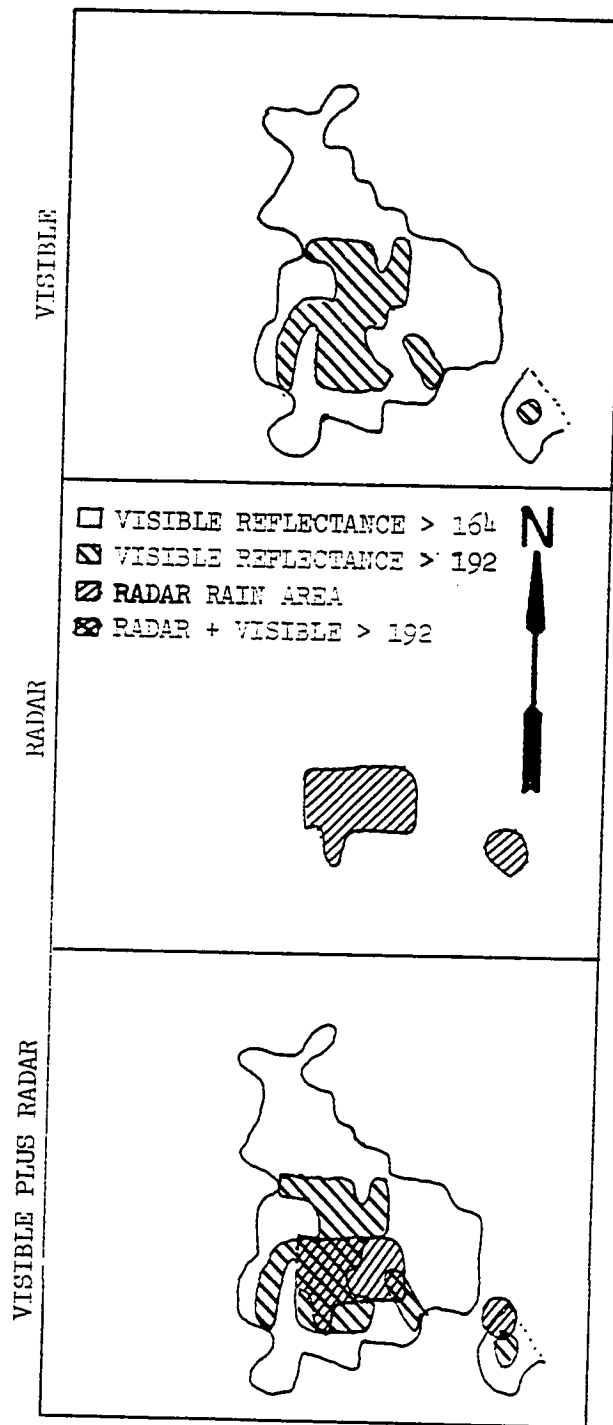


Fig. 68. Plot of radar rain areas and satellite visible reflectance data with count greater than 164 for case S0.

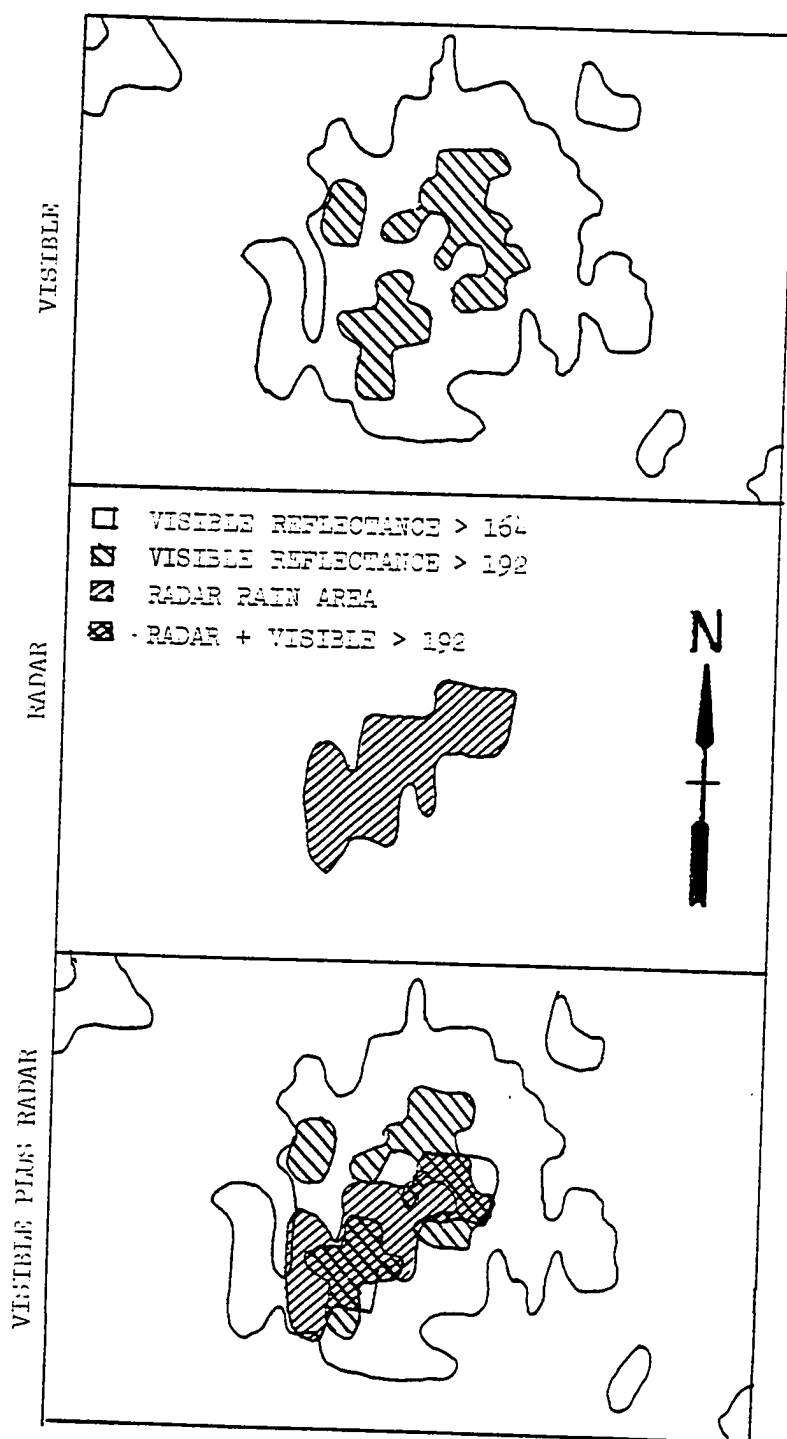


Fig. 69. Plot of radar rain areas and satellite visible reflectance data with count greater than 164 for case SP.

that there are basically two maxima in the correlation field along an approximate heading of northeast. Looking at the figure it is seen that there are two separate areas contained by the highest brightness contour level lying along the same heading. These are what give rise to the two maxima.

h. Radar Rain Rates Cross Infrared Temperature

The radar rain rate cross IR temperature correlation fields are difficult to interpret. This is due partly to the small number of data points in both data fields and in part to the fragmented nature of the complex. The maximum cross-correlations are not as large as for complex number two.

Table 37 gives the maximum cross-correlations for the single time XY fields. There was insufficient data to generate a

Table 37. Maximum single time XY cross-correlations for radar rain rates cross IR temperature. (see page 45)

Case	Cross-correlation
SM	----
SN	****
SO	.295
SP	.259
SQ	.242
**** Not statistically significant.	

field for case SM. Case SN is almost as bad. It has correlations as high as 0.479 but they are not statistically significant. The remaining three cases have significant correlations with magnitudes between 0.2 and 0.3. The location of these maxima varies but the general shape is the same for all three

cases. Fig. 70 shows the single time XY cross-correlation field for case SP. The shape of the positive correlation region is typical of cases SO and SQ even though it is slightly larger than for case SP. The maximum correlation tends to lie along an east-west ridge with a rapid decrease in magnitude to north and south. The high correlations to the upper left are not statistically significant.

i. Radar Rain Rates Cross Infrared Temperature Gradient Component

There appears to be more correlation between the radar rain rates and temperature gradient component than between the radar rain rates and IR temperature. Table 38 gives the maximum correlations for each of the single time XY cross-correlation fields. As this table indicates the correlation fields are multimodal. They also change considerably from case to case. This can be seen more easily in Fig. 71 where the cross-correlation fields for cases SP and SQ for a threshold of -1000 are presented. In this figure negative correlations have been blackened out to emphasize the pattern of the positive correlations. In case SP the general pattern is north-south and in case SQ it is northwest-southeast.

4. Convective Complex Number Six

As with convective complexes three and five, only the early stages of this complex are available. The radar returns indicate in general a multicelled structure with the number of cells increasing with time. Tables 39 and 40 present the

		X LAG											
		-5					0						+5
Y LAG	+5	0.000	0.000	0.000	0.104	0.061	0.060	0.118	0.242	-.034	0.189	0.037	
		0.000	0.000	0.000	0.184	0.055	-.097	0.042	0.187	-.240	0.170	-.293	
		0.000	0.000	0.312	-.254	0.235	0.097	0.062	0.037	0.036	-.044	0.000	
		0.000	-.051	0.080	-.150	-.225	-.234	0.162	-.057	-.420	0.000	0.000	
		0.127	-.131	-.151	-.259	-.078	-.319	0.012	-.203	-.013	0.000	0.000	
		-.335	0.243	-.086	-.124	-.149	-.280	-.024	0.065	-.180	-.029	0.000	
		-.128	0.020	0.058	0.173	-.144	-.026	-.096	-.032	0.270	0.266	0.000	
		-.391	0.278	0.063	0.277	0.085	0.177	0.019	-.235	-.183	0.047	-.385	
		0.000	0.045	-.143	0.175	-.015	0.308	0.055	-.100	-.363	0.231	0.312	
		0.000	-.058	-.249	-.093	-.234	0.248	0.273	-.350	-.143	0.431	0.000	
Y LAG	0	0.000	0.000	0.033	-.018	-.219	-.087	-.059	-.186	0.228	0.340	0.000	
	+5	0	0	0	8	105	346	407	228	71	66	23	
		0	0	0	47	169	291	367	277	118	36	5	
		0	0	44	127	260	297	348	200	86	26	0	
		0	45	135	295	341	386	275	154	51	4	0	
		38	143	284	480	548	459	239	100	70	0	0	
		99	229	457	620	759	578	259	121	64	17	0	
		92	329	567	697	795	691	404	183	64	57	3	
		24	306	572	734	750	683	553	317	143	74	27	
		0	153	490	717	713	621	526	365	253	118	23	
Y LAG	-5	0	34	355	626	725	556	371	242	240	87	0	
		0	3	217	508	608	470	295	150	69	26	0	

CORRELATIONS

NUMBER OF PAIRS

LAG DISTANCE IN X DIRECTION = 8 KM
LAG DISTANCE IN Y DIRECTION = 7 KM

Fig. 70. Radar rain rates cross IR temperature for case SF. Typical of cases SO and SQ.

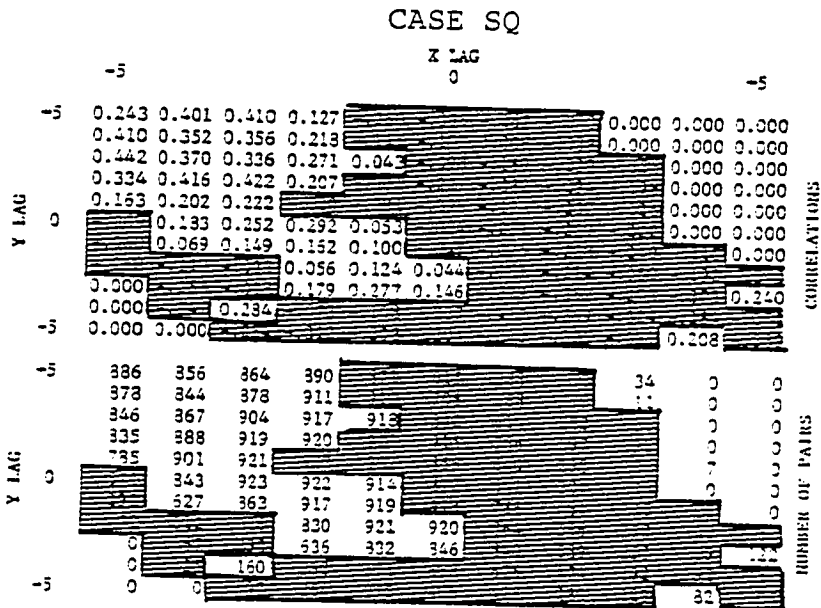
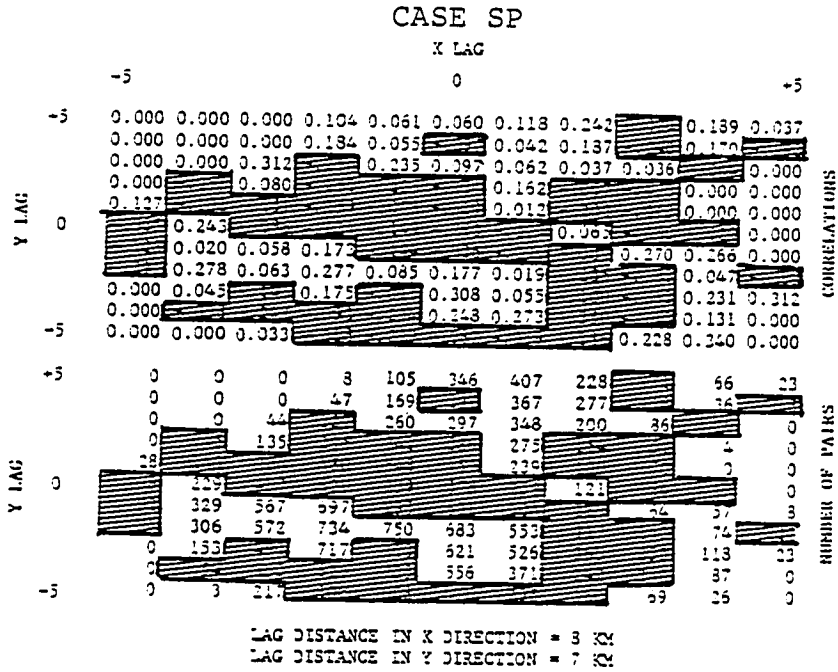


Fig. 71. Single time xy correlation fields for radar cross IP temperature gradient component for cases SP and SQ.

Table 38. Maximum single time XY cross-correlations for radar rain rates cross IR temperature gradient component and corresponding lags for complex number 5. (see page 45)

Case	Cross-correlations Threshold			
	-1000		0	
	Correlation	Lag X Y	Correlation	Lag X Y
SM	----	---	----	---
SN	----	---	----	---
SO	0.321	0, -1	0.316	0, -1
SP	0.263	0, -3	0.308	0, -3
	0.318	2, 5	0.258	2, 5
			0.278	-4, 2
SQ	0.390	0, 0	0.419	0, 0
	0.352	-2, -5	0.450	2, -2
	0.414	2, -2	0.411	-3, 2
	0.415	-3, 2	0.508	-2, -5

case designations for the radar and satellite data, respectively. Note that the radar cross satellite XYT case M is really only the first two times of XYT case N because there was no rain indicated at 2000 GMT by the radar. Also notice that no satellite scan was available for 2200 GMT but was available at 2206 GMT. It was felt that the six minute delay will not be significant. Fig. 72 is a plot of the total storm volumetric rain rates for the period 2015 to 2215 GMT, and the representative correlation areas. Reference will be made to this figure later.

a. Radar Rain Rates

As mentioned above this storm has several cells. This is illustrated in Fig. 73 which is a plot of the radar rain areas at 30 minute intervals. The rain rates inside the contours are all greater than 0.5 mm/hr. By 2200 GMT there are

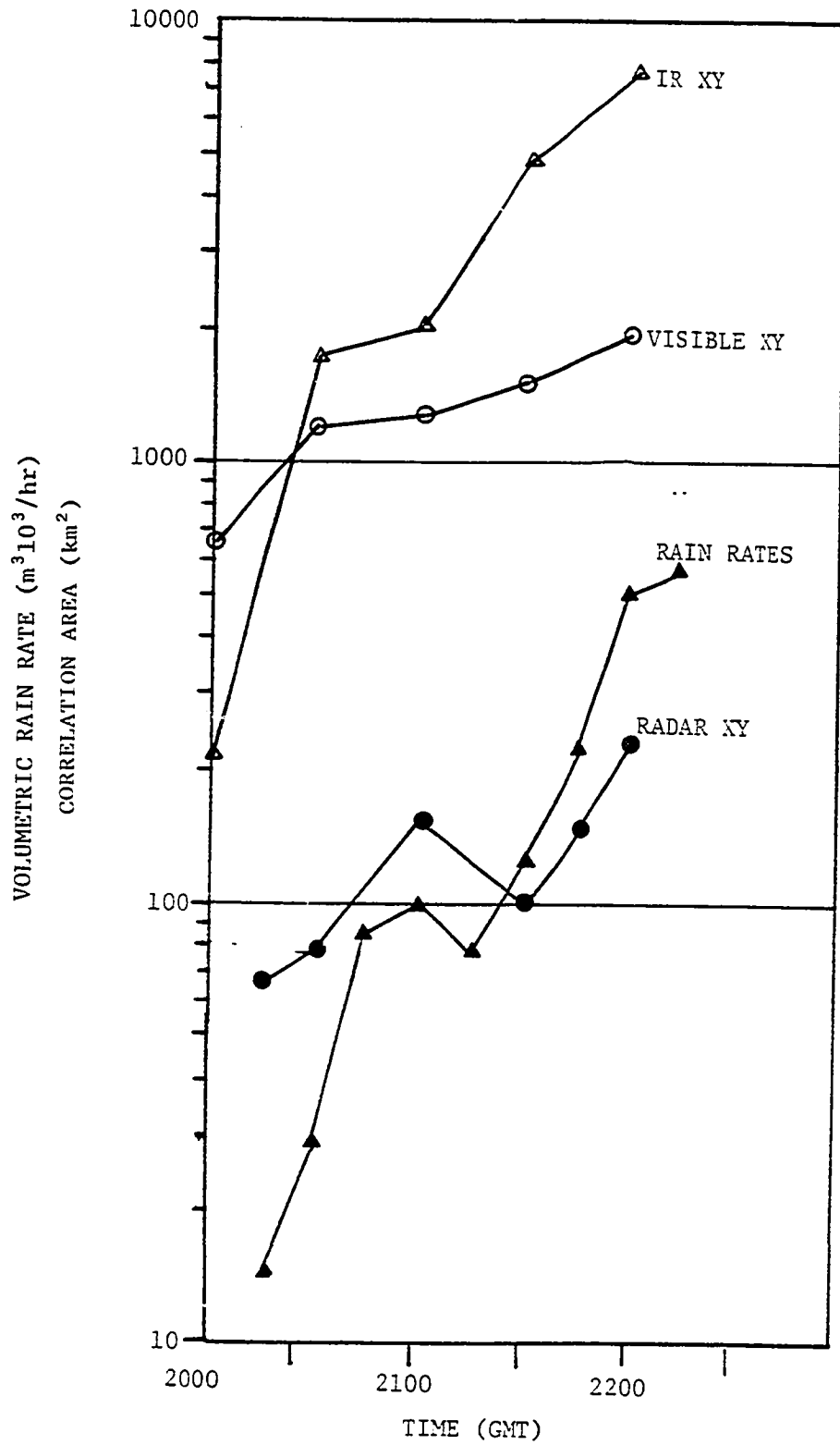


Fig. 72. Plot of volumetric rain rates and representative areas from NLP fits for convective complex number 6.

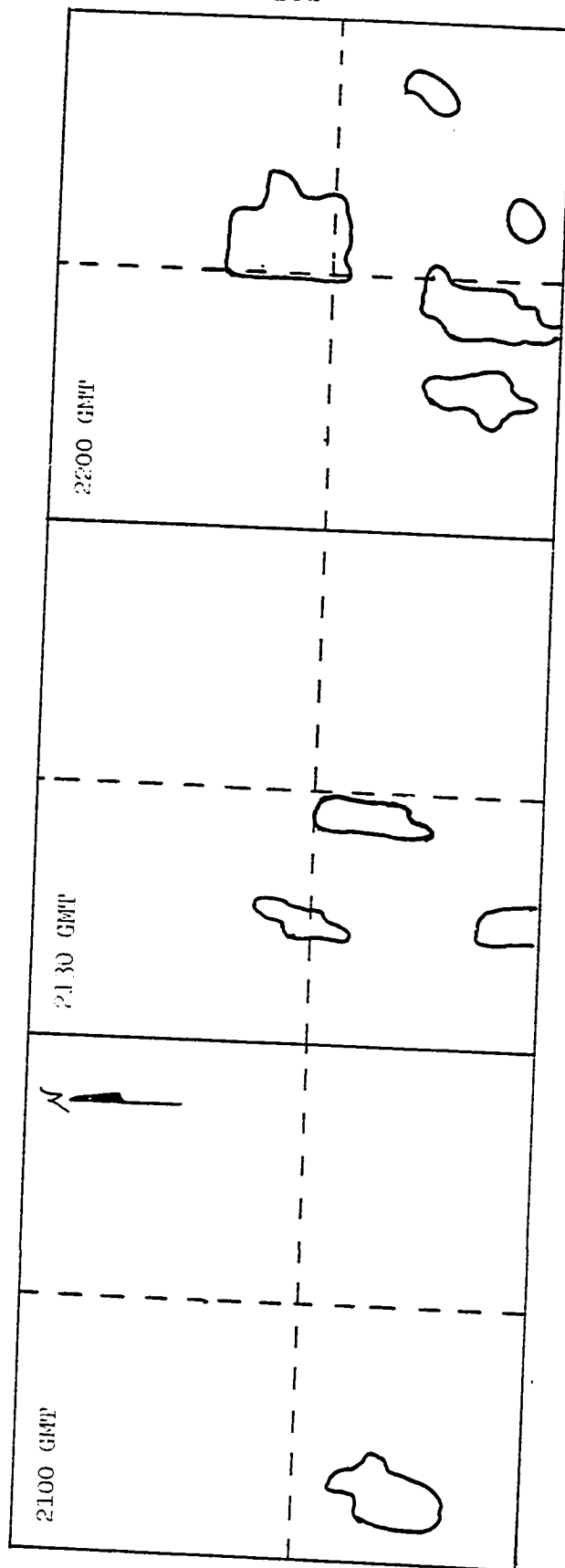


Fig. 73. Plot of radar rain areas for complex number 6.

Table 39. Case designations for convective complex number 6 radar data.

Time (GMT)	Auto-correlation Case		Cross-correlation Case	
	XYT	XY	XYT	XY
2015	M	SM	MN	
2030	MN	SN	MN	SM
2045	MN			
2100	NO	SO	MNO	SN
2115	NO			
2130	OP	SP	NO	SO
2145	OP	SQ		
2200	P	SR	O	SP
2215	P			

at least five separate areas of rain.

The function fits obtained to the raw correlation functions are listed in Table 41 and the parameters are plotted in Figs. 74 to 75. The single time XY correlation σ 's do not indicate any trend but appear to vary randomly. However, the σ 's determined in the XYT fits show more of a trend. The trend is more evident in the plot of the semi-axes of the correlation ellipse. The ellipse starts out fairly elongated ($a/b=3.28$) and becomes more circular with time. The final ratio of major to minor semi-axes (a/b) was 1.17. The lag zero correlation, A_7 , indicates that there is an increase in the noise level with time, i.e., A_7 becomes smaller. This is caused by the developing multicelled nature of the complex. This is the same as it was for complexes three and five. Also, notice in Fig. 72 that the apparent decrease in the representative area follows the decrease in rain rates. This apparent lag is probably due to the difference in time resolution in

Table 40. Case designations for convective complex number 6 satellite data.

<u>Time</u> <u>GMT</u>	<u>Correlation</u> <u>XYT</u>	<u>Case</u> <u>XY</u>
2000	M	SM
2030	MN	SN
2100	MNO	SO
2130	NO	SP
2206	O	SQ

the plotted data as before.

b. Visible Reflectance

As far as the visible reflectance is concerned, this storm starts out fairly unorganized and by the end of the data set becomes well organized. Figs. 76 to 78 are plots of the raw visible reflectance fields. Do recall that the plots are not rectified and, therefore, are distorted (not orthogonal) as previously discussed. As a reference, the prominent deep valley at 2100 GMT runs approximately north-south. At 2030 and 2100 GMT, there are several well developed clouds. By 2130 the westernmost cloud has fairly well dissipated, and there is one major cloud. Fig. 79 is a plot of the objective analysis of the data field at 2030 GMT. The analysis grid is coarser than the raw data; hence some resolution is lost. The two major bright areas are present and the north-south orientation are evident. Table 42 is a listing of the model correlation function parameters as determined using the NLP procedure. The parameters for the XYT and single time XY fits are plotted in Figs. 80 to 81.

Table 41. Parameters of model correlation function for complex number 6 radar. (see pages 44 and 45)

	CASE	TIME (GMT)	σ_{x+} km	σ_{x-} km	σ_{y+} km	σ_{y-} km	σ_z min	A_7	ρ_0	α	ϕ (°)	a km	b km	A km ²	V km/hr	θ (°)
SINGLE TIME XY	SL	2015	4.4	---	8.0	---	---	0.82	0.78	0.80	26	8.8	2.4	68	---	---
	SM	2030	4.1	---	9.5	---	---	0.66	0.76	0.76	19	10.1	2.5	80	---	---
	SN	2100	6.7	---	7.6	---	---	0.76	0.89	0.26	32	8.1	6.1	155	---	---
	SO	2130	4.1	---	8.0	---	---	0.61	0.78	0.27	11	8.1	3.9	100	---	---
	SP	2145	5.9	---	8.5	---	---	0.70	0.89	0.32	20	8.9	5.3	149	---	---
	SQ	2200	10.3	---	7.3	---	---	0.49	0.81	0.21	75	10.5	7.0	232	---	---
XYT ($\Delta t=0$)	L		5.8	---	9.5	---	---	0.69	0.86	0.75	28	10.5	3.4	114	---	---
	M		4.7	---	7.7	---	---	0.80	0.87	0.43	20	8.1	4.0	103	---	---
	N		6.3	---	8.3	---	---	0.65	0.89	0.19	18	8.5	6.1	161	---	---
	O		7.6	---	7.4	---	---	0.56	0.82	0.20	49	8.2	6.7	172	---	---
XYT	L		6.0	6.2	10.5	10.0	114	0.62	0.86	0.77	27	11.4	3.5	125	5.4	213
	M		5.5	5.6	8.8	9.2	50	0.64	0.87	0.45	21	9.4	4.8	141	11.1	36
	N		5.8	6.8	8.3	8.4	62	0.62	0.89	0.27	22	8.7	5.8	159	12.3	29
	O		8.7	9.3	8.0	8.0	135	0.47	0.82	0.11	68	9.2	7.8	225	12.8	55

The lag zero correlations, A_7 , appear to reflect the developing nature of the visible cloud and, more or less, increases with time. This is the opposite of what the radar A_7 parameter did. However, note that the raw lag zero correlations are all fairly high. This can be an indication that the correlation model used may not be the correct model. Fig. 82 shows the raw correlation field for 2100 GMT. Notice how the correlation drops off rapidly at first in the north-south directions, and then drops off more slowly and finally increases without ever passing through zero.

Fitting the model correlation function to this using least squares results in a low value for A_7 because a "flatter" curve fits the overall field better. So this increase in A_7 may be more of an indication that the model becomes more appropriate with time. This is true but notice that the raw

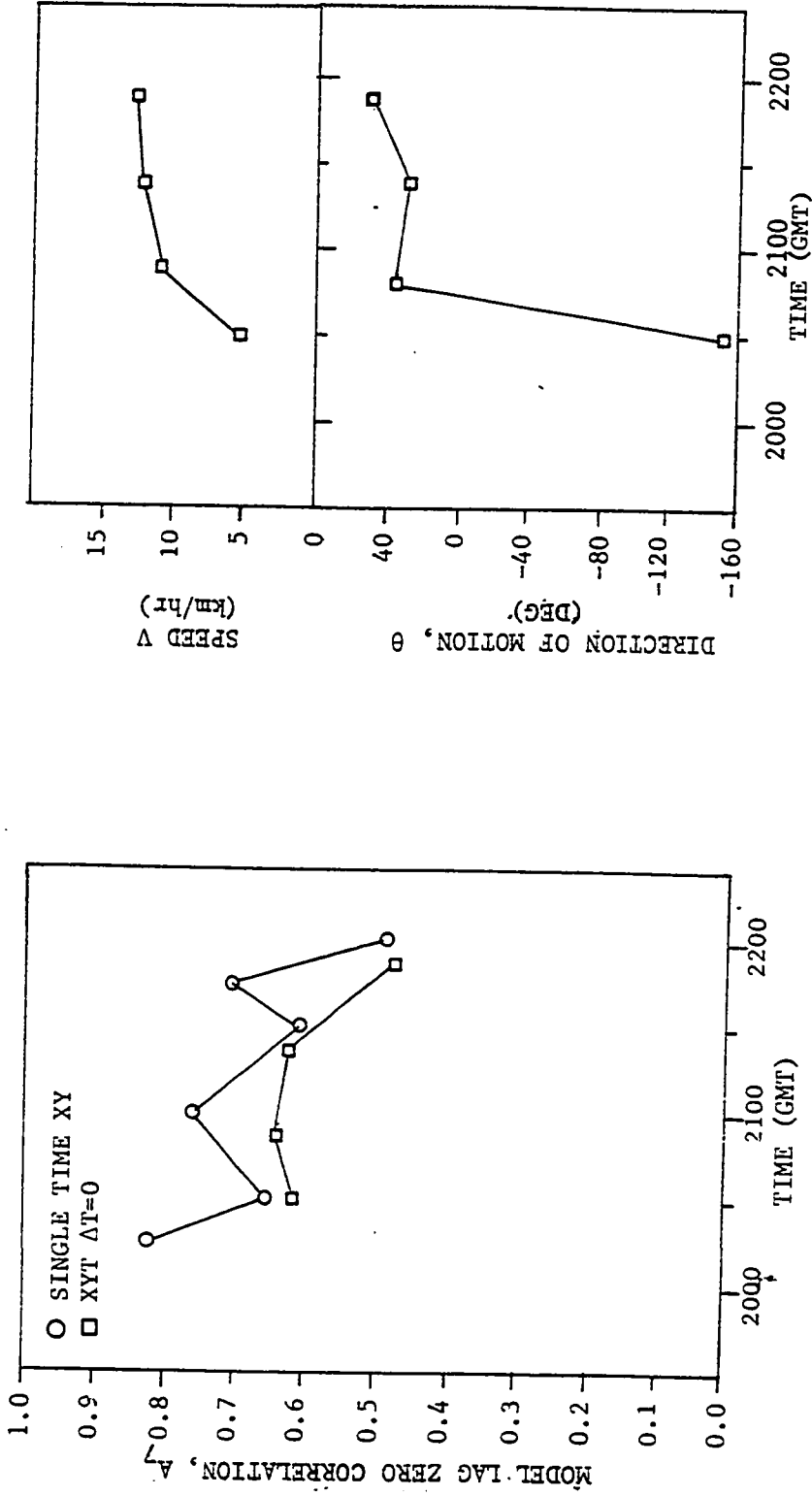


Fig. 74. Plots of model lag zero correlation (A_7), direction of motion (θ), and speed (V) for complex number 6 radar model fits.

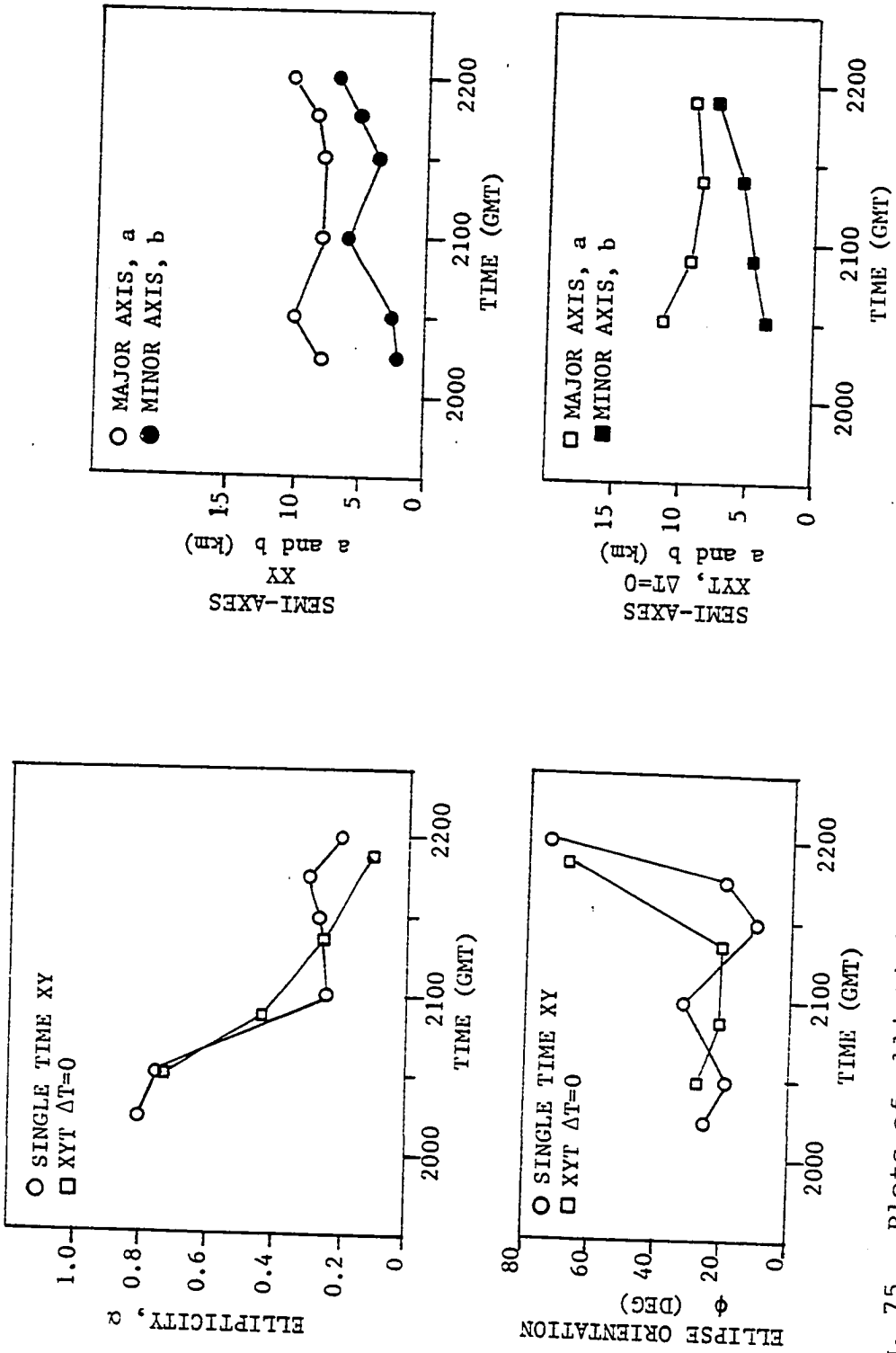


Fig. 75. Plots of ellipticity, (α), orientation angle (ϕ), and semi-axes of ellipse (a and b) for complex number 6 radar model fits.

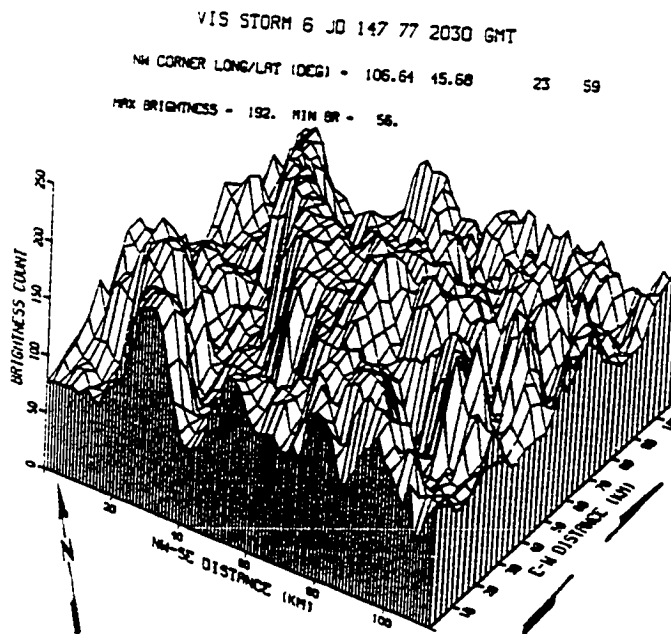
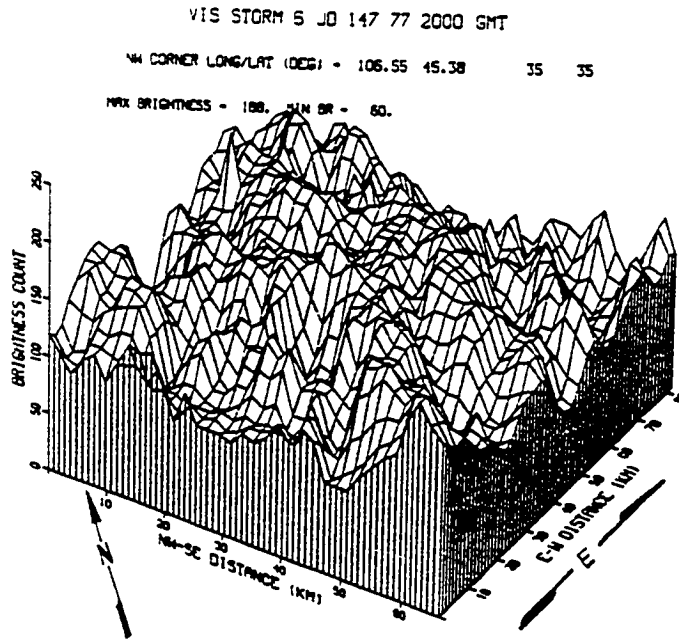
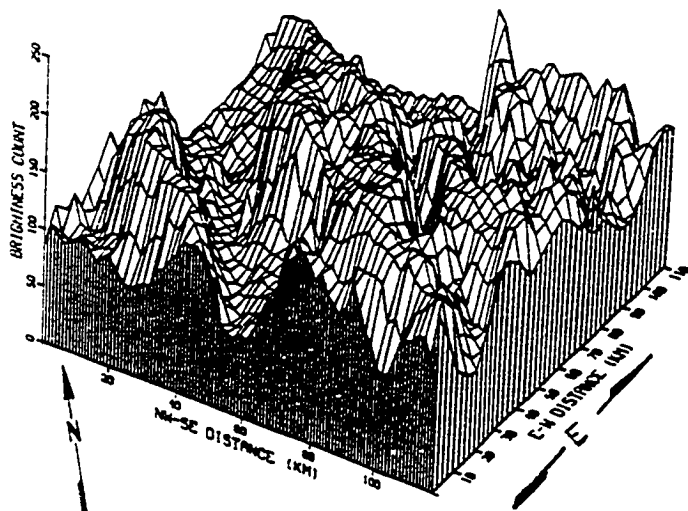


Fig. 76. Plot of complex number 6 raw visible reflectance data field for 2000 and 2030 GMT. (grid not rectified)

VIS STORM 6 JO 147 77 2100 GMT

NW CORNER LONG/LAT (DEG) - 106.56 45.87 24 61

MAX BRIGHTNESS - 192. MIN BR - 42.



VIS STORM 6 JO 147 77 2130 GMT

NW CORNER LONG/LAT (DEG) - 106.52 45.92 25 71

MAX BRIGHTNESS - 192. MIN BR - 18.

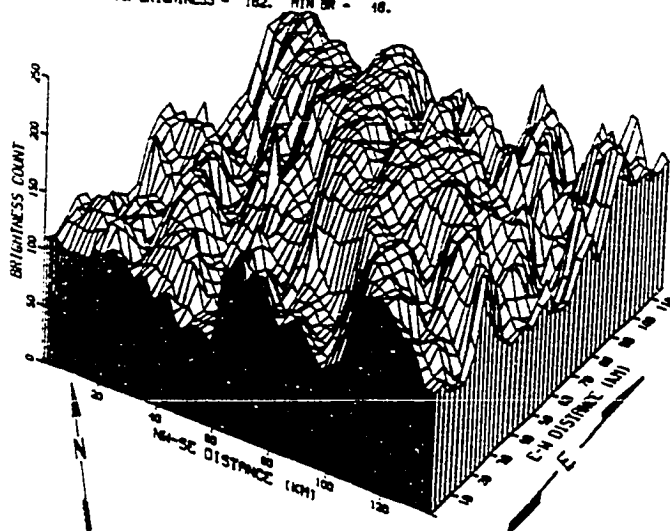


Fig. 77. Plot of complex number 6 raw visible reflectance data field for 2100 and 2130 GMT. (grid not rectified)

VIS STORM 6 JO 147 77 2206 GMT

NW CORNER LONG/LAT (DEG) = 106.49 45.02 34 40

MAX BRIGHTNESS = 180. MIN BR = 45.

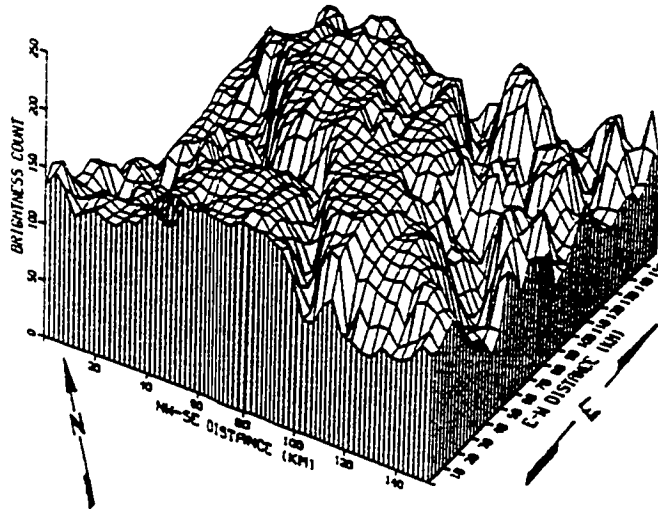


Fig. 78. Plot of complex number 6 raw visible reflectance data field for 2206 GMT. (grid not rectified)

SATELLITE VIS OR SSTORM 6 2030 GMT

NW CORNER LONG/LAT (DEG) = 106.70 45.74 20 20

MAX BRIGHTNESS = 180. MIN BR = 0.

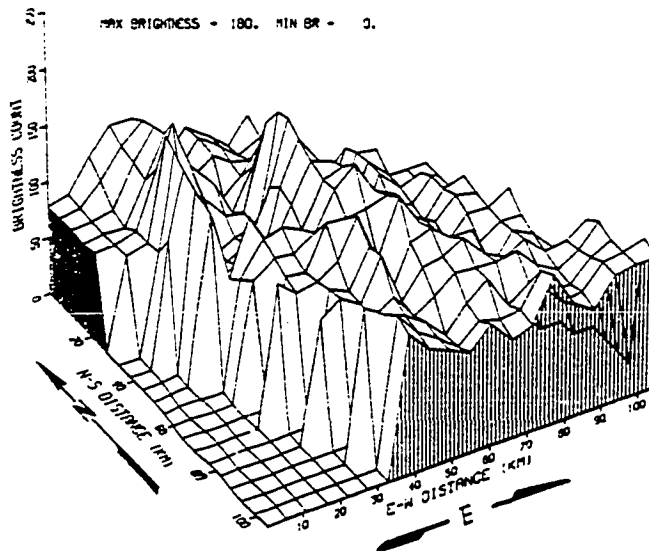


Fig. 79. Plot of objective analysis of visible data field at 2030 GMT for complex number 6.

lag zero correlations also increase with time. Hence, the correlations do reflect the developing nature of the visible reflectance field. This is the opposite of the radar and is probably due to the fact that the radar has finer resolution in space and time.

The σ 's and the ellipse semi-axes reflect the fact the storm starts out much longer than it is wide, Fig. 76, and then with time becomes broader, Fig. 77. The representative area increases with time; the increase initially corresponds well with the increase in rain rates but not at later times.

As expected the indicated velocity is greater than for the radar. The directions of motion agree with the radar direction only at 2200 GMT. As has been previously mentioned, this is due to the growth of the anvil.

Table 42. Parameters of model correlation function for convective complex number 6 visible reflectance as determined using NLP. (see pages 44 and 45)

	CASE	TIME (GMT)	σ_{x+}	σ_{x-}	σ_{y+}	σ_{y-}	σ_t	A_r	ν_0	α	ϕ	a	b	A	V	θ
			km	km	km	km	min				(°)	km	km	km ²	km/hr	(°)
SINGLE TIME XY	SM	2000	9.7	----	22.8	----	---	0.39	0.69	-0.58	164	23.6	7.6	562	----	---
	SN	2030	12.9	----	35.7	----	---	0.45	0.71	-0.55	168	36.5	10.6	1210	----	---
	SO	2100	13.3	----	32.0	----	---	0.37	0.77	-0.30	172	32.3	12.5	1270	----	---
	SP	2130	13.7	----	38.1	----	---	0.67	0.85	-0.30	173	38.3	13.0	1560	----	---
	SQ	2206	22.4	----	27.7	----	---	0.62	0.77	-0.04	175	27.7	22.3	1946	----	---
XYT ($\Delta t=0$)	M		10.1	----	30.2	----	---	0.40	0.70	-0.48	170	30.6	8.7	838	----	---
	N		12.8	----	38.1	----	---	0.51	0.79	-0.39	172	38.5	11.7	1410	----	---
	O		14.0	----	35.7	----	---	0.53	0.82	-0.28	173	35.9	13.4	1510	----	---
XYT	M		11.6	10.6	32.3	37.4	152	0.35	0.70	-0.49	170	35.3	9.5	1057	24.1	26
	N		12.1	12.7	41.7	40.9	155	0.46	0.79	-0.33	174	41.5	11.7	1520	21.9	79
	O		13.8	13.1	37.5	39.5	102	0.52	0.82	-0.23	175	38.6	13.0	1581	28.7	63

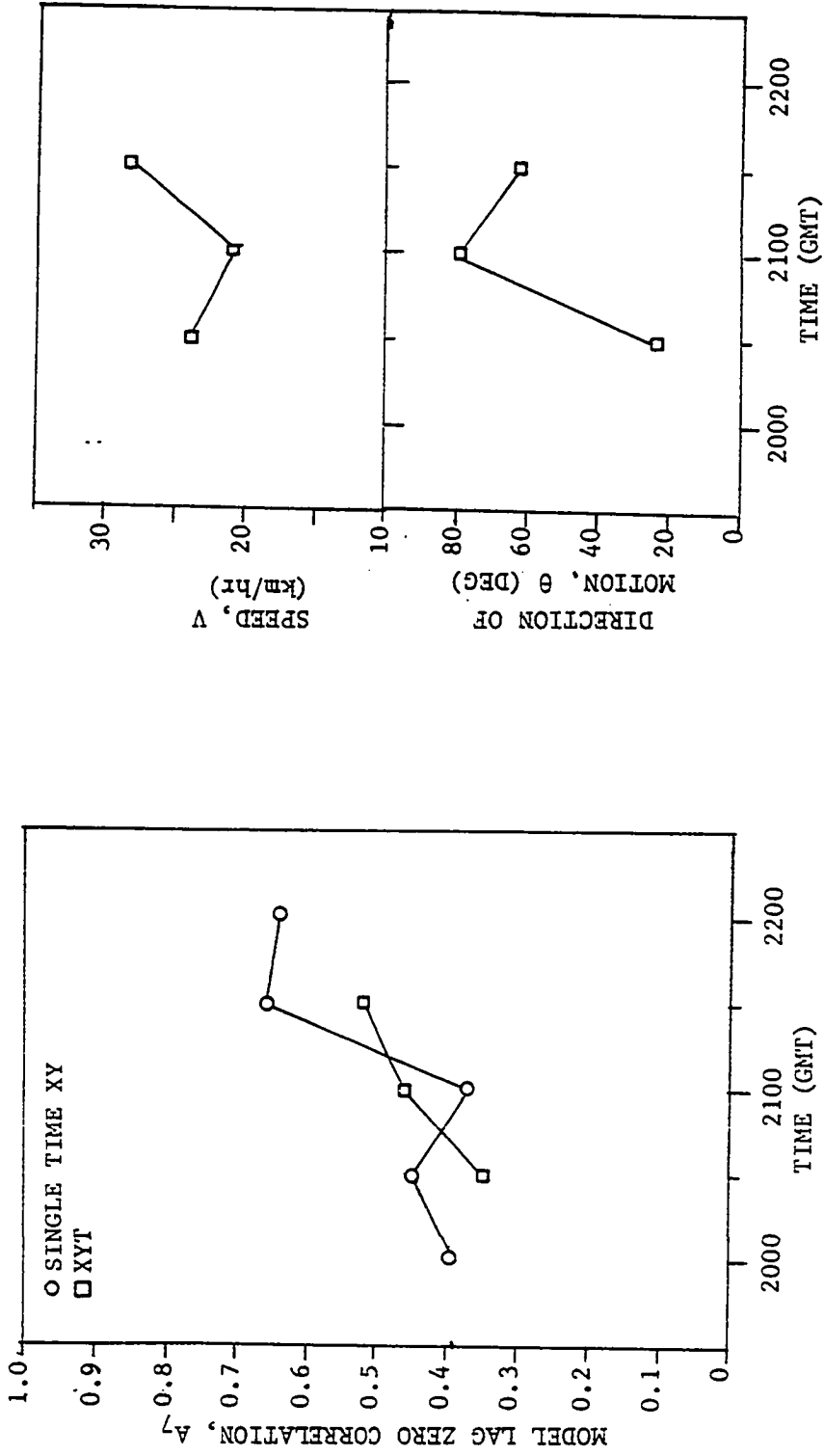


Fig. 80. Plots of model lag zero correlation (A_7), direction of motion (θ), and speed (V) for complex number 6 visible model fits.

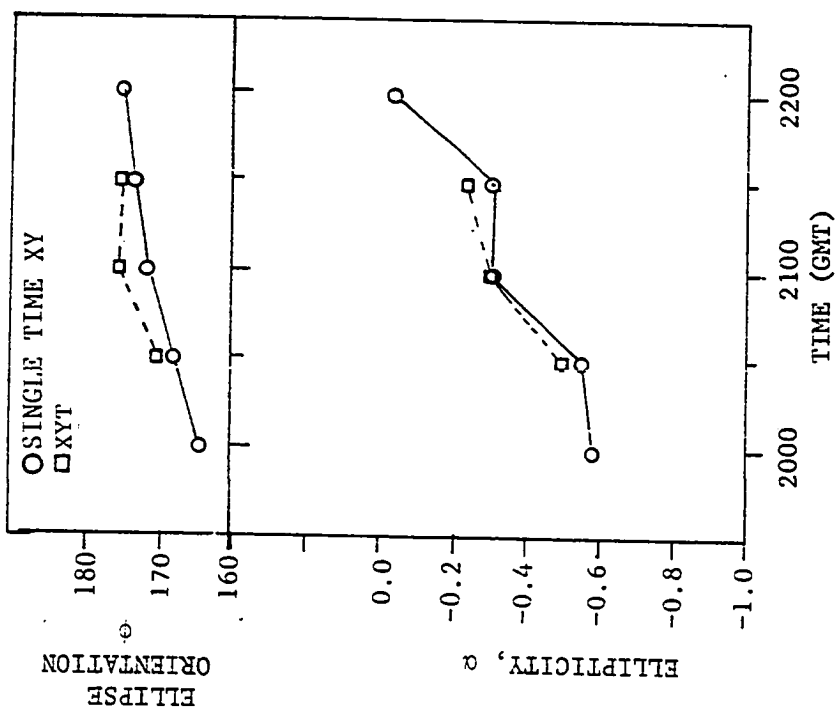
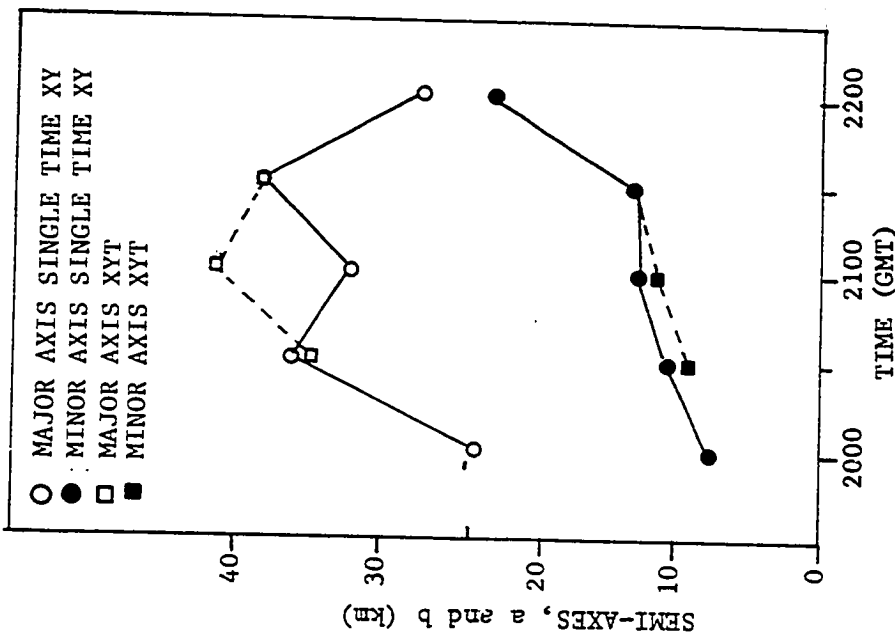


Fig. 81. Plots of ellipticity, (α), orientation angle (ϕ), and semi-axes of ellipse (a and b) for complex number 6 visible model fit.

		X LAG										
		-5	0								+5	
Y LAG	+5	-.074	-.032	0.080	0.153	0.107	0.199	0.162	0.100	0.016	-.194	-.289
		-.033	-.074	0.079	0.164	0.089	0.148	0.086	0.053	-.005	-.103	-.241
		0.036	0.047	0.111	0.140	0.125	0.133	0.065	-.001	-.033	-.176	-.217
		0.076	0.004	0.054	0.113	0.151	0.181	0.127	0.062	-.022	-.119	-.172
	0	0.075	0.007	0.055	0.094	0.243	0.292	0.164	0.091	-.002	-.116	-.126
		0.054	0.049	0.063	0.114	0.253	0.441	0.241	0.134	0.020	-.078	-.095
		0.046	-.005	0.066	0.089	0.305	0.625	0.345	0.113	0.038	-.050	-.018
		-.029	-.028	0.087	0.139	0.429	0.766	0.429	0.139	0.087	-.028	-.029
	-5	-.018	-.050	0.038	0.113	0.345	0.625	0.305	0.089	0.066	-.005	0.046
		-.095	-.078	0.020	0.134	0.241	0.441	0.263	0.114	0.063	0.049	0.054
		-.126	-.116	-.002	0.091	0.164	0.292	0.243	0.094	0.055	0.007	0.075
		-.172	-.119	-.022	0.062	0.127	0.181	0.151	0.113	0.054	0.004	0.076
		-.217	-.176	-.036	-.001	0.065	0.133	0.125	0.140	0.111	0.047	0.036
		-.241	-.103	-.005	0.053	0.086	0.148	0.089	0.164	0.079	-.074	-.033
		-.289	-.194	0.016	0.100	0.162	0.199	0.107	0.153	0.080	-.032	-.074

LAG DISTANCES IN X AND Y DIRECTIONS IS 3.5 KM EACH.

Fig. 82. Raw correlation field for complex number 6 visible case SO.

c. IR Temperature

The IR temperature field does not exhibit the multiple cloud structure as markedly as did the visible data. This is most likely due to the difference in resolution. Referring to Fig. 76 we see that it would take about 2-1/2 IR pixels to go across the westernmost cloud. As a result the maximum temperature recorded by the IR sensor will be lower than the actual peak temperature due to an averaging effect.

Table 43 is a listing of the correlation function parameters determined using the NLP procedure. Figs. 83 to 85

Table 43. Model correlation parameters for complex number 6 IR temperature. (see pages 44 and 45)

	CASE	TIME (GMT)	σ_{x+} km	σ_{x-} km	σ_{y+} km	σ_{y-} km	σ_t min	A_7	ρ_0	α	ϕ (°)	a km	b km	A km ²	V km/hr	θ (°)
SINGLE TIME XY	SM	2000	25.6	---	35.9	---	---	1.00	0.22	0.99	36	44.2	1.6	216	---	---
	SN	2030	18.0	---	30.7	---	---	0.70	0.47	-0.01	0	30.7	18.0	1730	---	---
	SO	2100	17.0	---	38.4	---	---	0.98	0.66	0.14	5	38.4	16.7	2021	---	---
	SP	2130	32.5	---	51.6	---	---	0.94	0.83	0.41	20	54.0	28.4	4819	---	---
	SQ	2206	65.5	---	36.9	---	---	0.92	0.92	0.28	78	66.7	34.8	7285	---	---
XYT ($\Delta t=0$)	M		22.8	---	88.2	---	---	0.68	0.71	0.32	5	88.5	21.5	5977	---	---
	N		40.8	---	70.8	---	---	0.73	0.81	0.63	24	76.1	29.5	7059	---	---
	O		76.4	---	53.7	---	---	0.72	0.88	0.56	61	84.2	40.3	10660	---	---
XYT	M		21.4	21.2	65.1	70.2	79	0.78	0.71	0.41	8	68.2	19.3	4134	30.8	40
	N		44.7	43.7	84.6	81.9	141	0.67	0.81	0.73	16	85.7	39.2	10548	28.9	24
	O		85.0	83.4	57.8	63.7	131	0.63	0.88	0.64	59	95.3	41.4	12406	26.4	72

are a plot of these parameters. The parameters determined for the single time XY fit for case SM (2000 GMT) does not appear to agree with the general trend. Since the raw correlation field was very small for case SM, a good fit could not be obtained. For this reason case SM will not be considered in the following discussion.

The single time XY lag zero correlation, A_7 , indicates that the IR temperature fields are very coherent. That is, the temperature fields are smooth. The area over which the temperature fields are coherent (area of correlation ellipse) increases with time. From Fig. 72 it can be seen that when case SM is considered the IR temperature correlation area curve is similar to the rain rate curve. For this complex the areas for the IR single time XY correlation fields appear to be more responsive than the equivalent areas for the visible.

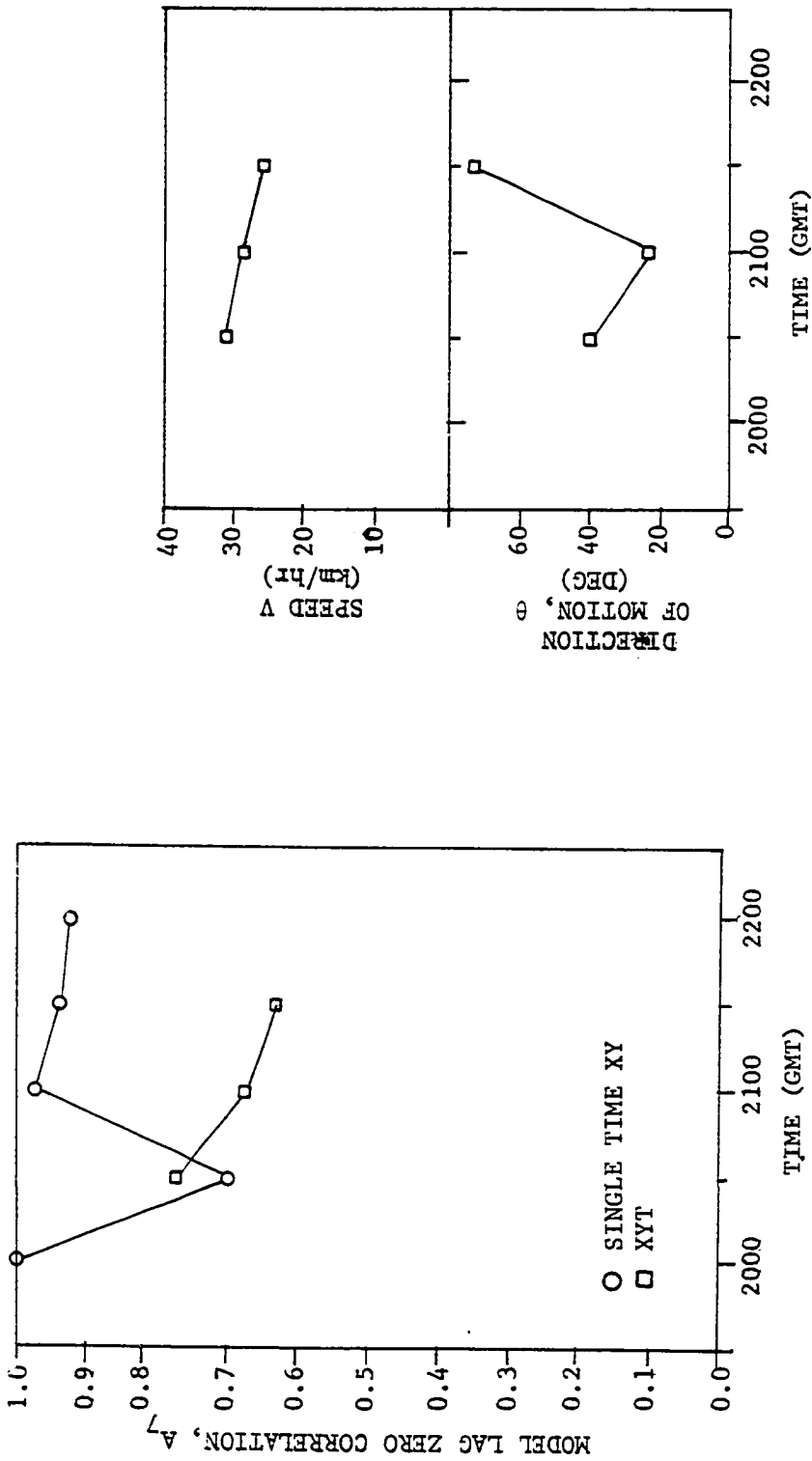


Fig. 83. Plots of model lag zero correlation (A_7), direction of motion (θ), and speed (V) for complex number 6 IR model fit.

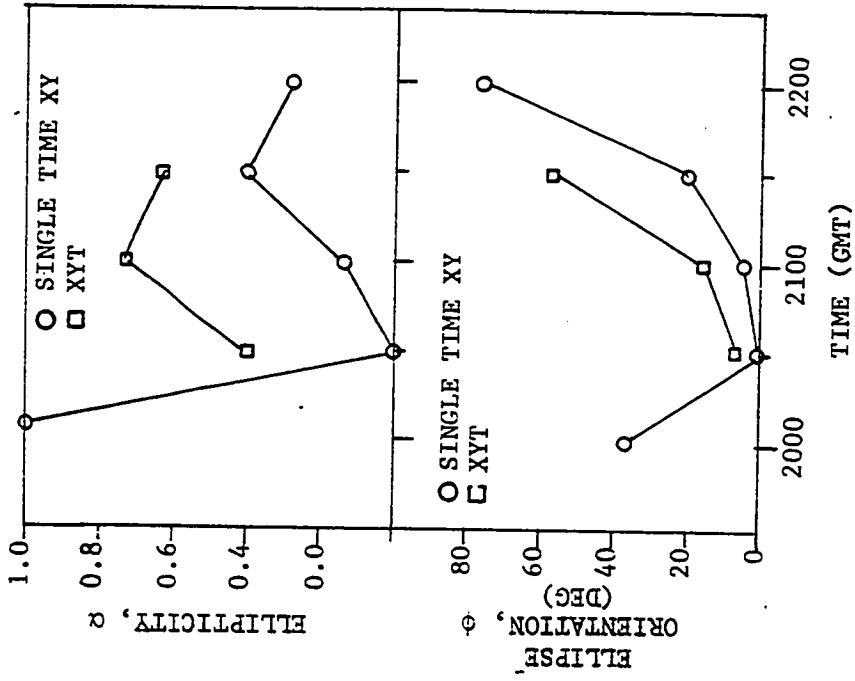
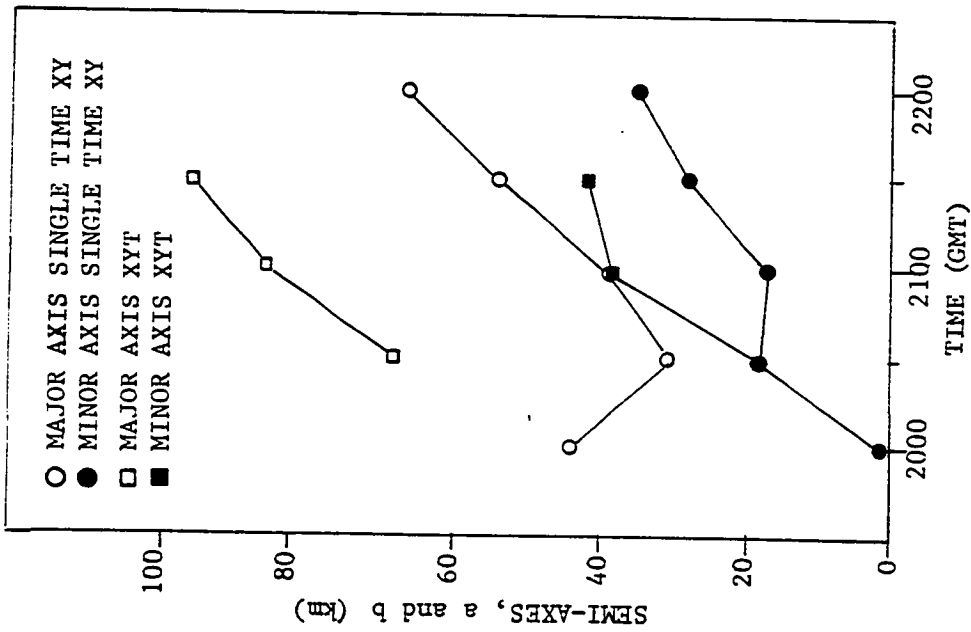


Fig. 84. Plots of ellipticity, (α), orientation angle (ϕ), and semi-axes of ellipse (a and b) for complex number 6 IR model fit.

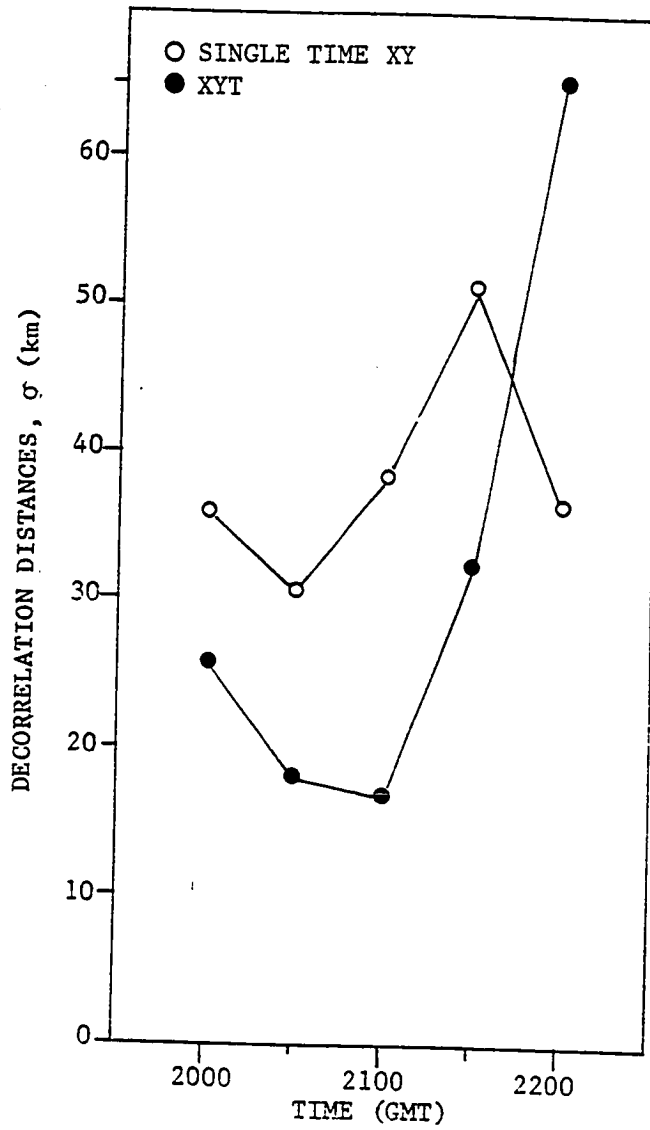


Fig. 85. Plots of XY decorrelation distances (σ 's) for complex number 6 IR model fits.

The problem of using just the σ 's for the purpose of characterizing a complex is well illustrated in the function fits. In Fig. 83 it can be seen that the σ_y parameter is larger than σ_x at first, but then for case SQ (2200 GMT) σ_x is the largest. This change does not appear at first to be a systematic change. However, when the orientation angle, ϕ , and the semi-axes, a and b , are examined there does appear to be a pattern. The elongation of the ellipse stays approximately constant with the ratio a/b varying between 1.7 and 2.3. However the orientation of the ellipse changes with time. Initially it is approximately north-south. Then the major axis turns clockwise until 1-1/2 hours later it is oriented along a heading of 78° . The reason for the reversal of the σ 's is that the largest σ is the one most aligned with the major axis of the ellipse. The corresponding parameters for the XYT function fit show approximately the same behavior. The large difference between the orientation of the IR and visible correlation ellipses is in marked contrast to their close alignment for complex number 2. This is a reflection of the different nature of the two complexes.

d. Infrared Temperature Gradient Component

The IR temperature gradient component correlation fields corresponding to a threshold of zero are noisier than those for a threshold of -1000. Because of this most of the raw correlation fields for a threshold of zero could not be fitted with the model correlation function. Table 44 lists the parameters

Table 44. XY correlation function parameters for complex number 6 IR temperature gradient component. (see pages 44 and 45)

	CASE	TIME (GMT)	σ_{x+} km	σ_{x-} km	σ_{y+} km	σ_{y-} km	σ_t min	Λ_1	ρ_0	α	ϕ (°)	a km	b km	A km ²	V km/hr	θ (°)
SINGLE TIME XY	SM	2000	16.9	----	24.0	----	---	0.61	0.86	-0.82	-33	28.2	8.2	726	----	---
	SN	2030	11.4	----	58.2	----	---	0.50	0.87	0.09	1	58.2	11.3	2065	----	---
	SO	2100	14.2	----	73.3	----	---	0.81	0.83	0.36	4	73.5	13.2	3043	----	---
	SP	2130	16.3	----	70.7	----	---	0.80	0.88	-0.08	-1	70.7	16.3	3608	----	---
	SQ	2206	31.5	----	122.2	----	---	0.74	0.87	0.78	12	124.7	19.4	7616	----	---
XYT ($\Delta t=0$)	M		20.0	----	12.8	----	---	0.66	0.79	-0.63	-63	21.9	9.0	620	----	---
	N		40.7	----	102.2	----	---	0.68	0.98	0.83	19	107.8	21.5	7290	----	---
	O		MISSING													
XYT	M		DID NOT CONVERGE													
	N		40.8	41.5	108.2	106.9	70	0.69	0.98	0.84	19	113.2	21.2	7530	33.5	293
	O		24.1	24.5	98.6	105.3	61	0.63	0.87	0.58	8	102.9	19.6	6349	45.8	90

of the function fits to the single time XY correlation and XYT correlations for the fields corresponding to a threshold of -1000. The model lag zero correlation, ellipse orientation, and semi-axes of the correlation ellipse are plotted in Fig. 86.

The temperature gradient component fields appear to be fairly coherent in space. This applies for both thresholds even though the thresholds' zero fields were noisier. The correlation ellipses are both broader and longer than the corresponding IR correlation ellipses. Also note that the orientation of the correlation ellipse is more constant than for the IR. A comparison of the gradient component field with the temperature field seems to indicate that the orientation of the IR correlation ellipse may not be the vector most useful for our purpose.

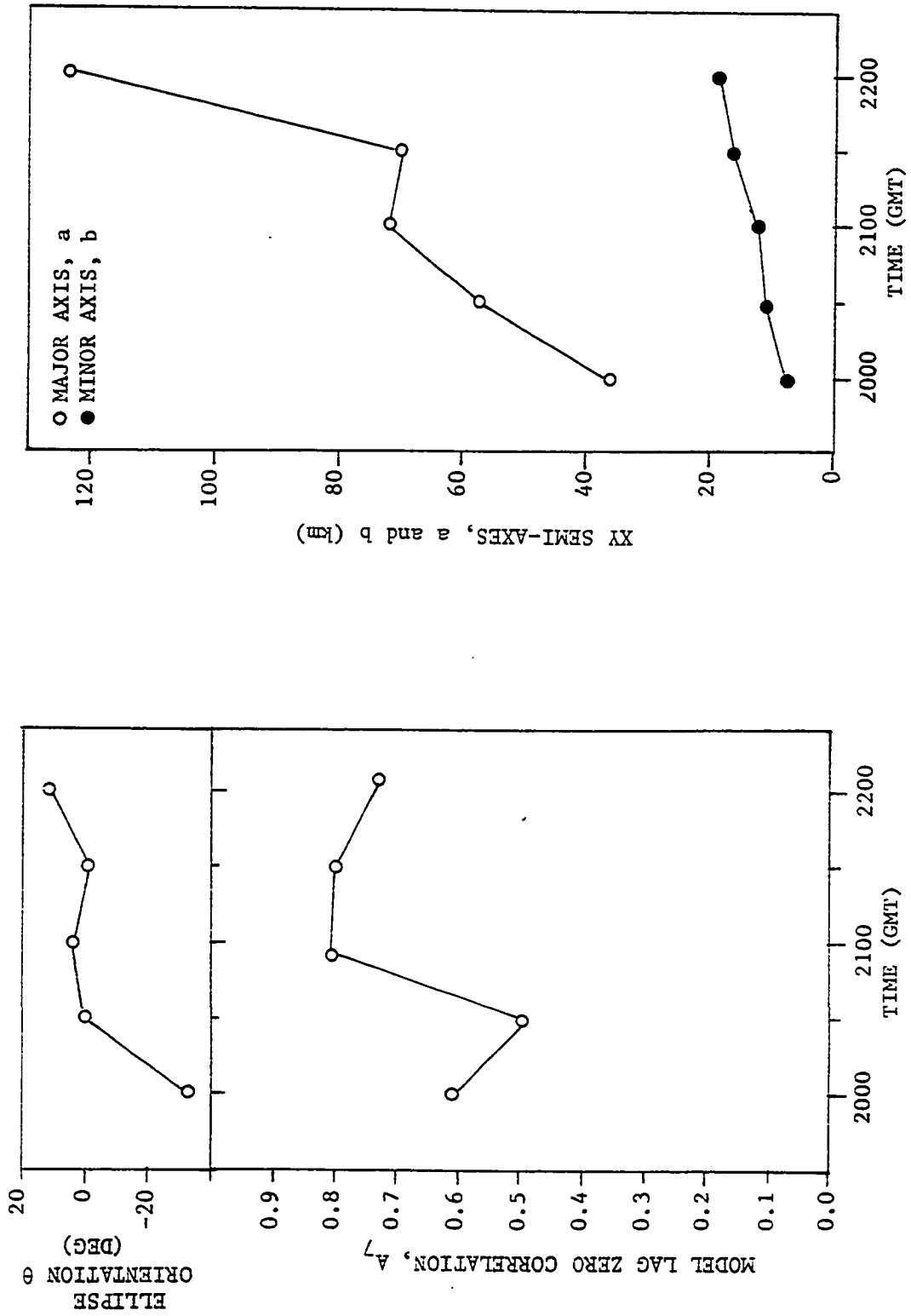


Fig. 86. Plots of model lag zero correlation (A_7), ellipse orientation (ϕ), and ellipse semi-axes for complex number 6 IR temperature gradient component.

e. Infrared Temperature Cross Visible Reflectance

The IR temperature cross visible reflectance correlation fields are highly variable. The single time XY cross-correlation fields are very lumpy and have several significant maxima. Table 45 lists the significant maxima and their corresponding lags. The values listed one above the other in cases SO and SP are adjacent and are both reported because their magnitudes were so close. Even though the positions vary it appears that the magnitude of the cross-correlation appears to be increasing with time. The magnitude of the correlation closest to lag zero is continuously increasing with time. Also the displacement seems to be decreasing.

Another consistent feature of the pattern is that even though the shape of the positive correlation region varies considerably it is always skewed toward the positive X direction. This indicates that the IR temperatures are more correlated with the visible reflectance to the east than to the west. Fig. 87 is a plot of an east-west cross section of two data fields that might give rise to such an east-west correlation structure.

Because of the highly variable nature of the single time XY correlation fields it was felt that nothing would be gained by analysis of the XYT correlation fields.

f. Infrared Temperature Gradient Component
Cross Visible Reflectance

After the analysis of the visible reflectance and IR temperature gradient component auto-correlation fields, it was felt

Table 45. Cross-correlation at maxima and corresponding lags for single time IR cross visible XY fields (bin size 6 km by 8 km). (see page 45)

Case	Local Maximum		
	Correlations and Lags		
SM	0.388 (2,-2)	0.549 (-3,-4)	0.493 (0,4)
SN	0.443 (-1,3)	0.428 (-5,4)	
SO	0.467 (-1,0)	0.584 (3,5)	
	0.466 (-1,1)		
SP	0.641 (1,0)	0.580 (4,6)	
	0.655 (1,-1)		

* Correlation (X lag, Y lag)

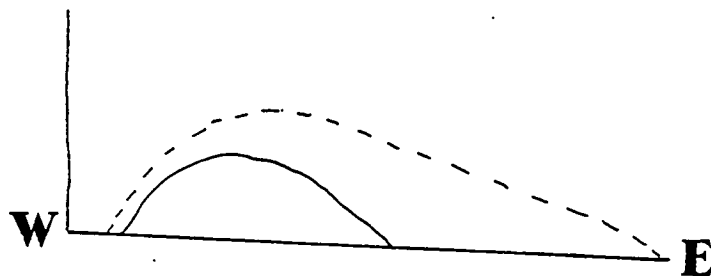


Fig. 87. E-W cross section of two data fields that would yield a correlation field skewed toward the east.

that the cross-correlation fields between these variables would also be highly variable. This expectation was upheld upon examination of the single time XY correlation fields. As has been seen in the previous cases the cross-correlation fields corresponding to a threshold of zero is significantly more noisy. There does appear to be significant correlation between these variables. For the fields corresponding to a threshold of -1000 the smallest maximum is 0.301 at 2000 GMT and the largest maximum is 0.584 at 2130 GMT. There is also a tendency for the maxima to be at negative X lags and positive Y lags. This implies that the temperature gradient component has a tendency to be more correlated with the visible reflectance to the northwest.

g. Radar Rain Rates Cross Visible Reflectance

The correlation between the radar rain rates and the visible reflectance for this convective complex was difficult to analyze. Only three cases SN (1930), SO (2100), and SQ (2200) of the possible four single time XY correlation fields were available for analysis. The structures of the fields vary for the cases; however, they all do indicate a region of positive correlation about lag zero. The maximum correlation lies due north in all three fields. This indicates that the radar rain rates are most correlated with the visible reflectance to the north about 5 km if the navigation errors are small. The maximum significant cross-correlation reported in all of the fields was 0.420.

h. Radar Rain Rates Cross Infrared Temperatures

As with the radar cross visible there are only four cases. However we have single time XY cross-correlation fields for all four. Table 46 is a listing of the maximum correlations and the corresponding lags at which they occur. The amount of displacement of the maxima from lag zero seems to indicate that the satellite data was navigated too far north. However, the magnitude of the displacement is not consistent with the magnitude of the displacement found for the radar rain rates cross visible reflectance, being larger by a factor of up to eight. If the navigation of the satellite data was shifted southward to reduce the magnitude of the displacement for the radar cross IR temperature, then the displacement for the radar cross visible would be shifted to the south by a corresponding amount.

Table 46. Cross-correlations at local maxima and corresponding lags for single time radar cross temperature XY fields (bin size 8 km by 10 km). (see page 45)

Case	Local Maximum Correlations and Lags	
SN	no significant correlation	
SO	0.490 (1,3) *	
SP	0.415 (1,4)	0.220 (-2,2)
SQ	0.375 (3,4)	0.420 (-3,0)
* correlation (X Lag, Y Lag)		

There is significant correlation between the radar rain rates and IR temperature. However, as has been the case previously the location of the maxima moves about considerably. It is felt that not all of this movement is due to navigation

errors, but represents the true changing nature of the correlation structure. The reasoning behind this is based on the variation of the location of the maximum cross-correlation between the IR temperature and visible reflectance. Since it is not likely that variation is due to navigation error, it is reasonable for some of the variation to show up in the radar cross IR temperature correlation fields. Due to this variation of the maximum and the presence of multiple maxima the XYT cross-correlation fields will not be analyzed.

i. Radar Rain Rates Cross Infrared Temperature
Gradient Component

The single time XY correlation fields are very noisy for both thresholds. There is a hint of a pattern in the correlation fields for cases SO (2100), SP (2130), and SQ (2200). There is an area of positive correlations generally oriented north-south but varying in overall shape. There is also a tendency for higher correlations at the northern and southern ends of the positive regions. The magnitude of the displacement is on the order of 20 to 30 km which seems to be rather large. The largest cross-correlation found in the fields corresponding to a threshold of -1000 was 0.393 with an average of 0.320. The corresponding values for a threshold of zero are a maximum of 0.459 and an average of 0.405. There was a maximum correlation of 0.635 for case SN (threshold of zero), however there is some question as to its significance because the number of product pairs was very low and it was not part of any general pattern.

CHAPTER VI

SUMMARY AND CONCLUSIONS

In the previous chapters the usefulness of rainfall estimation using satellite data was stated followed by brief descriptions of other current efforts toward this end. Then an objective analysis scheme that might be used to obtain estimates of surface rainfall from satellite imagery was outlined. In order to determine the feasibility of this approach it was proposed that the auto- and cross-correlation structure of radar derived rain rates and satellite visible reflectance and IR temperature be investigated. To this end four convective complexes were analyzed in considerable detail. The following is a summary of the results for these four convective complexes.

The area of the correlation ellipse does appear to be correlated with the radar rain rates. The amount of correlation is not the same for different variables and different storms; however, this should be expected. Figs. 88 and 89 show scatter diagrams of radar rain rate and visible reflectance correlation areas versus volumetric rain rate. In the diagram for the radar rain rates it is seen that there are at least two groupings, possibly three. The least squares straight lines for each

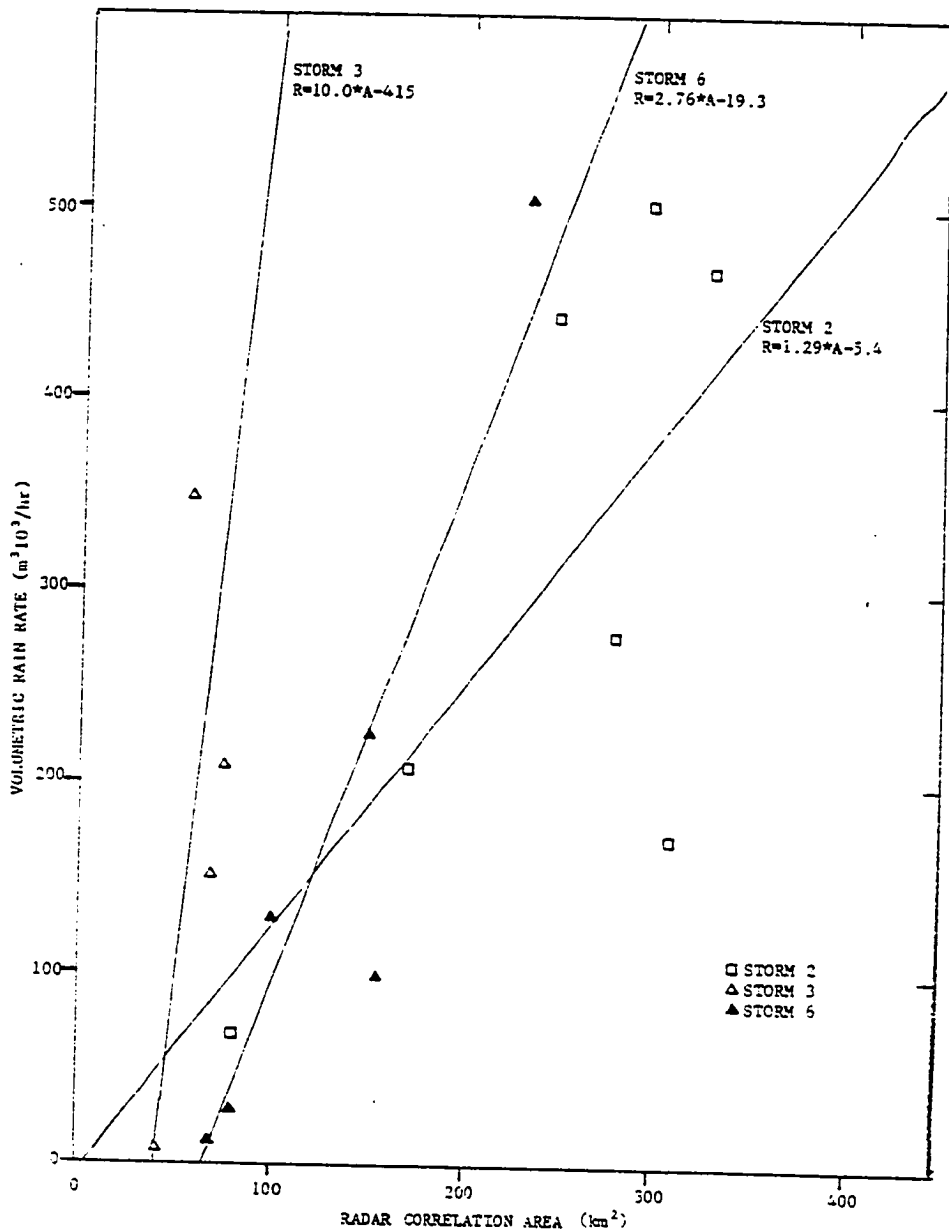


Fig. 88. Scatter diagram of radar rain correlation area versus volumetric rain rate.

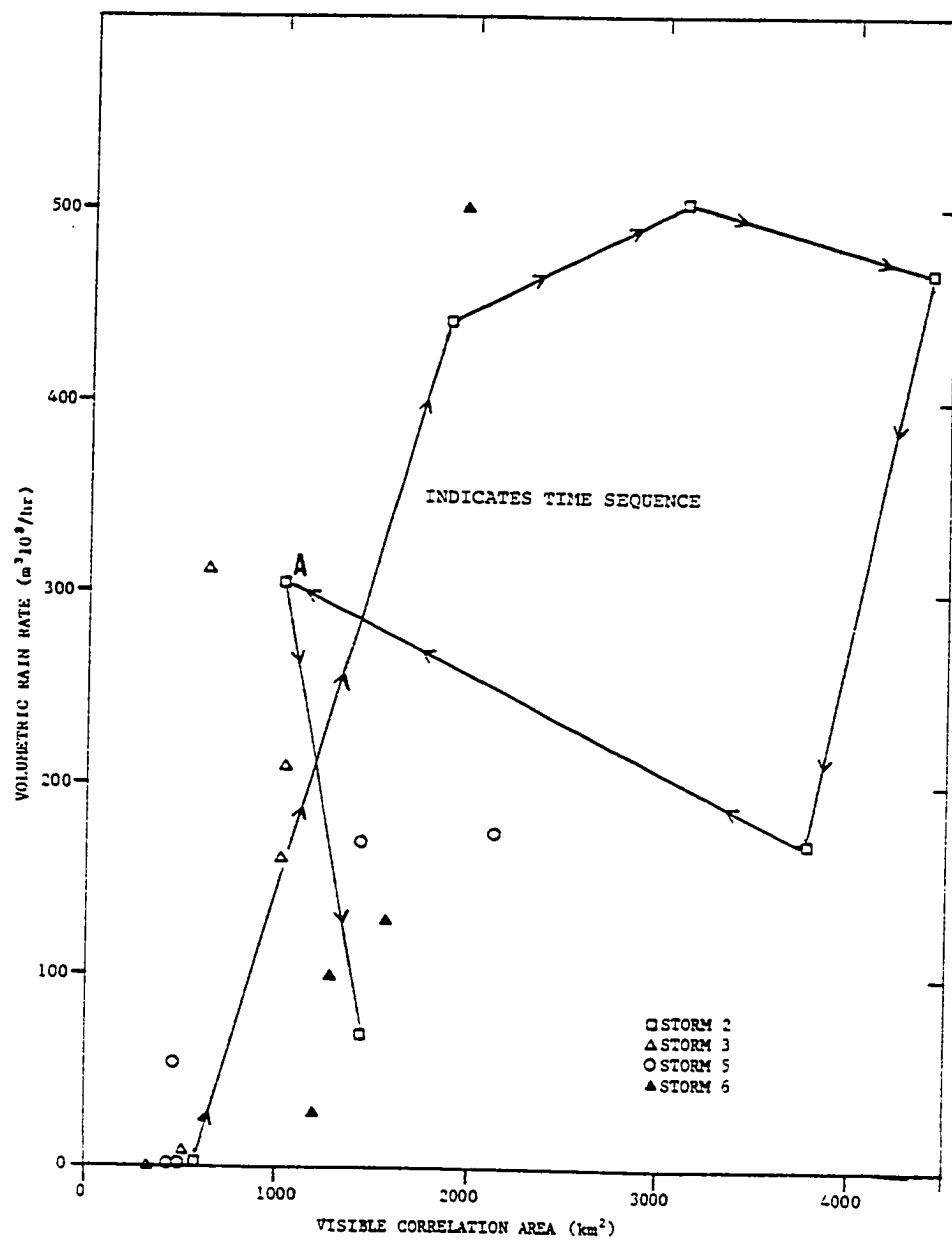


Fig. 89. Scatter diagrams of visible reflectance correlation area versus volumetric rain rate.

complex are mainly for reference as the number of values used in finding the fits was small. Complex number 3 values are distinct from those for complexes 2 and 6. The difference between complexes 2 and 6 is not as clear. This is an indication that a relationship between the area of the correlation ellipse and the radar rain rates might be developed with more data. Several investigators use a similar relationship to relate actual radar echo area to rain rate. The values for complex number 3 do not indicate the presence of any obvious relationship.

The scatter diagram for the visible reflectance area versus volumetric rain rate seems to indicate a different relationship exists during the developing and dissipating stages. However, when one considers that the point at A occurs during the dissipating stage of the storm, some uncertainty is introduced. When one refers to Figs. 12 and 53 it is seen that as has been mentioned earlier the visible correlation area appears to lag the rain rates by approximately 30 minutes. The scatter diagram was replotted, Fig. 90, with the visible correlation area shifted backward in time 30 minutes. This does not improve the results for complex number 3, but there is much improvement for the other complexes. The values for both complexes 5 and 6, both in the developing stage, tend to cluster together and indicate a common linear relationship. Also the values for complex number 2 seem to indicate a fairly linear relationship when one ignores the point at B. This is probably justified as the point at B occurred very early in the life

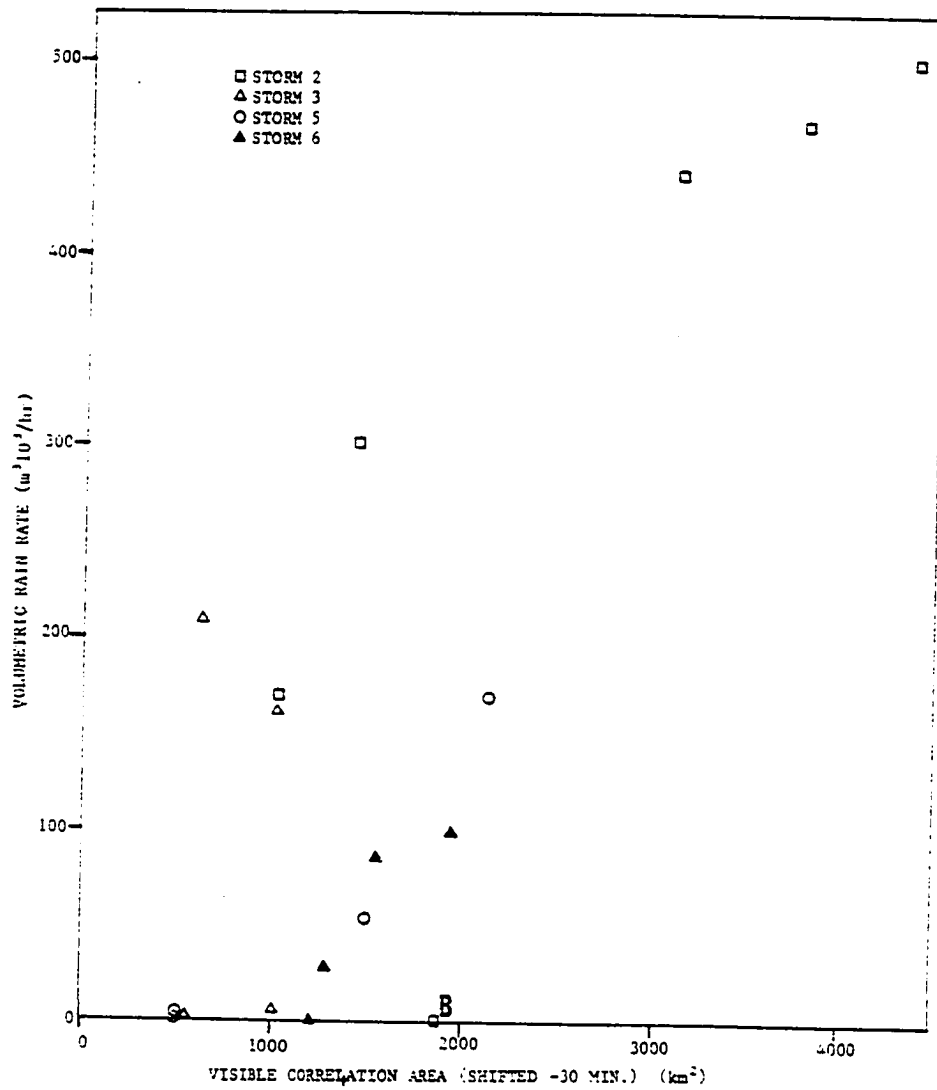


Fig. 90. Scatter diagram of visible reflectance correlation area (shifted -30 minutes in time) versus volumetric rain rate.

of the complexes when the indicated rain was very light.

Not much could be determined about the IR temperature correlation areas as the data were sparse. Referring to Figs. 12 and 72 it can be seen that the IR temperature correlation areas appear to be related to the rain rates as well as the visible correlation areas.

It was stated in Section 2, Chapter III, that the correlation ellipse semi-axes, a and b , were independent of the orientation of the ellipse. This allows one to present and characterize the development of a convective complex with time in a consistent manner. This was illustrated with several examples in the discussion of the individual complexes: complex number 2 radar, complex number 3 visible, complex number 6 radar, and complex number 6 IR temperature. There is also some indication that the ratio of the semi-axes, a/b for the IR temperature reflects the anvil growth better than the equivalent ratio for the visible reflectance.

There are other aspects of the relationship between rain rates and the satellite parameters. Table 47 is a listing of the maximum cross-correlations for each convective complex radar rain rate cross satellite. From the table it is clear that there is an indication that the less fragmented a complex is the better the cross-correlation. This is because fewer cells are being composited. This compositing would not make any difference if the cells were identically manifested in the radar returns and the satellite measurements for each time.

Table 47. Maximum radar rain rates cross satellite correlations for each convective complex. (see page 45)

Convective Complex	Radar Cross Visible	Number of Radar Cells	Radar Cross IR	Number of Radar Cells
2	0.530	1	0.526	1
3	0.356	2	0.345	4
5	0.383	4	0.295	4
6	0.420	3	0.490	3

The amount of correlations seems to vary considerably and is most variable during the developing stage of the convective complex. As illustrated in convective complex number 2, once the complex is well developed, the cross-correlation can be large. In general the radar rain rates appear to be equally correlated with both the visible reflectance and the IR temperature. There is an indication though that the radar may be more correlated with the visible reflectance than the IR temperature during the developing and dissipating stages. There is also significant correlation between the IR temperature and visible reflectance. The magnitude of the cross-correlation was not as large as expected based on previous work (Eddy and Hembree, 1977, and Eddy, 1978). The smaller magnitudes can be attributed to the smaller scale storms that were involved in this study. The storms in the previous studies were very large mature complexes with rain swaths

over a hundred miles long. On the other hand the current complexes were much smaller (at least for the period available) with rain swaths in the tens of miles. This holds even for convective complex number 2 for which we have essentially the entire life cycle.

The location of the maximum IR cross visible in the single time XY correlation fields was variable in most cases. This may reflect actual changes in the cross-correlation structure or relative navigation errors. It is felt that some of this variation is due to navigation problems even though both data fields represent satellite data for the same time period. This is based on the size of the offset and the magnitude of the changes in the offset from case to case within a given convective complex. The IR data was navigated with respect to the visible using a procedure suggested by Dr. David Reynolds at Colorado State University based upon how they generated the data sets. However, I do not feel that the procedure was adequate.

The navigation error also affected the determination of the direction of motion for all XYT correlation fields involving satellite data. The directions of motion determined agreed well with estimates made by examining plots of the satellite data; however, these are also in error if the navigation is in error. The agreement though does illustrate that when the navigation is correct then an estimate of the direction of motion can be determined. This is further backed up by the

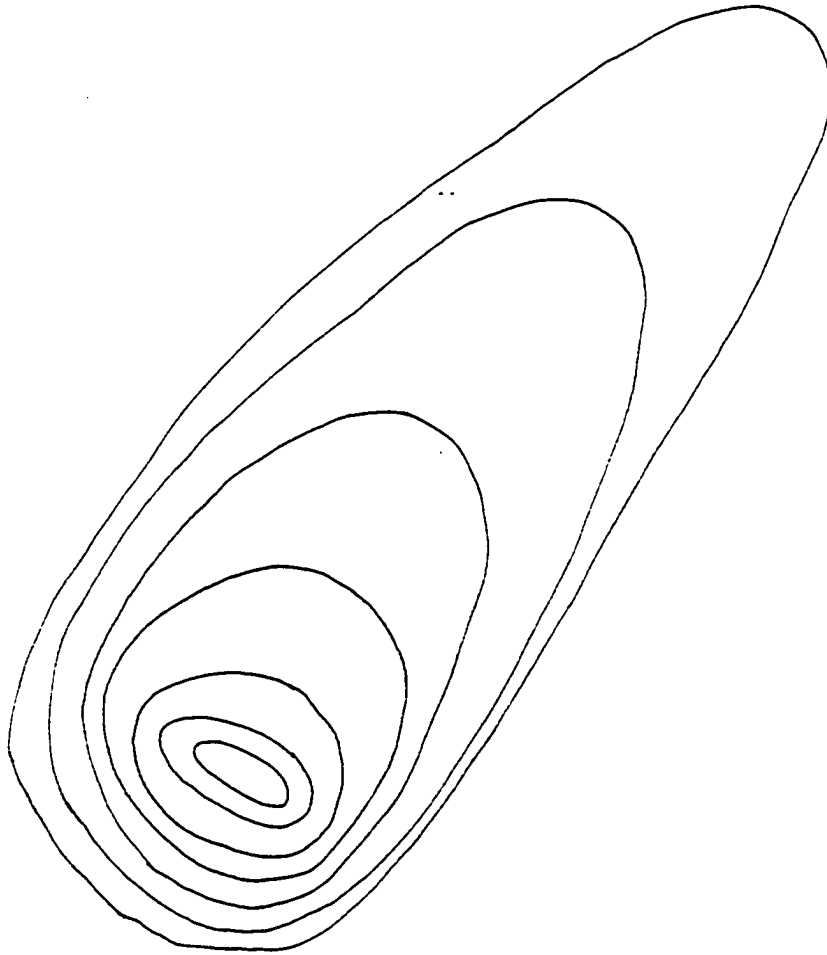


Fig. 91. Example of IR temperature field that would result in the major axis of correlation ellipse not parallel to axis of anvil.

directions of motion determined for the radar rain rate autocorrelations. For all complexes the objectively determined directions agreed well with those obtained from an examination of plots of the raw data fields.

However, the navigation error was large enough that it prevented the determination of the offset distances, d , and the offset direction, γ , in most of the cross-correlations. It also rendered many of the XYT cross-correlation fields difficult to interpret because of the compositing performed. One possible exception was complex number 3 where it appeared that the satellite pattern was slightly displaced to the north-northeast, downwind, of the radar.

The method used to define the IR temperature gradient component needs to be reexamined. Presently the temperature gradient is determined and then the component along the major axis of the IR correlation function is found. The reasoning was (Section 3, Chapter 4) that the orientation of the major axes should parallel the downwind direction. As it turns out this is not always true. In the convective complexes studied it is estimated that the differences in these directions were at times as large as 30° .

It is believed that this is due to two possible influences. First, two or more cells may have developed side by side across the axes of the anvil. The cold tops corresponding to these cells then merge resulting in the cloud top temperature distribution shown in Fig. 91. Notice that one could define two ellipse major axes: one through the ellipse formed

by the warmer temperatures (anvil) and one through the ellipse formed by the colder temperatures. When one finds the correlation structure of the entire field the major axes of the correlation ellipse represents a composite of these and would, therefore, not be parallel to the major axes of the anvil. Secondly, a single cell may be developing across the anvil axes and a similar cloud top pattern would develop with the same effect.

The result is that the temperature gradient component fields tend to be more parallel to the axes of the anvil than perpendicular to it. Because of this the actual cross-correlation of the gradient field with the other data fields could not be accurately determined. There is indication though that there is significant correlation between the radar rain rates and the IR temperature gradients.

It appears that it should be possible to obtain function fits to most of the auto-correlation fields for the purpose of classifying the complexes. A more complicated correlation model will be required to represent the structure of the cross-correlation fields. However, the IR temperature cross visible reflectance cross-correlation field can often be fitted with the model correlation function. This is especially true after the storm has developed. If objective analysis and/or sensor placement studies are to be performed using these fields a method using smoothed versions of the raw correlation fields must be developed for use where the current correlation model is not appropriate.

One of the major problems encountered was the size of the radar and visible satellite data fields. Any implementation of an objective analysis scheme using these fields would require at least a rewriting of existing programs to restructure the calculation and data management procedures. In addition the use of computer systems with larger memory capacity and greater speed would be very beneficial. A computer system with vector operations would also greatly simplify and speed up execution.

It has been demonstrated that there is significant correlation between the radar rain rates and the satellite parameters and that further study should be pursued. Of the two types of correlation fields calculated (XY and XYT), the single time XY correlation fields seem to offer the best prospect for further investigation. The XYT correlation fields are fairly well behaved for the auto-correlations but are distorted for most of the cross-correlations. This is due to the changing nature of the convective complex and the multimodal structure. Also the areas of the model correlation ellipse for the single time XY correlation fields tend to reflect the changes in the rain rates more closely than do the XYT model correlation areas. Also the development of the convective complexes can be more easily followed and characterized using the correlation ellipse semi-axes, a and b , and the ellipse orientation, ϕ , instead of the function parameters of ellipticity and decorrelation distance. To establish a better understanding of the correlation structure,

equivalent studies need to be performed on larger scale storms and on more storms for which the entire life cycle is available. Additional factors that could be examined are

1. the time change in the visible reflectance,
2. the time change in the IR temperature,
3. different thresholds for the visible reflectance and the IR temperatures used in determining the correlation fields,
4. correlations between dichotomized variables such as rain/no rain and cold/warm.

BIBLIOGRAPHY

- Barrett, E.C., 1970: The estimation of monthly rainfall from satellite data. Mon. Wea. Rev., 98, No. 4, 322-327.
- Brady, P.J., 1976: Multivariate experimental design in meteorology, Ph.D. dissertation, University of Oklahoma, 121 pp.
- _____, Michael Poellot, and Melvin Schroeder, 1979: Radar climatology for HIPLEX 1976-1978, 7th Conference on Inadvertent and Planned Weather Modification. Preprint October, Banff, Canada.
- Brandes, E.A., 1975: Optimizing rainfall estimates with the aid of radar. J. Appl. Meteor., 14, 1339-1345.
- Cadavid, H., G. Mejía, and H. Crutcher, 1978: An application of satellite imagery to convective rainfall evaluation in the tropics. Proceedings of the Third Conference on Hydrometeorology, Bogota, Columbia, Aug. 1979, 34-40 pp.
- Crawford, K.C., 1977: The design of a multivariate mesoscale field experiment. Ph.D. dissertation, University of Oklahoma, 157 pp.
- Eddy, A., 1963: Kinematic divergence and large scale energy conservation. Artic Meteorological Research Group, McGill University, Montreal, Publication No. 60, Scientific Report No. 8.
- _____, 1967: Two-dimensional statistical objective analysis of isotropic scalar data fields, Report No. 5, Atmospheric Science Group, The University of Texas. (condensed version published as "The Statistical Objective Analysis of Scalar Data Fields," J. Appl. Meteor. Vol. 6, 597-609.
- _____, 1973: The objective analysis of atmospheric structure. J. Meteor. Soc. Japan, 51, 450-457.
- _____, 1974: An approach to the design of meteorological field experiments. Mon. Wea. Rev., 102, 702-707.

- _____, 1976: Optimal raingage densities and accumulation times: a decision-making procedure. J. Appl. Meteor., 15, 962-971.
- _____, and L. Hembree, 1977: Space time sampling from SMS satellite data required to define convective storms, Final Report, WSMR Contract DAAG29-0-0100. 38 pp. (condensed version published in J. Meteor. Soc. Japan, 57, 199-202.)
- Eddy, A., and L. Hembree, 1978: The effects of rain gage densities on the analysis of storm total rainfall from convective complexes. Final Report, U.S. Bureau of Reclamation, Contract 7-07-83-V007, Sept., 1978, 82 pp.
- _____, and P. McDonald, 1977: An examination of objective analysis accuracy using MANOVA. Proceedings of Fifth Conference on Probability and Statistics in Atmospheric Sciences, Las Vegas, NV, Nov. 1977, 72-74.
- Follansbee, W., 1976: Estimation of daily precipitation over China and the U.S.S.R. using satellite imagery. NOAA Technical Memorandum, NESS 81, 30 pp.
- _____, and V. Oliver, 1975: A comparison of infrared imagery and video pictures in the estimation of daily rainfall from satellite data. NOAA Technical Memorandum, NESS 62, 1975, 14pp.
- Gandin, L.S., 1963: Objective analysis of meteorological fields, Leningrad (Translated by Israel Program for Scientific Translations, Jerusalem, 1965), 235 pp.
- Griffith, C., W. Woodley, D. Martin, et al, 1976: Rainfall estimation from geosynchronous satellite imagery during daylight hours. NOAA Technical Report, ERL 356-WMP07, 106 pp.
- _____, 1978: Rain estimation from geosynchronous satellite imagery-visible and infrared studies, Mon. Wea. Rev., 106, 1153-1171.
- Hembree, L. and A. Eddy, 1978: Design and analysis of surface sensor networks for the Oklahoma 1977 severe storm observational program. University of Oklahoma, School of Meteorology Report, March, 12 pp.
- Kays, M., 1974: Optimal sampling of a stratospheric sudden warming, University of Oklahoma, School of Meteorology Report, 149 pp.
- Lacy, C., 1973: Objective analysis using modeled space-time covariances: an evaluation, ECOM-5514, Atmospheric Sciences Laboratory, US Army Electronics Command, White Sands Missile Range, New Mexico.

- Lovejoy, S., and G.L. Austin, 1979: The delineation of rain area from visible and IR satellite data for GATE and mid-latitudes. Atmosphere-Ocean, 17, No.1, 77-92.
- Martin, D. and W. Scherer, 1973: Review of satellite rainfall estimation methods, Bull. of AMS, 54, 661-674.
- Oliver, V.J. and R.A. Scofield, 1977: A scheme for estimating convective rainfall from satellite imagery, NOAA Technical Memorandum NESS86, April, 47 pp.
- Pasteris, P.A., 1975: Objective analysis of northeast Oklahoma rainfall. University of Oklahoma, School of Meteorology Report, 92 pp.
- Phillips, N.A., 1976: The impact of synoptic observing and analysis systems of flow pattern forecasts. Bull. Amer. Meteor. Soc., 57, 1225-1240, 69 pp.
- Reynolds, D., T. Vonder Haar, 1978: Satellite support to the HIPLEX activities for 1978, Annual Report, U.S. Bureau of Reclamation, Contract 6-07-DR-20020, March.
- Scofield, R.A., 1978: The use of satellite imagery for analyzing some types of synoptic scale precipitation events. National Weather Digest, February, 20-25.
- Stout, J., D. Martin, and D. Sikdar, 1979: Estimating GATE rainfall with geosynchronous satellite images. Mon. Wea. Rev., 107, No. 5, 585-598.
- Thiebaux, H.J., 1977: Extending estimation accuracy with anisotropic interpolation. Mon. Wea. Rev., 105, 691-699.
- Woodley, W.L., A.R. Olsen, et al, 1975: Comparisons of gage and radar methods of convective rain measurement. J. Appl. Meteor., 14, 909-928.
- _____, J. Augustine, S. Browner, et al, 1979: Satellite rain estimation in the U.S. high plains, an interim report to the HIPLEX program office, U.S. Bureau of Reclamation. 33 pp.
- _____, B. Sancho, and A. Miller, 1972: Rainfall estimation from satellite cloud photographs. NOAA Technical Memorandum, ERL OD-11, 43 pp.
- Yerg, M.C., 1973: A systems approach to experimental design in meteorology, University of Oklahoma, School of Meteorology Report, 81 pp.